Functional Evaluation and Development of Novel Agonists and Modulators of Neuronal Ion Channels

Thesis by

Antoinette Elisabeth Maria Blom

In Partial Fulfillment of the

Requirements for the Degree of

Doctor of Philosophy

CALIFORNIA INSTITUTE OF TECHNOLOGY

Pasadena, California

2019

(Defended May 30th, 2019)

Antoinette Elisabeth Maria Blom
ORCID: 0000-0002-7441-4893

Zo niet, dan toch.

Acknowledgements

It was quite the change when I moved out to Pasadena, being nine time zones away from my family and one from my boyfriend (now husband), but I must say that my time at Caltech has been an exceptional experience. Over the past six years, I have met numerous wonderful people, who in one way or another, have helped me grow and develop as a scientist, and as a person. So here, I would like to take the time to thank some of those people who deserve a special thanks.

First, I would like to thank my advisor Prof. Dennis Dougherty for his unwavering support and mentorship. He is not only a brilliant scientist, but also an extraordinary advisor. He gives his students a lot of independence to experiment and explore new ideas for projects. Although frustrating at times, it has taught me how to look critically at problems and develop new solutions. I am truly grateful for all his guidance and support throughout my time at Caltech. I would also like to thank Ellen Dougherty for her support and hosting lovely dinners at her and Dennis's home.

I would like to recognize the members of my thesis committee, Prof. Doug Rees, Prof. Mikhail Shapiro, and Prof. Sarah Reisman, for the wonderful discussions and encouragement over the years. I am thankful for all our meetings during which they provided me with excellent feedback on my projects and ideas.

Prof. Henry Lester has basically been a co-advisor and I very much appreciate all his input. His enthusiasm for science and extraordinary knowledge of molecular neurobiology have been inspiring. In addition, I would like to thank the members of the Lester lab, in particular Prof. Brandon Henderson, for our vivid discussions and training on the microscope, Dr. Bruce Cohen, for his advice and feedback on working with voltage-gated ion channels, Purnima

Deshpande, for keeping the lab run smoothly, and Jonathan Wang for diligently providing our group with oocytes throughout the years.

I have had the pleasure of working with several great collaborators both at Caltech and in the UK. Our collaborators at the University of Bristol, Dr. Hugo Rego de Campello and Prof. Timothy Gallagher, have been such a pleasure to work with. I appreciate our positive skype discussions about the cytisine project. I thank Katie Chan and Dr. Justin Su in the Reisman group, and Melanie Pribisko Yen for synthesizing compounds and our exciting conversations about our projects.

The work at Caltech and in particular the labs in CCE would not run as well without the awesome administrators and technical staff. I would like to thank Linda Syme, Agnes Tong, and Alison Ross for helping me out navigating the administrative aspects of CCE, Joe Drew, for managing the chemistry stockroom and facilities, Dr. David vander Velde, for his NMR expertise, and Dr. Mona Shahgholi, for all her help and support regarding mass spec.

I owe a great deal to the past and current members of the Dougherty group, who helped me become a better and more capable scientist. I cherish the stimulating discussions, camping trips, happy hours, and everyday shenanigans, which made the frustrations in grad school seem insignificant. I only overlapped briefly with Dr. Ethan van Arnam, but his papers have been very helpful. I thank Dr. Kristina Daeffler for getting me started in the biolab, and Dr. Ximena Da Silva Tavares for our interesting conversations about immigration to the US. Fortunately, Dr. Noah Duffy stayed in Pasadena after his graduation, and I have really enjoyed our friendship and his sense of humor. Dr. Tim Miles has been a great source of inspiration, I appreciate hearing about his professional endeavors after Caltech. Dr. Chris Marotta also stayed around, and it has been great to been able to walk by his office and ask a random question about a project he worked on five years ago. The life of an opus captain is not always easy, so it has been wonderful

to have had him close by as a resource. Kayla Busby is such a cheery person, and one of the people that made me excited about Caltech during my visiting weekend. Dr. Matthew Davis, the computational expert of the group, I admire his warm and welcoming personality. Dr. Clinton Regan and Dr. Oliver Shafaat are exceptional scientists and it has been a pleasure working alongside of them. Dr. Betty Wong has been a great addition to the group, I truly value her help in developing my conflict resolution skills.

Dr. Michael Post has been a great friend, opus captain and leader of North Bay Nation, I admire his aptitude for communicating science and storytelling in general. Dr. Matthew Rienzo is a marvelous scientist, and magnificent writer, but most of all a truly wonderful friend. I thoroughly enjoyed our conversations whether about science, commiserating about graduate school, or life. Paul Walton, Master of memes, is one of a kind. Besides his passion for chemistry, he shared many of his hobbies, which were generally quite enjoyable, coffee, photography, strawberries, except for the tuna and beans. I thank Catriona Blunt for our friendship and great conversations about Europe and the UK. Stephen Grant is one of the most generous and dedicated people I know. I am truly thankful for our Wednesday lunches and his entertaining, weekly email updates. Bryce Jarman is exceptionally bright, and I am sure his creativity and scientific rigor will lead him to great things. In addition, he has been a wonderful friend and I am lucky to have gotten to know him. Richard Mosesso is an excellent scientist, comedian, and caring friend, you inspire me. Our famous Pokéwalks were always a welcome break in between writing and opus runs, thanks for listening to my rants and silly stories.

I would like to thank members of my cohort, Denise Grünfelder, Sam Ho, Tonia Ahmed Daniel Torelli, with whom I shared classes and brunches in our first year, and the occasional lunch after that. Your friendship helped me through the stressful times that arose from being new at Caltech, balancing classes, trying to join a research group and adjusting to the US.

During my time at Caltech, I joined several clubs and committees. I would like to thank the members of the GSC board of directors, and the Women In Chemistry committee members, in particular Emily Blythe and Samantha Shockley. Moreover, I want to thank the active members of the Caltech West Coast Swing club, Sebastian Lee, Steven Lee, Paul Nunez, Lani Kim, and JC Bryant. You guys have truly lightened the stressful times of trying to wrap up projects by taking me to the local dances and convention weekends.

Marcus Low and Matthew Smarte, have been the best housemates I could wish for. I really enjoyed our time in the Devon together, the dinners, the games, and adventures outside the apartment. I am absolutely grateful for the many times I have enjoyed Marcus's world-class meals and baked goods, I adore his passion for food (and chemistry) and his drive to bring people together. Matt has been an amazing friend, I enjoyed sharing our passions in music (Timber!), the occasional fun run, and watching and discussing the unfolding dramas in our favorite TV shows. Matt has an excellent sense of humor and I admire his willingness to speak up against injustice. I am really lucky to have you as my friends.

In addition to the people I met at Caltech, I am fortunate to have several great friends in distant places. Helle and Steve Yi, have always supported my development as a dancer (even though I now have transitioned to WCS) and cheered for me when I got accepted to Caltech. My friends in Salt Lake City, Tony Donato, Lisa Lesniewski, Mackers, Sarah Chalupa, Nate Omana, and Rachel Jones, who are so welcoming, supportive, and fun to be around. My friends from the Netherlands, Dorota Gazy and Babette van Hazebroek, for keeping me grounded when times got rough.

I could not imagine my time at Caltech without the continuous support of my wonderful husband Asher, who encouraged me from the beginning to the end. It has not always been easy, living in different states, but he has always been there to cheer me on and help me believe in

myself. I treasure sharing our passions in dance, fitness, and talking shit. I am excited to finally move back into the same house again soon, and I can't wait to see what, and where, our next adventure will be. I would also like to thank Asher's family, Doug, Eileen, Austin, and Renee, for welcoming me into their lives. It has been a joy to spend time with you all during our family trips in Santa Fe, Vegas and our trip to Hawaii. There you have it.

Lastly, I would like to thank my family for loving and supporting me, despite me moving across the world to pursue my doctorate. My parents, Henk and Esther, are simply the best and have been there for me every step of the way. I am so grateful that we get to facetime often and that they aren't afraid to fly 11+ hours to come visit me every now and then.

Abstract

This dissertation describes studies of activation of neuronal ion channels and evaluating new ligands to modulate this process. In chapter two, we expanded the binding model of cytisine to the α4β2 nicotinic acetylcholine receptor. We also determined how C(10)-modification of cytisine impacts the key binding interactions between cytisine and its binding site. To achieve this, we used non-canonical amino acid mutagenesis to probe the electrostatic binding interactions of a novel series of C(10)-cytisine derivatives. In order to perform similar studies in the α3β4 nAChR subtype, we describe the heterologous expression of mouse and human α3β4 nAChRs in *Xenopus Laevis* oocytes in appendix one. Chapter three describes the development and functional evaluation of a novel series of pyrrolidinoindolines for agonism and modulation of the $GABA_A$ receptor. Additionally, we performed mutagenesis studies to identify the binding site of these novel ligands. Appendix two describes a different screen for activation or modulation of $GABA_A$ receptors using a set of phenolic compounds implicated in Autism Spectrum Disorder. Chapter four shifts focus to voltage-gated ion channels: in this chapter, the ultimate goal was to photochemically control the activation of VGSCs and make progress towards developing a RubpyC17-based photoswitch that could be used in an artificial retina. To this end, we determined the functional effects of several ruthenium bipyridine analogs on voltage-gated sodium and potassium channels.

Published content and contributions

Blom, A.E.M., Rego Campello, H., Lester, H.A., Gallagher, T., Dougherty, D.A. (2019). "Probing binding interactions of cytisine derivatives to the α4β2 nicotinic acetylcholine receptor." Manuscript in preparation.

A.E.M.B. participated in the conception of the project, conducted all electrophysiology experiments, analyzed the data, and contributed to writing and editing of the manuscript.

Table of Contents

List of Figures

List of Tables

Chapter 1

General introduction

1.1 Neuronal communication

The brain is an exceptionally complex organ. It contains over one hundred billion neurons that each can form ten thousand connections with other neurons, resulting in a total of a 1,000 trillion synaptic connections. Communication between two neurons is conducted by electrochemical impulses called action potentials.[1] An action potential is propagated down the axon of a nerve cell to the synapse, which is the contact point between two neurons (**Figure 1.1A**). When an electrical signal reaches the synapse, vesicles filled with small-molecules, called neurotransmitters, will fuse to the cell membrane and release these neurotransmitters in the space between two neurons, the synaptic cleft (**Figure 1.1B**). The neurotransmitters diffuse across the synaptic cleft and bind to proteins, receptors, located on the membrane of the neighboring neuron. Upon binding, these proteins undergo a conformational change that allows ions to flow across the membrane, which can either promote or inhibit the propagation of an action potential in this neighboring neuron (**Figure 1.1C**). This process is called synaptic transmission, and its regulation is crucial for various important processes such as sensory perception, muscle control, memory, and conscious thought. When parts of this signaling process fail or become defective, devastating diseases can arise. We aim to create a better understanding of the chemical component of synaptic transmission; neurotransmitter binding and receptor activation.

Among the various proteins involved in synaptic transmission are ion channels, which are integral membrane proteins that control the flow of ions into or out the cell. Some ion channels are constitutively open,[2] but many are gated. For those, channel opening can occur

upon small-molecule binding,[3,4] a mechanical stimulus,[5] or a change in local membrane potential.[6] Besides classification by way of activation, these proteins are often further categorized by their structures, functional characteristics such as ion selectivity, and, for those activated by small molecules, by their ligand. This thesis provides studies, which focus on pentameric ligand-gated ion channels and voltage-gated ion channels.

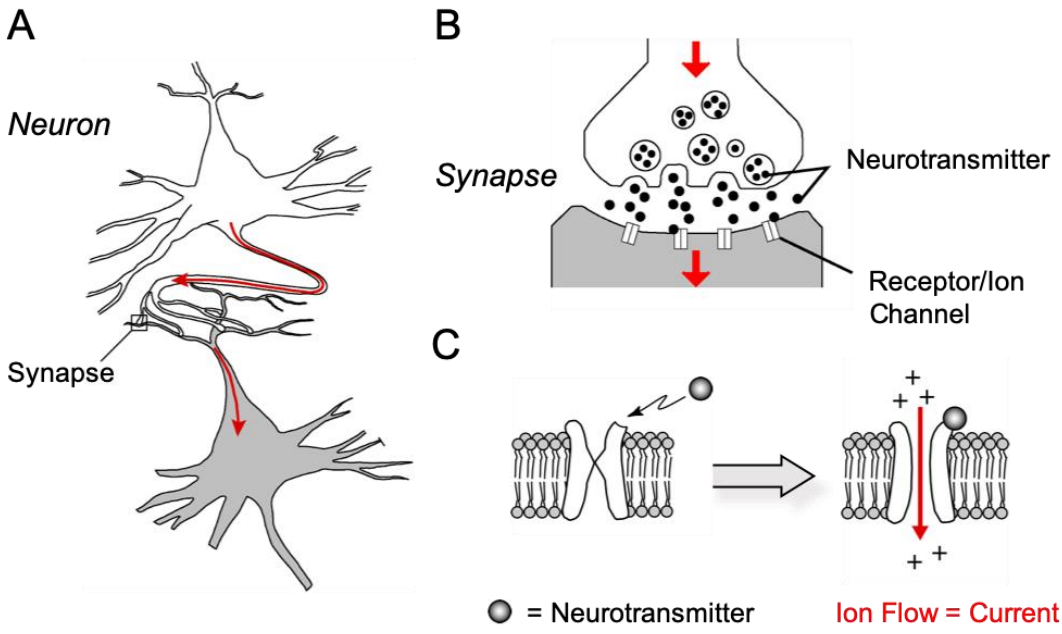

Figure 1.1 | Neuronal communication through synaptic transmission. (A) A schematic view of two neurons making contact at the synapse. The path of the action potential is highlighted in red. (B) The synapse, where vesicles fuse to the cell membrane and release neurotransmitters in the synaptic cleft. Neurotransmitters flow across and bind to receptors on the membrane of the neighboring neuron. (C) Upon binding of a neurotransmitter, ion channels will undergo a conformational change allowing ions to flow across the membrane. Figure adapted from Marotta 2015.[7]

1.2 Pentameric ligand-gated ion channels

Pentameric ligand-gated ion channels (pLGICs), also known as Cys-loop receptors, are a family of transmembrane ion channels which allow ions, such as Na^+, K^+, Ca^{2+}, or Cl^-, to cross the cell membrane upon binding of a small-molecule, i.e. a neurotransmitter. This protein family comprises both excitatory and inhibitory receptors. The excitatory receptors are cation-selective channels, consisting of nicotinic acetylcholine receptors (nAChR)[8] and type 3

serotonin (5HT-3) receptors[9], and allow for signal propagation. The inhibitory receptors are anion-selective channels, consisting of glycine receptors (GlyRs),[10] type A γ-aminobutyric acid receptors ($GABA_AR$),[11] and glutamate-gated chloride channels (GluCl),[12] which allow for signal termination.

pLGICs share the same overall architecture, consisting of five homologous or identical subunits that self-arrange around an ion-conducting pore (**Figure 1.2B and C**).[13] A single subunit contains three major domains (**Figure 1.2A**). First, a large extracellular domain (ECD) comprised of a series of β-sheets and loops. Second, a transmembrane domain (TMD) consisting of four transmembrane α-helices (M1-M4), of which M2 lines the pore. Third, an intracellular domain that mostly consists of the M3-M4 loop and is highly variable among subunits.[14] The ligand binding site lies at the interface of two subunits in the extracellular domain (yellow box in **Figure 1.2B, C**).

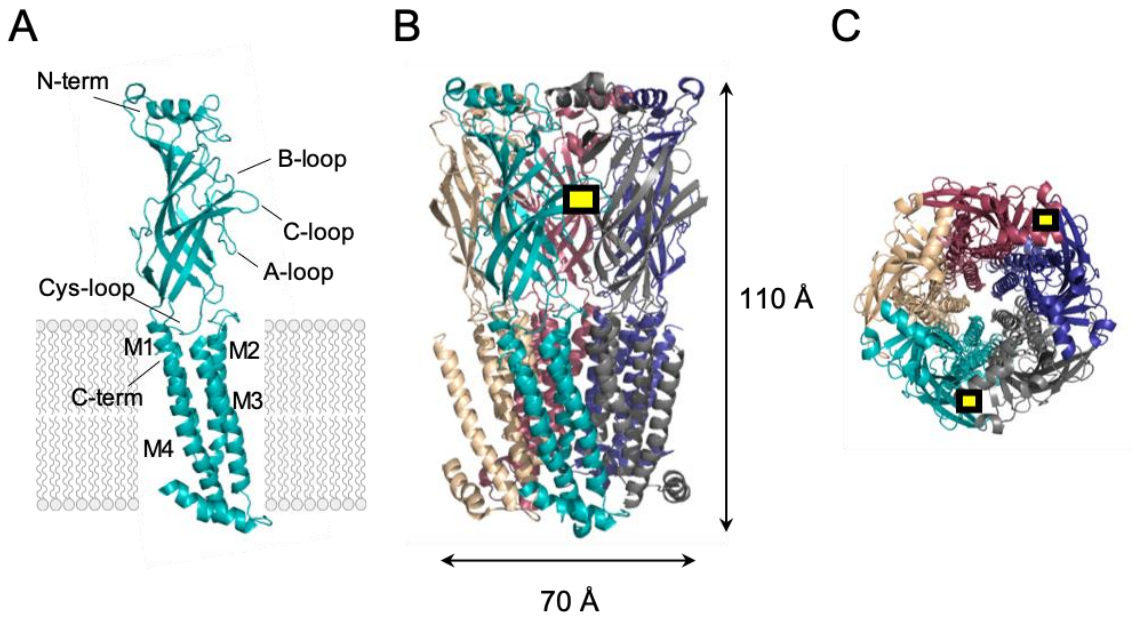

Figure 1.2 | Structural characteristics of pentameric ligand-gated ion channels. (A) One pLGIC subunit with the following structural features highlighted: the four transmembrane helices (M1-M4), N-terminus and C-terminus, the Cys-loop that gives this family its name, and the A-, B- and C-loops that line the binding pocket. (B) Side view of the α4β2 nAChR pentamer with the binding site located

at two subunit interfaces in the ECD highlighted in yellow. (C) Extracellular view of the protein looking into the pore with binding pockets highlighted in yellow. (PDB ID: 5kxi)

Until 2001, researchers used mutagenesis and biochemistry experiments to acquire all information regarding receptor composition and the binding site.[15] The first reported crystal structure appeared in 2001 for an Acetylcholine Binding protein (AChBP), which is a soluble protein with high structural homology to the extracellular domain of nAChRs.[16,17] Since then, several high-resolution structures of full-length eukaryotic receptors have been reported, among which are the human α4β2 nAChR[18] and the human α1β2γ2 $GABA_A$ receptor.[19] Numerous mutagenesis studies of many pLGICs combined with structural data have enabled us to rationalize trends in ligand selectivity based on noncovalent binding interactions.[20] Of the pLGIC family, this dissertation focuses on nAChRs and $GABA_A$Rs.

1.2.1 Nicotinic acetylcholine receptors

Nicotinic acetylcholine receptors (nAChRs) are composed of combinations of five subunits, the α1–10, β1–β5, γ, δ and ε subunits.[21] Various combinations of subunits are present in both the central nervous system (CNS) and peripheral nervous system (PNS) (**Figure 1.3**). The α1, β1, γ, δ and ε subunits form the fetal and muscle type receptors, whereas neuronal subtypes consist of either five identical subunits (α7, α8, α9) or they are heteromers consisting of combinations of α2- α6 or α10 and β2-β4 subunits.[22] The α4β2 and α7 subtypes are the most abundant in the brain.[22,23] The next most prevalent is the α3β4 subtype, which has been historically thought to only be expressed in the autonomic ganglia.[24] Each subtype is localized differently in the CNS and demonstrates distinct pharmacology. The endogenous ligand for nAChRs is acetylcholine, but most neuronal subtypes are also activated by nicotine, which is the psychoactive component in tobacco (**Figure 1.4D**).[25] nAChRs have been implicated as

targets for various neural diseases, such as nicotine addiction, epilepsy, Alzheimer's disease and neuromuscular diseases.[23,26–31]

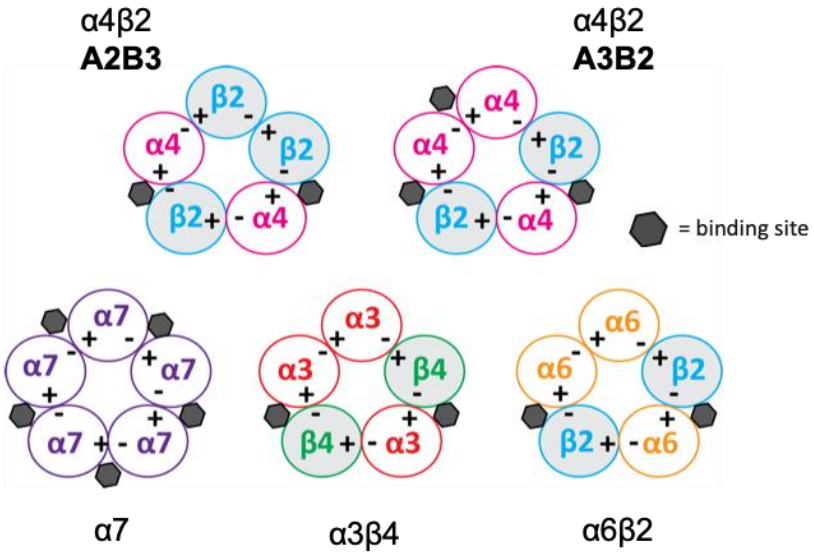

Figure 1.3 | A sample of the various nAChR subtypes in the CNS.

These receptors have been studied for many years, and drug discovery efforts have rendered several therapeutics, such as varenicline (Chantix®) and cytisine (Tabex) that mainly target the α4β2 subtype (**Figure 1.4D**), and galantamine (Razadyne®) to target the α7 subtype.[32–38] Although these agonists have higher affinities for these specific subtypes over others, they still bind to other subtypes to some extent. Gastrointestinal side-effects of varenicline and nicotine are commonly observed,[39] which could be a result of these off-target effects. Besides the diversity in subtypes, heteromeric receptors, such as α4β2 and α3β4, can assemble in multiple stoichiometries. The α4β2 subtype can arrange as $(\alpha4)_3(\beta2)_2$, which we refer to as A3B2, or $(\alpha4)_2(\beta2)_3$, which we refer to as A2B3 (**Figure 1.3**).[40,41] Developing agonists that distinguish between neuronal subtypes or stoichiometries remains challenging. Therefore, a better understanding of agonist binding in the various subtypes and stoichiometries is essential.

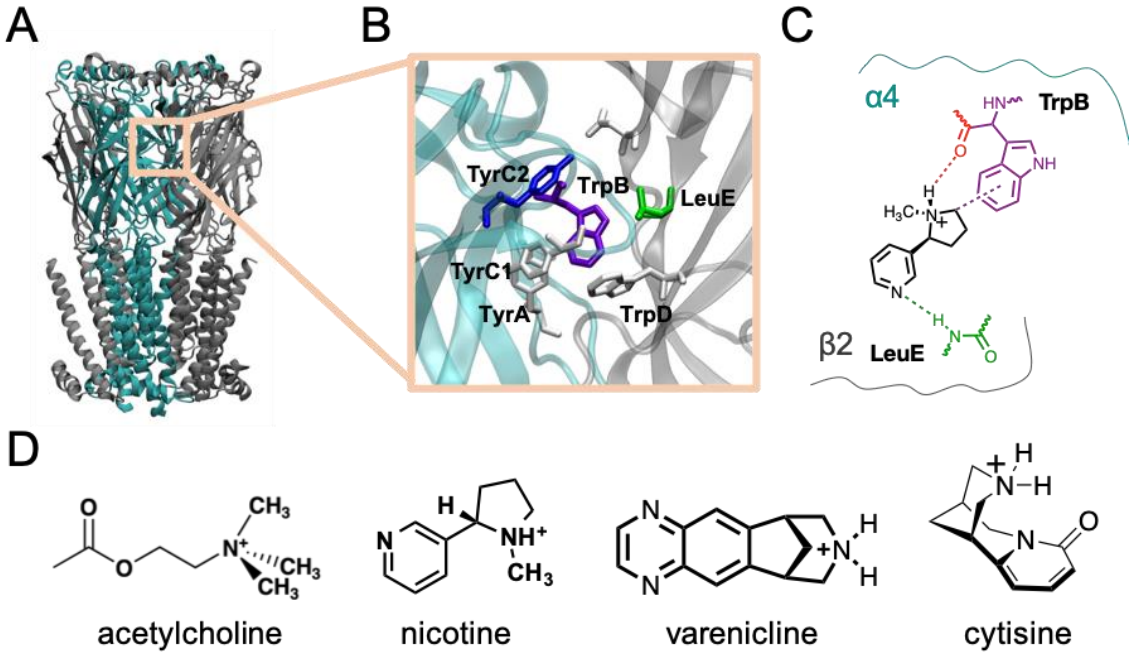

Figure 1.4 | The agonist binding site of the nAChR and four known agonists. (A) The structure of the α4β2 nAChR with the agonist binding site at two subunit interfaces highlighted (PDB ID: 5kxi). (B) A closer look at the agonist binding site with the aromatic residues lining the pocket highlighted. (C) A schematic view of the binding model for nicotine. (D) Chemical structures of four agonists to the nAChR: acetylcholine, nicotine, varenicline, and cytisine.

In α4β2 the agonist binding site lies at the interface of the primary α face and the complementary β2 face (**Figure 1.4A,B**). The site is formed by six loops (A, B, and C from the primary face, and D, E, and F from the complementary face) that contribute five aromatic residues, called the aromatic box.[16,42] These aromatic residues, three tyrosines (TyrA, TyrC1, TyrC2) and two tryptophans (TrpB, TrpD), are highly conserved across all pLGICs (**Figure 1.4B**).[43] Previous studies by our group have established a binding model for nicotine and other agonists to several nAChR subtypes (**Figure 1.4**).[20,44,45] For nicotine at the α4β2 subtype three key binding interactions were identified: a cation-π interaction to W154 in loop B (TrpB), a hydrogen bond to the backbone carbonyl of TrpB, and a hydrogen bond to L119 in Loop E (LeuE) of the complementary subunit (**Figure 1.4C**).[45,46] Although, generally these three interactions have been observed for nAChR agonists across different subtypes, it is possible

to discern agonist-specific and subtype-specific differences. For example, the cation-π interaction is sometimes formed to a different aromatic residue of the five in the binding pocket, and not every agonist makes both hydrogen bonds.[47] In chapter two, we expand on the binding model of cytisine for the α4β2 subtype. Moreover, we determine changes in energetic contributions of these binding interactions as a result of substitution at the pyridone ring of cytisine.

1.2.2 γ-aminobutyric acid type A receptors

Another pLGIC central to this work is the anion-selective $GABA_A$ receptor. For this receptor, a total of 19 homologous subunits exist that can assemble in at least 30 different subtypes *in vivo*.[48] The predominant isoform in the human brain is the α1β2γ2 subtype. Some types, including the α1β2γ2, are predominantly expressed at the post-synaptic termini and mediate phasic inhibition, while others are located at extrasynaptic sites and mediate tonic inhibition.[48–50] Dysfunction of this receptor results in anxiety disorders, epilepsy and neurodevelopmental disorders, including Autism Spectrum Disorders (ASD).[51–53]

Receptor activation occurs upon binding of GABA to the agonist binding site, also referred to as the orthosteric site, which lies in the ECD at the β+/α- subunit interfaces (**Figure 1.5B**).[11] This contrasts the nAChRs, where the agonist binding site is located at the α+/β- subunit interfaces (**Figure 1.4A**). Additional binding of other ligands to several allosteric sites on the pentameric complex can modulate this activation, and several of these are highlighted in **Figure 1.5A and B.**[54] Positive allosteric modulators (PAMs) potentiate the evoked response by an agonist, while negative allosteric modulators (NAMs) inhibit that response.[55,56] Researchers have also found allosteric agonists that are able to activate the receptors via allosteric sites. Some of these contain PAM properties as well and are so-called ago-PAMs.[55]

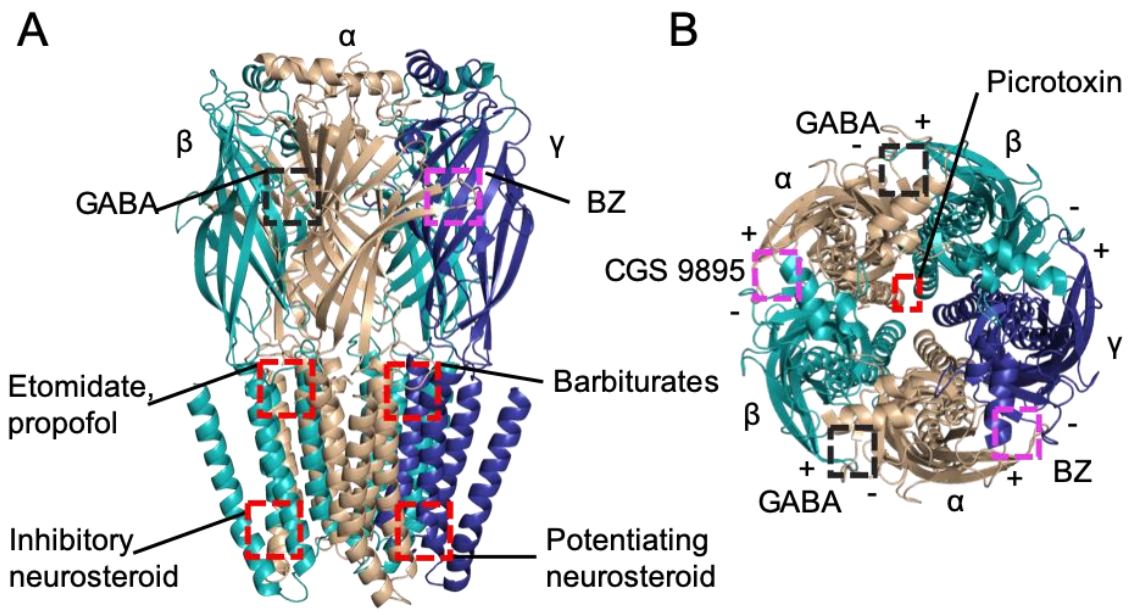

Figure 1.5 | Structure of the GABA$_A$R and its known ligand binding sites. (A) Side view of the α1β2γ2 GABA$_A$R structure with the orthosteric (black) and several allosteric binding sites highlighted (sites in ECD in purple, sites in TMD in red) (PDB ID: 6D6T). (B) Extracellular view of the α1β2γ2 GABA$_A$R structure looking down the ion-conducting pore.

Over the years many modulators of GABA$_A$ receptors have been identified and several positive allosteric modulators are widely used to treat anxiety disorders, such as Alprazolam (Xanax), Diazepam (Valium), and Flurazepam (Dalmane).[55,57,58] These three modulators are structurally similar (benzodiazepines) and bind to the same site on the receptor located in the ECD at the α+/γ- subunit interfaces (BZ-site, **Figure 1.5A,B**). The PAM CGS 9895 has been found to bind at a third allosteric site in the ECD, located at the respective site at the α+/β- subunit interface (**Figure 1.5B**).[59,60] The TMD also hosts several allosteric sites. Anesthetics, such as propofol, etomidate and pentobarbital, and neurosteroids all have been observed to modulate the GABA$_A$ receptors through interaction with the TMD (**Figure 1.5A**).[61–67] Propofol and etomidate bind at the β+/α- subunit interfaces at the top of M1 and M3,[61–63,68,69] while pentobarbital binds at the respective site at the α+/β- subunit interfaces (**Figure 1.5A**).[65] Recent X-ray crystal structures revealed the binding sites for the potentiating neurosteroid

tetrahydro-deoxycorticosterone (THDOC) to be intersubunit at the bottom of M3-M1-M4 and the inhibitory neurosteroid pregnenolone sulfate to be intrasubunit between M3 and M4 (**Figure 1.5A**).[70] A cryo-EM structure confirmed the binding site of picrotoxin in the pore at the bottom of the TM2 helices.[71]

Although $GABA_A$ receptor modulators have proven great therapeutic benefit, adverse effects remain a problem. Additionally, elucidating functions of individual subtypes is crucial for a better understanding of $GABA_AR$'s role in health and disease. Therefore, recent efforts have focused on finding subtype selective modulators. In chapter three, we describe the functional evaluation of a series pyrrolidinoindolines as novel positive allosteric modulators for the $GABA_AR$.

1.3 Voltage-gated ion channels

PLGICS are important for the decision whether an incoming signal will propagate to the next neuron. However, the large fluctuations in membrane potential during an action potential are created by voltage-gated ion channels (VGICs). VGICs are a large family that include voltage-gated sodium channels (Na_v or VGSCs), potassium channels (VGKCs) and calcium channels.[72] When the sum of excitatory and inhibitory signals resulting from pLGICs reach a threshold depolarization of the membrane, voltage-gated sodium channels will initiate the next action potential by creating an even larger depolarization of the membrane towards +30 mV (**Figure 1.6**). VGKCs open slower than VGSCs and their opening results in an outward flow of potassium ions resulting in repolarization of the membrane. At the same time VGSCs close and are temporarily unable to be activated. Upon hyperpolarization of the membrane, VGKCs close and the membrane returns to its resting potential around -60mV. After this refractory period VGSCs return to the closed state and a new action potential can

be initiated. In this dissertation, we focused on modulating activation of both VGSCs and VGKCs using small molecules.

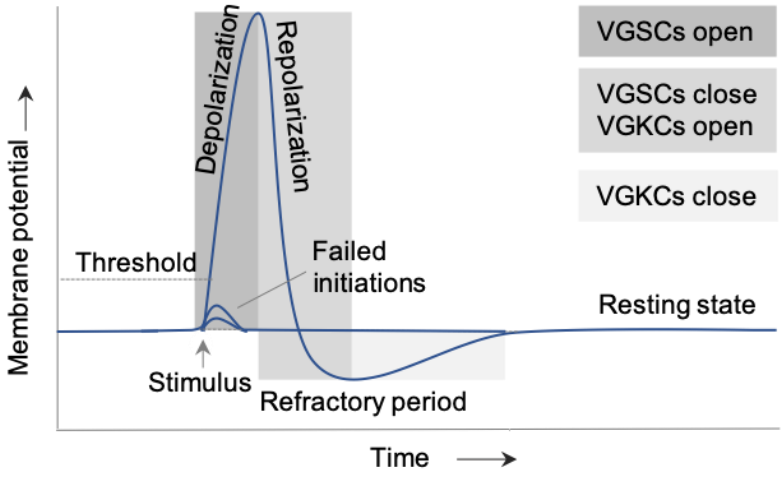

Figure 1.6 | The different stages of an action potential.

1.3.1 Voltage-gated sodium channels

VGSCs are activated by a depolarization of the cell membrane. Conventionally, a eukaryotic Na_v channel is a large complex of one single α subunit (260 kDa) and one or more smaller, β subunits (33-36 kDa) (**Figure 1.7A,B**).[72,73] Although the α subunit alone contains the sodium conducting pore and the gating domain, it requires heterodimerization with one or more β subunits to reconstitute the full native properties.[74] Nine α subunits (Na_v 1.1-1.9) and five β subunits (β1-4, β1B) have been identified so far.[74] Studies have associated mutations in genes encoding these VGSC subunits with a variety of disorders affecting skeletal muscle contraction, heart rhythm, and nervous system function, such as myotonia, Brugada syndrome, and congenital epilepsy.[75]

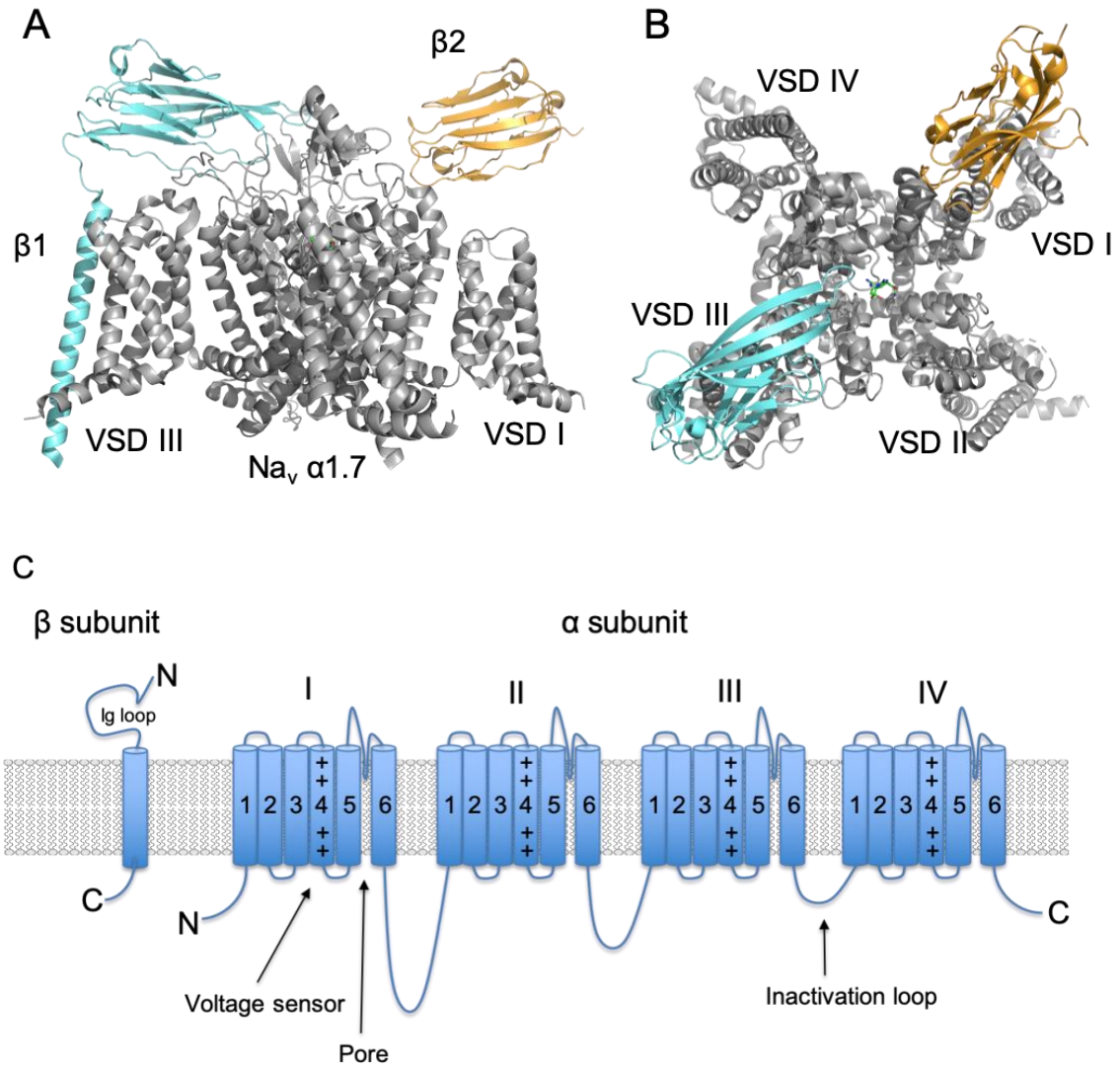

Figure 1.7 | Structure of a voltage-gated sodium channel. (A) Side view of the structure of the Na_vα1.7-β1-β2 complex (PDB ID: 6J8G). The α subunit is shown in grey, the β1 subunit is shown in teal, and the β2 subunit is shown in orange. VSDs are indicated. (B) Extracellular view of the Na_vα1.7-β1-β2 complex. (C) Structural topology of the eukaryotic Na_v channel α and β subunits. The center peptide chain is a generalized depiction of an α subunit containing four homologous domains, each comprising six helical segments referred to as S1-S6.

Different from pLGICs, the Na_v α subunit consists of one long peptide chain that contains four homologous domains (designated DI through DIV) and assembles in a pseudotetrameric structure (**Figure 1.7**).[76] Each domain comprises six helical segments (S): S1-S4 form voltage sensor domains (VSD, total of four per α subunit) and the four S5-S6

segments make up the sodium-conducting pore (**Figure 1.7C**).[77] These two functional domains are physically separated and have been shown to be able to function independently.[78,79] Both N- and C-termini lie on the intracellular side of the membrane. The connecting loop between DIII and DIV, containing a hydrophobic IFM motif, has been shown to play a crucial part in the inactivation of the channel.[80] Recently, mutations in the DI S6 have also shown to remove fast inactivation.[81,82]

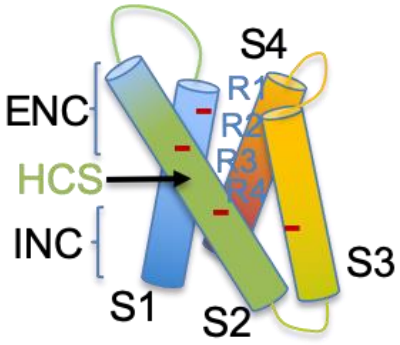

Figure 1.8 | Structure of the voltage-sensing domain. The transmembrane helices are colored from blue to red (S1-S4). Amino acids of the extracellular and intracellular negative charge cluster (ENC and INC) are highlighted as red minus signs, and positive gating charge arginine residues (R1-R4) are highlighted in blue. The hydrophobic constriction site (HCS) is designated in green.

The most unique feature of VGICs is the voltage sensing domain. S4 is called the voltage sensor and contains four conserved arginine residues (R1-4) (**Figure 1.8**). Researchers have proposed that S4 bears the gating charges that drive voltage-dependent activation.[83,84] The 'helical-screw' model suggests that the positive gating charges of the conserved arginines are neutralized in their TM positions by interacting with negatively charged amino acid side chains in S1 and S3 and the negative membrane potential exerts an electrostatic force to pull the gating charges inward toward the cytosol (**Figure 1.8**). Depolarization releases these gating charges, allowing S4 to move outward along a spiral pathway, while the gating charges move outward exchanging ion pair partners along the way. This voltage sensor movement causes conformational changes that result in pore opening.[83,84] Strong support for this model has emerged over the years from various studies attempting to test aspects of it.[85–93] Several animal

toxins exert their disturbing effects by interfering with the voltage sensing domains of VGSCs.[94–96] In chapter four, we describe progress towards light-induced modulation of VGSCs by evaluating the effects of ruthenium diamine photoswitches on VGSC function.

1.3.2 Voltage-gated potassium channels

Voltage-gated potassium channels (VGKCs) control the frequency and shape of the action potential waveform, the secretion of hormones and neurotransmitters, and cell membrane potential.[98] Eight α subunits (K_v1.1-1.8) and two β subunits (K_v2.1-2.2) have been identified. VGKCs are different from VGSCs as they are comprised of four identical subunits. Each subunit consists of six transmembrane regions, a short intracellular C-terminus and a long intracellular N-terminus. Similar to VGSCs, helix S1-S4 make up the voltage-sensing domain, while S5 and S6 form the ion-conducting pore.[99–101] In chapter four, we used the *Drosophila* Shaker K^+ channel (SH) to determine differences in functional effects of ruthenium bipyridine complexes on different VGIC subtypes.

1.4 Tools for systematic analysis of ion channel function

1.4.1 Non-canonical amino acid mutagenesis

Site-directed mutagenesis has proven very useful for biochemists to probe for functionally relevant residues in proteins. However, the twenty canonical amino acids are a fairly restrictive toolset to probe the complex structures of proteins and their interactions. Expansion of the genetic code has dramatically increased this toolset and has enabled the incorporation of many non-canonical amino acids into ion channels.[20,102] The introduction of subtle structural changes has identified critical noncovalent interactions and conformational requirements.[45,103]

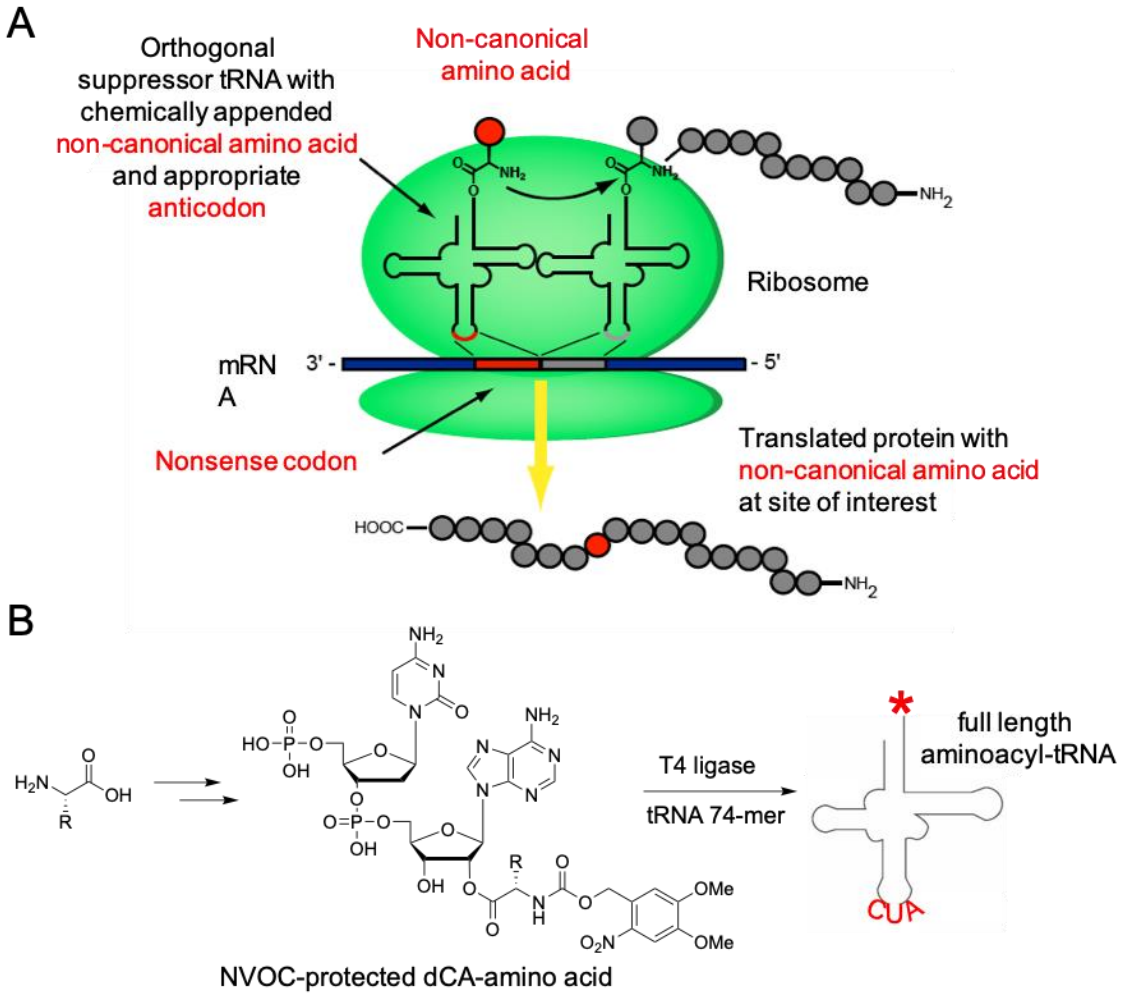

Figure 1.9 | Non-canonical amino acid mutagenesis via nonsense suppression. (A) Non-canonical amino acid mutagenesis via nonsense suppression using chemically acylated tRNA. (B) Full length aminoacyl suppressor tRNA is prepared by chemically appending a non-canonical amino acid to dCA, which is then enzymatically ligated to 74mer tRNA.

These non-canonical amino acids can be incorporated into proteins using a method called *in vivo* nonsense suppression (**Figure 1.9**). First, the gene encoding the protein of interest is modified by mutating the codon at the desired site to a stop codon. Second, after chemically synthesizing the desired non-canonical amino acid, this residue is chemically appended to dCA, followed by enzymatic ligation to 74mer tRNA carrying the appropriate anti-codon (**Figure 1.9B**).[20,104,105] Normally, the nonsense codon would cause premature termination of

translation resulting in truncated protein. However, when suppressor tRNA bearing the corresponding anticodon is present, the native polymerase will recognize the suppressor tRNA and stop codon as a match and produce full length protein containing the non-canonical amino acid. It is crucial that the tRNA is orthogonal to the host system to avoid charging the tRNA by endogenous aminoacyl tRNA synthetases.[20,104,105] Chemical acylation of the amino acid to the tRNA allows for great flexibility in functionalities to be incorporated.

1.4.2 Electrophysiology

To determine the effects of both canonical and non-canonical amino acid mutagenesis on receptor function, we used two-electrode voltage clamp (TEVC). In TEVC, the cell is impaled with two microelectrodes: one measures the membrane potential, while the other injects current to maintain the membrane potential at a constant, preset potential (**Figure 1.11A**).[106] Upon agonist application to the cell, ion channels will open and the membrane potential changes as a result of the ion flow in or out of the cell. The current injected through the current electrode is therefore a direct measure of the sum of currents through all ion channels at the membrane. Electrophysiology assays require only a small amount of protein for signal responses (microAmpères), which makes it an extremely useful tool to measure influences of subtle perturbations on receptor function.[107]

A commonly used heterologous expression system to study ion channels is the oocyte from *Xenopus laevis* (African clawed frog). This vertebrate cell is a classic expression system for functional evaluation of ion channels using TEVC, because of its size and robust expression of eukaryotic proteins.[108] Proteins are expressed by microinjecting the mRNA coding for the desired protein into the cell, followed by an incubation period of 24-48 hours, during which the (mutant) protein is translated, assembled and transported to the cell membrane.[104,109] The microinjection delivery method makes this approach quite amenable for the nonsense

suppression approach described earlier. For *in vivo* nonsense suppression, both mRNA and the chemically acylated tRNA are readily co-injected in *Xenopus laevis* oocytes (**Figure 1.10**).

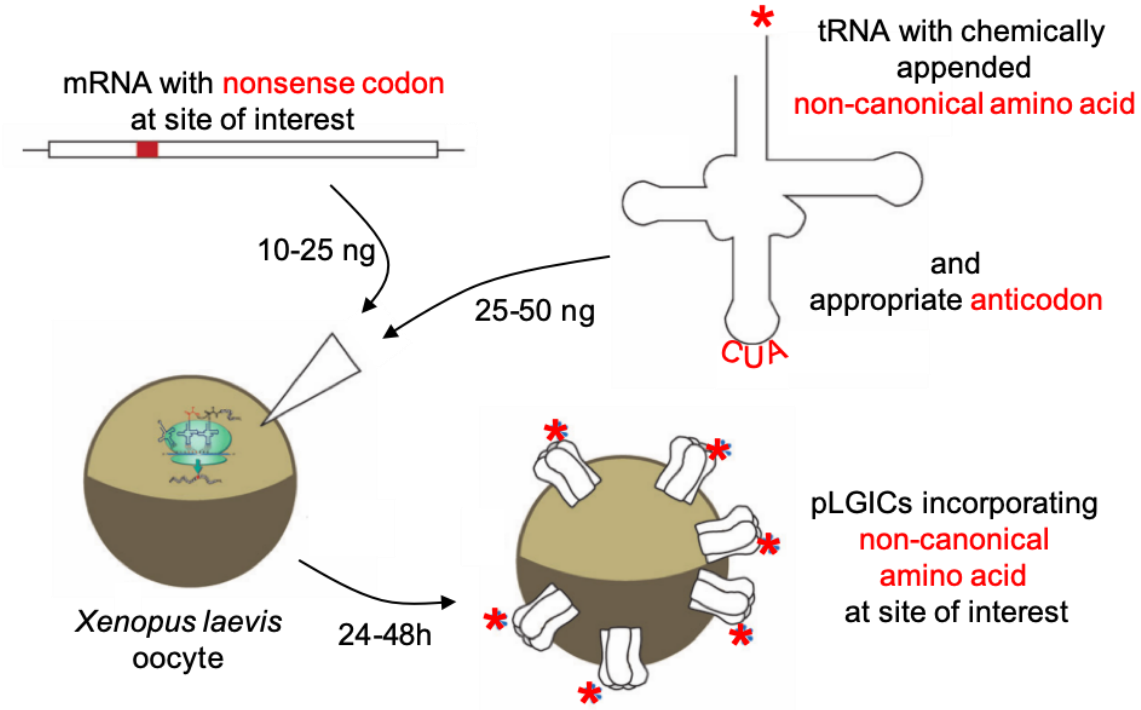

Figure 1.10 | *In vivo* nonsense suppression using a *Xenopus laevis* oocyte.

Different aspects of ion channel function may be evaluated using various electrophysiological assays. For all studies in this dissertation regarding pLGICs, the main goals were to assess functional effects of mutants and determine potency changes among substituted ligands. For activation of pLGICs the following events are considered: the cooperative binding of one or more agonists (binding) allows the receptor to undergo conformational changes towards an ion-permeable state (gating). The introduction of mutants or application of ligands may influence the energetics of agonist binding or gating, which results in a change in sensitivity of the pLGIC to its agonist.[110] Generally, researchers assume that mutations near the agonist binding site influence only the binding event, while those close to the pore are thought to mostly influence the gating event.[45] To measure these effects, we

performed dose-response experiments of which a typical protocol is shown in **Figure 1.11B**. Upon application of increasing agonist doses, the binding equilibrium is shifted towards the open state. At high doses, saturation is reached and current responses level off. Peak currents are normalized to the maximal response and plotted against the logarithm of the respective agonist concentrations. We then fit these data to the Hill equation:

$$I([A]) = \frac{I_{max}}{1 + (\frac{EC_{50}}{[A]})^{n_H}}$$

Where I is the whole cell current, [A] is the agonist concentration, I_{max} is the maximal current response, EC_{50} is the agonist concentration eliciting a half-maximal response, and n_H is the Hill coefficient (**Figure 1.11C**). The shift in EC_{50} compared to wild type is used as a readout for the magnitude of the energetic perturbation caused by the mutations or ligand substitution, where log(fold shift in EC_{50}) varies roughly with the ΔΔG value.

A different electrophysiology assay that renders information on receptor properties is a voltage jump experiment. For nAChRs described in chapter two, this assay is used to verify receptor stoichiometry. The two α4β2 stoichiometries demonstrate distinct behaviors at positive membrane potentials.[45] Upon nAChR activation, the negative membrane potential drives ion flow into the cell. Ion channel opening at positive potentials results in an outward current of ions. However, the α4β2 A2B3 stoichiometry prevents this outward flow at positive potentials, which we refer to as inward rectification (**Figure 1.11D**). Since we control the membrane potential in TEVC, we can change the membrane potential quickly to positive potentials upon receptor activation to measure the extent of inward rectification (**Figure 1.11E**). This allows us to distinguish between α4β2 stoichiometries.

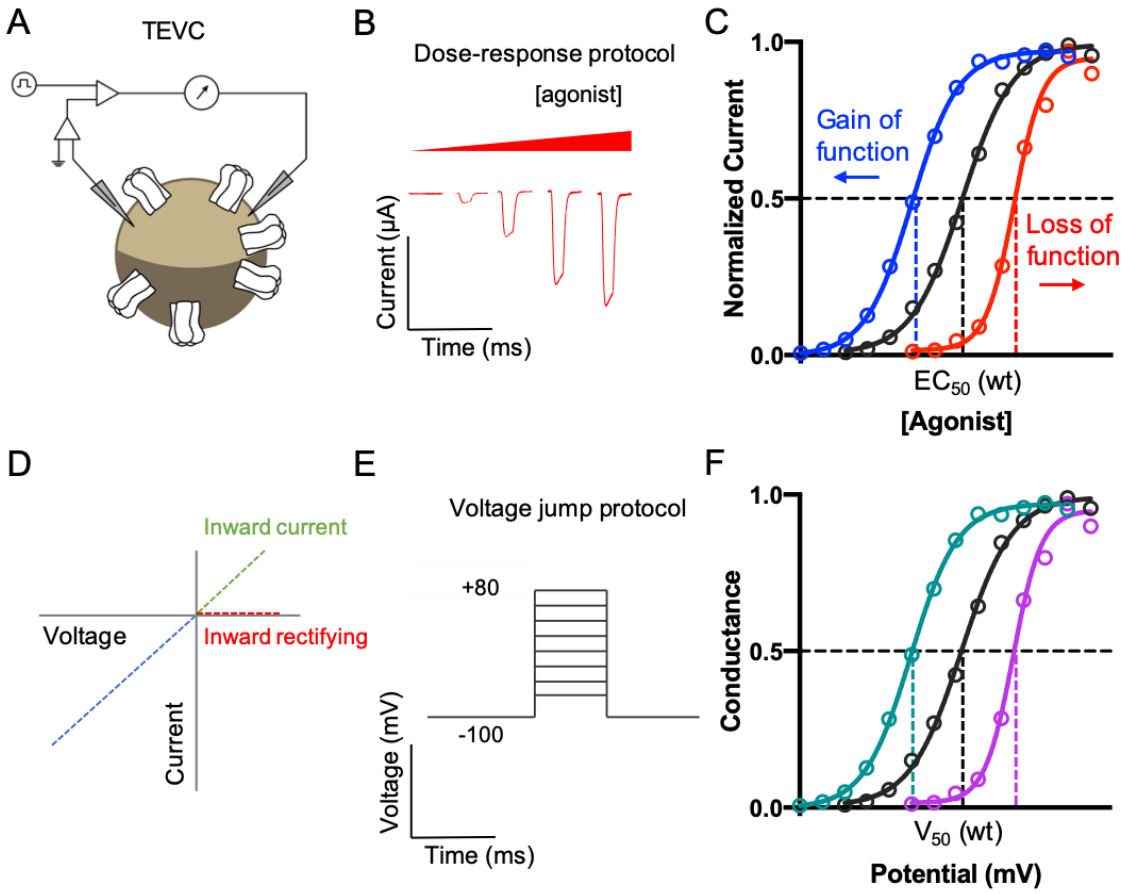

Figure 1.11 | Functional characterization of ion channels using two-electrode voltage clamp (TEVC). (A) Schematic presentation of the TEVC set up using a *Xenopus laevis* oocyte. (B) Dose-response protocol: current waveforms in response to agonist. Application of increasing doses of agonists results in increasing current responses. (C) Dose-response relationships illustrating wild type (black), gain of function (blue), loss of function (red) variants. (D) I-V plot of a voltage jump experiment on a pLGIC. At negative potentials, the I-V relationship is linear (blue). At positive potentials, this trend can either continue (green) or be inhibited (red). This phenomenon of current inhibition at positive potentials is called inward rectification. (E) Voltage jump protocol. Although this protocol differs slightly when used for pLGIC or VGICs, the concept is the same: the holding potential of the membrane is varied on a millisecond timescale and the currents for each voltage step are recorded. For voltage jump experiments on pLGICs, the voltage jump is executed upon agonist application. (F) G-V plot resulting from a voltage jump experiment on VGSCs. Sodium conductances were calculated from peak currents, membrane potential and the reversal potential.

Besides pLGIC characterization, we also used voltage jump experiments to determine activation characteristics of VGICs in chapter four. As depolarization of the membrane activates VGICs, a typical experiment involves varying the membrane potential in 5 mV

depolarization steps to obtain a current-voltage plot for VGKCs and a conductance-voltage plot for VGSCs. We determine sodium conductances (G_{Na}) from peak currents using the equation:

$$G_{Na}(V_m) = \frac{I_{Na}}{(V_m - V_{rev})}$$

where G_{Na} is the sodium conductance, I_{Na} is the peak current at a that depolarization step, V_m is the membrane potential, and V_{rev} is the reversal potential calculated for each individual cell. The reversal potential is the membrane potential at which the driving force for an inward sodium current – i.e. the concentration gradient of sodium ions – is equal to the electrical potential. We normalized individual conductance curves (G-V) to the maximum conductance amplitude per cell and fitted using the Boltzmann distribution equation:

$$G(V_m) = \frac{G_{max}}{1 + e^{\frac{V - V_{0.5}}{k}}}$$

where G is the normalized sodium conductance, V_m is the membrane potential of that depolarization step, $V_{0.5}$ is the half-activation potential, and k is the slope. $V_{0.5}$ represents the membrane potential at which half of the channel population is activated, which we used as a measure for the voltage-dependence of activation (**Figure 1.11F**).

1.4.3 Double-mutant cycle analysis

In addition to evaluating the effect of a single perturbation caused by a mutation or substitution of the ligand, we wish to determine if this single perturbation affects a specific interaction. To achieve this, we perform a double-mutant cycle analysis, which provides a quantitative measurement of the energetic coupling, or lack thereof, between two mutations. Historically, mutant cycle analyses have probed coupling between two amino acids in a protein,[111] but our group has found the methodology also quite useful when one mutation is to the protein and the other is to the ligand.[44,112] In a double-mutant cycle analysis four values

are obtained, the EC_{50} of the wild type, the EC_{50} values of the two single mutations, and the EC_{50} value of the collective double mutant. If the two mutations are not functionally coupled, that is if they are independent of one another, the product of the wild type EC_{50} and double mutant EC_{50} will be identical to the product of the single mutants (additive) (**Figure 1.12**). If the products are significantly distinct (nonadditive), then the two mutations are functionally coupled and thought to interact in a cooperative way. The extent to which the two perturbations are additive or nonadditive is expressed by the coupling constant Ω, which can be converted into coupling energy using the equation $\Delta\Delta G = RT\ln(\Omega)$. We deem two perturbations to be functionally coupled when the ΔΔG value is greater than 0.4 kcal/mol.

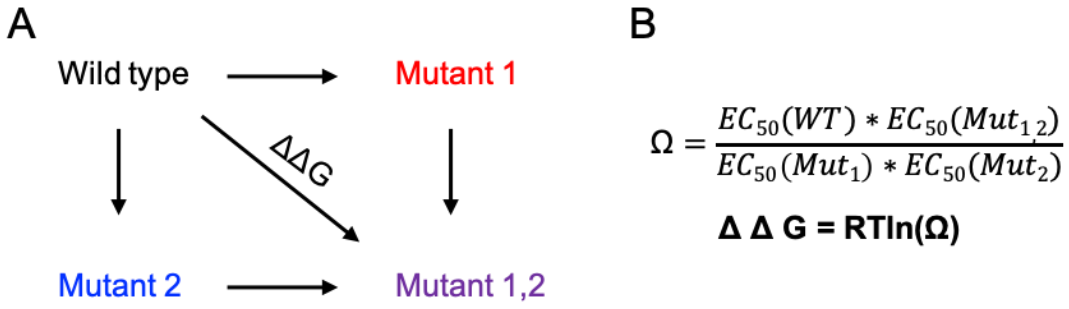

Figure 1.12 | Double-mutant cycle analysis. (A) Schematic depiction of a double-mutant cycle analysis. (B) Equations used to calculate the coupling constant Ω and ΔΔG values, where R is the ideal gas constant and T the temperature (25˚C)

1.5 Summary of dissertation work

The central theme of this dissertation is to study activation of ion channels and evaluating new ligands to modulate this process. We combined non-canonical amino acid mutagenesis with the design of small molecule ligands to probe receptor activation. The first two chapters and first two appendices focus on evaluating function of two pLGICs using novel agonists and modulators, while chapter four shifts focus to evaluating molecules for

modulation of voltage-gated ion channels. All studies used the heterologous model system *Xenopus laevis*.

In chapter two, we expanded the binding model of cytisine to the α4β2 nAChR. We determined how the key binding interactions between cytisine and the binding site of α4β2 nAChR are impacted by C(10)-modification of cytisine. To achieve this, we used two-electrode voltage-clamp electrophysiology and non-canonical amino acid mutagenesis to probe the electrostatic binding interactions of a novel series of C(10)-cytisine derivatives. In order to perform similar studies in the α3β4 nAChR subtype, we describe the heterologous expression of mouse and human α3β4 nAChRs in *Xenopous laevis* oocytes in appendix one. We determined mRNA injection ratios to obtain pure populations of the two receptor stoichiometries, and we determined a method to readily distinguish expression of either stoichiometry. These studies make progress toward elucidating subtype specific binding profiles.

Chapter three describes the development and functional evaluation of a novel series of pyrrolidinoindolines for agonism and modulation of the $GABA_A$ receptor. We also performed mutagenesis studies to identify the binding site of these novel ligands. Appendix 2 describes a different screen for activation or modulation of $GABA_A$ receptors using a set of phenolic compounds implicated in autism spectrum disorder.

Chapter four shifts focus to voltage-gated ion channels. In this chapter, the ultimate goal was to photochemically control the activation of VGSCs and make progress towards developing a RubpyC17-based photoswitch that could be used in an artificial retina. To this end, we determined the functional effects of several ruthenium bipyridine analogs on VGSCs and VGKCs.

Lastly, appendix three describes an improved synthetic route to 4,5,6,7-tetrafluoro-tryptophan that we employed for the incorporation of this non-canonical amino acid in chapter two.

1.6 References

(1) *Principles of Neural Science, Fifth Edition*, 5th edition.; Kandel, E. R., Schwartz, J. H., Jessell, T. M., Siegelbaum, S. A., Hudspeth, A. J., Eds.; McGraw-Hill Education / Medical: New York, 2012.

(2) Enyedi, P.; Czirják, G. Molecular Background of Leak K+ Currents: Two-Pore Domain Potassium Channels. *Physiol. Rev.* **2010**, *90* (2), 559–605. https://doi.org/10.1152/physrev.00029.2009.

(3) daCosta, C. J. B.; Baenziger, J. E. Gating of Pentameric Ligand-Gated Ion Channels: Structural Insights and Ambiguities. *Struct. Lond. Engl. 1993* **2013**, *21* (8), 1271–1283. https://doi.org/10.1016/j.str.2013.06.019.

(4) Nys, M.; Kesters, D.; Ulens, C. Structural Insights into Cys-Loop Receptor Function and Ligand Recognition. *Biochem. Pharmacol.* **2013**, *86* (8), 1042–1053. https://doi.org/10.1016/j.bcp.2013.07.001.

(5) Ranade, S. S.; Syeda, R.; Patapoutian, A. Mechanically Activated Ion Channels. *Neuron* **2015**, *87* (6), 1162–1179. https://doi.org/10.1016/j.neuron.2015.08.032.

(6) Catterall, W. A. Voltage-Gated Sodium Channels at 60: Structure, Function and Pathophysiology. *J. Physiol.* **2012**, *590* (Pt 11), 2577–2589. https://doi.org/10.1113/jphysiol.2011.224204.

(7) Marotta, C. B. Structure-Function Studies of Nicotinic Acetylcholine Receptors Using Selective Agonists and Positive Allosteric Modulators. phd, California Institute of Technology, 2015. https://doi.org/Marotta, Christopher Bruno (2015) Structure-Function Studies of Nicotinic Acetylcholine Receptors Using Selective Agonists and Positive Allosteric Modulators. Dissertation (Ph.D.), California Institute of Technology. doi:10.7907/Z9V122Q9. http://resolver.caltech.edu/CaltechTHESIS:05292015-144036736 <http://resolver.caltech.edu/CaltechTHESIS:05292015-144036736>.

(8) Albuquerque, E. X.; Pereira, E. F. R.; Alkondon, M.; Rogers, S. W. Mammalian Nicotinic Acetylcholine Receptors: From Structure to Function. *Physiol. Rev.* **2009**, *89* (1), 73–120. https://doi.org/10.1152/physrev.00015.2008.

(9) Thompson, A. J.; Lummis, S. C. R. 5-HT3 Receptors. *Curr. Pharm. Des.* **2006**, *12* (28), 3615–3630.

(10) Danysz, W.; Parsons, C. G. Glycine and N-Methyl-D-Aspartate Receptors: Physiological Significance and Possible Therapeutic Applications. *Pharmacol. Rev.* **1998**, *50* (4), 597–664.

(11) Olsen, R. W.; Sieghart, W. GABA A Receptors: Subtypes Provide Diversity of Function and Pharmacology. *Neuropharmacology* **2009**, *56* (1), 141–148. https://doi.org/10.1016/j.neuropharm.2008.07.045.

(12) Althoff, T.; Hibbs, R. E.; Banerjee, S.; Gouaux, E. X-Ray Structures of GluCl in Apo States Reveal a Gating Mechanism of Cys-Loop Receptors. *Nature* **2014**, *512* (7514), 333–337. https://doi.org/10.1038/nature13669.

(13) Sauguet, L.; Shahsavar, A.; Delarue, M. Crystallographic Studies of Pharmacological Sites in Pentameric Ligand-Gated Ion Channels. *Biochim. Biophys. Acta* **2015**, *1850* (3), 511–523. https://doi.org/10.1016/j.bbagen.2014.05.007.

(14) Kracun, S.; Harkness, P. C.; Gibb, A. J.; Millar, N. S. Influence of the M3-M4 Intracellular Domain upon Nicotinic Acetylcholine Receptor Assembly, Targeting and Function. *Br. J. Pharmacol.* **2008**, *153* (7), 1474–1484. https://doi.org/10.1038/sj.bjp.0707676.

(15) Dougherty, D. Cation-Pi Interactions in Chemistry and Biology: A New View of Benzene, Phe, Tyr, and Trp. *Science* **1996**, *271* (5246), 163–168.

(16) Brejc, K.; van Dijk, W.; Klaassen, R.; Schuurmans, M.; van Der Oost, J.; Smit, A.; Sixma, T. Crystal Structure of an ACh-Binding Protein Reveals the Ligand-Binding Domain of Nicotinic Receptors. *Nature* **2001**, *411* (6835), 269–276. https://doi.org/10.1038/35077011.

(17) Sixma, T. K.; Smit, A. B. Acetylcholine Binding Protein (AChBP): A Secreted Glial Protein That Provides a High-Resolution Model for the Extracellular Domain of Pentameric Ligand-Gated Ion Channels. *Annu. Rev. Biophys. Biomol. Struct.* **2003**, *32*, 311–334. https://doi.org/10.1146/annurev.biophys.32.110601.142536.

(18) Morales-Perez, C. L.; Noviello, C. M.; Hibbs, R. E. X-Ray Structure of the Human A4β2 Nicotinic Receptor. *Nature* **2016**, *advance online publication*. https://doi.org/10.1038/nature19785.

(19) Zhu, S.; Noviello, C. M.; Teng, J.; Walsh, R. M.; Kim, J. J.; Hibbs, R. E. Structure of a Human Synaptic GABAA Receptor. *Nature* **2018**, *559* (7712), 67–72. https://doi.org/10.1038/s41586-018-0255-3.

(20) Van Arnam, E. B.; Dougherty, D. A. Functional Probes of Drug-Receptor Interactions Implicated by Structural Studies: Cys-Loop Receptors Provide a Fertile Testing Ground. *J Med Chem* **2014**, *57* (15), 6289–6300. https://doi.org/10.1021/jm500023m.

(21) Hurst, R.; Rollema, H.; therapeutics, B.-D. Nicotinic Acetylcholine Receptors: From Basic Science to Therapeutics. *Pharmacol. Ther.* **2013**.

(22) Gotti, C.; Zoli, M.; Clementi, F. Brain Nicotinic Acetylcholine Receptors: Native Subtypes and Their Relevance. **2006**, *27* (9), 482–491. https://doi.org/10.1016/j.tips.2006.07.004.

(23) Romanelli, M. N.; Gratteri, P.; Guandalini, L.; Martini, E.; Bonaccini, C.; Gualtieri, F. Central Nicotinic Receptors: Structure, Function, Ligands, and Therapeutic Potential. *ChemMedChem* **2007**, *2* (6), 746–767. https://doi.org/10.1002/cmdc.200600207.

(24) in neurobiology, P.-R. The Kinetic Properties of Neuronal Nicotinic Receptors: Genetic Basis of Functional Diversity. *Prog. Neurobiol.* **1993**.

(25) Brunzell, D. H.; Stafford, A. M.; Dixon, C. I. Nicotinic Receptor Contributions to Smoking: Insights from Human Studies and Animal Models. *Curr Addict Rep.* **2015**, *2* (1), 33–46. https://doi.org/10.1007/s40429-015-0042-2.

(26) Sher, E.; Chen, Y.; Sharples, T.; topics in … B.-L. Physiological Roles of Neuronal Nicotinic Receptor Subtypes: New Insights on the Nicotinic Modulation of Neurotransmitter Release, Synaptic Transmission and Plasticity. *Curr. Top. …* **2004**.

(27) F, D.-B.; in pharmacological sciences, W.-S. Nicotinic Acetylcholine Receptors and the Regulation of Neuronal Signalling. *Trends Pharmacol. Sci.* **2004**.

(28) Hogg, R.; & B.-D. Nicotinic Acetylcholine Receptors as Drug Targets. *Curr. Drug Targets-CNS …* **2004**.

(29) Gotti, C.; Clementi, F. Neuronal Nicotinic Receptors: From Structure to Pathology. **2004**, *74* (6), 363–396.

(30) Jensen, A. A.; Frølund, B.; Liljefors, T.; Povl, K.-L. Neuronal Nicotinic Acetylcholine Receptors: Structural Revelations, Target Identifications, and Therapeutic Inspirations. *J Med Chem* **2005**, *48* (15), 4705–4745. https://doi.org/10.1021/jm040219e.

(31) Drago, J.; CD, M.; Horne, M.; and Molecular …, F.-D. Neuronal Nicotinic Receptors: Insights Gained from Gene Knockout an Knocking Mutant Mice. *Cell. Mol. …* **2003**.

(32) Coe, J. W.; Brooks, P. R.; Vetelino, M. G.; Wirtz, M. C.; Arnold, E. P.; Huang, J.; Sands, S. B.; Davis, T. I.; Lebel, L. A.; Fox, C. B.; et al. Varenicline: An Alpha4beta2 Nicotinic Receptor Partial Agonist for Smoking Cessation. *J Med Chem* **2005**, *48* (10), 3474–3477. https://doi.org/10.1021/jm050069n.

(33) Southan, C.; Sharman, J. L.; Benson, H. E.; Faccenda, E.; Pawson, A. J.; Alexander, S. P.; Buneman, O.; Davenport, A. P.; C, M., John; Peters, J. A.; et al. The IUPHAR/BPS Guide to PHARMACOLOGY in 2016: Towards Curated Quantitative Interactions between 1300 Protein Targets and 6000 Ligands. *Nucleic Acids Res* **2016**, *44* (D1), D1054-68. https://doi.org/10.1093/nar/gkv1037.

(34) Mihalak, K. B.; Carroll, F. I.; Luetje, C. W. Varenicline Is a Partial Agonist at Alpha4beta2 and a Full Agonist at Alpha7 Neuronal Nicotinic Receptors. *Mol. Pharmacol.* **2006**, *70* (3), 801–805. https://doi.org/10.1124/mol.106.025130.

(35) Woodruff-Pak, D. S.; Vogel, R. W.; Wenk, G. L. Galantamine: Effect on Nicotinic Receptor Binding, Acetylcholinesterase Inhibition, and Learning. *Proc. Natl. Acad. Sci. U. S. A.* **2001**, *98* (4), 2089–2094.

(36) Maelicke, A. Allosteric Modulation of Nicotinic Receptors as a Treatment Strategy for Alzheimer's Disease. *Dement. Geriatr. Cogn. Disord.* **2000**, *11 Suppl 1*, 11–18. https://doi.org/10.1159/000051227.

(37) Walker, N.; Howe, C.; Glover, M.; McRobbie, H.; Barnes, J.; Nosa, V.; Parag, V.; Bassett, B.; Bullen, C. Cytisine versus Nicotine for Smoking Cessation. *N. Engl. J. Med.* **2014**, *371* (25), 2353–2362. https://doi.org/10.1056/NEJMoa1407764.

(38) West, R.; Zatonski, W.; Cedzynska, M.; Lewandowska, D.; Pazik, J.; Aveyard, P.; Stapleton, J. Placebo-Controlled Trial of Cytisine for Smoking Cessation. *N. Engl. J. Med.* **2011**, *365* (13), 1193–1200. https://doi.org/10.1056/NEJMoa1102035.

(39) Leung, L. K.; Patafio, F. M.; Rosser, W. W. Gastrointestinal Adverse Effects of Varenicline at Maintenance Dose: A Meta-Analysis. **2011**, *11* (1). https://doi.org/10.1186/1472-6904-11-15.

(40) Nelson, M. E.; Kuryatov, A.; Choi, C. H.; Zhou, Y.; Lindstrom, J. Alternate Stoichiometries of Alpha4beta2 Nicotinic Acetylcholine Receptors. *Mol Pharmacol* **2003**, *63* (2), 332–341.

(41) Wang, J.; Kuryatov, A.; Sriram, A.; Jin, Z.; Kamenecka, T. M.; Kenny, P. J.; Lindstrom, J. An Accessory Agonist Binding Site Promotes Activation of A4β2* Nicotinic Acetylcholine Receptors. *J Biol Chem* **2015**, *290* (22), 13907–13918. https://doi.org/10.1074/jbc.M115.646786.

(42) Lester, H. A.; Dibas, M. I.; Dahan, D. S.; Leite, J. F.; Dougherty, D. A. Cys-Loop Receptors: New Twists and Turns. *Trends Neurosci.* **2004**, *27* (6), 329–336. https://doi.org/10.1016/j.tins.2004.04.002.

(43) Corringer, P. J.; Le Novère, N.; Changeux, J. P. Nicotinic Receptors at the Amino Acid Level. *Annu. Rev. Pharmacol. Toxicol.* **2000**, *40*, 431–458. https://doi.org/10.1146/annurev.pharmtox.40.1.431.

(44) Blum, A. P.; Lester, H. A.; Dougherty, D. A. Nicotinic Pharmacophore: The Pyridine N of Nicotine and Carbonyl of Acetylcholine Hydrogen Bond across a Subunit Interface to a Backbone NH. *Proc Natl Acad Sci USA* **2010**, *107* (30), 13206–13211. https://doi.org/10.1073/pnas.1007140107.

(45) Xiu, X.; Puskar, N. L.; Shanata, J. A.; Lester, H. A.; Dougherty, D. A. Nicotine Binding to Brain Receptors Requires a Strong Cation-Pi Interaction. *Nature* **2009**, *458* (7237), 534–537. https://doi.org/10.1038/nature07768.

(46) Tavares, X. D. S. da S.; Blum, A. P.; Nakamura, D. T.; Puskar, N. L.; Shanata, J. A.; Lester, H. A.; Dougherty, D. A. Variations in Binding among Several Agonists at Two Stoichiometries of the Neuronal, A4β2 Nicotinic Receptor. *J Am Chem Soc* **2012**, *134* (28), 11474–11480. https://doi.org/10.1021/ja3011379.

(47) Puskar, N. L.; Xiu, X.; Lester, H. A.; Dougherty, D. A. Two Neuronal Nicotinic Acetylcholine Receptors, Alpha4beta4 and Alpha7, Show Differential Agonist Binding Modes. *J Biol Chem* **2011**, *286* (16), 14618–14627. https://doi.org/10.1074/jbc.M110.206565.

(48) Olsen, R. W.; Sieghart, W. International Union of Pharmacology. LXX. Subtypes of Gamma-Aminobutyric Acid(A) Receptors: Classification on the Basis of Subunit Composition, Pharmacology, and Function. Update. *Pharmacol Rev* **2008**, *60* (3), 243–260. https://doi.org/10.1124/pr.108.00505.

(49) Brickley, S. G.; Mody, I. Extrasynaptic GABA(A) Receptors: Their Function in the CNS and Implications for Disease. *Neuron* **2012**, *73* (1), 23–34. https://doi.org/10.1016/j.neuron.2011.12.012.

(50) Farrant, M.; Nusser, Z. Variations on an Inhibitory Theme: Phasic and Tonic Activation of GABA(A) Receptors. *Nat Rev Neurosci* **2005**, *6* (3), 215–229. https://doi.org/10.1038/nrn1625.

(51) Braat, S.; Kooy, R. The GABAA Receptor as a Therapeutic Target for Neurodevelopmental Disorders. *Neuron* **2015**, *86* (5), 1119–1130. https://doi.org/10.1016/j.neuron.2015.03.042.

(52) Chuang, S.-H.; Reddy, D. S. Genetic and Molecular Regulation of Extrasynaptic GABA-A Receptors in the Brain: Therapeutic Insights for Epilepsy. *J. Pharmacol. Exp. Ther.* **2018**, *364* (2), 180–197. https://doi.org/10.1124/jpet.117.244673.

(53) Jacob, T. C.; Moss, S. J.; Jurd, R. GABA(A) Receptor Trafficking and Its Role in the Dynamic Modulation of Neuronal Inhibition. *Nat. Rev. Neurosci.* **2008**, *9* (5), 331–343. https://doi.org/10.1038/nrn2370.

(54) Miller, P. S.; Smart, T. G. Binding, Activation and Modulation of Cys-Loop Receptors. *Trends Pharmacol Sci* **2010**, *31* (4), 161–174. https://doi.org/10.1016/j.tips.2009.12.005.

(55) Sieghart, W. Allosteric Modulation of GABAA Receptors via Multiple Drug-Binding Sites. *Adv Pharmacol* **2015**, *72*, 53–96. https://doi.org/10.1016/bs.apha.2014.10.002.

(56) Olsen, R. W. Analysis of γ-Aminobutyric Acid (GABA) Type A Receptor Subtypes Using Isosteric and Allosteric Ligands. *Neurochem Res* **2014**, *39* (10), 1924–1941. https://doi.org/10.1007/s11064-014-1382-3.

(57) Olsen, R. W. Allosteric Ligands and Their Binding Sites Define γ-Aminobutyric Acid (GABA) Type A Receptor Subtypes. *Adv Pharmacol* **2015**, *73*, 167–202. https://doi.org/10.1016/bs.apha.2014.11.005.

(58) Gupta, S. Recent Advances in Benzodiazepine Receptor (BZR) Binding Studies. *Prog Drug Res* **1995**, *45*, 67–106.

(59) Maldifassi, M. C.; Baur, R.; Sigel, E. Molecular Mode of Action of CGS 9895 at A1 B2 Γ2 GABAA Receptors. *J Neurochem* **2016**, *138* (5), 722–730. https://doi.org/10.1111/jnc.13711.

(60) Ramerstorfer, J.; Furtmüller, R.; Isabella, S.-J.; Varagic, Z.; Sieghart, W.; Ernst, M. The GABAA Receptor A+β− Interface: A Novel Target for Subtype Selective Drugs. *J Neurosci* **2011**, *31* (3), 870–877. https://doi.org/10.1523/JNEUROSCI.5012-10.2011.

(61) Li, G.-D. D.; Chiara, D. C.; Sawyer, G. W.; Husain, S.; Olsen, R. W.; Cohen, J. B. Identification of a GABAA Receptor Anesthetic Binding Site at Subunit Interfaces by Photolabeling with an Etomidate Analog. *J Neurosci* **2006**, *26* (45), 11599–11605. https://doi.org/10.1523/JNEUROSCI.3467-06.2006.

(62) Desai, R.; Ruesch, D.; Forman, S. A. Gamma-Amino Butyric Acid Type A Receptor Mutations at Beta2N265 Alter Etomidate Efficacy While Preserving Basal and Agonist-Dependent Activity. *Anesthesiology* **2009**, *111* (4), 774–784. https://doi.org/10.1097/ALN.0b013e3181b55fae.

(63) Bali, M.; Akabas, M. H. Defining the Propofol Binding Site Location on the GABAA Receptor. *Mol Pharmacol* **2004**, *65* (1), 68–76. https://doi.org/10.1124/mol.65.1.68.

(64) Bali, M.; Jansen, M.; Akabas, M. H. GABA-Induced Intersubunit Conformational Movement in the GABAA Receptor Alpha 1M1-Beta 2M3 Transmembrane Subunit Interface: Experimental Basis for Homology Modeling of an Intravenous Anesthetic Binding Site. *J Neurosci* **2009**, *29* (10), 3083–3092. https://doi.org/10.1523/JNEUROSCI.6090-08.2009.

(65) Chiara, D. C.; Jayakar, S. S.; Zhou, X.; Zhang, X.; Savechenkov, P. Y.; Bruzik, K. S.; Miller, K. W.; Cohen, J. B. Specificity of Intersubunit General Anesthetic-Binding Sites in the Transmembrane Domain of the Human A1β3γ2 γ-Aminobutyric Acid Type A (GABAA) Receptor. *J Biol Chem* **2013**, *288* (27), 19343–19357. https://doi.org/10.1074/jbc.M113.479725.

(66) Mihic, S.; Ye, Q.; Wick, M.; Koltchine, V.; Krasowski, M.; Finn, S.; Mascia, M.; Valenzuela, C.; Hanson, K.; Greenblatt, E.; et al. Sites of Alcohol and Volatile Anaesthetic Action on GABA(A) and Glycine Receptors. *Nature* **1997**, *389* (6649), 385–389. https://doi.org/10.1038/38738.

(67) Chen, Z.-W. W.; Manion, B.; Townsend, R.; Reichert, D. E.; Covey, D. F.; Steinbach, J. H.; Sieghart, W.; Fuchs, K.; Evers, A. S. Neurosteroid Analog Photolabeling of a Site in the Third Transmembrane Domain of the B3 Subunit of the GABA(A) Receptor. *Mol Pharmacol* **2012**, *82* (3), 408–419. https://doi.org/10.1124/mol.112.078410.

(68) Eaton, M. M.; Cao, L. Q.; Chen, Z.; Franks, N. P.; Evers, A. S.; Akk, G. Mutational Analysis of the Putative High-Affinity Propofol Binding Site in Human B3 Homomeric GABAA Receptors. *Mol Pharmacol* **2015**, *88* (4), 736–745. https://doi.org/10.1124/mol.115.100347.

(69) Yip, G. M.; Chen, Z.-W. W.; Edge, C. J.; Smith, E. H.; Dickinson, R.; Hohenester, E.; Townsend, R.; Fuchs, K.; Sieghart, W.; Evers, A. S.; et al. A Propofol Binding Site on Mammalian GABAA Receptors Identified by Photolabeling. *Nat Chem Biol* **2013**, *9* (11), 715–720. https://doi.org/10.1038/nchembio.1340.

(70) Laverty, D.; Thomas, P.; Field, M.; Andersen, O. J.; Gold, M. G.; Biggin, P. C.; Gielen, M.; Smart, T. G. Crystal Structures of a GABAA-Receptor Chimera Reveal New Endogenous Neurosteroid-Binding Sites. *Nat Struct Mol Biol.* **2017**, *24* (11), 977. https://doi.org/10.1038/nsmb.3477.

(71) Masiulis, S.; Desai, R.; Uchański, T.; Serna Martin, I.; Laverty, D.; Karia, D.; Malinauskas, T.; Zivanov, J.; Pardon, E.; Kotecha, A.; et al. GABAA Receptor Signalling Mechanisms Revealed by Structural Pharmacology. *Nature* **2019**, *565* (7740), 454–459. https://doi.org/10.1038/s41586-018-0832-5.

(72) Yu, F. H.; Catterall, W. A. Overview of the Voltage-Gated Sodium Channel Family. *Genome Biol* **2003**, *4* (3), 207. https://doi.org/10.1186/gb-2003-4-3-207.

(73) Catterall, W. A 3D View of Sodium Channels. *Nature* **2001**, *409* (6823), 988–989, 991. https://doi.org/10.1038/35059188.

(74) A, O., Heather; Isom, L. L. Sodium Channel β Subunits: Emerging Targets in Channelopathies. *Annu Rev Physiol* **2015**, *77*, 481–504. https://doi.org/10.1146/annurev-physiol-021014-071846.

(75) George, A. L. Inherited Disorders of Voltage-Gated Sodium Channels. *J. Clin. Invest.* **2005**, *115* (8), 1990–1999. https://doi.org/10.1172/JCI25505.

(76) Brackenbury, W. J.; Isom, L. L. Na+ Channel β Subunits: Overachievers of the Ion Channel Family. *Front Pharmacol* **2011**, *2*. https://doi.org/10.3389/fphar.2011.00053.

(77) Catterall, W. A.; Goldin, A. L.; Waxman, S. G. International Union of Pharmacology. XLVII. Nomenclature and Structure-Function Relationships of Voltage-Gated Sodium Channels. *Pharmacol Rev* **2005**, *57* (4), 397–409. https://doi.org/10.1124/pr.57.4.4.

(78) Swartz, K. J. Sensing Voltage across Lipid Membranes. *Nature* **2008**, *456* (7224), 891–897. https://doi.org/10.1038/nature07620.

(79) Groome, J. R. The Voltage Sensor Module in Sodium Channels. *Handb Exp Pharmacol* **2014**, *221*, 7–31. https://doi.org/10.1007/978-3-642-41588-3_2.

(80) West, J.; Patton, D.; Scheuer, T.; Wang, Y.; Goldin, A.; Catterall, W. A Cluster of Hydrophobic Amino Acid Residues Required for Fast Na(+)-Channel Inactivation. *Proc Natl Acad Sci USA* **1992**, *89* (22), 10910–10914. https://doi.org/10.1073/pnas.89.22.10910.

(81) Oelstrom, K.; P, G.-O., Marcel; Holmgren, M.; Chanda, B. Evolutionarily Conserved Intracellular Gate of Voltage-Dependent Sodium Channels. *Nat Commun* **2014**, *5*, 3420. https://doi.org/10.1038/ncomms4420.

(82) Wang, S.-Y. Y.; Bonner, K.; Russell, C.; Wang, G. K. Tryptophan Scanning of D1S6 and D4S6 C-Termini in Voltage-Gated Sodium Channels. *Biophys J* **2003**, *85* (2), 911–920. https://doi.org/10.1016/S0006-3495(03)74530-5.

(83) Catterall, W. A. Molecular Properties of Voltage-Sensitive Sodium Channels. *Annu. Rev. Biochem.* **1986**, *55*, 953–985. https://doi.org/10.1146/annurev.bi.55.070186.004513.

(84) Guy, H. R.; Seetharamulu, P. Molecular Model of the Action Potential Sodium Channel. *Proc. Natl. Acad. Sci. U. S. A.* **1986**, *83* (2), 508–512.

(85) Stühmer, W.; Conti, F.; Suzuki, H.; Wang, X. D.; Noda, M.; Yahagi, N.; Kubo, H.; Numa, S. Structural Parts Involved in Activation and Inactivation of the Sodium Channel. *Nature* **1989**, *339* (6226), 597–603. https://doi.org/10.1038/339597a0.

(86) Rogers, J. C.; Qu, Y.; Tanada, T. N.; Scheuer, T.; Catterall, W. A. Molecular Determinants of High Affinity Binding of Alpha-Scorpion Toxin and Sea Anemone Toxin in the S3-S4 Extracellular Loop in Domain IV of the Na+ Channel Alpha Subunit. *J. Biol. Chem.* **1996**, *271* (27), 15950–15962. https://doi.org/10.1074/jbc.271.27.15950.

(87) Cestèle, S.; Qu, Y.; Rogers, J. C.; Rochat, H.; Scheuer, T.; Catterall, W. A. Voltage Sensor-Trapping: Enhanced Activation of Sodium Channels by Beta-Scorpion Toxin Bound to the S3-S4 Loop in Domain II. *Neuron* **1998**, *21* (4), 919–931.

(88) Yang, N.; Horn, R. Evidence for Voltage-Dependent S4 Movement in Sodium Channels. *Neuron* **1995**, *15* (1), 213–218.

(89) Yang, N.; George, A. L.; Horn, R. Probing the Outer Vestibule of a Sodium Channel Voltage Sensor. *Biophys. J.* **1997**, *73* (5), 2260–2268. https://doi.org/10.1016/S0006-3495(97)78258-4.

(90) Yang, N.; George, A. L.; Horn, R. Molecular Basis of Charge Movement in Voltage-Gated Sodium Channels. *Neuron* **1996**, *16* (1), 113–122.

(91) DeCaen, P. G.; Yarov-Yarovoy, V.; Zhao, Y.; Scheuer, T.; Catterall, W. A. Disulfide Locking a Sodium Channel Voltage Sensor Reveals Ion Pair Formation during Activation. *Proc. Natl. Acad. Sci. U. S. A.* **2008**, *105* (39), 15142–15147. https://doi.org/10.1073/pnas.0806486105.

(92) DeCaen, P. G.; Yarov-Yarovoy, V.; Scheuer, T.; Catterall, W. A. Gating Charge Interactions with the S1 Segment during Activation of a Na+ Channel Voltage Sensor. *Proc. Natl. Acad. Sci. U. S. A.* **2011**, *108* (46), 18825–18830. https://doi.org/10.1073/pnas.1116449108.

(93) Yarov-Yarovoy, V.; DeCaen, P. G.; Westenbroek, R. E.; Pan, C.-Y.; Scheuer, T.; Baker, D.; Catterall, W. A. Structural Basis for Gating Charge Movement in the Voltage Sensor of a Sodium Channel. *Proc. Natl. Acad. Sci. U. S. A.* **2012**, *109* (2), E93-102. https://doi.org/10.1073/pnas.1118434109.

(94) Clairfeuille, T.; Cloake, A.; Infield, D. T.; Llongueras, J. P. P.; Arthur, C. P.; Li, Z. R.; Jian, Y.; F, M.-E., Marie-France; Bougis, P. E.; Ciferri, C.; et al. Structural Basis of α-Scorpion Toxin Action on Nav Channels. *Science* **2019**, *363* (6433), eaav8573. https://doi.org/10.1126/science.aav8573.

(95) Xu, H.; Li, T.; Rohou, A.; Arthur, C. P.; Tzakoniati, F.; Wong, E.; Estevez, A.; Kugel, C.; Franke, Y.; Chen, J.; et al. Structural Basis of Nav1.7 Inhibition by a Gating-Modifier Spider Toxin. *Cell* **2019**, *176* (4), 702-715.e14. https://doi.org/10.1016/j.cell.2018.12.018.

(96) Pedraza Escalona, M.; Possani, L. D. Scorpion Beta-Toxins and Voltage-Gated Sodium Channels: Interactions and Effects. *Front Biosci Landmark Ed* **2013**, *18*, 572–587.

(97) Catterall, W. A.; Wisedchaisri, G.; Zheng, N. The Chemical Basis for Electrical Signaling. *Nat Chem Biol* **2017**, *13* (5), 455. https://doi.org/10.1038/nCHeMBIO.2353.

(98) Alexander, S. P.; Catterall, W. A.; Kelly, E.; Marrion, N.; Peters, J. A.; Benson, H. E.; Faccenda, E.; Pawson, A. J.; Sharman, J. L.; Southan, C.; et al. The Concise Guide to PHARMACOLOGY 2015/16: Voltage-Gated Ion Channels. *Br J Pharmacol* **2015**, *172* (24), 5904–5941. https://doi.org/10.1111/bph.13349.

(99) Hoshi, T.; Zagotta, W.; Aldrich, R. Biophysical and Molecular Mechanisms of Shaker Potassium Channel Inactivation. *Science* **1990**, *250* (4980), 533–538.

(100) MacKinnon, R.; Aldrich, R. W.; Lee, A. W. Functional Stoichiometry of Shaker Potassium Channel Inactivation. *Science* **1993**, *262* (5134), 757–759.

(101) Zagotta, W. N.; Hoshi, T.; Aldrich, R. W. Restoration of Inactivation in Mutants of Shaker Potassium Channels by a Peptide Derived from ShB. *Science* **1990**, *250* (4980), 568–571.

(102) Liu, C. C.; Schultz, P. G. Adding New Chemistries to the Genetic Code. *Annu Rev Biochem* **2010**, *79* (1), 413–444. https://doi.org/10.1146/annurev.biochem.052308.105824.

(103) Lummis, S. C.; Beene, D. L.; Lee, L. W.; Lester, H. A.; Broadhurst, R.; Dougherty, D. A. Cis-Trans Isomerization at a Proline Opens the Pore of a Neurotransmitter-Gated Ion Channel. *Nature* **2005**, *438* (7065), 248–252. https://doi.org/10.1038/nature04130.

(104) Nowak, M.; Gallivan, J.; Silverman, S.; Labarca, C.; Dougherty, D.; Lester, H. In Vivo Incorporation of Unnatural Amino Acids into Ion Channels in Xenopus Oocyte Expression System. *Methods Enzymol.* **1998**, *293*, 529.

(105) Ryu, Y.; Schultz, P. G. Efficient Incorporation of Unnatural Amino Acids into Proteins in Escherichia Coli. *Nat. Methods* **2006**, *3* (4), 263–265. https://doi.org/10.1038/nmeth864.

(106) Papke, R. L.; Smith-Maxwell, C. High Throughput Electrophysiology with Xenopus Oocytes. *Comb. Chem. High Throughput Screen.* **2009**, *12* (1), 38–50.

(107) Dougherty, D. Unnatural Amino Acids as Probes of Protein Structure and Function. *Curr Opin Chem Biol* **2000**, *4* (6), 645–652.

(108) Papke, R. L.; Stokes, C. Working with OpusXpress: Methods for High Volume Oocyte Experiments. *Methods* **2010**, *51* (1), 121–133. https://doi.org/10.1016/j.ymeth.2010.01.012.

(109) Nowak, M.; Kearney, P.; Sampson; Saks, M.; Labarca, C.; Silverman, S.; Zhong, W.; Thorson, J.; Abelson, J.; Davidson, N. Nicotinic Receptor Binding Site Probed with Unnatural Amino Acid Incorporation in Intact Cells. *Science* **1995**, *268* (5209), 439–442. https://doi.org/10.1126/science.7716551.

(110) Gleitsman, K. R.; Shanata, J.; Frazier, S. J.; Lester, H. A.; Dougherty, D. A. Long-Range Coupling in an Allosteric Receptor Revealed by Mutant Cycle Analysis. *Biophys J* **2009**, *96* (8), 3168–3178. https://doi.org/10.1016/j.bpj.2008.12.3949.

(111) Horovitz, A. Double-Mutant Cycles: A Powerful Tool for Analyzing Protein Structure and Function. *Fold Des* **1996**, *1* (6), R121–R126. https://doi.org/10.1016/S1359-0278(96)00056-9.

(112) Post, M. R.; Limapichat, W.; Lester, H. A.; Dougherty, D. A. Heterologous Expression and Nonsense Suppression Provide Insights into Agonist Behavior at A6β2 Nicotinic Acetylcholine Receptors. *Neuropharmacology* **2015**, *97*, 376–382. https://doi.org/10.1016/j.neuropharm.2015.04.009.

Chapter 2

Probing Binding Interactions of a Novel Series C(10)-Cytisine Derivatives to the α4β2 Nicotinic Acetylcholine Receptor*

2.1 Abstract

Nicotinic acetylcholine receptors (nAChR) are crucial for communication between synapses in the central nervous system. As such, they are also implicated in several neuropsychiatric and addictive diseases. Previous studies have established a binding model for several agonists to several nAChR subtypes. Here, we expand the binding model of cytisine to the α4β2 nAChR. We determined how the key binding interactions between cytisine and the binding site of α4β2 nAChR are impacted by C(10)-modification of cytisine. To achieve this, we used two-electrode voltage-clamp electrophysiology and non-canonical amino acid mutagenesis to probe the agonist binding interactions of a novel series of C(10)-cytisine derivatives. In contrast to the well-studied agonists nicotine and acetylcholine, cytisine and the C(10)-derivatives studied here make an additional cation-π interaction to TyrC2. Surprisingly, double mutant-cycle analyses revealed that all C(10)-derivatives make a stronger cation-π interaction to TyrC2 than cytisine, whereas the hydrogen bond to LeuE in the complementary subunit is generally diminished relative to that for cytisine. This study suggests a model for how cytisine derivatives substituted at C(10) (as well as C(9)/C(10)) adjust their binding orientation in response to pyridone ring-substitution.

2.2 Introduction

Nicotinic acetylcholine receptors (nAChRs) have been studied for their role in synaptic transmission and consequently their involvement in neural disorders such as

* The work described in this chapter was done in collaboration with Dr. Hugo Rego Campello, Prof. Timothy Gallagher, and Prof. Henry A. Lester.

nicotine addiction, epilepsy, and Parkinson's disease.[1,2] Tobacco use causes more than 7 million deaths per year worldwide, and smoking is the leading cause of preventable death (WHO 2017). In addition, smoking costs the United States nearly $170 billion in direct medical care for adults each year (Federal Trade Commission 2016). Nicotine's behavioral effects result from its interaction with nAChRs.[3] Various studies have linked polymorphisms in nAChR genes to risk of tobacco and alcohol dependence and established that nicotine functions as an intracellular chaperone of nAChRs.[4] However, developing new treatments for these targets remains challenging, as the various subtypes of nAChRs are structurally similar, and the mechanism of receptor activation, and how this may or may not vary with subtype, is still not completely understood.

nAChRs are pentameric ligand-gated ion channels and part of the Cys-loop receptor family. Neuronal nAChRs are composed of five subunits, forming heteromers of α2-α11 and β2-β4, or α-only homomers[5,6] Various combinations of subunits and stoichiometries exist, but the most abundant in the brain is the α4β2 nAChR, the high affinity nicotine receptor, assembling into both $(\alpha4)_2(\beta2)_3$ and $(\alpha4)_3(\beta2)_2$ stoichiometries (for simplicity, we refer to these as A2B3 and A3B2, respectively).[7,8] Both stoichiometries are functional and have distinct biophysical properties. Changes in subunit stoichiometry are linked to both nicotine addiction and autosomal dominant nocturnal frontal lobe epilepsy.[9] Therefore, gaining a better understanding of differential agonist effects on these two stoichiometries of the α4β2 nAChR is desired.

Previous studies have established a binding model for nicotine and other agonists to several nAChR subtypes (**Figure 1**).[10–12] For the α4β2 subtype three key binding interactions were identified: a cation-π interaction to W154 in loop B (TrpB), a hydrogen bond to the backbone carbonyl of TrpB, and a hydrogen bond to L119 in Loop E (LeuE) of the

complementary subunit. It has been shown that the cation-π interaction is sometimes formed to a different aromatic residue of the five in the binding pocket; such is the case for acetylcholine and epibatidine in the α7 receptor, where this interaction is to TyrA instead of the more common TrpB.[13] Not all agonists make both hydrogen bonds. For example, as would be expected for a quaternary ammonium ion, acetylcholine does not make the hydrogen bond to the backbone carbonyl of TrpB.

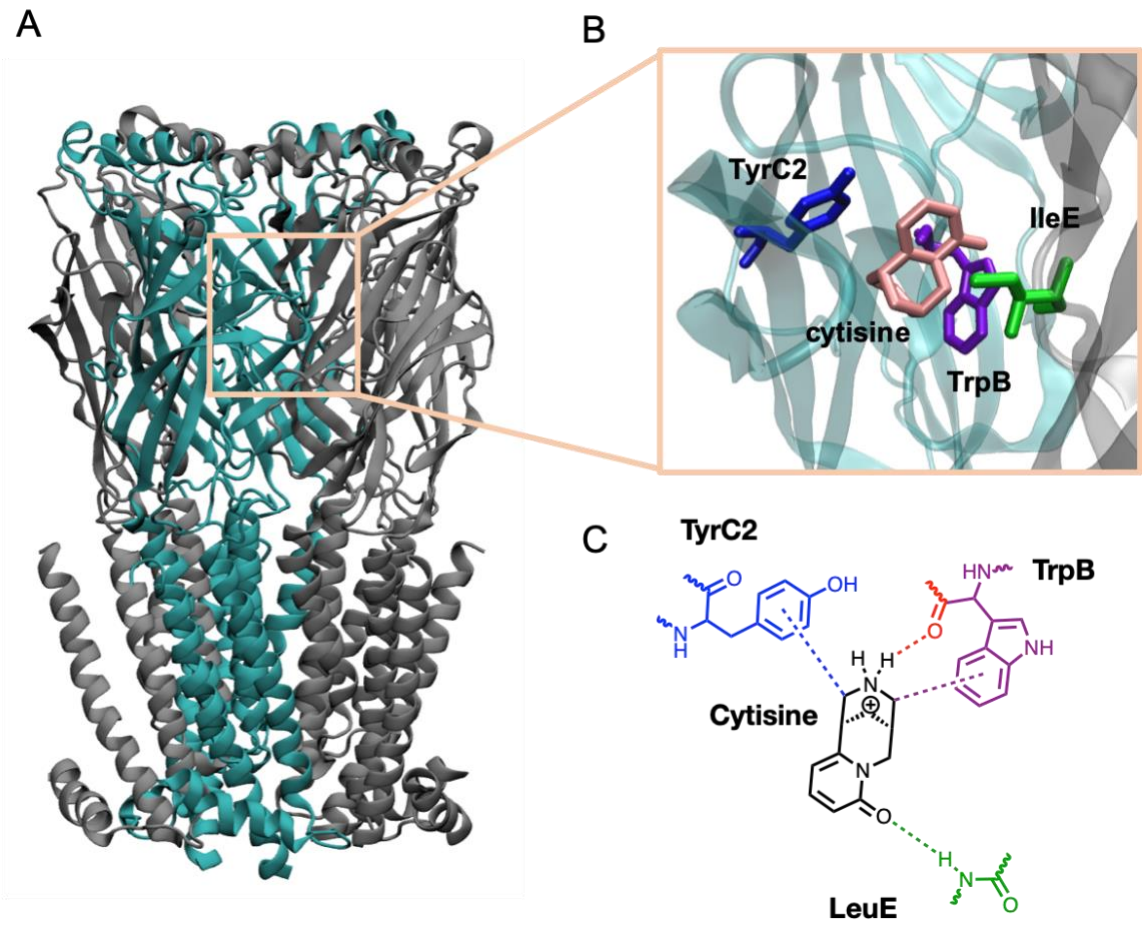

Figure 2.1 | Agonist binding site at the α4β2 nAChR. (A) Side view of the crystal structure of human α4β2 receptor nAChR (PDB: 5KXI), α4 subunit in teal, β2 subunit in grey. The agonist binding site at the α4/β2-interface is indicated with a square. (B) Closer look at the binding pocket. Crystal structure shown here is AChBP with cytisine bound (PDB: 4BQT). Functionally relevant residues probed in this study are highlighted: TrpB (purple), LeuE (green) (Ile in AChBP), TyrC2 (blue). (C) Schematic view of ligand-binding interactions of cytisine; cation-π interactions in purple and blue, hydrogen bonds in green and red.

In addition to these structure-function studies, drug discovery efforts targeting nAChRs have produced many compounds with differential efficacy. The partial agonist (-)-cytisine, marketed as Tabex®, has been available in Eastern Europe for smoking cessation for many years.[14–22] Various cytisine derivatives have been developed, including functionalization at the piperidine ring,[23–28] and at the pyridone ring.[29–33] In addition, cytisine played a role in the development of varenicline, marketed as Chantix® for smoking cessation.[34] Cytisine also shows a novel subtype selectivity, in that it is a partial agonist for the A3B2 nAChR, but does not activate A2B3, where it is effectively a competitive antagonist. Interestingly, the three binding interactions exhibit distinct binding strengths for cytisine in the two stoichiometries of α4β2.[35] The cation-π interaction to TrpB is comparable in both A2B3 and A3B2, but the hydrogen bonds appear to have differential strengths; in A2B3 the hydrogen bond to LeuE is stronger, whereas in A3B2 the hydrogen bond to the backbone carbonyl of TrpB is more pronounced. More recent studies suggest that in A3B2 cytisine not only binds at the canonical binding site at the α+/β- interface, but also at the α/α-interface.[36]

Several variants on the cytisine structure did not maintain the ability to activate nAChRs. Functionalization at C(10) alone has not yet been studied extensively, but is of interest as substituents at this site are positioned to interact with the complementary subunit in the binding pocket; this region of the binding pocket has been proposed to be most effective in creating subtype selectivity. Recent advances in synthetic strategies have made several C(10)-modified cytisine derivatives readily available,[37,38] including some with enhanced selectivity for α4β2 over α3β4 and α7.[32,33,39] More recently, direct C-H functionalization of cytisine itself has increased both the accessibility and range of C(10)-variants that are available, and these can now be synthesized (for the first time) in enantiomerically pure form.[39]

In the present study, we set out to determine how C(10)-modification of cytisine, as well as a series of C(9), C(10)-disubstituted variants, impact the key binding interactions between cytisine and the binding site of α4β2 nAChR. To achieve this goal, we used two-electrode voltage-clamp electrophysiology and non-canonical amino acid mutagenesis to probe the agonist binding interactions of a novel series of cytisine derivatives. In contrast to the well-studied agonists nicotine and acetylcholine, cytisine and the C(10)-derivatives make a second cation-π interaction to TyrC2. Double-mutant cycle analyses revealed that this cation-π interaction to TyrC2 is the binding parameter most strongly impacted by pyridone ring-substitution, with the hydrogen bond to LeuE in the complementary subunit (and associated with the pyridone C=O as the H-bond acceptor) being second in impact. Interestingly, pyridone substitution generally enhances the TyrC2 cation-π interaction but diminishes the LeuE hydrogen bond.

2.3 Results and discussion

2.3.1 Cytisine and its C(10) derivatives all make a dual cation-π interaction in nAChR α4β2

Previous studies have shown that three interactions dictate the binding of agonists such as acetylcholine and nicotine to the α4β2 receptor: a cation-π interaction with TrpB, a hydrogen bond to the backbone carbonyl of TrpB, and a hydrogen bond to backbone NH of LeuE. More recently, our group has shown that, in addition to the cation-π interaction with TrpB, secondary ammonium agonists, such as metanicotine, TC299423, varenicline, and nornicotine make a second cation-π interaction at TyrC2 in α4β2 (**Figure 2.1**).[40] The common structural feature that distinguishes these agonists from acetylcholine and nicotine (pKa 7.9) is a protonated secondary amine. Cytisine also contains a protonated secondary amine (pKa 7.8),[21] and we therefore hypothesized that this secondary cation-π interaction could be similarly relevant for cytisine binding to α4β2.

To test for a cation-π interaction at TyrC2, we conducted nonsense-suppression-based fluorination studies. In these experiments, the codon for Y202 was mutated to a TAG stop codon. *In vitro* transcribed mutant mRNA was injected into *Xenopus laevis* oocytes alongside bioorthogonal $tRNA_{CUA}$ that has been chemically coupled to a non-canonical amino acid. To probe for the cation-π interaction, Y202 was replaced by a series of residues with electron withdrawing groups on the aromatic side chain to weaken the interaction. Historically, a series of fluorinated phenylalanines (F_nPhe) have been used to probe Tyr residues, as directly fluorinating tyrosine causes the phenol group to deprotonate at physiological pH. Electrostatic potential calculations show that as n increases to 3 (F_3Phe), the negative electrostatic component of the aromatic ring has been completely removed, greatly weakening a cation-π interaction. If a cation-π interaction is functionally relevant for binding, weakening the interaction is accompanied by a right-shifted EC_{50}. Concentration-response curves were determined using two-electrode voltage clamp electrophysiology. So-called fluorination plots show the relationship of EC_{50} to the calculated gas-phase cation-π interaction strength. Typically, when a cation-π interaction is present, a linear correlation is observed.

Substituting TyrC2 in A3B2 for fluorinated phenylalanines (F_2-Phe, F_3-Phe) produced substantial EC_{50} shifts for cytisine as compared to Phe, but the observed trend was not so linear as we expected (**Figure 2.2, Table 2.1**). Mutating Tyr (wild type) to Phe gives a 5.1 fold loss of function, larger than usual, suggesting that the C(4) hydroxyl might be important. The fold shift for F_1-Phe is smaller than expected (3.2 fold), which could be explained by the fluorine rescuing the need for steric bulk at the 4-position that is lacking at Phe. Lack of steric bulk at the 4-position in F_2-Phe yields a larger loss of function than expected (106 fold) based on electrostatics alone. To investigate whether the C(4) hydroxyl of TyrC2 forms a hydrogen bond, we also tested OMe-Tyr and Me-Phe. Both mutants have EC_{50} values closer to wild

type than Phe, with respective fold shifts of 3.5 and 2.8, suggesting that steric effects at the C(4) position play a role. To further confirm the idea of a cation-π interaction, we tested Br-Phe and CN-Phe (**Figure 2.2, Table 2.1**). These residues are isosteric, but CN-Phe is much more deactivating than Br-Phe. Their respective fold shifts in EC_{50}, 26 and 2.3, support the argument for a cation-π interaction.

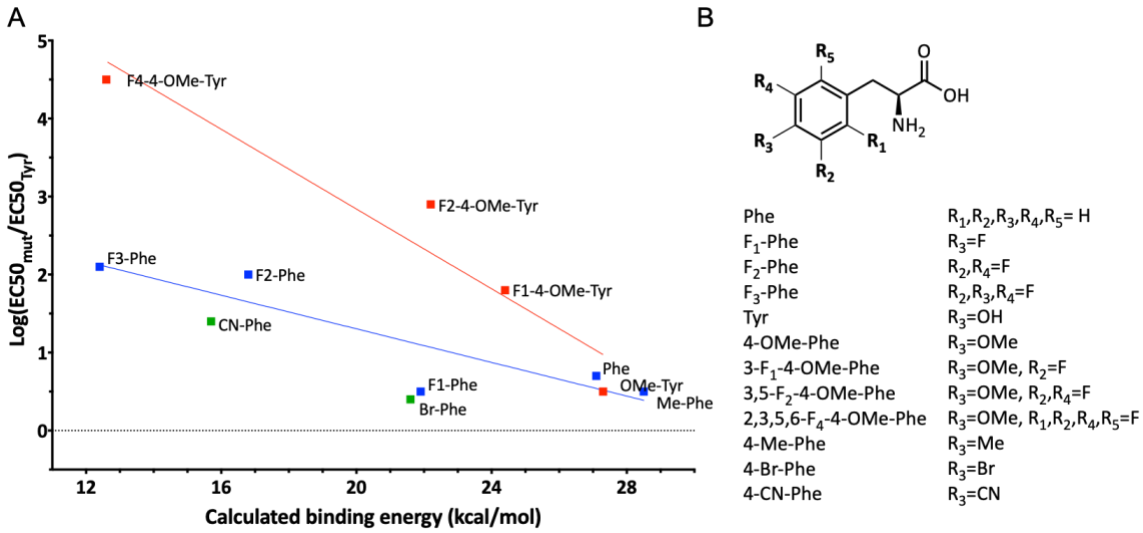

Figure 2.2 | Fluorination plot for cytisine at TyrC2 in the A3B2 stoichiometry. (A) Fluorination plot showing F_n-Phe series in blue (R^2=0.80), F_n-Ome-Tyr series in red (R^2=0.92), and CN-Phe and Br-Phe in green. The x-axis is the calculated binding energy between Na^+ and each side chain in the gas phase.[41] The y-axis is the log fold shift in EC_{50}. (B) Fluorinated amino acids used in this experiment. R= H unless explicitly stated.

Table 2.1 | Cytisine EC_{50} values for non-canonical amino acids at TyrC2 in A3B2.

Residue	EC_{50} (μM)	n_H	Fold shift	N	$\lvert I_{max} \rvert$ (μA)
Tyr	0.0013 ± 0.00002	1.9 ± 0.05	1.0	12	0.22-26.8
Phe	0.0066 ± 0.00014	1.4 ± 0.04	5.1	13	0.064-21.7
4-F_1-Phe	0.0042 ± 0.00015	1.6 ± 0.08	3.2	13	0.34-20.0
3,5-F_2-Phe	0.138 ± 0.014	1.2 ± 0.04	106	14	0.29-9.5
3,4,5-F_3-Phe	0.160 ± 0.0063	1.1 ± 0.05	123	13	0.44-8.0
4-Br-Phe	0.0031 ± 0.00007	1.7 ± 0.06	2.3	14	0.09-8.3

4-CN-Phe	0.034	± 0.0009	1.3	± 0.04	26	16	0.14-13.8
4-Me-Phe	0.0037	± 0.0002	1.6	± 0.10	2.8	14	0.08-15.0
4-OMe-Tyr	0.0045	± 0.0001	1.4	± 0.04	3.5	15	0.60-27.0
3-F_1-4-OMe-Tyr	0.077	± 0.002	1.3	± 0.04	59	16	2.01-8.9
3,5-F_2-4-OMe-Tyr	1.11	± 0.048	0.95	± 0.04	852	11	0.16-3.7
2,3,5,6-F_4-4-OMe-Tyr	41.8	± 2.7	1.1	± 0.07	32154	9	0.03-0.20

In an effort to obtain a more detailed fluorination plot for cytisine, we tested a fluorinated 4-OMe-Tyr series (F_n-4-OMe-Tyr). This series shows that having a constant substituent at C(4) yields a clear linear trend, further corroborating the cation-π interaction (**Figure 2.2, Table 2.1**). To confirm that this interaction is present in both α4β2 stoichiometries, TyrC2 in A2B3 was also substituted with the fluorinated phenylalanine series (Phe, F_1Phe, F_2-Phe, F_3-Phe). The fluorination plot for A2B3 resembled that observed for A3B2 (**Figure 2.3, Table 2.2**). Thus, cytisine continues the trend that agonists containing a protonated secondary amine make dual cation-π interactions.

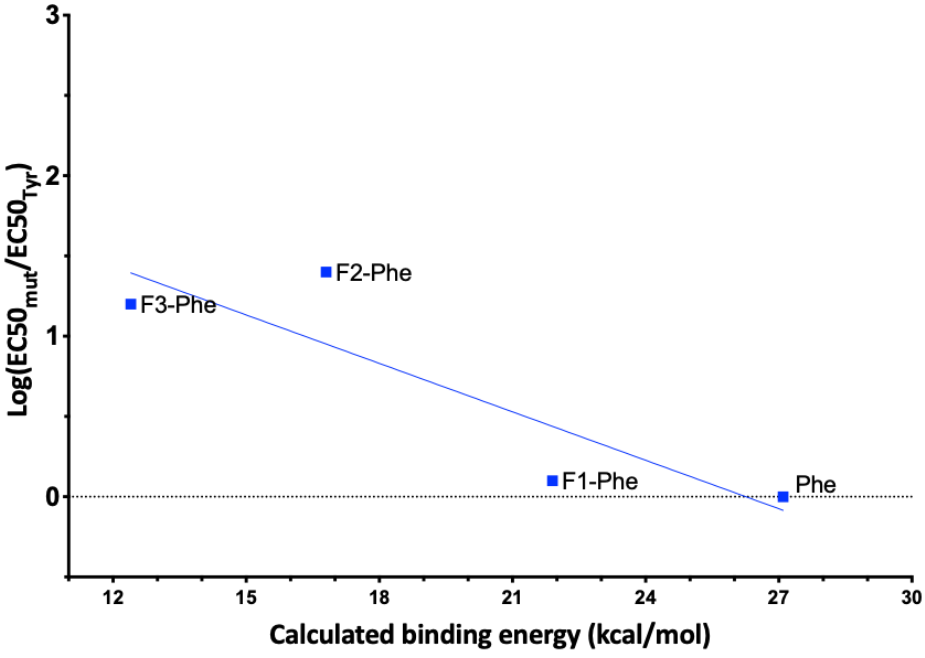

Figure 2.3 | Fluorination plot for cytisine at TyrC2 in the A2B3 stoichiometry. (A) Fluorination plot showing F_n-Phe series in blue (R^2=0.77). The x-axis is the calculated binding energy between a sodium ion and each side chain in the gas phase.[41] The y-axis is the log fold shift in EC_{50}.

Table 2.2 | Cytisine EC_{50} values for non-canonical amino acids at TyrC2 in A2B3.

Residue	EC_{50} (μM)	n_H	Fold shift to WT	Fold shift to Phe	N	$\|I_{max}\|$ (μA)
Tyr	0.0056 ± 0.0001	1.4 ± 0.04	1.0		13	0.11-1.90
Phe	0.012 ± 0.0003	1.4 ± 0.05	2.1	1.0	18	0.054-0.84
4-F_1-Phe	0.014 ± 0.0005	1.4 ± 0.07	2.5	1.2	16	0.022-0.54
3,5-F_2-Phe	0.337 ± 0.023	1.3 ± 0.10	60	28	8	0.009-0.10
3,4,5-F_3-Phe	0.202 ± 0.009	1.3 ± 0.07	36	17	13	0.034-0.30

All substituted cytisines show a substantial loss of function for F_3-Phe relative to Phe at TyrC2 (**Table 2.11**). This confirms that all the compounds studied here make a dual cation-π interaction in the α4β2 nAChR.

2.3.2 Impact of cytisine C(10)-modification on EC_{50} and efficacy

Identifying the second cation-π interaction to TyrC2 expanded the binding model for cytisine, and consequently added to the list of agonists exhibiting this new binding pattern. Previous work has shown that there is variation in the standard binding model, including the lack of a backbone hydrogen bond to TrpB for acetylcholine, and the absence of a functionally important LeuE hydrogen bond for varenicline.[35] We hypothesized that making subtle, systematic changes to the cytisine structure would allow us to manipulate the individual binding interactions more precisely than simply comparing more structurally diverse agonists. The C(9) and C(10) positions are shown in **Figure 2.4B,** and C(10)-substitution would more directly impact on the electronic properties of the pyridone carbonyl and the resulting LeuE interaction. Based on structural studies of the Acetylcholine binding protein (AChBP)

functionalization at C(10) is expected to interact with the complementary subunit in the binding pocket and could provide relevant information on subtype selectivity. Indeed, in binding affinity studies some of these compounds have enhanced selectivity for α4β2 over α3β4 and α7.[39] We therefore selected a series of C(10)-modified cytisine derivatives to test our hypothesis. As described in **Figure 2.4**, we will refer to monosubstituted cytisine derivatives by the new substituent, which is always at C(10). Disubstituted compounds contain a Br at C(9) along with a C(10) substituent.

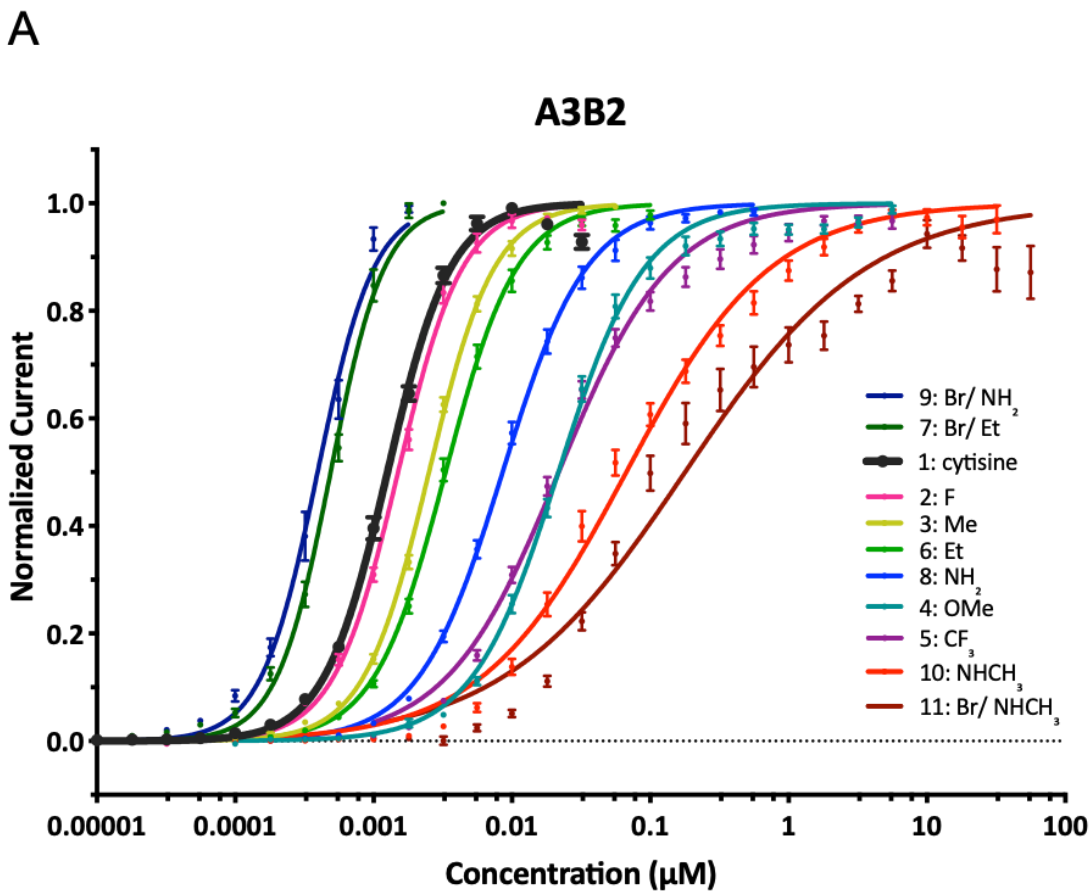

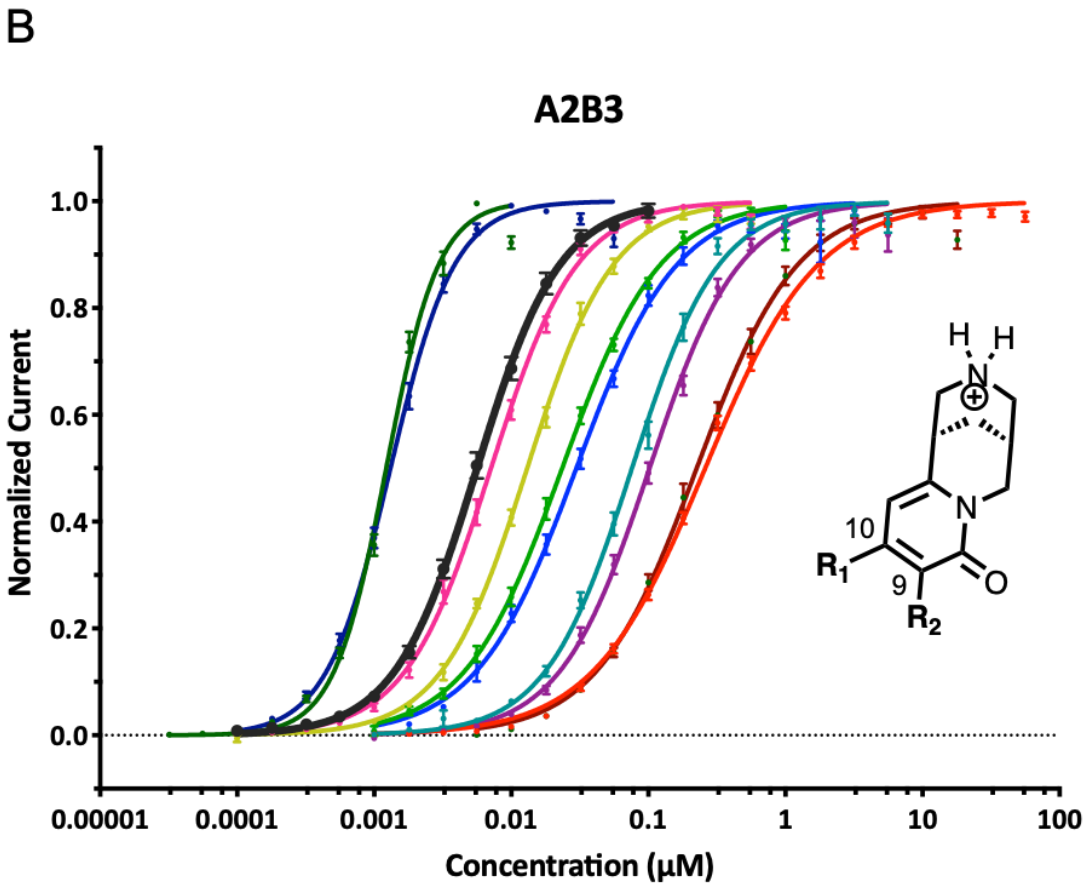

Figure 2.4 | Dose-response curves of cytisine derivatives in the two stoichiometries of α4β2. (A) Dose-response curves of cytisine derivatives in A3B2. (B) Dose-response curves of cytisine derivatives in A2B3. Inset in B shows the structure of cytisine with C(9) and C(10) highlighted. All single substituents correspond to R_1 at the C(10)-position, for which R_2=H. C(9) and C(10) disubstituted variants have R_2 = Br. Note that the dose-response curve for **11** (Br/NHMe) in A3B2 is presented here with a monophasic fit, but values in Table 2 reflect EC_{50} and Hill coefficients obtained through a biphasic fit.

Table 2.3 | EC_{50} values for cytisine derivatives at WT A3B2.

Ligand		EC_{50} (nM)			n_H			Fold shift	N	Efficacy	$\lvert I_{max} \rvert$ (μA)
1	Cytisine	1.3	±	0.019	1.9	±	0.05	1.0	12	0.73	0.22-26.8
2	F	1.5	±	0.07	1.9	±	0.05	1.2	13	0.62	1.47-35.1
3	Me	2.5	±	0.16	1.8	±	0.04	1.9	13	0.67	0.37-47.2
4	OMe	22	±	1.3	1.4	±	0.04	17	13	0.84	0.45-31.6
5	CF_3	22	±	0.08	1.1	±	0.03	17	13	0.71	1.46-58.9
10	NHMe	25	±	67	1.5	±	0.18	19	10	0.74	6.61-51.9

		530	±	160	1.3	±	0.40			
11	Br/ NHMe	60	±	42	1.3	±	0.16	46	12	0.84	0.89-30.4
		3296	±	0.04	3.0	±	0.10			
6	Et	3.3	±	0.06	1.7	±	0.04	2.5	16	0.51	1.08-35.7
7	Br/ Et	0.49	±	0.1	2.2	±	0.10	0.4	8	0.46	0.76-6.75
8	NH_2	8.6	±	0.2	1.4	±	0.04	6.6	9	0.28	0.52-37.3
9	Br/ NH_2	0.39	±	0.01	2.1	±	0.12	0.3	14	0.25	0.68-22.9

Table 2.4 | EC_{50} values for cytisine derivatives at WT A2B3.

Ligand		**EC_{50} (nM)**			**n_H**			**Fold shift**	**N**	**Efficacy**	**$\|I_{max}\|$ (μA)**
1	Cytisine	5.6	±	0.12	1.4	±	0.04	1.0	13	0.05	0.1 – 2.1
2	F	7.1	±	0.14	1.4	±	0.03	1.3	14	0.10	0.4 – 16.4
3	Me	13	±	0.23	1.4	±	0.03	2.3	12	0.16	0.5 – 8.7
4	OMe	76	±	1.8	1.4	±	0.04	14	13	0.08	0.3 – 1.0
5	CF_3	102	±	2.6	1.3	±	0.04	18	14	0.06	0.9 – 5.1
10	NHMe	260	±	4.2	1.1	±	0.02	44	12	0.19	1.1 – 4.5
11	Br/ NHMe	225	±	6.0	1.2	±	0.03	37	13	0.29	0.35 - 2.2
6	Et	24	±	0.50	1.2	±	0.03	4.3	16	0.16	0.34 -3.9
7	Br/ Et	1.2	±	0.021	2.3	±	0.08	0.21	14	0.33	0.86 – 8.6
8	NH_2	30	±	0.77	1.2	±	0.03	5.4	16	0.18	0.40 - 3.7
9	Br/ NH_2	1.3	±	0.022	1.9	±	0.05	0.23	23	0.29	0.83 – 5.4

Figure 2.4 presents the concentration-response curves of all derivatives. Agonist activity was determined in both (A2B3 and A3B2) stoichiometries of α4β2 and in α7. The potency for α7 was much lower (>100 μM, **Figure 2.5, Table 2.5**) than for α4β2 (<1 μM), so further experiments were focused on the two stoichiometries of α4β2 only. Various substitutions were included in this series, including groups with differing steric and electronic influences. We hypothesized that a C(10) electron withdrawing or electron donating group would modulate the hydrogen bond acceptor capacity of the pyridone carbonyl. These effects could potentially give opposing EC_{50} fold shifts. However, all cytisine derivatives with just a

single substitution (at C(10)) demonstrated decreased potency for both α4β2 subtypes (**Figure 2.4, Table 2.3, Table 2.4**). The smallest shifts in EC_{50} relative to cytisine were observed for **2** (R_1=F) and **3** (R_1=Me), 1.2 and 2.0-fold in A3B2 respectively (**Figure 2.4A**). The largest shifts in EC_{50} were observed for **4** (R_1=OMe) and **10** (R_1=NHMe), 16 and 42-fold in A3B2, respectively. Similar trends were seen in the A2B3 stoichiometry (**Figure 2.4B**). Efficacy of all derivatives was higher than cytisine in A2B3, but comparable to cytisine in A3B2. Recall that the parent cytisine is effectively inactive at A2B3, and so it appears that any C(10) substituent renders cytisine viable in this less active stoichiometry.

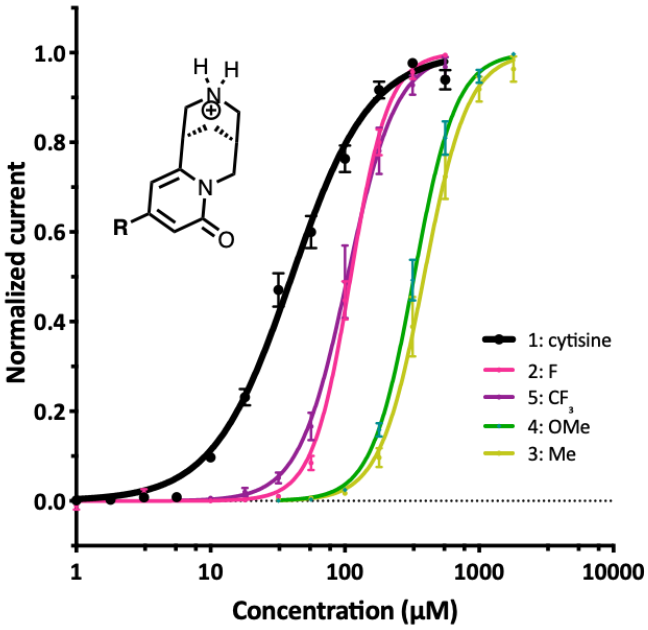

Figure 2.5 | Dose-response curves of cytisine derivatives to the α7 nAChR. The cytisine structure indicated the position of the substituent at C(10). The EC_{50} of **10** (R_1=NHMe) was too far right-shifted to record a full dose-response curve.

Table 2.5 | EC_{50} values for cytisine derivatives at WT α7. ND: not determined.

Ligand		EC_{50} (μM)			n_H			Fold shift	N	Efficacy	$\lvert I_{max} \rvert$ (μA)
1	Cytisine	40.2	±	1.3	1.5	±	0.07	1.0	11	ND	0.86-14.0
2	F	111	±	1.9	3.1	±	0.2	2.8	6	ND	0.05-5.6

5	CF_3	105	±	4.3	2.4	±	0.2	2.6	7	0.16	0.22-4.1
4	OMe	327	±	7.7	2.8	±	0.2	8.1	8	0.37	0.37-17.5
3	Me	388	±	14	2.7	±	0.2	9.7	7	0.35	0.42-11.4

Given the observed EC_{50} shifts, we speculated that the decreased potency is actually correlated with increasing size of the substituent, rather than with electronic contribution of this group. To probe this, we tested a series of four additional derivatives with increasing steric bulk, but without substantially different electrostatic effects: **6** (R_1=Et), **12** (R_1=C(Me)CH_2), **13** (R_1=$CH(Me)_2$), **14** (R_1=$C(Me)_3$). EC_{50} values for these compounds were increasingly right shifted with increasing size (**Figure 2.6, Table 2.6**).

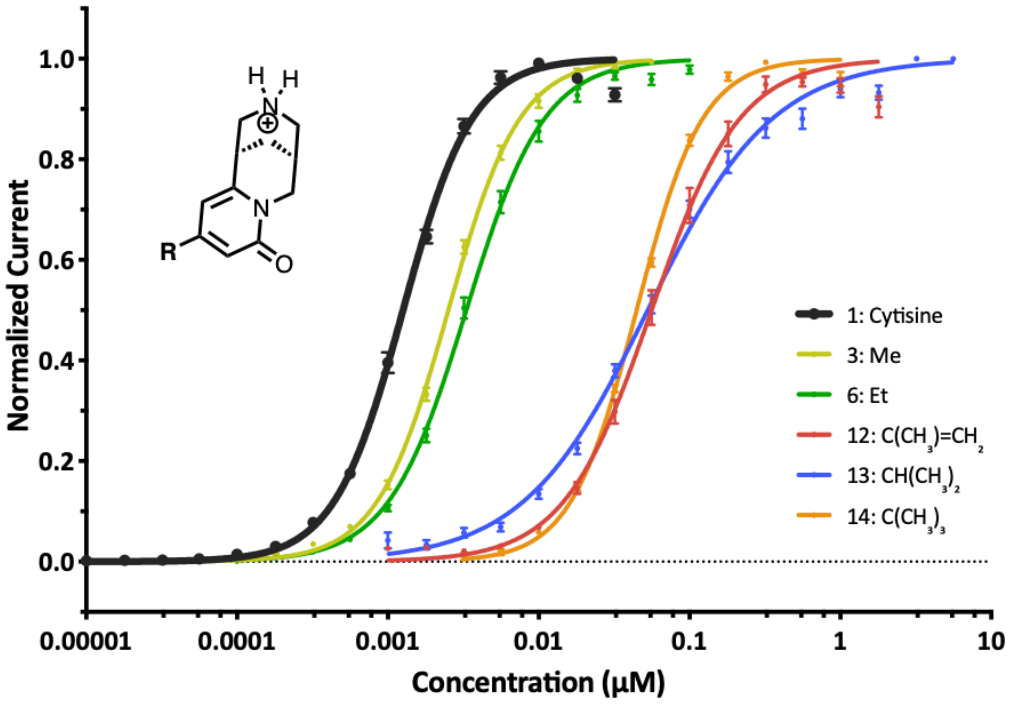

Figure 2.6 | Investigation of steric effects on C(10)-substitution in A3B2. (A) Dose-response curves for C(10)-derivatives with increased steric bulk. Cytisine derivatives used in this series; **3** (Me), **6** (Et), **12** ($C(Me)=CH_2$), **13** ($CH(Me)_2$), **14** ($C(Me)_3$).

Table 2.6 | EC_{50} values for cytisine derivatives, sterics series, at WT A3B2. Volume of ligand was calculated after equilibrium geometry optimization using HF-6-31** in vacuum.

Ligand		EC_{50} (nM)			n_H			Fold shift	N	Effi-acy	$\lvert I_{max} \rvert$ (μA)	Volume (Å^3)
1	cytisine	1.3	±	0.019	1.9	±	0.05	1.0	12	0.73	0.22-27	198.21
3	Me	2.5	±	0.16	1.8	±	0.04	1.9	13	0.67	0.37-47	216.33
6	Et	3.3	±	0.059	1.7	±	0.04	2.5	16	0.51	1.1-36	234.29
12	$C(Me)=CH_2$	56	±	1.7	1.5	±	0.06	44	12	0.14	0.28-5.8	248.52
13	$CH(Me)_2$	53	±	1.5	1.4	±	0.03	42	17	0.06	0.055-4.0	252.31
14	$C(Me)_3$	45	±	0.51	2.0	±	0.04	35	10	0.67	1.0-24	269.51

Addition of a bromine at the C(9) position (in addition to a C(10)-residue) results in a left-shifted EC_{50} when the C(10)-substituent is an NH_2 or Et group (**Figure 2.4**). Introducing a bromine at C(9) did not produce the same increase in potency when the C(10)-substituent is NHMe (**10**). In an attempt to explain this difference in activity we performed HF 6-31G** calculations on both structures. Ligand **7** (Br/Et) and **11** (Br/NHMe) are isosteric, and the electrostatic potentials of the carbonyl and amine are similar as well (**Table 2.7**). Conformational analysis indicates that for **10** (NHMe) and **11** (Br/NHMe) the C(10)-substituent stays in the plane of the pyridone ring in the lowest energy conformer, presumably to facilitate conjugation of the nitrogen lone pair with the ring. In contrast, for both **6** (Et) and **7** (Br/Et) the C(10)-substituent is positioned close to perpendicular to the ring (**Figure 2.7**) in what is presumably a steric effect. We speculate that having the C(10)-substituent perpendicular to the ring contributes to the gain in potency that is seen for **7** (Br/Et) and **9** (Br/NH_2) relative to **6** (Et) and **8** (NH_2). Since the C(10) substituent in **11** (Br/NHMe) is less likely to adopt this conformation, this could prevent favorable repositioning of the ligand resulting in a similar EC_{50} as NHMe-cytisine. LogP and LogD do not yield any correlation with the EC_{50} fold shifts **(Figure 2.8)**.

Table 2.7 | Calculated electrostatic potentials of carbonyl and amine in cytisine derivatives, as well as the total volume of the ligand.

Ligand		Carbonyl (kcal/mol)	Amine (kcal/mol)	Volume (Å^3)
5	CF_3	8.35	170.61	229.67
2	F	4.59	169.97	202.59
1	cytisine	2.85	167.89	198.21
3	Me	0.94	166.11	216.33
6	Et	0.44	165.84	234.29
12	$C(Me)=CH_2$	0.35	165.97	248.52
13	$CH(Me)_2$	0.11	165.61	252.31
4	OMe	0.03	165.60	224.91
14	$C(Me)_3$	0.03	165.21	269.51
7	Br/ Et	-2.11	168.01	252.59
8	NH_2	-3.63	164.70	208.15
9	Br/ NH_2	-5.85	166.89	226.00
10	NHMe	-5.86	164.14	228.16
11	Br/NHMe	-8.12	165.54	246.29

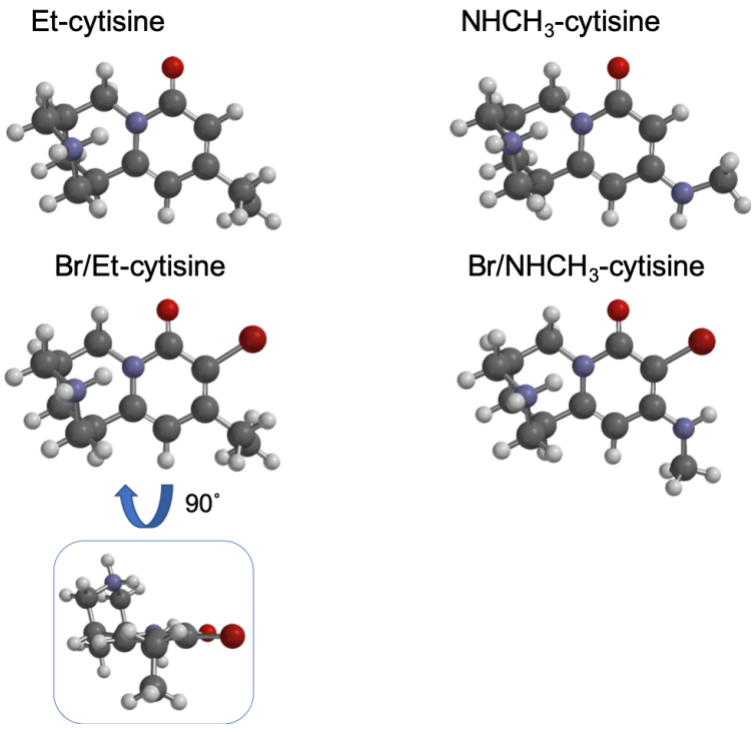

Figure 2.7 | Conformational analysis of cytisine derivatives with NHMe and Et-substituents at C(10). Lowest energy conformers of **6** (R_1=Et) and **7** (Br/Et) have the C(10)-substituent perpendicular to the pyridone ring, while **10** (R_1=NHMe) and **11** (Br/NHMe) have the substituent in the plane of the pyridone ring.

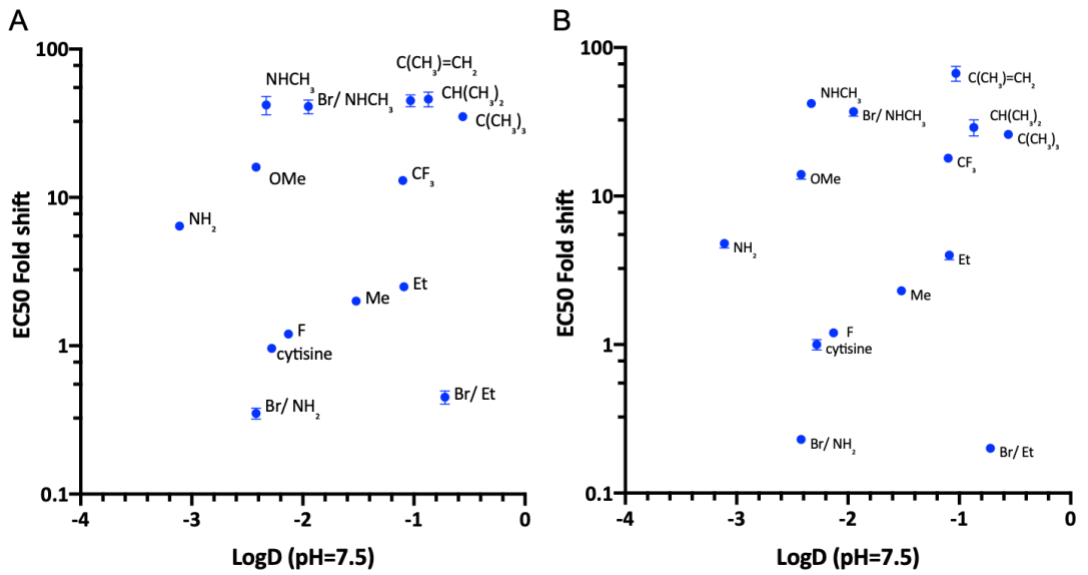

Figure 2.8 | EC_{50} fold shifts of C(10) derivatives plotted as a function of $logD_{7.5}$. (A) Values for A3B2 stoichiometry and (B) values for A2B3 stoichiometry.

2.3.3 Differential impacts of cytisine C(10)-modification on individual binding interactions

As a global measure of receptor activation, EC_{50} can be influenced by a number of receptor-independent physico-chemical properties, such as agonist solubility and hydrophobicity. Subtype selectivity, however, is more likely to arise via ligand interactions with side-chain or backbone moieties, and it is those we wish to evaluate. To probe these interactions, we employed strategies based on non-canonical amino acid incorporation (**Figure 2.9**) as described previously.[35] To probe the TrpB cation-π interaction, we replaced W154 by F_4-Trp.[42] To test hydrogen bonding to the backbone carbonyl of this residue, we substitute the *i* + 1 residue, T155, with its α-hydroxy analogue, Tah (threonine, α-hydroxy).[11,43] To test the hydrogen bond to LeuE in the β2 subunit, L119 is replaced by Lah (Leucine, α-hydroxy).[10] To probe the TyrC2 cation-π interaction, we replaced Y202 with F_3-Phe. To quantify the functional effect of a mutant, we calculate the EC_{50} fold shift, which is EC_{50} for the mutant receptor divided by wild type recovery response (i.e., producing wild type receptor

by incorporating the wild type residue by nonsense suppression). We typically consider an EC_{50} fold shift larger than 2 as meaningful. All EC_{50} fold shifts observed for the four binding interactions are larger than 2, suggesting that all derivatives make all four binding interactions.

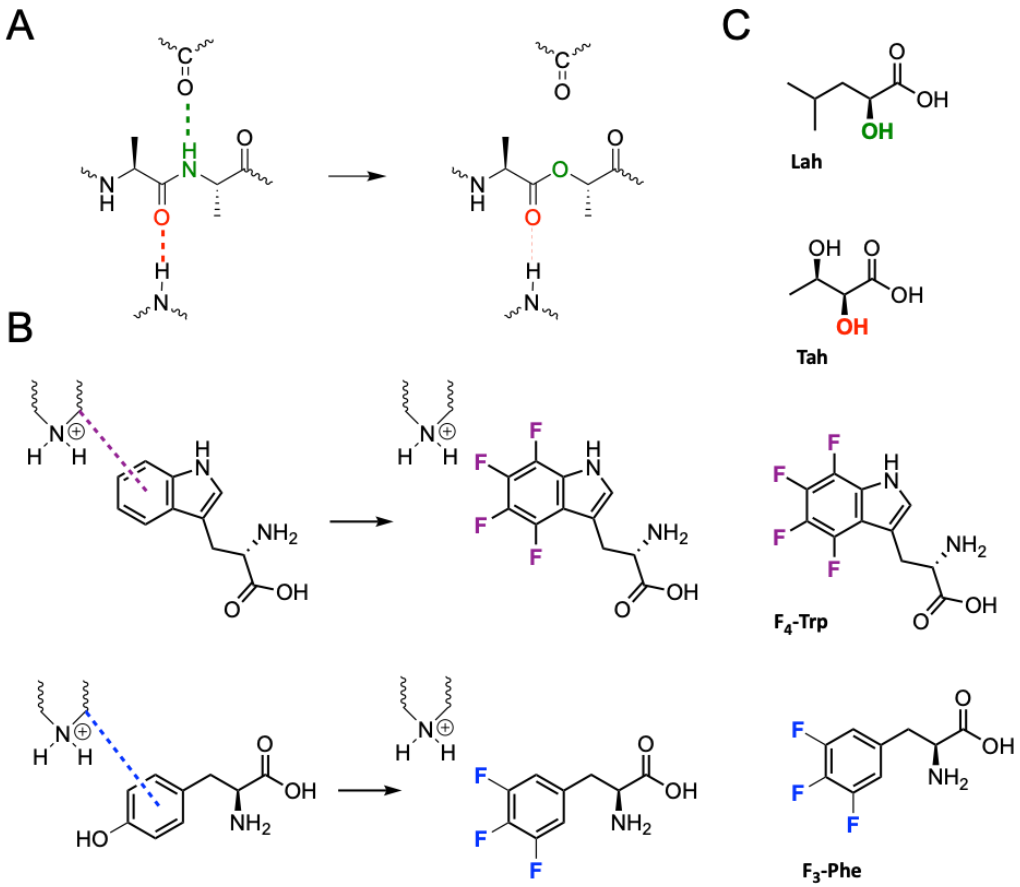

Figure 2.9 | Strategy to selectively probe electrostatic interactions contributing to binding of the ligand. (A) To probe backbone hydrogen bonds, α-hydroxy acids are incorporated resulting in the loss of hydrogen bond donor (backbone NH) and weakened hydrogen bond acceptor (backbone carbonyl). (B) To probe cation-π interactions Trp and Tyr are substituted by a series of fluorinated derivatives. (C) Non-canonical amino acids used in this study; α-hydroxy acid of Thr (Tah), α-hydroxy acid of Leu (Lah), F_4-Trp, F_3-Phe.

To study how cytisine modification has impacted the binding interactions relative to cytisine we have employed double-mutant cycle analyses. Typically, mutant cycle analyses have probed coupling between two amino acids in a protein,[44] but we have found the methodology

useful when one mutation is to the protein and the other is to the ligand.[10,40] Here, we performed a similar analysis to determine if the four known binding interactions are more or less important for the binding of the C(10) and C(9), C(10)-substituted cytisines and to quantify this effect in terms of free energy. In this mutant cycle analysis, the first mutant is the incorporation of a non-canonical amino acid, either F_4-Trp, Tah, Lah or F_3-Phe, probing for one of the four key binding interactions. The second 'mutant' is a cytisine analogue, one of the C(10)-modified cytisines; a representative analysis is based on ligand (**5**) presented in **Figure 2.10**. The extent to which the two perturbations are additive or nonadditive is expressed by the coupling constant Ω, which can be converted into coupling energy using the equation $\Delta\Delta G = RT\ln(\Omega)$. Functional coupling between the two perturbations is observed when $\Delta\Delta G$ is non-zero. In the present system a positive $\Delta\Delta G$ means that the protein mutation causes a larger loss of function for the new agonist than is observed for cytisine (or the increased potency of the new agonist is smaller than cytisine). This finding suggests the binding interaction being probed is stronger/more important for binding of the new agonist than for the binding of cytisine. When the $\Delta\Delta G$ value is negative, as in the case of the interaction illustrated in **Figure 2.10**, the protein mutation causes a smaller loss of function for the new agonist than for cytisine (or the gain of function by the new agonist is larger). This observation suggests the probed interaction is weaker/less important for the new agonist. We generally consider a coupling of at least 2-fold to be meaningful, which corresponds to $|\Delta\Delta G| > 0.4$ kcal/mol.

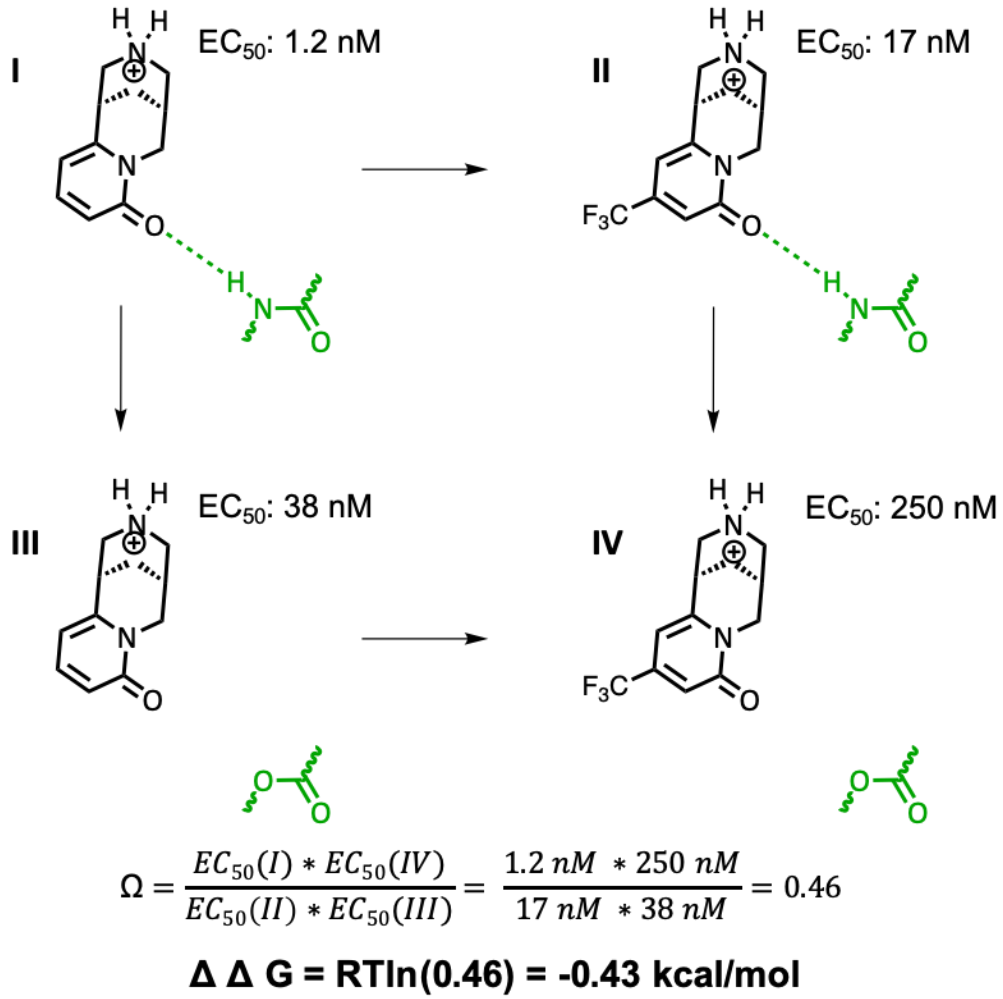

$$\Omega = \frac{EC_{50}(I) * EC_{50}(IV)}{EC_{50}(II) * EC_{50}(III)} = \frac{1.2\,nM\ * 250\ nM}{17\ nM\ * 38\ nM} = 0.46$$

Δ Δ G = RTln(0.46) = -0.43 kcal/mol

Figure 2.10 | Double-mutant cycle analysis. Ligand **5** (CF_3) is used as an example. EC_{50} I reflects the response of cytisine (**1**) with the wild-type amino acid. EC_{50} II and EC_{50} III both reflect one perturbation; cytisine derivative **5** (R_1=CF_3) with wild-type residue and cytisine with the non-canonical amino acid (Lah) respectively. EC_{50} IV corresponds to the "double mutant" where the response is measured for the (**5**) with the non-canonical amino acid present. The impact of substitution in terms of energy is calculated using the equation ΔΔG = RTln(Ω).

Before considering specific compounds, it is useful to examine general trends across the series. Even with simple substituents, many features of a molecule can change. By inspecting the total series, one can discern more general features. This is aided by the presentation in **Figure 2.11**. The ΔΔG values observed here range from -1.62 to 1.27 kcal/mol. Recall that we are looking at the *differences* in contributions of individual binding interactions

to the binding of C(10) and C(9)C(10)-substituted cytisine variants relative to cytisine, so there are some quite meaningful variations. To be clear, all cytisine derivatives still engage in the specific interaction being probed, but our focus is on how the magnitudes of those interactions differ from the same interaction with cytisine itself.

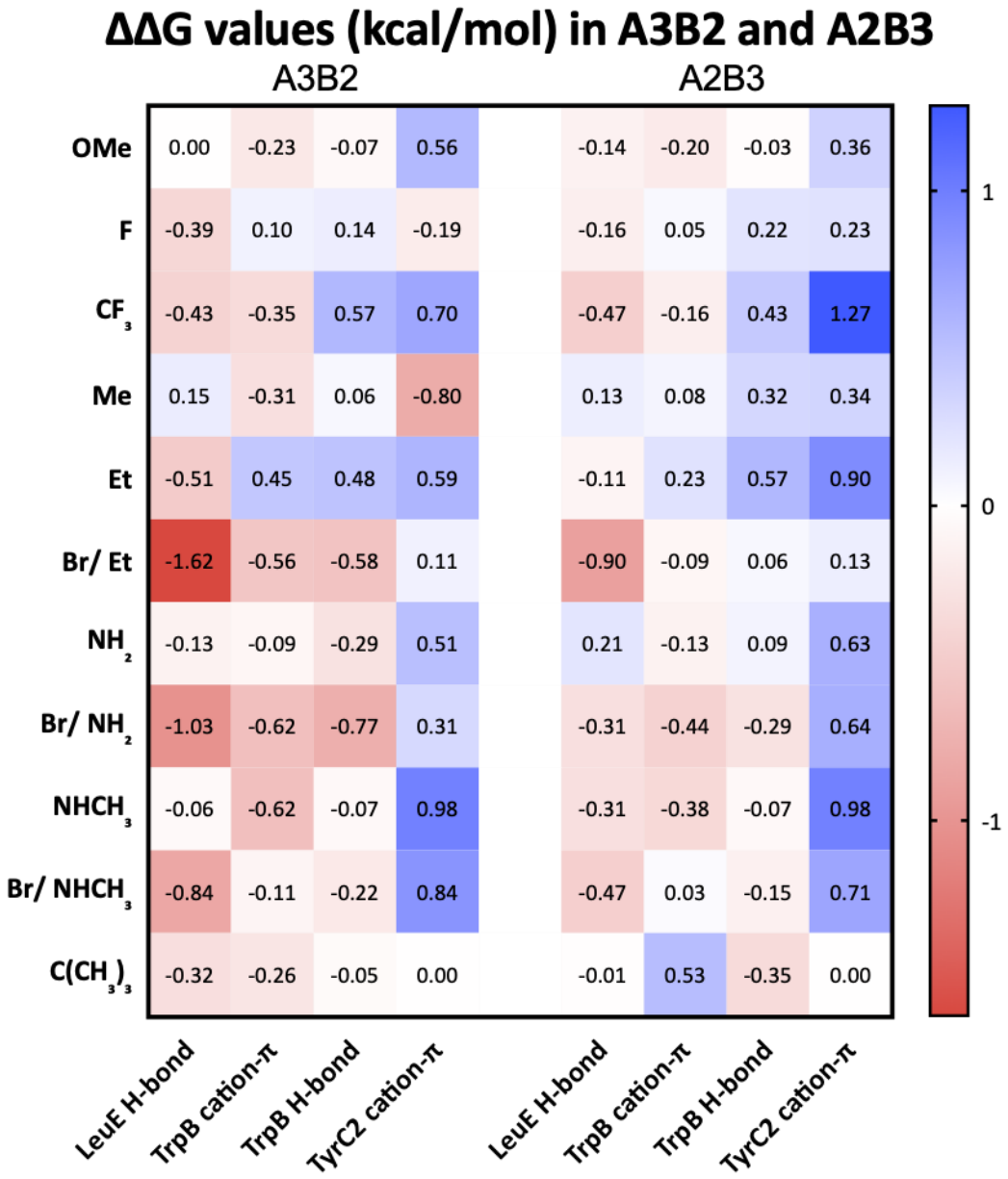

Figure 2.11 | The energetic contributions of cytisine substitution on the individual binding interactions expressed as ΔΔG values. Values are calculated using the equations in Figure 5. A positive ΔΔG suggests the protein mutation causes a larger loss of function for the new agonist than

cytisine. This suggests the binding interaction being probed is stronger/more important for binding of the new agonist than for the binding of cytisine to the receptor. When the ΔΔG value is negative, the protein mutation causes a smaller loss of function for the new agonist than cytisine. This suggests the probed interaction is weaker/less important for the new agonist. We generally consider a coupling of at least 2-fold to be meaningful, which corresponds to $|\Delta\Delta G| > 0.4$ kcal/mol.

Similar trends appear for the two α4β2 stoichiometries, although the effects are generally stronger for the A3B2 arrangement. This is seen by the larger fraction of coupling energies that rise of above the $|\Delta\Delta G| > 0.4$ kcal/mol threshold, color-coded in blue. The cation-π interaction to TyrC2 generally appears to be of greater importance in the C(10)-derivatives than for cytisine, in that meaningful, positive coupling energies are observed in both stoichiometries for almost all agonist-receptor pairings. The C(10)-fluoro and methyl ligands **2** and **3** are exceptions here. The cation-π interaction to TrpB is generally less perturbed by substitution, especially, again, in the A2B3 stoichiometry, which is readily seen via the color coding in **Figure 2.11**.

Considering the two hydrogen bonding interactions probed, the hydrogen bond to LeuE (which involves the pyridone C=O as an acceptor) is generally weakened by C(10) substitution, and again the effect is largest in the A3B2 stoichiometry; this is most pronounced in the C(9) and C(10)-disubstituted ligands **7, 9** and **11**. As with the cation-π interaction to TrpB, the hydrogen bond to the TrpB carbonyl is less influenced by pyridone ring-substitution.

These global patterns suggest a model for the overall effect that C(10) substitution has on ligand binding. Interactions with TrpB, both the cation-π interaction and the backbone hydrogen bond, are not strongly perturbed. This is consistent with the essential role that this protein residue plays in receptor function. Interestingly, the hydrogen bond to LeuE is more frequently weakened, while the cation-π interaction to TyrC2 is strengthened. This suggests

that a C(10) substituent leads to repositioning of the ligand (relative to the key protein residues), away from LeuE (weakening the H-bond in this region) and toward TyrC2 (strengthening the cation-π interaction), an adjustment that that is depicted in **Figure 2.12**.

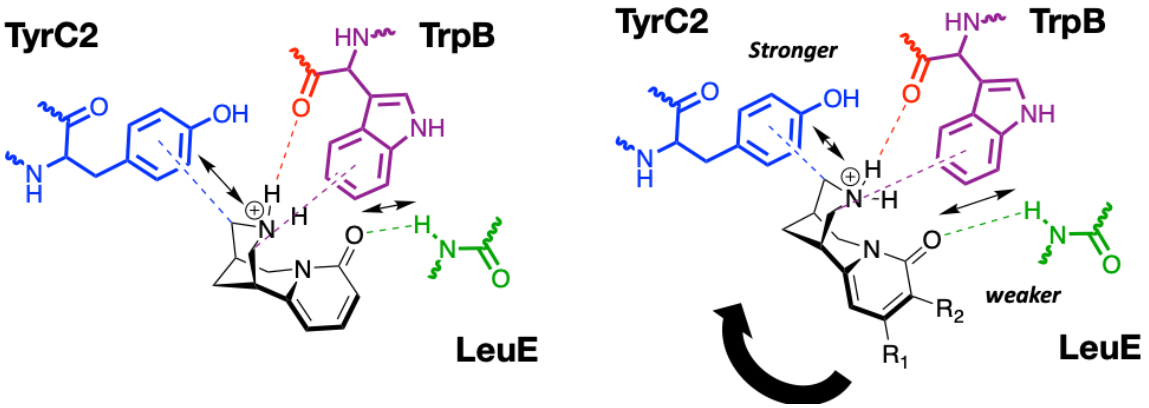

Figure 2.12 | Proposed model based on results in this study. Repositioning of the ligand in a way such that it is closer to TyrC2 and further away from LeuE supports the general trends observed in this study. The R_1 and R2 moieties are at positions C(10) and C(9), respectively. Generally speaking, the cation-π interaction with TyrC2 was enhanced, the hydrogen bond with LeuE was diminished, and the two interactions to TrpB appear to be less impacted.

The largest right shifted EC_{50} values for the wild type receptor were observed for **10** (NHMe) and **11** (Br/NHMe) (**Figure 2.4**). For **10** (NHMe) the cation-π to TrpB was weakened and for **11** (Br/NHMe) the hydrogen bond to LeuE was weakened relative to cytisine, but the cation-π to TyrC2 was stronger for both (**Figure 2.11**). Surprising are the effects seen for **6** (Et) and **7** (Br/Et) (**Figure 2.11**). Ligand **6** (Et) shows decreased potency compared to cytisine, while **7** (Br/Et) shows increased potency. However, the ΔΔG values of three individual binding interactions are positive for **6** (Et), while these are negative for **7** (Br/Et), suggesting stronger interactions in **6** (Et) than **7** (Br/Et) in both stoichiometries. Based on wild-type EC_{50} fold shift alone, one might have expected the opposite.

A similar trend is seen for **8** (NH_2) and **9** (Br/NH_2); ΔΔG values for ligand **9** are consistently more negative. It is unclear what causes this effect. It is possible that other, yet

undiscovered, electrostatic interactions are present in the binding pocket, or that new interactions are present for **9** (Br/NH_2) and **7** (Br/Et) only. Also, contributions of hydrophobic forces (likely to be significant for a Br residue) play a role in agonist binding but are not included in this analysis.

Phe EC_{50} values sometimes deviate substantially from the wild-type response (Tyr) (**Table 2.11 and 2.15**). Some Phe EC_{50} values are much lower (**5** (CF_3): 0.1-fold), some are higher (**8** (NH_2) 3-fold). This suggests that the hydroxyl of TyrC2 affects binding more for these two compounds than for cytisine. We note again that such a prominent role for the OH of TyrC2 has not typically been observed in other studies.

Table 2.8 | EC_{50} and n_H values for nonsense-suppression experiments at W154 in A3B2.

Ligand		Residue	EC_{50} (nM)			n_H			Fold shift	N	$\lvert I_{max} \rvert$ (μA)
1	Cytisine	Trp	1.236	±	0.024	2.2	±	0.08		21	0.082 – 4.0
		F_4-Trp	13.81	±	0.81	1.1	±	0.07	116	10	0.075 – 0.15
10	NHMe	Trp	41	±	55	1.4	±	0.19		12	1.5 – 16
			1282	±	121	1.7	±	0.58			
		F_4-Trp	1047	±	51	1.1	±	0.06	26	14	0.080 – 0.70
5	CF_3	Trp	19.25	±	0.72	1.4	±	0.07		10	0.055 – 6.05
		F_4-Trp	782.7	±	82	0.91	±	0.08	41	10	0.087 – 0.54
4	OMe	Trp	15.19	±	0.39	1.9	±	0.08		17	0.18 – 8.8
		F_4-Trp	762.9	±	61	0.99	±	0.07	51	10	0.021 – 0.23
2	F	Trp	1.608	±	0.039	2.1	±	0.10		11	0.22 – 7.3
		F_4-Trp	151.8	±	7.9	1.1	±	0.05	96	11	0.069 – 0.64
3	Me	Trp	3.298	±	0.086	1.8	±	0.07		17	0.056 – 6.6
		F_4-Trp	138.1	±	8.1	1.1	±	0.07	46	10	0.087 – 0.56
6	Et	Trp	2.684	±	0.078	1.7	±	0.08		12	0.051 – 15
		F_4-Trp	458.2	±	12	1.0	±	0.03	170	11	0.063 – 0.58
8	NH_2	Trp	8.455	±	0.46	1.5	±	0.10		13	0.16 – 15
		F_4-Trp	546.6	±	72	1.0	±	0.13	65	9	0.033 – 0.78
14	$C(Me)_3$	Trp	44.12	±	1.1	1.7	±	0.06		15	1.9 – 29
		F_4-Trp	2681	±	120	1.3	±	0.07	61	12	0.072 – 0.75
9	Br/NH_2	Trp	0.6481	±	0.042	1.9	±	0.21		11	0.78 – 14
		F_4-Trp	21.12	±	0.98	1.0	±	0.05	33	11	0.063 – 0.97
7	Br/Et	Trp	0.4148	±	0.023	2.4	±	0.28		9	1.3 – 17
		F_4-Trp	14.25	±	0.55	1.1	±	0.05	34	12	0.077 – 1.9
11	Br/NHMe	Trp	31.19	±	24	1.4	±	0.12		12	0.89 – 25
			2558	±	138	2.2	±	1.41			
		F_4-Trp	1891	±	94	1.2	±	0.07	61	13	0.074 – 0.22

Table 2.9 | EC_{50} and n_H values for nonsense-suppression experiments at T155 in A3B2.

	Ligand	Residue	EC_{50} (nM)			n_H			Fold shift	N	$\lvert I_{max} \rvert$
1	Cytisine	Thr	1.7	±	0.030	1.7	±	0.05		12	0.26 - 12
		Tah	46	±	1.1	1.2	±	0.03	27	12	0.30 - 13
10	NHMe	Thr	40	±	78	1.7	±	0.44		14	0.26 – 17
			772	±	291	0.84	±	0.15			
		Tah	998	±	33	1.4	±	0.06	25	11	0.28 - 14
5	CF_3	Thr	23	±	0.75	1.3	±	0.05		10	0.15 – 16
		Tah	1436	±	39	1.4	±	0.04	62	12	0.059 – 8.3
4	OMe	Thr	20	±	0.35	1.5	±	0.04		10	0.59 – 9.6
		Tah	434	±	15	1.3	±	0.05	22	10	0.015 – 9.3
2	F	Thr	1.8	±	0.029	1.5	±	0.03		12	0.72 – 7.0
		Tah	60	±	1.7	1.2	±	0.03	33	12	0.28 - 13
3	Me	Thr	3.4	±	0.088	1.5	±	0.06		13	0.098 – 8.2
		Tah	104	±	3.2	1.3	±	0.05	31	14	0.042 - 14
6	Et	Thr	3.1	±	0.10	1.4	±	0.06		12	0.086 – 7.3
		Tah	174	±	4.4	1.2	±	0.03	56	12	0.46 - 11
8	NH_2	Thr	13	±	0.37	1.3	±	0.04		13	0.15 – 7.6
		Tah	223	±	4.0	1.2	±	0.02	17	12	2.4 - 15
14	$C(Me)_3$	Thr	43	±	0.98	1.9	±	0.07		21	0.30 – 15
		Tah	1074	±	14	1.4	±	0.02	25	11	0.16 – 8.7
9	Br/NH_2	Thr	0.40	±	0.0089	2.2	±	0.10		13	0.031 – 6.0
		Tah	3.7	±	0.084	1.4	±	0.04	9.3	13	0.45 – 17
7	Br/Et	Thr	0.50	±	0.016	2.0	±	0.12		12	0.30 – 7.7
		Tah	5.6	±	0.13	1.3	±	0.03	11	11	1.6 – 20
11	Br/NHMe	Thr	38	±	47	1.3	±	0.13		20	0.13 – 34
			3358	±	145	1.4	±	0.43			
		Tah	965	±	31	1.3	±	0.05	25	10	0.97 - 12

Table 2.10 | EC_{50} and n_H values for nonsense-suppression experiments at L119 in A3B2.

	Ligand	Residue	EC_{50} (nM)			n_H			Fold shift	N	$\lvert I_{max} \rvert$
1	Cytisine	Leu	1.2	±	0.023	1.9	±	0.06		13	0.069 – 2.8
		Lah	38	±	0.92	1.1	±	0.03	32	15	0.67 - 23
10	NHMe	Leu	41	±	91	1.5	±	0.28		11	0.064 – 1.1
			1259	±	152	1.1	±	0.35			
		Lah	1334	±	20	1.5	±	0.03	33	13	0.13 – 5.5
5	CF_3	Leu	17	±	0.66	1.2	±	0.06		10	0.012 – 1.3
		Lah	250	±	4.6	1.1	±	0.02	15	12	0.030 – 7.6
4	OMe	Leu	18	±	0.34	1.6	±	0.05		11	0.057 – 1.0
		Lah	532	±	13	1.2	±	0.03	30	12	0.10 – 7.4
2	F	Leu	2.0	±	0.029	2.0	±	0.05		14	0.057 – 0.90
		Lah	36	±	0.55	1.2	±	0.02	18	14	0.53 – 7.9
3	Me	Leu	2.8	±	0.074	1.8	±	0.07		11	0.11 – 1.0
		Lah	126	±	2.6	1.1	±	0.02	45	11	0.050 – 2.7
6	Et	Leu	4.5	±	0.24	1.2	±	0.07		11	0.075 – 1.4
		Lah	79	±	3.1	1.2	±	0.05	18	12	0.31 – 4.9
8	NH_2	Leu	9.5	±	0.19	1.4	±	0.03		15	0.48 – 16
		Lah	233	±	4.1	1.2	±	0.02	25	14	0.077 – 49
14	$C(Me)_3$	Leu	49	±	0.86	1.8	±	0.05		16	0.14 – 11
		Lah	952	±	17	1.4	±	0.03	19	16	0.79 - 33
9	Br/NH_2	Leu	0.41	±	0.0068	2.2	±	0.07		12	0.32 – 5.2
		Lah	2.4	±	0.043	1.6	±	0.04	5.9	11	1.1 – 28
7	Br/Et	Leu	0.40	±	0.020	1.4	±	0.10		13	0.055 – 0.47
		Lah	1.0	±	0.047	1.6	±	0.10	2.5	12	0.20 – 7.1
11	Br/NHMe	Leu	37	±	48	1.4	±	0.23		13	0.32 – 11
			2917	±	127	1.6	±	0.70			
		Lah	410	±	11	1.2	±	0.03	11	14	10 - 46

Table 2.11 | EC_{50} and n_H values for nonsense-suppression experiments at Y202 in A3B2.

	Ligand	Residue	EC_{50} (nM)			n_H			Fold shift	N	$\lvert I_{max} \rvert$
1	Cytisine	Phe	6.647	±	0.14	1.4	±	0.04		13	0.064 – 22
		F_3-Phe	160.4	±	6.3	1.1	±	0.05	24	13	0.44 – 8.0
10	NHMe	Phe	53	±	71	1.3	±	0.25		18	0.10 – 12
			5724	±	69	1.4	±	0.34			
		F_3-Phe	5255	±	298	1.0	±	0.06	99	15	0.025 – 2.9
5	CF_3	Phe	6.906	±	0.78	0.78	±	0.06		12	0.64 – 8.6
		F_3-Phe	456.8	±	38	1.17	±	0.11	66	12	0.14 – 0.83
4	OMe	Phe	27.85	±	4.4	0.71	±	0.10		14	0.25 – 6.3
		F_3-Phe	1481	±	124	0.76	±	0.05	53	16	0.17 – 0.83
2	F	Phe	10.22	±	0.69	0.78	±	0.04		15	0.31 – 8.9
		F_3-Phe	185.4	±	10	0.88	±	0.04	18	16	0.21 – 1.1
3	Me	Phe	14.12	±	1.1	0.76	±	0.05		14	0.16 – 7.5
		F_3-Phe	138.2	±	8.4	1.0	±	0.06	9.8	13	0.059 – 0.50
6	Et	Phe	2.31	±	0.077	1.9	±	0.11		14	0.040 – 3.3
		F_3-Phe	157	±	6.9	1.3	±	0.07	68	10	0.15 – 1.3
8	NH_2	Phe	35.97	±	1.1	1.4	±	0.05		14	0.50 – 8.5
		F_3-Phe	2174	±	67	1.2	±	0.04	60	11	0.088 – 5.7
14	$C(Me)_3$	Phe	158.7	±	12	0.96	±	0.07		12	0.064 – 0.67
		F_3-Phe	6032	±	589	1.0	±	0.09	38	9	0.017 – 0.32
9	Br/NH_2	Phe	0.6849	±	0.018	2.5	±	0.15		11	0.043 – 7.7
		F_3-Phe	29.96	±	0.84	1.1	±	0.03	44	6	0.30 – 2.4
7	Br/Et	Phe	0.4146	±	0.020	2.6	±	0.28		15	0.053 – 7.6
		F_3-Phe	12.59	±	1.3	0.73	±	0.06	30	9	0.10 – 10
11	Br/NHMe	Phe	3.0	±	42	1.6	±	0.24		17	0.081 – 13
			264	±	111	1.2	±	0.41			
		F_3-Phe	276.3	±	52	1.0	±	0.10	92	16	0.49 – 5.4
			8878	±	102	2.7	±	1.7			

Table 2.12 | EC_{50} and n_H values for nonsense-suppression experiments at W154 in A2B3.

	Ligand	Residue	EC_{50} (nM)			n_H			Fold shift	N	$\lvert I_{max} \rvert$
1	Cytisine	Trp	4.0	±	0.21	1.3	±	0.09		15	0.053 – 1.1
		F_4-Trp	97	±	3.5	0.97	±	0.03	23	9	0.057 – 0.17
10	NHMe	Trp	150	±	5.9	1.2	±	0.05		13	0.16 – 4.3
		F_4-Trp	1798	±	58	1.2	±	0.04	12	14	0.088 – 1.1
5	CF_3	Trp	70	±	2.2	1.2	±	0.05		14	0.18 – 4.5
		F_4-Trp	1110	±	38	1.3	±	0.05	16	10	0.14 – 0.75
4	OMe	Trp	43	±	2.2	1.5	±	0.10		14	0.10 – 2.6
		F_4-Trp	711	±	25	1.2	±	0.05	17	10	0.054 – 0.41
2	F	Trp	7.7	±	0.27	1.6	±	0.08		14	0.13 – 2.1
		F_4-Trp	195	±	7.9	1.1	±	0.05	25	13	0.051 – 0.22
3	Me	Trp	6.3	±	0.22	1.6	±	0.08		12	0.24 – 2.1
		F_4-Trp	151	±	6.8	1.2	±	0.06	24	11	0.023 – 0.26
6	Et	Trp	16	±	0.55	1.6	±	0.08		14	0.072 – 0.79
		F_4-Trp	380	±	32	1.1	±	0.10	24	11	0.011 – 0.84
8	NH_2	Trp	33	±	1.2	1.3	±	0.06		16	0.28 - 6.2
		F_4-Trp	587	±	20	1.0	±	0.03	18	9	0.023 – 0.85
14	$C(Me)_3$	Trp	142	±	5.9	1.4	±	0.07		11	0.088 – 2.3
		F_4-Trp	6153	±	553	1.2	±	0.13	43	17	0.015 – 1.2
9	Br/NH_2	Trp	1.9	±	0.11	1.8	±	0.19		12	0.15 - 11
		F_4-Trp	19	±	0.80	1.1	±	0.05	10	12	0.14 – 1.2
7	Br/Et	Trp	0.86	±	0.024	2.9	±	0.20		10	0.33 – 1.4
		F_4-Trp	15.9	±	0.74	1.1	±	0.05	18	6	0.060 – 0.25
11	Br/NHMe	Trp	138	±	3.9	1.2	±	0.04		11	0.21 – 3.2
		F_4-Trp	3038	±	194	1.2	±	0.08	22	18	0.017 – 0.19

Table 2.13 | EC_{50} and n_H values for nonsense-suppression experiments at T155 in A2B3.

	Ligand	Residue	EC_{50} (nM)			n_H			Fold shift	N	$\lvert I_{max} \rvert$
1	Cytisine	Thr	7.2	±	0.18	1.4	±	0.04		12	0.19 – 0.56
		Tah	128	±	2.5	1.2	±	0.02	18	10	0.024 – 0.43
10	NHMe	Thr	175	±	3.3	1.33	±	0.03		13	0.048 – 0.49
		Tah	2759	±	52	1.4	±	0.03	16	12	0.23 – 2.3
5	CF_3	Thr	106	±	1.6	1.3	±	0.02		11	0.12 – 0.48
		Tah	3664	±	47	1.4	±	0.02	35	11	0.23 – 1.9
4	OMe	Thr	85	±	1.8	1.3	±	0.03		13	0.050 – 0.61
		Tah	1406	±	23	1.3	±	0.03	17	10	0.20 – 0.7.8
2	F	Thr	5.5	±	0.15	1.3	±	0.04		9	0.020 – 0.43
		Tah	171	±	2.5	1.2	±	0.02	31	11	0.023 – 1.8
3	Me	Thr	11	±	0.24	1.4	±	0.04		7	0.043 – 0.68
		Tah	329	±	4.1	1.3	±	0.02	30	19	0.38 – 2.5
6	Et	Thr	15	±	0.20	1.5	±	0.03		15	0.031 – 0.59
		Tah	680	±	12	1.3	±	0.03	45	14	0.11 – 0.94
8	NH_2	Thr	42	±	0.55	1.2	±	0.02		12	0.056 – 0.87
		Tah	849	±	11	1.2	±	0.02	20	13	0.053 – 0.47
14	$C(Me)_3$	Thr	230	±	5.4	1.3	±	0.03		14	0.093 – 0.42
		Tah	2035	±	54.56	1.2	±	0.03	8.8	15	0.052 – 1.6
9	Br/NH_2	Thr	1.4	±	0.032	1.8	±	0.07		14	0.099 – 1.8
		Tah	16	±	0.17	1.3	±	0.02	11	15	0.12 – 1.2
7	Br/Et	Thr	0.89	±	0.019	2.4	±	0.11		14	0.20 – 1.6
		Tah	18	±	0.37	1.3	±	0.03	20	15	0.23 – 3.3
11	Br/NHMe	Thr	187	±	3.0	1.2	±	0.02		13	0.22 – 0.94
		Tah	2328	±	37	1.3	±	0.02	12	15	0.20 – 2.7

Table 2.14 | EC_{50} and n_H values for nonsense-suppression experiments at L119 in A2B3.

	Ligand	Residue	EC_{50} (nM)			n_H			Fold shift	N	$\lvert I_{max} \rvert$
1	Cytisine	Leu	4.923	±	0.096	1.3	±	0.03		11	0.078 – 1.3
		Lah	191.9	±	5.1	1.0	±	0.02	39	12	0.081 – 0.11
10	NHMe	Leu	155.6	±	6.7	1.0	±	0.04		7	0.21 – 1.9
		Lah	3783	±	76	1.4	±	0.04	24	11	0.079 – 1.0
5	CF_3	Leu	57.05	±	1.3	1.3	±	0.03		14	0.16 – 3.0
		Lah	990.4	±	20	1.4	±	0.03	17	12	0.59 – 3.7
4	OMe	Leu	64.82	±	1.9	1.2	±	0.04		10	0.043 – 0.31
		Lah	2052	±	30	1.2	±	0.02	32	13	0.036 – 3.1
2	F	Leu	5.235	±	0.13	1.5	±	0.05		11	0.031 – 0.47
		Lah	168	±	3.4	1.3	±	0.03	32	10	0.064 – 0.63
3	Me	Leu	8.688	±	0.29	1.3	±	0.05		11	0.11 – 2.0
		Lah	461.8	±	8.3	1.3	±	0.03	53	11	0.43 – 3.5
6	Et	Leu	18.33	±	0.40	1.4	±	0.04		11	0.097 – 1.1
		Lah	628	±	13	1.3	±	0.03	34	9	0.43 – 1.6
8	NH_2	Leu	43.03	±	0.85	1.1	±	0.02		15	0.3 – 2.4
		Lah	2246	±	39	1.2	±	0.02	52	14	0.044 – 8.2
14	$C(Me)_3$	Leu	155.4	±	3.9	1.3	±	0.04		12	0.030 – 0.29
		Lah	5281	±	91	1.3	±	0.03	34	15	0.11 – 0.95
9	Br/NH_2	Leu	1.479	±	0.024	1.9	±	0.05		14	0.59 – 3.1
		Lah	31.27	±	0.97	1.2	±	0.04	21	15	0.24 – 20
7	Br/Et	Leu	0.8675	±	0.018	2.0	±	0.07		16	0.17 – 2.2
		Lah	8.113	±	0.22	1.4	±	0.05	9.4	11	0.96 – 4.6
11	Br/NHMe	Leu	160.3	±	4.6	1.3	±	0.04		12	0.080 – 0.81
		Lah	2975	±	41	1.2	±	0.02	19	15	0.12 – 2.7

Table 2.15 | EC_{50} and n_H values for nonsense-suppression experiments at Y202 in A2B3.

	Ligand	Residue	EC_{50} (nM)			n_H			Fold shift	N	$\lvert I_{max} \rvert$
1	Cytisine	Phe	12.01	±	0.35	1.4	±	0.05		18	0.076 – 0.84
		F_3-Phe	201.9	±	9.2	1.3	±	0.07	17	13	0.034 – 0.30
10	NHMe	Phe	106.2	±	5.7	1.3	±	0.08		11	0.064 – 0.31
		F_3-Phe	7995	±	606	1.1	±	0.08	75	12	0.022 – 0193
5	CF_3	Phe	6.174	±	0.17	1.5	±	0.05		16	0.045 – 0.24
		F_3-Phe	718.5	±	53	1.2	±	0.10	116	14	0.008 – 0.040
4	OMe	Phe	41.9	±	3.2	1.4	±	0.14		10	0.017 – 0.086
		F_3-Phe	1375	±	101	1.4	±	0.13	33	11	0.010 – 0.19
2	F	Phe	7.883	±	0.53	1.2	±	0.09		12	0.036 – 0.16
		F_3-Phe	195.1	±	12	1.4	±	0.11	25	12	0.015 – 0.022
3	Me	Phe	8.589	±	0.30	1.2	±	0.05		12	0.036 – 0.30
		F_3-Phe	245.9	±	28	1.0	±	0.13	29	11	0.007 – 0.032
6	Et	Phe	7.851	±	1.4	1.0	±	0.14		9	0.017 – 0.072
		F_3-Phe	580.4	±	51	1.1	±	0.11	74	9	0.006 – 0.17
8	NH_2	Phe	85.26	±	3.4	1.4	±	0.07		5	0.054 – 0.136
		F_3-Phe	4039	±	231	1.3	±	0.10	48	10	0.010 – 0.096
14	$C(Me)_3$	Phe	297.6	±	19	1.5	±	0.14		11	0.014 – 0.13
		F_3-Phe	5008	±	878	1.4	±	0.33	17	6	0.005 – 0.017
9	Br/NH_2	Phe	2.09	±	0.10	1.6	±	0.12		10	0.064 – 1.6
		F_3-Phe	96.34	±	6.2	1.0	±	0.07	48	6	0.16 – 0.89
7	Br/Et	Phe	1.346	±	0.042	2.1	±	0.13		13	0.082 – 0.34
		F_3-Phe	25.84	±	1.5	1.1	±	0.07	20	13	0.025 – 0.27
11	Br/NHMe	Phe	10.29	±	0.46	1.4	±	0.08		10	0.21 -0.98
		F_3-Phe	557.5	±	27	1.3	±	0.07	54	11	0.023 – 0.16

2.4 Conclusions

In this study, we used two-electrode voltage-clamp electrophysiology and non-canonical amino acid mutagenesis to probe the agonist binding interactions of a novel series of cytisine derivatives in the α4β2 nAChR. In contrast to the well-studied agonists nicotine and acetylcholine, cytisine and the C(10)-substituted cytisine derivatives studied here make a second cation-π interaction to TyrC2. Surprisingly, double-mutant cycle analyses revealed that all C(10)-derivatives make a stronger cation-π interaction to TyrC2 than cytisine, whereas the hydrogen bond to LeuE in the complementary subunit is generally diminished. The results suggest a model for how cytisine derivatives adjust their binding orientation within the binding site of α4β2 nAChR in response to pyridone substitution.

2.5 Experimental procedures

Molecular biology

Circular DNA of rat nAChR α4 and β2 subunits were in a pGEMhe plasmid (wild type expression) and a pAMV plasmid (non-canonical amino acid expression). Site-directed mutagenesis was performed using the QuickChange protocol (Agilent Stratagene). cDNA in pGEMhe was linearized with restriction enzyme SbfI, whereas cDNA in pAMV was linearized with NotI (New England Biolabs). Purified linear DNA (Qiaquick PCR Purification kit, Qiagen) was then transcribed *in vitro* using the T7 mMessage Machine kit (Ambion). The resulting mRNA was isolated using the RNeasy RNA purification kit (Qiagen) and quantified by UV-vis spectroscopy (NanoDrop 2000, ThermoFisher Scientific). cDNA and mRNA were stored at -20˚C and -80˚C respectively.

For non-canonical amino acid incorporation, the residue of interest was mutated to the amber (UAG) stop codon (sites in the α4 subunit) or the opal (UGA) stop codon (sites in

the β2 subunit). 74-nucleotide THG73 tRNA (for UAG) and 74-nucleotide TQOpS' tRNA (for UGA) were prepared by *in vitro* transcription from a DNA oligonucleotide template, modified to prevent nontemplated nucleotide addition, using the MEGAshortscript T7 kit (Ambion).[45] 74-mer tRNA was isolated using Chroma Spin DEPC-H_2O columns (Clontech). Hydroxy or amino acid-dCA conjugates were enzymatically ligated to truncated 74-nucleotide TQOpS' tRNA (Lah) or THG73 tRNA (all other non-canonical residues) as described previously.[46,47] tRNA amino acid or tRNA-hydroxy acid products were confirmed by matrix-assisted laser desorption ionization time-of-flight mass spectrometry on a 3-hydroxypicolinic acid matrix. Deprotection of the nitroveratryloxycarbonyl group on the tRNA amino acids was carried out by photolysis for 3 min using a 365 nm LED (M365LP1, 1150 mW, mounted LED, Thorlabs) immediately prior to injection.

For all experiments, EC_{50} values were obtained using a hypersensitive mutation in the α4 subunit (L9'A). Previous studies report that cytisine is only slightly active at the wild type A2B3 stoichiometry.[48] However, using the α4L9'A mutation, we find that cytisine does activate the A2B3 stoichiometry.[35,36] Besides increasing efficacy, the mutation also yields left shifted EC_{50} values for both stoichiometries as compared to true wild type, which allows one to probe effects of other mutations or cytisine derivatives. Lastly, the pore mutation results in different rectification between the two stoichiometries; this difference can be determined via-voltage jump experiments to verify which receptor stoichiometry is being observed.[11] For convenience, what is referred to as wild type receptor is assumed to have the L9'A mutation in the α4 subunit.

Oocyte preparation and injection

Xenopus laevis oocytes (stage V-VI) were harvested and injected with RNAs according to previously described protocols.[46] Oocytes were injected with 50-75 nl mRNA in nuclease-free water. Post injection, oocytes were incubated at 18°C in ND96 solution (96 mM NaCl, 2mM KCl, 1mM $MgCl_2$, 1.8 mM $CaCl_2$, 5 mM HEPES, pH 7.5) supplemented with 0.05 mg/ml gentamycin (Sigma), 2.5 mM sodium pyruvate (Acros Organics), and 0.67 mM theophylline (Sigma).

For expression of wild-type α4β2 receptors, α4L9'A and β2 mRNA were mixed in 1:3 or 10:1 ratio by mass to obtain the A2B3 and A3B2 stoichiometry, respectively. Each cell was injected with 25 ng mRNA in a single injection and incubated for 24 h before recording.

For non-canonical amino acid incorporation into the α subunit, α4L9'A and β2 mRNA were mixed in a 3:1 ratio for expression of A2B3 and a 100:1 ratio by mass for expression of A3B2 receptors. One exception to this was the incorporation of Phe and F_3-Phe into the α-subunit, where a ratio of 150:1 was used for expression of A3B2. For non-canonical amino acid incorporation into the β-subunit, α4L9'A and β2 mRNA were mixed in a 1:40 ratio for expression of A2B3 and a 10:1 ratio by mass for expression of A3B2 receptors. mRNA mixtures and deprotected tRNA were mixed in a 1:1 volume ratio prior to injection. In cases where 24 h incubation resulted in responses too low for systematic study, a second injection of mRNA and tRNA was performed and cells were incubated for a total of 48 h before recording.

The reliability of the non-canonical amino acid incorporation was confirmed through read-through/reaminoacylation experiments as previously described.[35] Briefly, the fidelity of non-canonical amino acid incorporation was confirmed at each site by a wild-type recovery

experiment in which the tRNA was charged with the wild-type residue. If the wild-type recovery yielded concentration-response relations resembling wild type, desired incorporation for the non-canonical residue was assumed also. As a negative control, unacylated 76-mer tRNA with mRNA was injected alongside the mutant and wild-type recovery conditions. Negligible current from the unacylated 76-mer injection confirmed the lack of undesirable reaminoacylation events.

Chemical preparation

Cytisine and all cytisine derivatives were synthesized by Hugo Rego Campello, Ph.D. at the University of Bristol, UK.

Whole-cell electrophysiology

All electrophysiological recordings were performed using the OpusXpress 6000A (Axon Instruments) in two-electrode voltage clamp mode at ambient temperature (20-25°C). Oocytes were impaled with borosilicate glass pipettes filled with 3 M KCl (R = 0.3-3.0 MΩ) and clamped at a holding potential of -60 mV. Ca^{2+} free ND96 solution was used as running buffer. Agonists were prepared in in Ca^{2+} free ND96 and 1 mL was applied over 15 s followed by a 2 min washout with buffer at a rate of 3 mL min^{-1} (chamber volume, 500 μL). For Br/NH_2-cytisine and Br/Et-cytisine, which cause slower deactivation, the washout duration post agonist application was extended to 5 min. Dose-response measurements were performed using a series of ~2-fold concentration steps, spanning multiple orders of magnitude, for a total of 8-24 doses. Data for each mutant and agonist combination were obtained from at least two different batches of oocytes. Efficacy experiments involved testing of two to three maximally activating acetylcholine concentrations, followed by the maximally activating concentration of the test compound of interest, followed by two doses of acetylcholine. Data

were sampled at 50 Hz. We performed voltage-jump experiments to verify receptor stoichiometry of wild-type and mutant receptors as described previously.[11]

Data analysis

Two-electrode voltage-clamp traces were processed in Clampfit 10.3 (Axon Instruments). Raw traces were filtered using a low pass Gaussian filter at 5 Hz, followed by a subtraction of the average baseline current preceding agonist application. Normalized peak currents were averaged and fit to the Hill equation, $I_{norm} = 1/(1 + (EC_{50}/[\text{agonist}]^{nH})$ in Prism 8 (GraphPad Software, Inc.), where I_{norm} is the normalized peak current at a given agonist concentration, EC_{50} is the agonist concentration that elicits a half-maximum response, and n_H is the Hill coefficient. Peak currents were normalized to the maximum current observed for that cell. Some compounds showed a biphasic dose-response relation; these data were fitted to a biphasic dose-response equation, $I_{norm} = 1*\text{frac}/(1 + 10^{((\log EC50\_1 - \log[\text{agonist}])*nH1)}) + 1*(1-\text{frac})/(1 + 10^{((\log EC50\_2 - \log[\text{agonist}])*nH2)})$, where EC50_1 and EC50_2 correspond to nH1 and nH2, respectively. The efficacy of compounds was measured as I_{max} of the compound divided by the I_{max} of acetylcholine. Unless otherwise stated, EC_{50} and n_H data are shown as mean ± standard error of the mean (SEM). Coupling energies for double-mutant cycles were calculated using the equation: $\Delta\Delta G = -R*T*\ln((EC_{50\,WT\text{-}cyt}*EC_{50\,mut\text{-}ligand})/(EC_{50\,WT\text{-}ligand}*EC_{50\,mut\text{-}cyt}))$, where R is the gas constant, T is temperature, cyt is cytisine, mut denotes mutant, and ligand refers to the various cytisine derivatives used in this study. The value for T used here was 298 K. Geometry and electrostatics calculation were performed in Spartan. LogD values were calculated by Justin A. Hilf, Ph.D. using ACD/Percepta Platform, Advanced Chemistry Development, Inc., Toronto, ON, Canada, www.acdlabs.com, 2019.

Compounds **10** (NHMe) and **11** (Br/NHMe) exhibit a biphasic response in A3B2, representing two distinct binding sites: binding at the α/β-interface and at the α/α-interface.

For the purpose of calculating fold shifts and to make comparisons with other derivatives, we solely used the first EC_{50}, assuming the binding site at the α/β-interface is always the highest affinity one.

Acknowledgements

We thank Dr. Hugo Rego Campello and Prof. Timothy Gallagher at the University of Bristol for synthesizing the cytisine derivatives and the valuable, intellectual discussions. Lastly, we thank Dr. Justin A. Hilf and Prof. Brian Stoltz for their assistance in calculating logD values.

2.6 References

(1) Jensen, A. A.; Frølund, B.; Liljefors, T.; Povl, K.-L. Neuronal Nicotinic Acetylcholine Receptors: Structural Revelations, Target Identifications, and Therapeutic Inspirations. *J Med Chem* **2005**, *48* (15), 4705–4745. https://doi.org/10.1021/jm040219e.

(2) Gotti, C.; Zoli, M.; Clementi, F. Brain Nicotinic Acetylcholine Receptors: Native Subtypes and Their Relevance. **2006**, *27* (9), 482–491. https://doi.org/10.1016/j.tips.2006.07.004.

(3) Brunzell, D. H.; Stafford, A. M.; Dixon, C. I. Nicotinic Receptor Contributions to Smoking: Insights from Human Studies and Animal Models. *Curr Addict Rep.* **2015**, *2* (1), 33–46. https://doi.org/10.1007/s40429-015-0042-2.

(4) Lester, H. A.; Xiao, C.; Srinivasan, R.; Son, C. D.; Miwa, J.; Pantoja, R.; Banghart, M. R.; Dougherty, D. A.; Goate, A. M.; Wang, J. C. Nicotine Is a Selective Pharmacological Chaperone of Acetylcholine Receptor Number and Stoichiometry. Implications for Drug Discovery. **2009**, *11* (1), 167–177.

(5) Hogg, R.; & B.-D. Nicotinic Acetylcholine Receptors as Drug Targets. *Curr. Drug Targets-CNS …* **2004**.

(6) Gotti, C.; Clementi, F. Neuronal Nicotinic Receptors: From Structure to Pathology. **2004**, *74* (6), 363–396.

(7) Nelson, M. E.; Kuryatov, A.; Choi, C. H.; Zhou, Y.; Lindstrom, J. Alternate Stoichiometries of Alpha4beta2 Nicotinic Acetylcholine Receptors. *Mol Pharmacol* **2003**, *63* (2), 332–341.

(8) Wang, J.; Kuryatov, A.; Sriram, A.; Jin, Z.; Kamenecka, T. M.; Kenny, P. J.; Lindstrom, J. An Accessory Agonist Binding Site Promotes Activation of Α4β2* Nicotinic Acetylcholine Receptors. *J Biol Chem* **2015**, *290* (22), 13907–13918. https://doi.org/10.1074/jbc.M115.646786.

(9) Walsh, R. M.; Roh, S.-H. H.; Gharpure, A.; L, M.-P., Claudio; Teng, J.; Hibbs, R. E. Structural Principles of Distinct Assemblies of the Human A4β2 Nicotinic Receptor. *Nature* **2018**, *557* (7704), 261–265. https://doi.org/10.1038/s41586-018-0081-7.

(10) Blum, A. P.; Lester, H. A.; Dougherty, D. A. Nicotinic Pharmacophore: The Pyridine N of Nicotine and Carbonyl of Acetylcholine Hydrogen Bond across a Subunit Interface to a Backbone NH. *Proc Natl Acad Sci USA* **2010**, *107* (30), 13206–13211. https://doi.org/10.1073/pnas.1007140107.

(11) Xiu, X.; Puskar, N. L.; Shanata, J. A.; Lester, H. A.; Dougherty, D. A. Nicotine Binding to Brain Receptors Requires a Strong Cation-Pi Interaction. *Nature* **2009**, *458* (7237), 534–537. https://doi.org/10.1038/nature07768.

(12) Van Arnam, E. B.; Dougherty, D. A. Functional Probes of Drug-Receptor Interactions Implicated by Structural Studies: Cys-Loop Receptors Provide a Fertile Testing Ground. *J Med Chem* **2014**, *57* (15), 6289–6300. https://doi.org/10.1021/jm500023m.

(13) Puskar, N. L.; Xiu, X.; Lester, H. A.; Dougherty, D. A. Two Neuronal Nicotinic Acetylcholine Receptors, Alpha4beta4 and Alpha7, Show Differential Agonist Binding Modes. *J Biol Chem* **2011**, *286* (16), 14618–14627. https://doi.org/10.1074/jbc.M110.206565.

(14) Etter, J.-F. Cytisine for Smoking Cessation: A Literature Review and a Meta-Analysis. *Arch. Intern. Med.* **2006**, *166* (15), 1553–1559. https://doi.org/10.1001/archinte.166.15.1553.

(15) Etter, J.-F.; Lukas, R. J.; Benowitz, N. L.; West, R.; Dresler, C. M. Cytisine for Smoking Cessation: A Research Agenda. *Drug Alcohol Depend.* **2008**, *92* (1–3), 3–8. https://doi.org/10.1016/j.drugalcdep.2007.06.017.

(16) Cahill, K.; Lindson-Hawley, N.; Thomas, K. H.; Fanshawe, T. R.; Lancaster, T. Nicotine Receptor Partial Agonists for Smoking Cessation. *Cochrane Database Syst. Rev.* **2016**, No. 5, CD006103. https://doi.org/10.1002/14651858.CD006103.pub7.

(17) Walker, N.; Howe, C.; Glover, M.; Hayden, M.; Barnes, J.; Nosa, V.; Parag, V.; Bassett, B.; Bullen, C. Cytisine versus Nicotine for Smoking Cessation. **2014**, *371* (25), 2353–2362. https://doi.org/10.1056/NEJMoa1407764.

(18) West, R.; Zatonski, W.; Cedzynska, M.; Lewandowska, D.; Pazik, J.; Aveyard, P.; Stapleton, J. Placebo-Controlled Trial of Cytisine for Smoking Cessation. *N. Engl. J. Med.* **2011**, *365* (13), 1193–1200. https://doi.org/10.1056/NEJMoa1102035.

(19) Canu Boido, C.; Sparatore, F. Synthesis and Preliminary Pharmacological Evaluation of Some Cytisine Derivatives. *Il Farm.* **1999**, *54* (7), 438–451. https://doi.org/10.1016/S0014-827X(99)00049-X.

(20) Rollema, H.; Shrikhande, A.; Ward, K. M.; Coe, J. W.; Tseng, E.; Wang, E. Q.; Vries, D. M.; Cremers, T. H. I. F.; Bertrand, S.; Bertrand, D. Preclinical Properties of the A4β2 NAChR Partial Agonists Varenicline, Cytisine and Dianicline Translate to Clinical Efficacy for Nicotine Dependence. **2009**, *78* (7), 918–919. https://doi.org/10.1016/j.bcp.2009.06.077.

(21) Rollema, H.; Shrikhande, A.; Ward, K.; Iii, T. F.; Coe, J.; BT, O.; Tseng, E.; Wang, E.; Mather, R.; Hurst, R. Pre-clinical Properties of the A4β2 Nicotinic Acetylcholine Receptor Partial Agonists Varenicline, Cytisine and Dianicline Translate to Clinical Efficacy for Nicotine Dependence. **2010**, *160* (2), 334–345. https://doi.org/10.1111/j.1476-5381.2010.00682.x.

(22) Peng, C.; Stokes, C.; Mineur, Y. S.; Picciotto, M. R.; Tian, C.; Eibl, C.; Tomassoli, I.; Guendisch, D.; Papke, R. L. Differential Modulation of Brain Nicotinic Acetylcholine Receptor Function by Cytisine, Varenicline, and Two Novel Bispidine Compounds: Emergent Properties of a Hybrid Molecule. *J Pharmacol Exp Ther* **2013**, *347* (2), 424–437. https://doi.org/10.1124/jpet.113.206904.

(23) Ivachtchenko, A. V.; Khvat, A.; Tkachenko, S. E.; Sandulenko, Y. B.; Vvedensky, V. Y. Access to Novel Substituted Diazaadamantanes via Semi-Natural Tetrahydrocytisine. *Tetrahedron Lett* **2004**, *45* (36), 6733–6736. https://doi.org/10.1016/j.tetlet.2004.07.056.

(24) Philipova, I.; Stavrakov, G.; Vassilev, N.; Nikolova, R.; Shivachev, B.; Dimitrov, V. Cytisine as a Scaffold for Ortho-Diphenylphosphinobenzenecarboxamide Ligands for Pd-Catalyzed Asymmetric Allylic Alkylation. *J Organomet Chem* **2015**, *778*, 10–20. https://doi.org/10.1016/j.jorganchem.2014.12.001.

(25) Marcaurelle, L. A.; Johannes, C.; Yohannes, D.; Tillotson, B. P.; Mann, D. Diversity-Oriented Synthesis of a Cytisine-Inspired Pyridone Library Leading to the Discovery of Novel Inhibitors of Bcl-2. *Bioorg Med Chem Lett* **2009**, *19* (9), 2500–2503. https://doi.org/10.1016/j.bmcl.2009.03.037.

(26) Rouden, J.; Ragot, A.; Gouault, S.; Cahard, D.; Plaquevent, J.-C.; Lasne, M.-C. Regio- and Diastereoselective Functionalization of (−)-Cytisine: An Unusual N–C Acyl Migration. *Tetrahedron Asymmetry* **2002**, *13* (12), 1299–1305. https://doi.org/10.1016/S0957-4166(02)00271-9.

(27) Houllier, N.; Gouault, S.; Lasne, M.-C.; Rouden, J. Regio- and Diastereoselective Functionalization of (−)-Cytisine. *Tetrahedron* **2006**, *62*, 11679–11686. https://doi.org/10.1016/j.tet.2006.09.057.

(28) Dallanoce, C.; Frigerio, F.; Martelli, G.; Grazioso, G.; Matera, C.; Pomè, D. Y.; Pucci, L.; Clementi, F.; Gotti, C.; De Amici, M. Novel Tricyclic Delta(2)-Isoxazoline and 3-Oxo-2-Methyl-Isoxazolidine Derivatives: Synthesis and Binding Affinity at Neuronal Nicotinic Acetylcholine Receptor Subtypes. *Bioorg. Med. Chem.* **2010**, *18* (12), 4498–4508. https://doi.org/10.1016/j.bmc.2010.04.065.

(29) Yohannes, D.; Hansen, C. P.; Akireddy, S. R.; Hauser, T. A.; Kiser, M. N.; Gurnon, N. J.; Day, C. S.; Bhatti, B.; Caldwell, W. S. First Total Synthesis of (+/-)-3-Hydroxy-11-Norcytisine: Structure Confirmation and Biological Characterization. *Org Lett* **2008**, *10* (23), 5353–5356. https://doi.org/10.1021/ol802145b.

(30) Imming, P.; Klaperski, P.; Stubbs, M. T.; Seitz, G.; Gündisch, D. Syntheses and Evaluation of Halogenated Cytisine Derivatives and of Bioisosteric Thiocytisine as Potent and Selective NAChR Ligands. *Eur. J. Med. Chem.* **2001**, *36* (4), 375–388.

(31) Marrière, E.; Rouden, J.; Tadino, V.; Lasne, M.-C. Synthesis of Analogues of (−)-Cytisine for in Vivo Studies of Nicotinic Receptors Using Positron Emission Tomography. *Org. Lett.* **2000**, *2* (8), 1121–1124. https://doi.org/10.1021/ol005685m.

(32) Chellappan, S. K.; Xiao, Y.; Tueckmantel, W.; Kellar, K. J.; Kozikowski, A. P. Synthesis and Pharmacological Evaluation of Novel 9- and 10-Substituted Cytisine Derivatives. Nicotinic Ligands of Enhanced Subtype Selectivity. *J Med Chem* **2006**, *49* (9), 2673–2676. https://doi.org/10.1021/jm051196m.

(33) Kozikowski, A. P.; Chellappan, S. K.; Xiao, Y.; Bajjuri, K. M.; Yuan, H.; Kellar, K. J.; Petukhov, P. A. Chemical Medicine: Novel 10-Substituted Cytisine Derivatives with Increased Selectivity for Alpha4beta2 Nicotinic Acetylcholine Receptors. *ChemMedChem* **2007**, *2* (8), 1157–1161. https://doi.org/10.1002/cmdc.200700073.

(34) Coe, J. W.; Brooks, P. R.; Vetelino, M. G.; Wirtz, M. C.; Arnold, E. P.; Huang, J.; Sands, S. B.; Davis, T. I.; Lebel, L. A.; Fox, C. B.; et al. Varenicline: An Alpha4beta2 Nicotinic Receptor Partial Agonist for Smoking Cessation. *J Med Chem* **2005**, *48* (10), 3474–3477. https://doi.org/10.1021/jm050069n.

(35) Tavares, X. D. S. da S.; Blum, A. P.; Nakamura, D. T.; Puskar, N. L.; Shanata, J. A.; Lester, H. A.; Dougherty, D. A. Variations in Binding among Several Agonists at Two Stoichiometries of the Neuronal, A4β2 Nicotinic Receptor. *J Am Chem Soc* **2012**, *134* (28), 11474–11480. https://doi.org/10.1021/ja3011379.

(36) Marotta, C. B.; Rreza, I.; Lester, H. A.; Dougherty, D. A. Selective Ligand Behaviors Provide New Insights into Agonist Activation of Nicotinic Acetylcholine Receptors. *ACS Chem Biol* **2014**, *9* (5), 1153–1159. https://doi.org/10.1021/cb400937d.

(37) Durkin, P.; Magrone, P.; Matthews, S.; Dallanoce, C.; Gallagher, T. Lactam Enolate-Pyridone Addition: Synthesis of 4-Halocytisines. *Synlett* **2010**, *2010* (18), 2789–2791. https://doi.org/10.1055/s-0030-1259006.

(38) Hirschhäuser, C.; Haseler, C. A.; Gallagher, T. Core Modification of Cytisine: A Modular Synthesis. *Angew Chem Int Ed Engl* **2011**, *50* (22), 5162–5165. https://doi.org/10.1002/anie.201100441.

(39) Campello, H. R.; Villar, S. G. D.; Honraedt, A.; Minguez, T.; Oliveira, A. S. F.; Ranaghan, K. E.; Shoemark, D. K.; Bermudez, I.; Gotti, C.; Sessions, R. B.; et al. Unlocking Nicotinic Selectivity via Direct C–H Functionalization of (−)-Cytisine. *Chem* **2018**, *0* (0). https://doi.org/10.1016/j.chempr.2018.05.007.

(40) Post, M. R.; Tender, G. S.; Lester, H. A.; Dougherty, D. A. Secondary Ammonium Agonists Make Dual Cation-π Interactions in A4β2 Nicotinic Receptors. *eNeuro* **2017**, *4* (2), ENEURO.0032-17.2017. https://doi.org/10.1523/ENEURO.0032-17.2017.

(41) Duffy, N. H. Studies of the Serotonin Type 3A Receptor and the Chemical Preparation of TRNA. phd, California Institute of Technology, 2014. https://doi.org/Duffy, Noah Hanville

(2014) Studies of the Serotonin Type 3A Receptor and the Chemical Preparation of tRNA. Dissertation (Ph.D.), California Institute of Technology. doi:10.7907/X1YA-DM13. http://resolver.caltech.edu/CaltechTHESIS:05062014-151417635 <http://resolver.caltech.edu/CaltechTHESIS:05062014-151417635>.

(42) Dougherty, D. A. Cys-Loop Neuroreceptors: Structure to the Rescue? *Chem Rev* **2008**, *108* (5), 1642–1653. https://doi.org/10.1021/cr078207z.

(43) Cashin, A. L.; Torrice, M. M.; A, M., Kathryn; Lester, H. A.; Dougherty, D. A. Chemical-Scale Studies on the Role of a Conserved Aspartate in Preorganizing the Agonist Binding Site of the Nicotinic Acetylcholine Receptor. *Biochemistry* **2007**, *46* (3), 630–639. https://doi.org/10.1021/bi061638b.

(44) Horovitz, A. Double-Mutant Cycles: A Powerful Tool for Analyzing Protein Structure and Function. *Fold Des* **1996**, *1* (6), R121–R126. https://doi.org/10.1016/S1359-0278(96)00056-9.

(45) Kao, C.; Zheng, M.; Rüdisser, S. A Simple and Efficient Method to Reduce Nontemplated Nucleotide Addition at the 3 Terminus of RNAs Transcribed by T7 RNA Polymerase. *RNA N. Y. N* **1999**, *5* (9), 1268–1272.

(46) Nowak, M.; Gallivan, J.; Silverman, S.; Labarca, C.; Dougherty, D.; Lester, H. In Vivo Incorporation of Unnatural Amino Acids into Ion Channels in Xenopus Oocyte Expression System. *Methods Enzymol.* **1998**, *293*, 529.

(47) England, P. M.; Lester, H. A.; Dougherty, D. A. Incorporation of Esters into Proteins: Improved Synthesis of Hydroxyacyl TRNAs. *Tetrahedron Lett* **1999**, *40* (34), 6189–6192. https://doi.org/10.1016/s0040-4039(99)01300-3.

(48) Moroni, M.; Zwart, R.; Sher, E.; Cassels, B. K.; Bermudez, I. Alpha4beta2 Nicotinic Receptors with High and Low Acetylcholine Sensitivity: Pharmacology, Stoichiometry, and Sensitivity to Long-Term Exposure to Nicotine. *Mol Pharmacol* **2006**, *70* (2), 755–768. https://doi.org/10.1124/mol.106.023044.

Chapter 3

Development of a Novel Series Positive Allosteric Modulators of the $GABA_A$ Receptor*

3.1 Abstract

γ-aminobutyric acid type A ($GABA_A$) receptors are key mediators of central inhibitory neurotransmission and have been implicated in several disorders of the central nervous system (CNS). Several positive allosteric modulators of this receptor provide great therapeutic benefits to patients. However, adverse effects remain a challenge. Subtype selective targeting of $GABA_A$ receptors could mitigate this problem. Additionally, the identification of subtype selective ligands could aid in the elucidation of subtype specific functions in the brain. In this chapter, we describe the development and functional evaluation of a novel series of pyrrolidinoindolines for agonism and modulation of the $GABA_A$ receptor. Additionally, we performed mutagenesis to identify the binding site of these ligands. We found that substitution at the C(5) position for an halogen, such as Br or I, greatly increased the PAM potency relative to the parent ligand, while substitutions at other positions generally decreased potency. Mutagenesis studies suggest that the binding site is lies in the transmembrane domain.

3.2 Introduction

γ-aminobutyric acid type A ($GABA_A$) receptors are key mediators of central inhibitory neurotransmission, and as such these receptors have been drug targets for numerous CNS disorders.[1–6] The $GABA_A$ receptor is an anion-selective, pentameric ligand-gated ion channel that is part of the larger Cys-loop receptor family. A functional receptor results from the assembly of five homologous subunits. A total of 19 homologous subunits exist, that can

* The work described in this chapter was done in collaboration with Katie Chan, Dr. Justin Su, and Prof. Sarah Reisman.

assemble in at least 30 different subtypes *in vivo*.[7] Some types, among which the α1β2γ2, are predominantly expressed at the post-synaptic termini and mediated phasic inhibition, while others are located at extrasynaptic sites and mediate tonic inhibition.[7–9] The large diversity of subtypes and differential localization in the brain emphasize their importance, but also form a challenge as current $GABA_AR$ therapeutics modulate a broad range of subtypes, which can result in adverse effects.

Each $GABA_A$ subunit consists of an N-terminal extracellular domain (ECD), a transmembrane domain (TMD) that comprises four transmembrane α-helices (M1-M4), an extracellular M2-M3 loop and C-terminus, and an intracellular domain composed of the M3-M4 loop.[10–12] Receptor activation occurs upon binding of an agonist to the orthosteric site, which is located in the ECD at the β+/α- subunit interfaces. This activation can be modulated by additional binding of other ligands to several allosteric sites on the pentameric complex.[13] Positive allosteric modulators (PAMs) potentiate the evoked response by an agonist, while negative allosteric modulators (NAMs) inhibit that response.[14,15] Allosteric agonists that are able to activate the receptors via allosteric sites have also been found. Some of these contain PAM properties as well and are so-called ago-PAMs.[14] Over the years various modulators of $GABA_A$ receptors have been identified and several positive allosteric modulators are widely used to treat anxiety and panic disorders, such as Alprazolam (Xanax), Diazepam (Valium), and Flurazepam (Dalmane) (**Figure 3.1**).[14–16]

Although $GABA_A$ receptor modulators have proven great therapeutic benefit, adverse effects remain a problem. Additionally, elucidating functions of individual subtypes is crucial for a better understanding of $GABA_AR$'s role in health and disease. Therefore, recent efforts have been focused on finding subtype selective modulators. Various novel modulators have been derived from the α+/β- interface binding PAM CGS 9895 (**Figure 3.1**).[17,18] For example,

a series of pyrazolopyridinones by Blackaby *et al.* showed increased selectivity for α3β3γ2 over α1β3γ2.[19] Two different series of pyrazoloquinolinones exhibited selectivity for α6β3γ2 and β1- containing receptors respectively.[20,21]

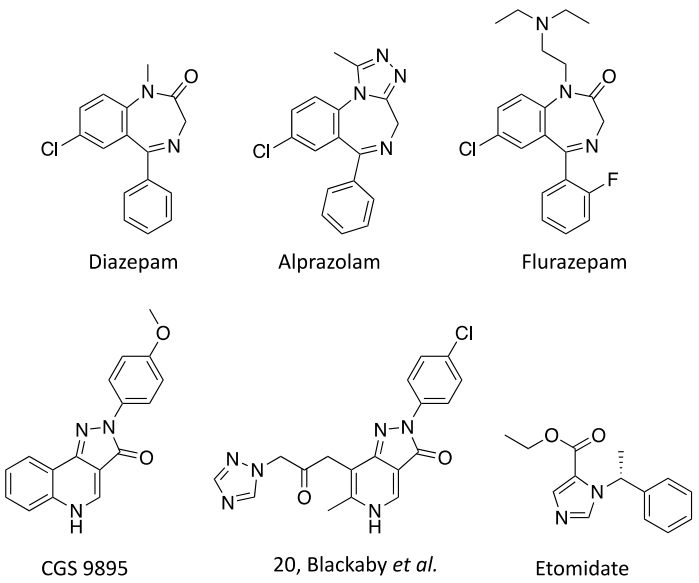

Figure 3.1 | Chemical structures of a few positive allosteric modulators of the $GABA_A$ receptor.

When reviewing the chemical structures of these recent efforts, a structurally similar compound, Physostigmine, comes to mind. Physostigmine (**Figure 3.2**), also known as eserine or Antilirium, is a reversible acetylcholinesterase inhibitor.[22] This enzyme is responsible for the breakdown of acetylcholine, so inhibition results in the prolonged activity of this neurotransmitter and thus indirectly stimulates nicotinic acetylcholine receptors. It has been used to treat glaucoma and delayed gastric emptying.[23,24] It was also explored as a potential therapy for Alzheimer's disease, but failed to show convincing therapeutic benefit in clinical trials. In addition, it has been found to potentiate and inhibit nicotinic acetylcholine receptors as well.[25–28] To our knowledge, no reports have been published of physostigmine activity at $GABA_A$ receptors.

Preliminary screen of novel physostigmine derivatives for Cys-loop receptor activity

In a previous study, Dr. Kristina Daeffler and Dr. Christopher Marotta screened five physostigmine derivatives (**Figure 3.2**), synthesized by Dr. Lindsey Repka and Dr. Alex Maolanon, against seven LGICs: α7 (T6'S) nAChR, the A3B2 α4(L9'A)β2 nAChR, muscle-type nAChR, the α1β2γ2 $GABA_A$ receptor, the 5-HT3A receptor, glycine receptor and the GluR2 receptor.[29,30] Most compounds exhibited inhibition with different potencies for the nAChRs and no activity at the other channels tested. Surprisingly, compound AMAO-1-86 was identified as a weak partial agonist and a PAM for the α1β2γ2 $GABA_A$ receptor (**Table 3.1**). No agonism and diminished PAM activity was observed for the α1β2 $GABA_A$ receptor (**Table 3.1**). Further studies were performed to characterize the inhibition of nAChRs by AMAO-1. IC_{50} curves and voltage-jump experiments suggested inhibition through channel blocking. Even though no $GABA_A$ receptor activity has been previously reported for physostigmine, AMAO-1-86 appears to selectively potentiate α1β2γ2 $GABA_A$ receptors over other Cys-loop receptors.

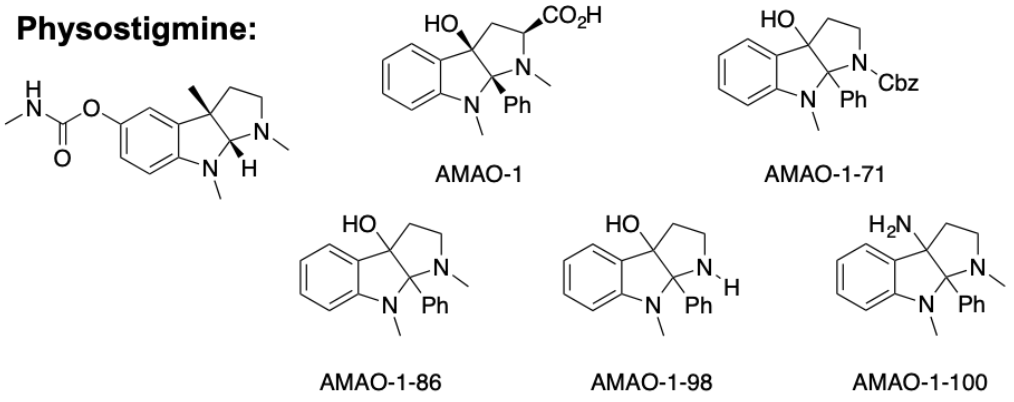

Figure 3.2 | Chemical structures of the first generation physostigmine derivatives. These molecules were synthesized by Dr. Lindsey Repka and Alex Maolanon. Adapted from Marotta, C.B. 2015.[30]

Table 3.1 | Functional effects of the compounds in Figure 3.1 on Cys-loop receptors. Relative modulation of the current response as a result of co-application of endogenous agonist EC_{50} dose and 20-40 μM of compound. Adapted from Marotta, C.B. 2015.[30]

Receptor	AMAO-1	AMAO-1-71	AMAO-1-86	AMAO-1-98	AMAO-1-100
Muscle (9')	-21 ± 1	-29 ± 3	-53 ± 3	-7 ± 3	-81 ± 6
A3B2 α4(L9'A)β2	-28 ± 2	-47 ± 4	-29 ± 6	-11 ± 2	-44 ± 2
A7 (T6'S)	-62 ± 4	-68 ± 7	-92 ± 4	-57 ± 10	-96 ± 3
5-HT_{3A}	-3 ± 2	-23 ± 4	-3 ± 5	3 ± 12	-11 ± 8
αβγ $GABA_A$	-27 ± 4	-27 ± 11	**52 ± 10**	-27 ± 21	10 ± 5
αβ $GABA_A$			**16 ± 2**		
GluR2	-6 ± 1	0 ± 2	-9 ± 6	-11 ± 5	-12 ± 5
Glycine	-6	-9 ± 9	3 ± 7	18 ± 10	-16 ± 6

In this chapter, we expand on these previous, preliminary studies and present the biological evaluation of a novel series physostigmine derivatives as potential positive allosteric modulators of the $GABA_A$ receptor. All of the compounds were tested for agonism and allosteric modulation properties at the α1β2γ2 $GABA_A$ receptor via two electrode voltage clamp experiments. Additionally, we performed mutagenesis studies to identify the binding site of these ligands.

3.3 Results and discussion

3.3.1 Characterization of the PAM 163 at the a1β2γ2 $GABA_A$ receptor

Based on the selective PAM profile of AMAO-1-86 among Cys-loop receptors, we decided to further characterize this ligand. The data obtained in **Table 3.2** is based on racemic mixtures of the designated compounds, so we first set out to determine if both enantiomers were active at the α1β2γ2 $GABA_A$ receptor. For convenience, AMAO-1-86 is from here onwards referred to as 163 and its enantiomers as (-)-163-1 and (+)-163-2. Katie Chan from the Reisman group at Caltech synthesized a new batch of racemic 163 and purified the two

enantiomers. In addition, a new derivative was synthesized with an OMe substituent on the phenyl ring, *para* to the bicycle N (159). All four compounds were tested for agonism and modulation at the α1β2γ2 $GABA_A$ receptor as shown in **Figure 3.3**.

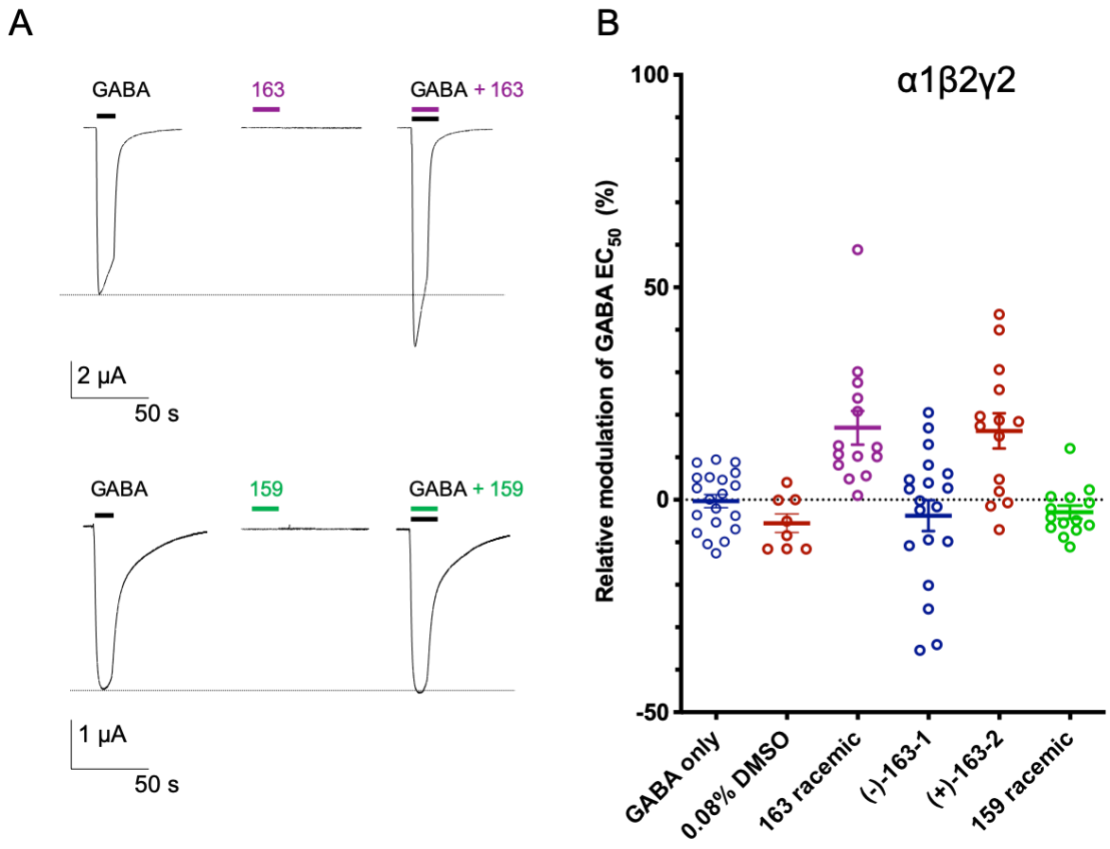

Figure 3.3 | Functional effects of 163 and 159 on the α1β2γ2 $GABA_A$ receptor. A) Wave forms of the α1β2γ2 current responses from a GABA only dose and co-application with racemic 163 or 159. For clarity, only one GABA response is shown here. B) Relative modulation of a GABA EC_{50} dose as a result of co-application with ligands of interest at a 40 μM concentration.

To assess functional effects, we used a similar protocol as previously described by Marotta *et al.*[30] Briefly, the current responses of three identical GABA concentration were recorded, followed by a dose of the test-ligand at 40 μM. After a 30 s incubation period, a test dose was applied containing both GABA and the test-ligand. Finally, two doses of GABA were applied. The first test dose evaluates agonism properties, the second dose tests for modulation of the GABA response, which can be potentiating or inhibiting. The first three

GABA doses aim to establish a baseline of the GABA response at that concentration, and the purpose of the last two GABA doses is to verify proper functioning of the receptor post modulation and control for independent rise in current amplitude.

The racemic mixture of 163 showed less potent PAM properties (17 ± 4.0%) than was observed in the previous study. This could be a result of a different purification method or preparation of the stock solution. In order to account for solvent effects, a control experiment was executed containing 0.08% of DMSO. In addition, we performed a GABA only control to assess the inherent variability of the current responses. Of the two 163 enantiomers, only for (+)-163-2 has potentiation been observed with a mean of 16 ± 4.1%. For ligand 159, no agonism (not shown) nor modulation effects were observed (**Figure 3.3**, **Table 3.2, Figure 3.9**).

Table. 3.2 | Relative modulation of GABA EC_{50} responses in WT $GABA_A$ receptors. Values are expressed as mean ± SEM.

Subtype	Ligand	Relative modulation of GABA EC_{50} (%)	N	|I| (μA)
α1β2γ2	GABA only	-0.3 ± 1.6	20	0.5 – 7.7
α1β2γ2	0.08% DMSO	-5.5 ± 2.2	8	1.3 - 32.6
α1β2γ2	159	-2.9 ± 1.6	14	0.8 – 10.8
α1β2γ2	163-racemic	17 ± 4.0	14	0.1 – 9.9
α1β2γ2	(-)-163-1	-3.7 ± 3.7	19	0.3 – 10.1
α1β2γ2	(+)-163-2	16 ± 4.1	14	3.7 – 14.2
α1β2	163-racemic	28 ± 5.2	10	0.8 – 9.3
α1β2	(-)-163-1	9.2 ± 1.1	11	0.3 – 2.3
α1β2	(+)-163-2	17 ± 2.6	13	0.4 – 3.3

Preliminary data in **Table 3.1** showed decreased potentiating effects for the α1β2 $GABA_A$ receptor. To further elucidate enantiomeric effects for this subtype, we performed the same experiment for this subtype using the new batch of racemic 163 and the separate enantiomers. For the racemic mixture a mean potentiation of 28 ± 5.2% was observed (**Figure 3.4**). Surprisingly, both enantiomers showed potentiation for this subtype: (-)163-1 9.2 ± 1.1%

and 163-2 17 ± 2.6%. These results indicate that the γ2 subunit is not required for the potentiating effects of 163. Thus, the binding site of this PAM is likely located on either the α or β subunit or at the interface of these two subunits.

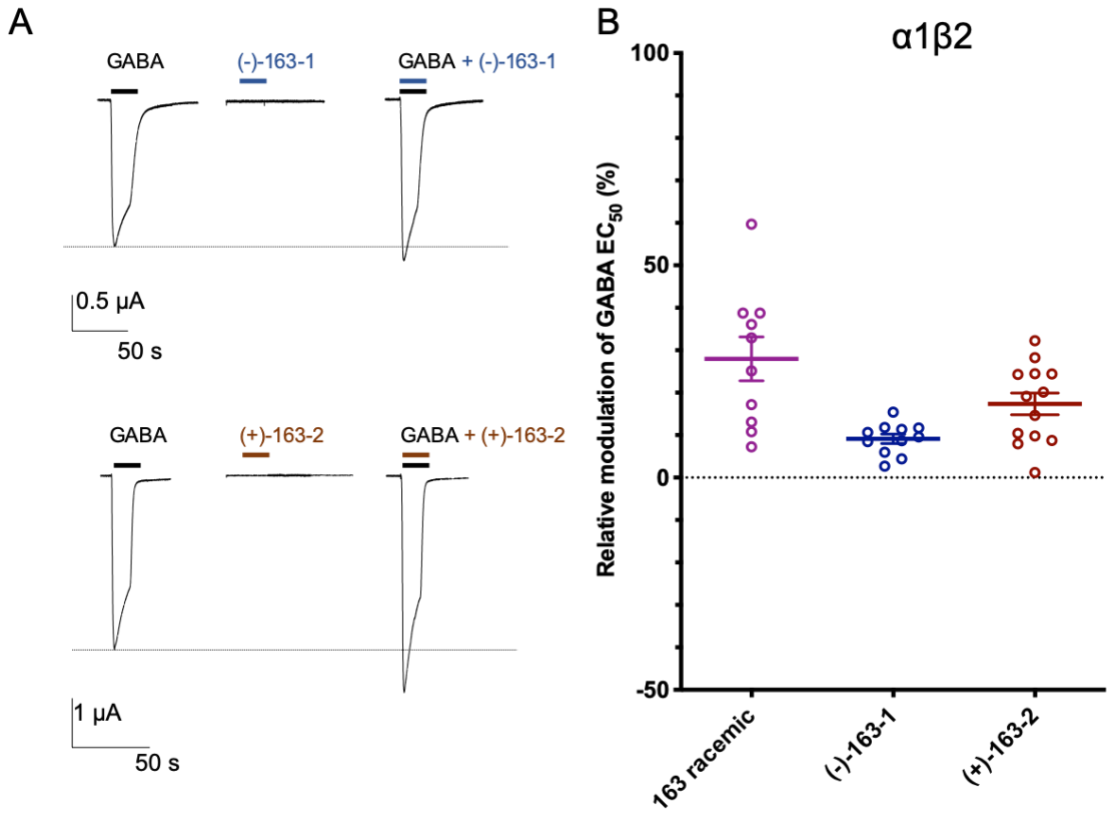

Figure 3.4 | Functional effects of 163 on the α1β2 $GABA_A$ receptor. A) Wave forms of the α1β2 current responses from a GABA only dose and co-application with (-)-163-1 or (+)-163-2. For clarity, only one GABA response is shown here. B) Relative modulation of a GABA EC_{50} dose as a result of co-application with ligands of interest at a 40 μM concentration.

The amplitude of potentiation is dependent on several factors, among which are both the PAM concentration and the GABA concentration at which we tested the modulation. Next, we determined the effect of 40 μM racemic 163 on the GABA EC_{50} (ΔEC_{50}(163-rac)) at the α1β2γ2 receptor. The observed 163-induced shift in GABA EC_{50} is 12.8 μM as shown in **Figure 3.5A**. This shift is comparable to the induced shift seen for this subtype by the benzodiazepine Triazolam, 16-50 μM.[31] Moreover, we wanted to determine the potency of

163 itself. Well-studied modulators, such as flurazepam and zolpidem, have EC_{50}s in the nanomolar range, 272 nM and 335 nM respectively.[32] The PAM tested here, (+)-163-2, appears to be less potent with an EC_{50} of 112 µM when co-applied with GABA EC_5, as shown in **Figure 3.5B**.

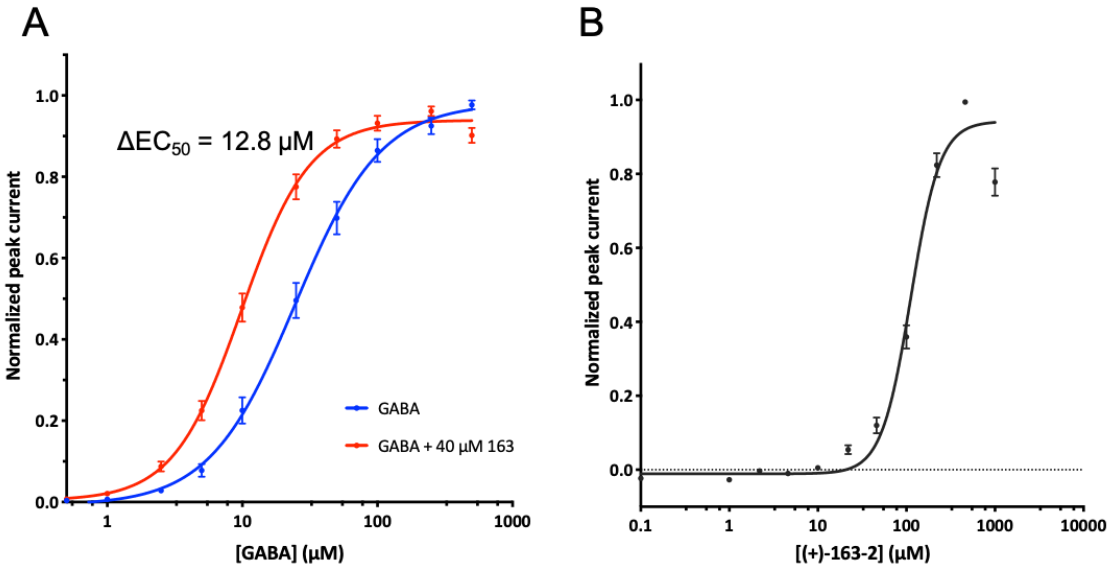

Figure 3.5 | Functional characterization of 163 at the α1β2γ2 $GABA_A$ receptor. A) PAM-induced shift in GABA EC_{50}. PAM concentration used here was 40 µM of racemic 163. B) PAM EC_{50} when co-applied with GABA EC_5 doses.

Table 3.3 | EC_{50} values of 163, GABA, and GABA co-application with 163.

Subtype	Compound	EC_{50} (µM)			n_H			N	| I_{max} | (µA)
α1β2γ2	(+)-163-2	112	±	4.9	2.6	±	0.27	16	0.91 - 20.2
α1β2γ2	GABA	22.7	±	0.45	1.3	±	0.03	40	1.69 - -9.77
α1β2γ2	GABA + 163 rac	9.89	±	0.48	1.7	±	0.13	22	6.12 - 16.30

The potentiation experiments in **Figure 3.3 and 3.4** provided valuable information regarding the general behavior of the compounds, that is whether it potentiates or inhibits the GABA response. As we have now established that it as a PAM, further potentiation experiments use the GABA EC_{10-15} instead of EC_{50}. Using the EC_{10-15} allows for a larger potentiation window than EC_{50}, which enables the detection of more subtle differences between mutants or derivatives. **Figure 3.5A** and **Table 3.4** illustrate this difference in

modulation potency. For the α1β2γ2 subtype, racemic 163 causes a 62% potentiation of the GABA EC_{10} response, while at the GABA EC_{50} this is only 17%, about a 3.6-fold increase.

Table 3.4 | Relative modulation of GABA EC_{50} and EC_{10} responses in α1β2γ2 $GABA_A$ receptors.

Mutant	[GABA]	Relative modulation (%)	N	|I| (μA)
α1β2γ2 WT	EC_{50}	17 ± 4.0	14	0.1 – 9.9
α1β2γ2 WT	EC_{10}	62 ± 6.1	18	0.8 – 4.4

3.3.2 Progress towards elucidating the binding site of the PAM 163

GABA activates the $GABA_A$ receptor through binding in the ECD at the interface of the β+/α- subunits. Besides this orthosteric site, several allosteric binding sites have been established, of which the most well-known is the benzodiazepine site (BZ-site) in the ECD at the α+/γ- interface.[33,34] More recently observed is the binding site in the ECD at the α+/β- site for the ligand CGS9895.[34–37] Most of these sites have been established by way of radioligand binding essays, photoaffinity labeling, or mutagenesis combined with a steric hindrance approach. In addition to binding sites in the ECD, several anesthetics and neurosteroids affect channel activity through binding in the TMD. Recent X-ray crystal structures and cryo-EM structures have shed light on the TM residues involved here.[38,39]

In order to determine the binding site for the PAM 163, we performed mutagenesis on residues that have previously been implicated in binding of known modulators. For the first screen we selected α1(H129R)[33] and α1(Y209Q)[35,40–42] to probe the BZ-site, β2(Q88C) to probe the α+/β- site,[34] and triple mutant α1(S297I)β2(N289I)γ2(S319I) to probe for anesthetic sites in the TMD.[35,43] All three ECD mutants were potentiated to a similar extend as the WT receptor (mean 62 ± 6.1%), however the triple TMD mutant was not affected by 163 at this concentration (mean 1.0 ± 3.0%) as shown in **Figure 3.7 and Table 3.5**. These results highly suggest that 163 does not assert its potentiating affects through binding at the interfaces at the ECD, but on one or more interfaces in the TMD.

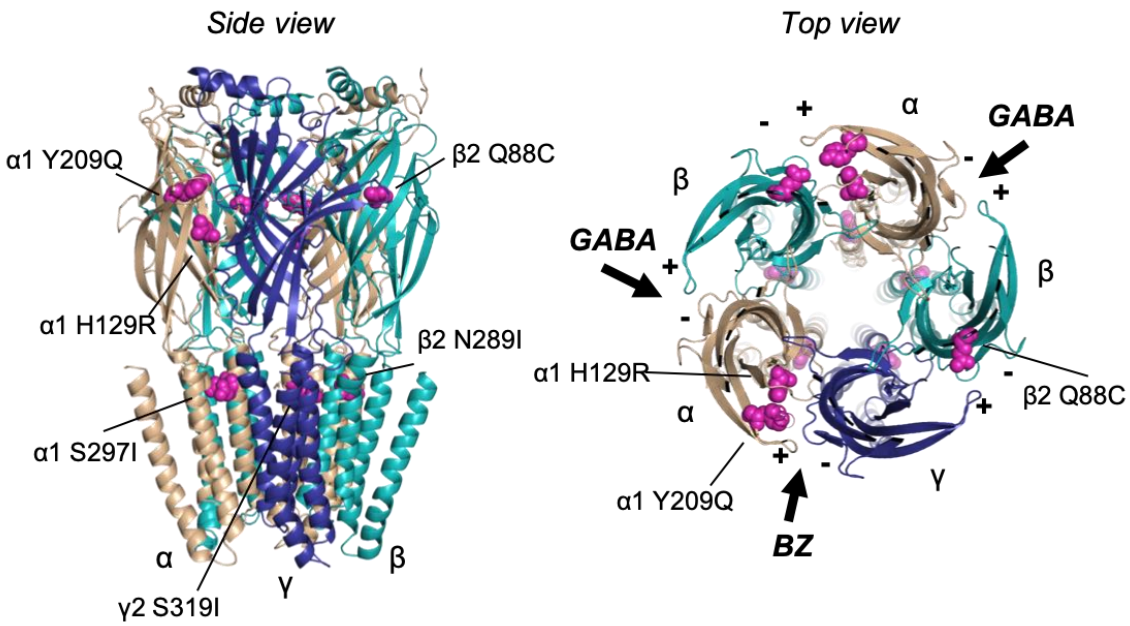

Figure 3.6 | Structure of the human α1β2γ2 $GABA_A$ receptor with the probed residues highlighted. (Left) Side view of the receptor, (Right) extracellular view into the pore (PDB ID: 6D6T). Mutated residues are labeled and highlighted in pink.

Table 3.5 | Relative modulation of GABA EC_{10} responses by racemic 163 in ECD mutant receptors. Values are expressed as mean ± SEM.

Mutant	Relative modulation of GABA EC_{10} (%)			N	|I| (μA)
α1β2γ2 WT	62	±	6.1	18	0.8 – 4.4
α1(H129R)β2γ2	88	±	8.1	11	0.1 – 0.7
α1(Y209Q)β2γ2	86	±	8.9	8	0.2 -1.5
α1β2(Q88C)γ2	69	±	5.8	10	0.1 – 3.7

To further determine which interfaces are involved in binding in the TMD, we performed potentiation experiments for the single and double mutants of α1β2γ2, as well as the α1β2 subtype (**Figure 3.7, Table 3.6**). Analysis of the α1β2γ2 mutant responses suggests involvement of the β2 subunit in binding, as only the single and double mutant receptors that contain a mutation in the β2 subunit demonstrate greatly reduced potentiation. The potentiation in both single mutants in the α1 and γ2 subunits resembles that of the α1β2γ2 WT receptor. Potentiation experiments in the α1β2 subtype were less conclusive. Great variability in potentiation was observed among experiments performed on different days.

Some mutants were tested on three different batches of oocytes, but no single population could be established. Factors that could have played a role are cell health and degradation of the ligand. Injecting mRNA to express the α1β2 subtype rendered more dying oocytes after 24 hrs, than for the α1β2γ2 mutants.

The β2(N289I) mutation is located in the TMD, close to the top of TM2, at β+/α- interface (**Figure 3.6**). This residue has been implicated in the binding of several anesthetics, such as Etomidate, Propofol, and Loreclezole.[35,44]

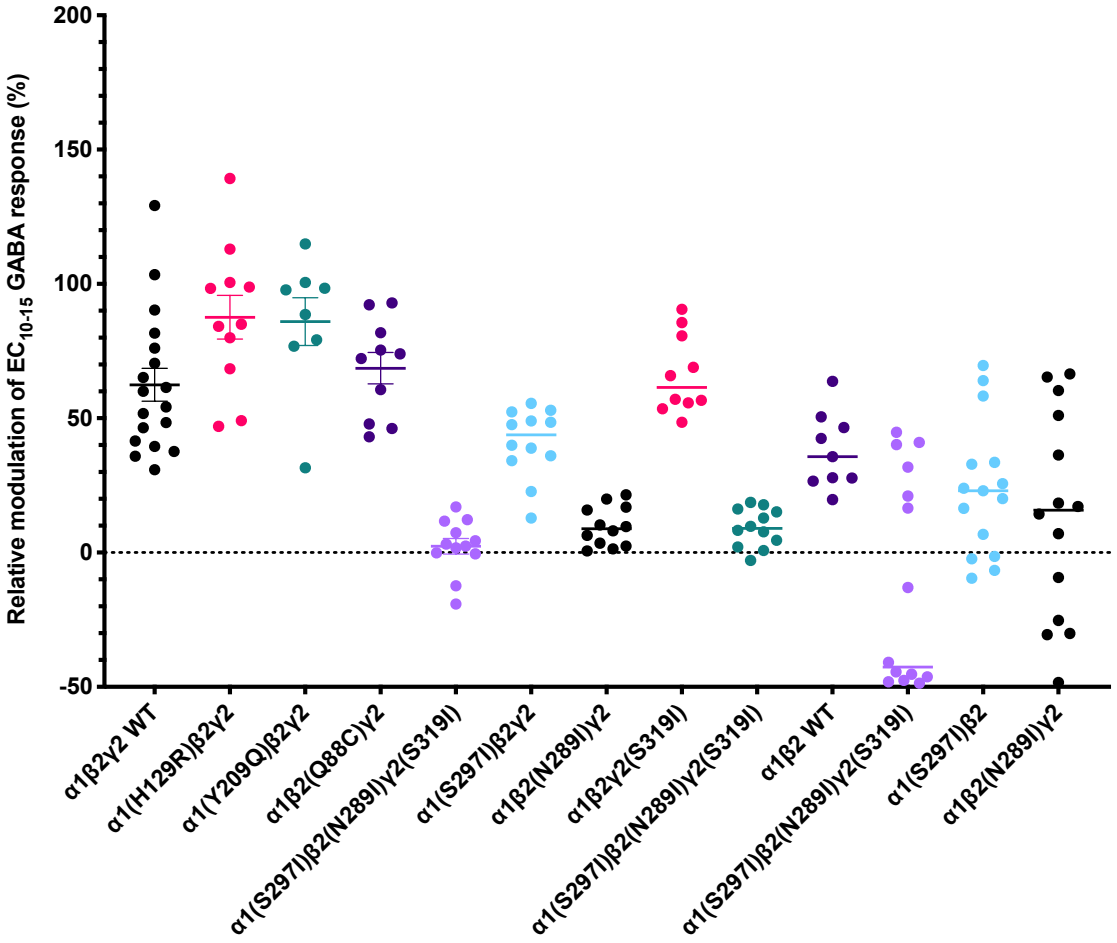

Figure 3.7 | Relative modulation of GABA $EC_{10\text{-}15}$ responses by racemic 163 in mutant receptors. Relative modulation was measured after co-application of GABA $EC_{10\text{-}15}$ with 40 μM of racemic 163.

Table 3.6 | Relative modulation of GABA EC_{10} responses by racemic 163 in TMD mutant receptors. Values are expressed as mean ± SEM.

Mutant	Relative modulation of GABA EC_{10-15} (%)			N	|I| (μA)
α1β2γ2 WT	62	±	6.1	18	0.8 – 4.4
α1(S297I)β2(N289I)γ2(S319I)	1.1	±	3.0	12	0.1 – 1.7
α1(S297I)β2γ2	41	±	3.7	12	0.1 – 2.4
α1β2(N289I)γ2	9.7	±	2.1	12	1.2 – 5.3
α1β2γ2(S319I)	66	±	4.7	10	0.2 – 0.5
α1(S297I)β2(N289I)γ2	9.2	±	2.0	12	0.4 – 2.5
α1β2 WT	38	±	4.7	9	0.1 – 1.9
α1(S297I)β2(N289I)	-3.3	±	13	11	0.1 – 0.8
α1(S297I)β2	16	±	5.1	9	0.1 – 1.6
α1β2(N289I)	24	±	16	8	0.05 – 1.2

We performed potentiation experiments by co-applying the 40 μM PAM with an EC_{10} dose of GABA. To determine the EC_{10} values of the constructed mutant receptors, we determined the full concentration-response curves and found EC_{50} values corresponding to those reported in previous studies (**Table 3.7**).[35,43]

Table 3.7 | GABA EC_{50} values of $GABA_A$ WT and mutant receptors. Individual TMD mutants of α1(S297I)β2(N289I)γ2(S319I) are referred to as M in the table.

Mutant	EC_{50} (μM)			n_H			N	$\|I_{max}\|$ (μA)
α1β2γ2 WT	22.7	±	0.45	1.3	±	0.03	40	1.7 - -9.8
α1β2 WT	2.98	±	0.07	1.5	±	0.05	7	5.8 - 25
α1(H129R)β2γ2	16.4	±	0.47	1.7	±	0.06	17	0.37 – 4.0
α1(Y209Q)β2γ2	21.5	±	0.81	1.6	±	0.08	6	4.2 - 8.6
α1β2(Q88C)γ2	26.6	±	1.8	1.4	±	0.11	6	0.9 – 8.0
α1(S297I)β2(N289I)γ2(S319I)	0.527	±	0.01	1.8	±	0.05	13	3.5 – 6.4
α1(S297I)β2γ2	0.737	±	0.02	1.8	±	0.08	19	1.1 - 25
α1β2(N289I)	26.9	±	0.59	1.8	±	0.06	11	0.04 - 17
α1β2γ2(S319I)	20.2	±	0.65	1.7	±	0.08	6	0.05 – 4.3
α1(S297I)β2(N289I)γ2	1.04	±	0.028	2.0	±	0.09	11	0.4 - 19
α1(S297I)β2	0.101	±	0.0032	2.0	±	0.11	8	0.5 – 4.3
α1β2(N289I)	2.78	±	0.075	1.4	±	0.05	10	1.0 – 3.7
α1(S297I)β2(N289I)	0.0568	±	0.0022	2.2	±	0.17	7	0.6 – 4.8

3.3.3 Optimization of allosteric modulation potency

In order to improve the potency of the PAM, we decided to design a novel series of derivatives and explore which positions permit substitutions while retaining or improving its PAM activity. First, we determined the absolute stereochemistry of the active enantiomer (+)-163-2. Both stereocenters are *(S)* as shown in **Figure 3.8**. Based on the parent structure of (+)-163-2, we explored substitutions at C(3a), C(5), N(1), and the C(4) on the phenyl ring at C(8a) see **Figure 3.8** for numbering and **Figure 3.9** for the complete library of ligands. Generally, none of the derivatives demonstrated agonistic properties, except for (-)-51 and (+)-282 activated the receptor at very low efficacy. Note that reported values in this section represent the relative modulation of GABA EC_{10} responses.

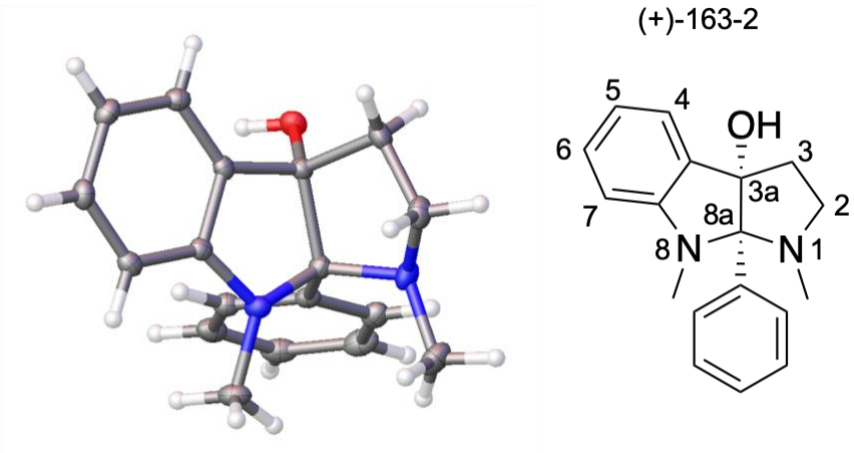

Figure 3.8 | Structural characterization of (+)-163-2. On the left, X-ray structure of (+)-163-2. On the right, schematic structure including numbering of atoms.

Most derivatives demonstrate a similar activity pattern for the two enantiomers as we have observed for 163. If the ligand shows any activity, the *(S),(S)* enantiomer is the active one of the two. One exception to this is ligand pair (-)-66 and (+)-67 ($R_{C(8a)}$= 4-Br-phenyl), which both show substantial potentiation. It is worth noting that ligand (+)-286 and (-)-287 ($R_{C(5)}$= morpholine), and (+)-50 and (-)-51 ($R_{C(5)}$= I) have flipped signs in optical rotation as

compared to all other derivatives. **Figure 3.10** shows the potentiation of N(1) and C(3a) derivatives.

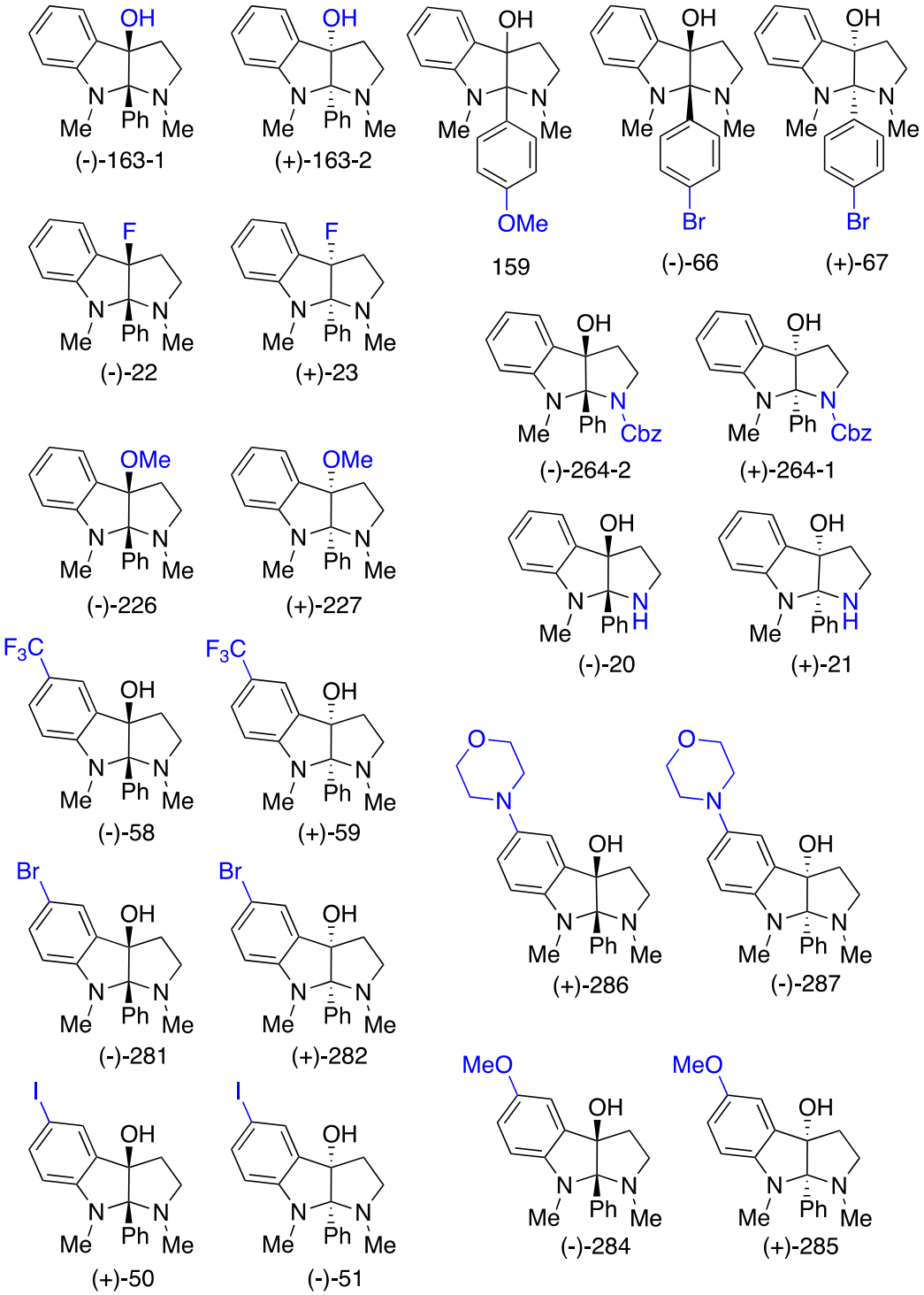

Figure 3.9 | Novel series of physostigmine derivatives evaluated in this study.

Removal of the methyl group or addition of a Cbz-group at N(1) resulted in decreased potentiation, 41 ± 3% and 9.6 ± 5.2% respectively, relative to (+)-163-2 (125 ± 15%). Replacement of the hydroxyl at C(3a) appears to be permissive for fluorine (100 ± 11%.), but not to a methoxy-group (21 ± 3.0%).

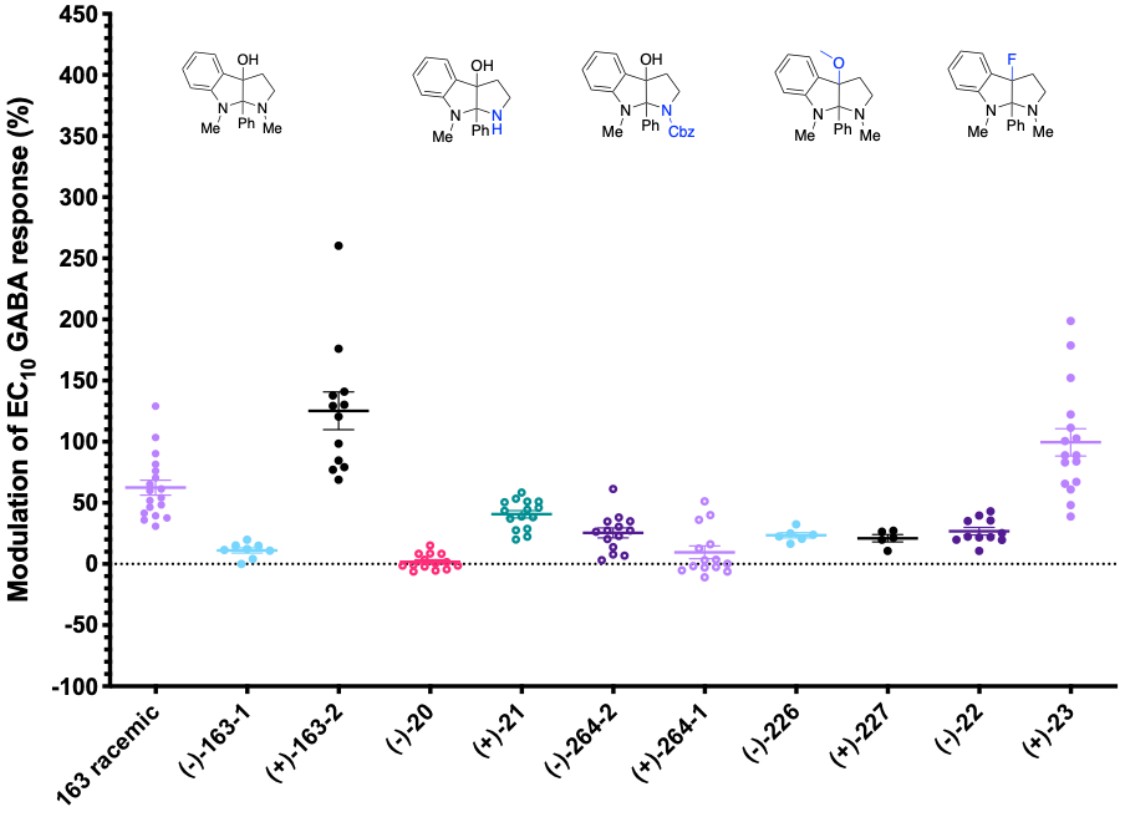

Figure 3.10 | Functional effects of C3a, N1, and C8a derivatives on the α1β2γ2 $GABA_A$ receptor.

These results combined with data from the preliminary data in **Table 3.1** suggest that substitution on the pyrrolidine does not render increased potency relative to (+)-163-2. So next, we looked at substitution at C(5) at the indoline (**Figure 3.11, Table 3.8**). Introducing a methoxy- or morpholino-group drastically reduced the potentiation efficacy, 17 ± 3.2% and -4.8 ± 1.8% respectively. Potentiation by ligand 59 ($R_{C(5)}$= CF_3) resembled that of (+)-163-2 at 108 ± 9.5%. Surprisingly, introducing a halogen, Br or I, at C(5) greatly increased potentiation with a relative modulation of 213 ± 21% and 231 ± 24% respectively. These two ligands

appear to have the largest potentiation effects on the α1β2γ2 $GABA_A$ receptor at 40 μM of all derivatives we studied here.

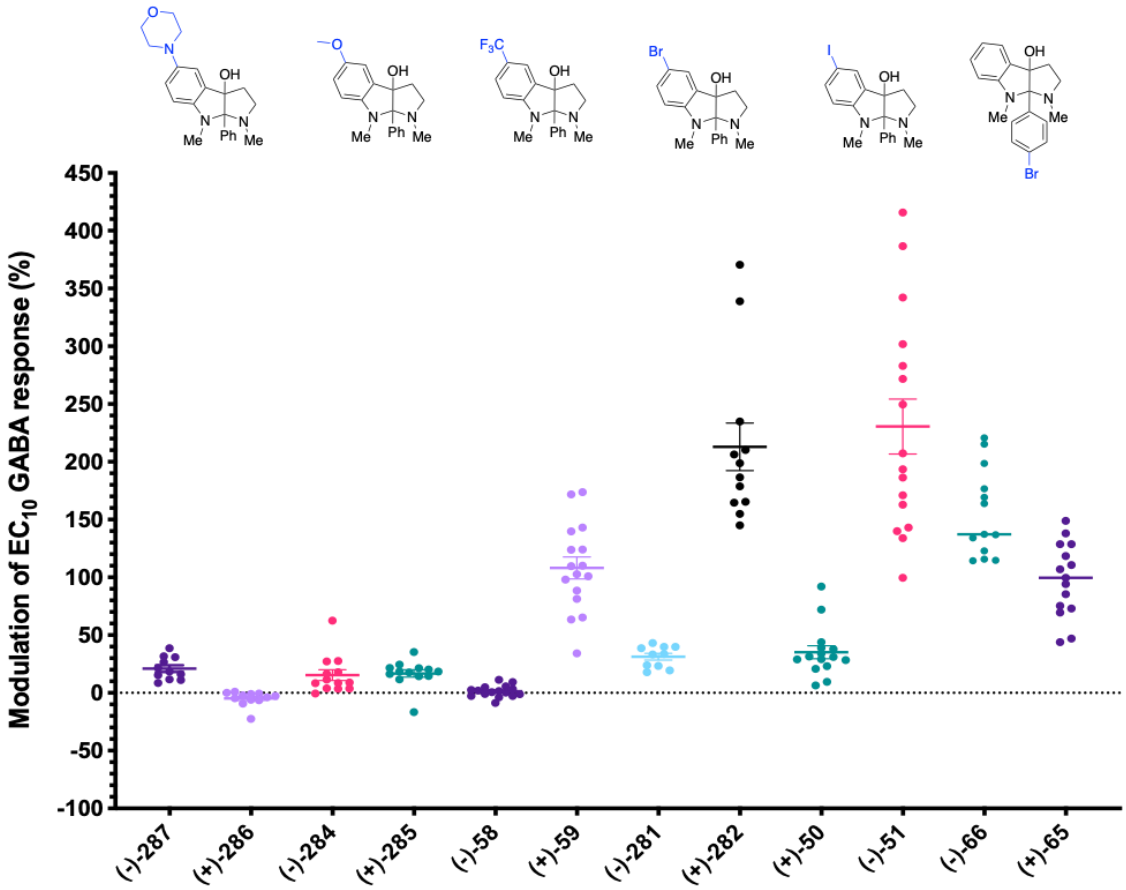

Figure 3.11 | Functional effects of C(5) derivatives on the α1β2γ2 $GABA_A$ receptor.

Recall that 159 ($R_{C(8a)}$= 4-OMe-Ph) did not exhibit any PAM properties, neither did (+)-285 ($R_{C(5)}$= OMe). However, (+)-282 ($R_{C(5)}$= Br) demonstrated increased PAM properties relative to (+)-163-2. Considering the spatial positioning of the Br at C(5), we asked the question whether a ligand with a 4-Br-Ph at C(8a) would also render PAM properties. If the binding pocket does not permit substitution at this position, perhaps the *R,R* enantiomer would be able to fit upside down where the Bromine occupies the same position as ligand (+)-282. The electrostatic potential maps of (+)-163-2, (+)-282 and (-)-66 are depicted in **Figure 3.12**. (-)-66 is shown with the 4-Br-Ph group on top to mimic the orientation of (+)-282, which

indeed resembles this structure. Placing the aromatic ring of the indoline in the same position renders the 4-Br-Ph group twisted (almost perpendicular) when compared to (+)-282. This could prevent binding in this orientation. Interestingly, both enantiomers demonstrated substantial potentiation of 155 ± 11% for (-)-66 and 98 ± 8.3% for (+)-65 (**Figure 3.11**). These results indicate that not only is the *para*-position of Ph at C(8a) permissive to Br, but it is probable that the *R,R* enantiomer is able to fit in the upside down orientation. All mean potentiation values are reported in **Table 3.8**.

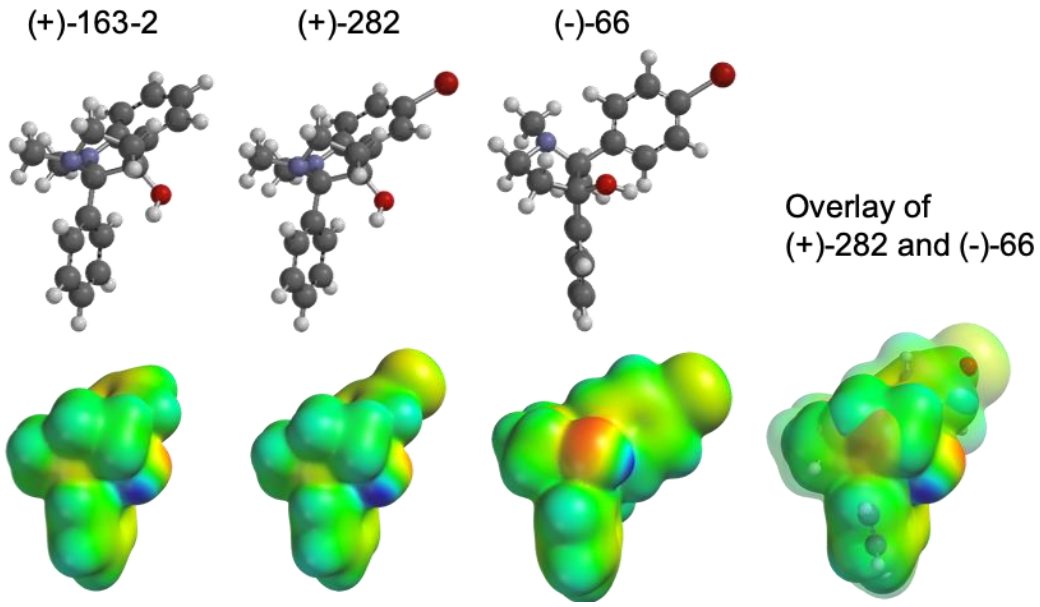

Figure 3.12 | Electrostatic potential surfaces of selected derivatives. Geometry optimization was performed using HF 6-31G**. Color scale red to blue ranges from -50 kcal/mol to +50 kcal/mol.

Table 3.8 | Mean values of GABA EC_{10} modulation of the α1β2γ2 subtype by all derivatives.

Ligand	$R_{C(3a)}$	$R_{N(1)}$	$R_{C(5)}$	$R_{C(8a)}$	Relative modulation of GABA EC_{10} (%)	N	$\lvert I_{max} \rvert$ (μA)
163 racemic	OH	Me	H	Ph	62 ± 6.1	18	0.8 – 4.4
(-)-163-1	OH	Me	H	Ph	11 ± 2.2	8	2.1 – 3.6
(+)-163-2	OH	Me	H	Ph	125 ± 15	12	0.5 – 6.0
(-)-20	OH	NH	H	Ph	1.8 ± 1.7	14	0.8 – 5.2
(+)-21	OH	NH	H	Ph	41 ± 3	15	0.2 – 11.2

(-)-264-2	OH	Cbz	H	Ph	25	±	4.1	14	0.06 – 7.8
(+)-264-1	OH	Cbz	H	Ph	9.6	±	5.2	14	0.4 – 9.7
(-)-226	OMe	Me	H	Ph	24	±	2.2	6	0.43-1.18
(+)-227	OMe	Me	H	Ph	21	±	3.0	5	0.54-0.84
(-)-22	F	Me	H	Ph	27	±	3	11	0.7 – 6.5
(+)-23	F	Me	H	Ph	100	±	11	16	0.9 – 11.4
(-)-284	OH	Me	OMe	Ph	15	±	4.6	13	0.9 – 4.2
(+)-85	OH	Me	OMe	Ph	17	±	3.2	13	0.7 – 11.0
(-)-87	OH	Me	Morpholine	Ph	21	±	2.9	11	1.2 – 4.9
(+)-286	OH	Me	Morpholine	Ph	-4.8	±	1.8	12	0.9 – 8.6
(-)-58	OH	Me	CF_3	Ph	1.3	±	1.2	16	0.6 – 6.3
(+)-59	OH	Me	CF_3	Ph	108	±	9.5	16	0.9 – 8.3
(-)-281	OH	Me	Br	Ph	31	±	3.0	10	0.5 – 4.3
(+)-282	OH	Me	Br	Ph	213	±	21	12	2.3 – 19.2
(-)-51	OH	Me	I	Ph	231	±	24	16	2.2 – 6.2
(+)-50	OH	Me	I	Ph	35	±	5.6	15	0.5 – 2.7
159 racemic	OH	Me	H	4-OMe-Ph	-2.9*	±	1.6	20	0.5 – 7.7
(-)-66	OH	Me	H	4-Br-Ph	155	±	11	13	0.63 – 6.8
(+)-65	OH	Me	H	4-Br-Ph	98	±	8.3	15	1.1 – 5.6

* relative modulation of GABA EC_{50}.

3.4 Conclusions and future directions

In this study, we described the functional evaluation of a novel series of physostigmine derivatives at the α1β2γ2 $GABA_A$ receptor. First, we characterized our lead positive allosteric modulator 163, which has an EC_{50} of 112 μM and causes a 12.8 μM shift in GABA EC_{50}. Second, we performed mutagenesis studies to elucidate the binding site of this PAM. We found that the TMD triple mutant α1(S297I)β2(N289I)γ2(S319I) lost complete sensitivity to

the racemic mixture of 163, while other ECD mutants displayed no change. This suggests that the binding site is located in the TMD at the top of TM2.

Next, we explored substitution of 163 at various positions to achieve increased efficacy. Most ligands showed only PAM effects for the *S,S* enantiomer. The most potent PAMs were (+)-282 and (-)-51, which both contain a halogen at the C(5) position. Substitutions at the pyrrolidine generally resulted in loss of potency. One ligand demonstrated increased potentiation efficacy relative to the parent ligand 163 for both enantiomers. We suspect that the generally inactive enantiomer in this case might be able to fit into the binding pocket in an upside-down orientation due to its 4-Br-Ph substitution at C(8a).

Future studies could include additional mutagenesis studies to determine other residues involved in binding. Additional characterization of (-)-51 ($R_{C(5)}$= I) would be valuable to determine its EC_{50}, as well as potentiation studies using other $GABA_A$ receptor subtypes and Cys-loop receptors to determine its selectivity profile.

3.5 Experimental procedures

Molecular biology

Circular DNA of human $GABA_A$ receptor α1, β2s and γ2s subunits were in a pGEMhe plasmid (wild type expression). For both β2s and γ2s only the short isoforms were used, however for convenience we refer to the subunits as β2 and γ2. Site-directed mutagenesis was performed using the QuickChange protocol (Agilent Stratagene). cDNA in pGEMhe was linearized with restriction enzyme NheI (for α1 and γ2 subunits), and Sph1 (for the β2 subunit) (New England Biolabs). Purified linear DNA (Qiaquick PCR Purification kit, Qiagen) was then transcribed *in vitro* using the T7 mMessage Machine kit (Ambion). The resulting mRNA was isolated using the RNeasy RNA purification kit (Qiagen) and quantified by UV-vis

spectroscopy (NanoDrop 2000, ThermoFisher Scientific). cDNA and mRNA were stored at -20˚C and -80˚C respectively.

Oocyte preparation and mRNA injection

Xenopus laevis oocytes (stage V-VI) were harvested and injected with mRNA according to previously described protocols.[45] Oocytes were injected with 50-75 nl mRNA in nuclease-free water. Post injection, oocytes were incubated at 18˚C in ND96 solution (96 mM NaCl, 2mM KCl, 1mM $MgCl_2$, 1.8 mM $CaCl_2$, 5 mM HEPES, pH 7.5) supplemented with 0.05 mg/ml gentamycin (Sigma), 2.5 mM sodium pyruvate (Acros Organics), and 0.67 mM theophylline (Sigma).

For expression of wild-type α1β2γ2 receptors, α1, β2, and γ2 mRNA were mixed in 2:2:1 ratio by mass. For expression of wild-type α1β2 receptors, α1 and β2 mRNA were mixed in 1:1 ratio by mass. Each cell was injected with 5 ng or 15 ng mRNA in a single injection for the α1β2γ2 and α1β2, respectively. Oocytes were then incubated for 24 h before recording. Proper injection ratios for mutant receptors were determined after analysis of the dose-response curve and optimized when necessary. All ECD mutant receptors were injected with a 2:2:1 ratio, as well as the triple TMD mutant. Injection ratios for the TMD mutants were as follows: αMβγ and αMβMγ: 2:2:1; αβMγ: 2:10:1; αβγM: 1:1:8; αMβ, αβM and αMβM: 1:1.

Electrophysiology

All electrophysiological recordings were performed using the OpusXpress 6000A (Axon Instruments) in two-electrode voltage clamp mode at ambient temperature (20-25˚C). Oocytes were impaled with borosilicate glass pipettes filled with 3 M KCl (R = 0.3-3.0 MΩ) and clamped at a holding potential of -60 mV. ND96 solution with Ca^{2+} was used as running buffer. GABA and test-ligand solutions were prepared in ND96 with Ca^{2+} and 1 mL was

applied over 15 s followed by a 5 min washout with buffer at a rate of 3 mL min^{-1} (chamber volume, 500 μL). Data for each condition were obtained from at least two different batches of oocytes. Data were sampled at 50 Hz.

For potentiation experiments an adapted protocol previously described by Marotta 2015 was used.[30] The protocol is as follows: three identical GABA doses were applied, followed by a dose of the test-ligand at 40 μM. After a 30 s incubation period, a test dose was applied containing both GABA and the test-ligand. Finally, two doses of GABA were applied. The first test dose evaluates agonism properties, the second dose tests for modulation of the GABA response, which can be potentiating or inhibiting. The first three GABA doses aim to establish a baseline of the GABA response at that concentration, and the purpose of the last two GABA doses is to verify proper functioning of the receptor post modulation and control for independent rise in current amplitude. Dose-response measurements were performed using a series of ~2-fold concentration steps, spanning multiple orders of magnitude, for a total of 8-24 doses.

Two-electrode voltage-clamp traces were processed in Clampfit 10.3 (Axon Instruments). Raw traces were filtered using a low pass Gaussian filter at 5 Hz, followed by a subtraction of the average baseline current preceding ligand application. For potentiation experiments the current responses from the five GABA doses were averaged (GABA only) and subtracting this from the response of the co-application dose (GABA + test-ligand) gave the calculated change in response. Multiplying this value with 100% rendered the relative modulation (inhibition/potentiation) of the GABA response by the test-ligand. Relative modulation is reported as the mean ± standard error of the mean (SEM). For the GABA concentration either the EC_{50} or EC_{10} was used as specified in the results section. For dose-response experiments, normalized peak currents were averaged and fit to the Hill equation,

I_{norm} = 1/(1 + (EC_{50}/[agonist]^{nH}) in Prism 8 (GraphPad Software, Inc.), where I_{norm} is the normalized peak current at a given agonist concentration, EC_{50} is the agonist concentration that elicits a half-maximum response, and n_H is the Hill coefficient. Peak currents were normalized to the maximum current observed for that cell. Unless otherwise stated, EC_{50} and n_H data are shown as mean ± standard error of the mean (SEM). Geometry calculations were performed in Spartan 14 v1.1.9.

Chemical synthesis and characterization

Syntheses of the PAMs were performed by members of the Reisman group at Caltech. Compounds 163 and 159 were synthesized by Katie Chan, all other derivatives were synthesized by Dr. Justin Su. X-ray crystallography and analysis of the resulting data were performed by Dr. Julie Hofstra.

3.6 References

(1) Atack, J. R. GABAA Receptor Subtype-Selective Modulators. I. A2/A3-Selective Agonists as Non-Sedating Anxiolytics. *Curr. Top. Med. Chem.* **2011**, *11* (9), 1176–1202.

(2) Atack, J. R. GABAA Receptor Subtype-Selective Modulators. II. α5-Selective Inverse Agonists for Cognition Enhancement http://www.eurekaselect.com/87840/article (accessed May 8, 2019).

(3) Rudolph, U.; Möhler, H. GABAA Receptor Subtypes: Therapeutic Potential in Down Syndrome, Affective Disorders, Schizophrenia, and Autism. *Annu. Rev. Pharmacol. Toxicol.* **2014**, *54*, 483–507. https://doi.org/10.1146/annurev-pharmtox-011613-135947.

(4) Braat, S.; Kooy, R. The GABAA Receptor as a Therapeutic Target for Neurodevelopmental Disorders. *Neuron* **2015**, *86* (5), 1119–1130. https://doi.org/10.1016/j.neuron.2015.03.042.

(5) Stephens, D. N.; King, S. L.; Lambert, J. J.; Belelli, D.; Duka, T. GABAA Receptor Subtype Involvement in Addictive Behaviour. *Genes Brain Behav.* **2017**, *16* (1), 149–184. https://doi.org/10.1111/gbb.12321.

(6) Ebert, B.; Wafford, K. A.; Deacon, S. Treating Insomnia: Current and Investigational Pharmacological Approaches. *Pharmacol. Ther.* **2006**, *112* (3), 612–629. https://doi.org/10.1016/j.pharmthera.2005.04.014.

(7) Olsen, R. W.; Sieghart, W. International Union of Pharmacology. LXX. Subtypes of Gamma-Aminobutyric Acid(A) Receptors: Classification on the Basis of Subunit Composition, Pharmacology, and Function. Update. *Pharmacol Rev* **2008**, *60* (3), 243–260. https://doi.org/10.1124/pr.108.00505.

(8) Brickley, S. G.; Mody, I. Extrasynaptic GABA(A) Receptors: Their Function in the CNS and Implications for Disease. *Neuron* **2012**, *73* (1), 23–34. https://doi.org/10.1016/j.neuron.2011.12.012.

(9) Farrant, M.; Nusser, Z. Variations on an Inhibitory Theme: Phasic and Tonic Activation of GABA(A) Receptors. *Nat Rev Neurosci* **2005**, *6* (3), 215–229. https://doi.org/10.1038/nrn1625.

(10) Miller, P. S.; Aricescu, A. Crystal Structure of a Human GABAA Receptor. *Nature* **2014**, *512* (7514), 270–275. https://doi.org/10.1038/nature13293.
(11) Chua, H. C.; Chebib, M. GABAA Receptors and the Diversity in Their Structure and Pharmacology. *Adv Pharmacol* **2017**, *79*, 1–34. https://doi.org/10.1016/bs.apha.2017.03.003.
(12) Zhu, S.; Noviello, C. M.; Teng, J.; Walsh, R. M.; Kim, J. J.; Hibbs, R. E. Structure of a Human Synaptic GABAA Receptor. *Nature* **2018**, *559* (7712), 67–72. https://doi.org/10.1038/s41586-018-0255-3.
(13) Miller, P. S.; Smart, T. G. Binding, Activation and Modulation of Cys-Loop Receptors. *Trends Pharmacol Sci* **2010**, *31* (4), 161–174. https://doi.org/10.1016/j.tips.2009.12.005.
(14) Sieghart, W. Allosteric Modulation of GABAA Receptors via Multiple Drug-Binding Sites. *Adv Pharmacol* **2015**, *72*, 53–96. https://doi.org/10.1016/bs.apha.2014.10.002.
(15) Olsen, R. W. Allosteric Ligands and Their Binding Sites Define γ-Aminobutyric Acid (GABA) Type A Receptor Subtypes. *Adv Pharmacol* **2015**, *73*, 167–202. https://doi.org/10.1016/bs.apha.2014.11.005.
(16) Gupta, S. Recent Advances in Benzodiazepine Receptor (BZR) Binding Studies. *Prog Drug Res* **1995**, *45*, 67–106.
(17) Yokoyama, N.; Ritter, B.; Neubert, A. 2-Arylpyrazolo[4,3-c]Quinolin-3-Ones: Novel Agonist, Partial Agonist, and Antagonist of Benzodiazepines. *J Med Chem* **1982**, *25* (4), 337–339.
(18) Bennett, D. Pharmacology of the Pyrazolo-Type Compounds: Agonist, Antagonist and Inverse Agonist Actions. *Physiol Behav* **1987**, *41* (3), 241–245.
(19) Blackaby, W. P.; Atack, J. R.; Bromidge, F.; Lewis, R.; Russell, M.; Smith, A.; Wafford, K.; M, M., Ruth; Street, L. J.; Castro, J. L. Pyrazolopyridinones as Functionally Selective GABAA Ligands. **2005**, *15* (22), 4998–5002. https://doi.org/10.1016/j.bmcl.2005.08.006.
(20) Simeone, X.; Siebert, D. C. B. C.; Bampali, K.; Varagic, Z.; Treven, M.; Rehman, S.; Pyszkowski, J.; Holzinger, R.; Steudle, F.; Scholze, P.; et al. Molecular Tools for GABAA Receptors: High Affinity Ligands for B1-Containing Subtypes. *Sci Rep* **2017**, *7* (1), 5674. https://doi.org/10.1038/s41598-017-05757-4.
(21) Treven, M.; Siebert, D. C. B. C.; Holzinger, R.; Bampali, K.; Fabjan, J.; Varagic, Z.; Wimmer, L.; Steudle, F.; Scholze, P.; Schnürch, M.; et al. Towards Functional Selectivity for A6β3γ2 GABAA Receptors: A Series of Novel Pyrazoloquinolinones. *Br J Pharmacol* **2017**. https://doi.org/10.1111/bph.14087.
(22) Bolognesi, M.; Andrisano, V.; Bartolini, M.; Minarini, A.; Rosini, M.; Tumiatti, V.; Melchiorre, C. Hexahydrochromeno[4,3-b]Pyrrole Derivatives as Acetylcholinesterase Inhibitors. *J Med Chem* **2001**, *44* (1), 105–109.
(23) Jacoby, H. I. Gastric Emptying. In *Reference Module in Biomedical Sciences*; Elsevier, 2017. https://doi.org/10.1016/B978-0-12-801238-3.64921-8.
(24) Shiroma, L. O.; Costa, V. P. 56 - Parasympathomimetics. In *Glaucoma (Second Edition)*; Shaarawy, T. M., Sherwood, M. B., Hitchings, R. A., Crowston, J. G., Eds.; W.B. Saunders, 2015; pp 577–582. https://doi.org/10.1016/B978-0-7020-5193-7.00056-X.
(25) Militante, J.; Ma, B.-W. W.; Akk, G.; Steinbach, J. H. Activation and Block of the Adult Muscle-Type Nicotinic Receptor by Physostigmine: Single-Channel Studies. *Mol Pharmacol* **2008**, *74* (3), 764–776. https://doi.org/10.1124/mol.108.047134.
(26) Hamouda, A. K.; Kimm, T.; Cohen, J. B. Physostigmine and Galanthamine Bind in the Presence of Agonist at the Canonical and Noncanonical Subunit Interfaces of a Nicotinic Acetylcholine Receptor. *J Neurosci* **2013**, *33* (2), 485–494. https://doi.org/10.1523/JNEUROSCI.3483-12.2013.
(27) Jin, X.; M, M., Megan; Germann, A. L.; Akk, G.; Steinbach, J. H. The E Loop of the Transmitter Binding Site Is a Key Determinant of the Modulatory Effects of Physostigmine on Neuronal Nicotinic A4β2 Receptors. *Mol Pharmacol* **2017**, *91* (2), 100–109. https://doi.org/10.1124/mol.116.106484.
(28) Jin, X.; M, M., Megan; Germann, A. L.; Akk, G.; Steinbach, J. H. The E Loop of the Transmitter Binding Site Is a Key Determinant of the Modulatory Effects of Physostigmine

on Neuronal Nicotinic A4β2 Receptors. *Mol Pharmacol* **2017**, *91* (2), 100–109. https://doi.org/10.1124/mol.116.106484.

(29) Daeffler, K. N.-M. Functional Evaluation of Noncovalent Interactions in Neuroreceptors and Progress Toward the Expansion of Unnatural Amino Acid Methodology. phd, California Institute of Technology, 2014. https://doi.org/Daeffler, Kristina Nicole-McCleary (2014) Functional Evaluation of Noncovalent Interactions in Neuroreceptors and Progress Toward the Expansion of Unnatural Amino Acid Methodology. Dissertation (Ph.D.), California Institute of Technology. doi:10.7907/ST7S-DB65. http://resolver.caltech.edu/CaltechTHESIS:05042014-135648744 <http://resolver.caltech.edu/CaltechTHESIS:05042014-135648744>.

(30) Marotta, C. B. Structure-Function Studies of Nicotinic Acetylcholine Receptors Using Selective Agonists and Positive Allosteric Modulators. phd, California Institute of Technology, 2015. https://doi.org/Marotta, Christopher Bruno (2015) Structure-Function Studies of Nicotinic Acetylcholine Receptors Using Selective Agonists and Positive Allosteric Modulators. Dissertation (Ph.D.), California Institute of Technology. doi:10.7907/Z9V122Q9. http://resolver.caltech.edu/CaltechTHESIS:05292015-144036736 <http://resolver.caltech.edu/CaltechTHESIS:05292015-144036736>.

(31) Baburin, I.; Khom, S.; Timin, E.; Hohaus, A.; Sieghart, W.; Hering, S. Estimating the Efficiency of Benzodiazepines on GABAA Receptors Comprising Γ1 or Γ2 Subunits. *Brit J Pharmacol* **2008**, *155* (3), 424–433. https://doi.org/10.1038/bjp.2008.271.

(32) Hanson, S. M.; Czajkowski, C. Structural Mechanisms Underlying Benzodiazepine Modulation of the GABA(A) Receptor. *J Neurosci* **2008**, *28* (13), 3490–3499. https://doi.org/10.1523/JNEUROSCI.5727-07.2008.

(33) Wieland, H.; Lüddens, H.; Seeburg, P. A Single Histidine in GABAA Receptors Is Essential for Benzodiazepine Agonist Binding. *J Biol Chem* **1992**, *267* (3), 1426–1429.

(34) Ramerstorfer, J.; Furtmüller, R.; Isabella, S.-J.; Varagic, Z.; Sieghart, W.; Ernst, M. The GABAA Receptor A+β− Interface: A Novel Target for Subtype Selective Drugs. *J Neurosci* **2011**, *31* (3), 870–877. https://doi.org/10.1523/JNEUROSCI.5012-10.2011.

(35) Maldifassi, M. C.; Baur, R.; Sigel, E. Molecular Mode of Action of CGS 9895 at A1 B2 Γ2 GABAA Receptors. *J Neurochem* **2016**, *138* (5), 722–730. https://doi.org/10.1111/jnc.13711.

(36) Baur, R.; Tan, K. R.; Lüscher, B. P.; Gonthier, A.; Goeldner, M.; Sigel, E. Covalent Modification of GABAA Receptor Isoforms by a Diazepam Analogue Provides Evidence for a Novel Benzodiazepine Binding Site That Prevents Modulation by These Drugs. *J. Neurochem.* **2008**, *106* (6), 2353–2363. https://doi.org/10.1111/j.1471-4159.2008.05574.x.

(37) Olsen, R. W. Analysis of γ-Aminobutyric Acid (GABA) Type A Receptor Subtypes Using Isosteric and Allosteric Ligands. *Neurochem Res* **2014**, *39* (10), 1924–1941. https://doi.org/10.1007/s11064-014-1382-3.

(38) Laverty, D.; Thomas, P.; Field, M.; Andersen, O. J.; Gold, M. G.; Biggin, P. C.; Gielen, M.; Smart, T. G. Crystal Structures of a GABAA-Receptor Chimera Reveal New Endogenous Neurosteroid-Binding Sites. *Nat Struct Mol Biol.* **2017**, *24* (11), 977. https://doi.org/10.1038/nsmb.3477.

(39) Masiulis, S.; Desai, R.; Uchański, T.; Serna Martin, I.; Laverty, D.; Karia, D.; Malinauskas, T.; Zivanov, J.; Pardon, E.; Kotecha, A.; et al. GABAA Receptor Signalling Mechanisms Revealed by Structural Pharmacology. *Nature* **2019**, *565* (7740), 454–459. https://doi.org/10.1038/s41586-018-0832-5.

(40) Buhr, A.; Schaerer, M.; Baur, R.; Sigel, E. Residues at Positions 206 and 209 of the Alpha1 Subunit of Gamma-Aminobutyric AcidA Receptors Influence Affinities for Benzodiazepine Binding Site Ligands. *Mol Pharmacol* **1997**, *52* (4), 676–682.

(41) Buhr, A.; Sigel, E. A Point Mutation in the Gamma2 Subunit of Gamma-Aminobutyric Acid Type A Receptors Results in Altered Benzodiazepine Binding Site Specificity. *Proc Natl Acad Sci USA* **1997**, *94* (16), 8824–8829.

(42) Sigel, E.; Ernst, M. The Benzodiazepine Binding Sites of GABAA Receptors. *Trends Pharmacol Sci* **2018**, *39* (7), 659–671. https://doi.org/10.1016/j.tips.2018.03.006.
(43) Walters, R.; Hadley, S.; Morris, K.; Amin, J. Benzodiazepines Act on GABAA Receptors via Two Distinct and Separable Mechanisms. *Nat Neurosci* **2000**, *3* (12), 1274–1281. https://doi.org/10.1038/81800.
(44) Wingrove, P. B.; Wafford, K. A.; Bain, C.; Whiting, P. J. The Modulatory Action of Loreclezole at the Gamma-Aminobutyric Acid Type A Receptor Is Determined by a Single Amino Acid in the Beta 2 and Beta 3 Subunit. **1994**, *91* (10), 4569–4573.
(45) Nowak, M.; Gallivan, J.; Silverman, S.; Labarca, C.; Dougherty, D.; Lester, H. In Vivo Incorporation of Unnatural Amino Acids into Ion Channels in Xenopus Oocyte Expression System. *Methods Enzymol.* **1998**, *293*, 529.

Chapter 4

Study of Light-Induced Modulation of Voltage-Gated Sodium Channels using Ruthenium Diimine Photoswitches*

4.1 Abstract

Retinal degenerative diseases such as age-related macular degeneration (AMD) and retinitis pigmentosa (RP) result in the loss of photoreceptors in the retina, a major cause of blindness for which there are very few treatments and no cure. Finding a way to render these cells sensitive to light could potentially (partially) restore vision. Previous studies have shown that, upon irradiation with 488 nm light and in the presence of a reductant or oxidant, a Ruthenium bipyridine complex with a C17-tail (RubpyC17) can alter the membrane potential in both non-excitable and excitable cells. This observation suggests the viability of a molecularly driven artificial retina using RubpyC17 as a so-called photoswitch. The relationship between ruthenium-mediated electron transfer and the light-induced membrane depolarization process, potentially via channel modulation, is still poorly understood. To determine functional interactions between a series of Rubpy-complexes and voltage-gated ion channels, we have expressed these proteins in *Xenopus laevis* oocytes and performed two-electrode voltage clamp to evaluate channel function. We found RubpyC17 to cause an increase in the activation potential for both voltage-gated sodium and potassium channels. From the derivatives tested, RuOleic acid demonstrated the most substantial effect: a right shift in $V_{0.5}$ in both types of voltage-gated ion channels as well as a decrease in peak current for potassium channels. This decrease in peak current can be temporarily attenuated by irradiation of 455 nm light.

* This work was done in collaboration with the labs of Dr. Mark Humayun (USC), Prof. Robert Chow (USC), Prof. Harry Gray (Caltech), and Prof. Robert H. Grubbs (Caltech).

4.2 Introduction

Retinal degenerative diseases such as age-related macular degeneration (AMD) and retinitis pigmentosa (RP) result in the loss of photoreceptors in the retina, a major cause of blindness for which there are very few treatments and no cure.[1] Despite the loss of photoreceptors, a significant number of inner retinal ganglion cells (RGC) remain intact and are still able to transmit visual information to the brain. The only currently approved vision restoration treatment entails an implanted, prosthetic retinal 'chip' that electrically stimulates the remaining retinal neurons after loss of photoreceptors. In this way light-induced neural signaling to the visual cortex is (partially) restored. Alternative strategies have been proposed, including optogenetic or optopharmacological tools that would enable direct optical stimulation of the remaining neurons. However, the search for more elegant and less invasive methods continues. The main contributor for initiating an action potential in RGCs is the voltage-gated sodium channel isoform 1.6 (Na_V 1.6).[2] If these channels could be rendered light sensitive by introduction of an appropriate redox-active chemical species, visual function in otherwise degenerated retinas could potentially be (partially) restored. Recently, an azobenzene-based photoswitch has been reported to elicit photosensitivity in mice with degenerated retinal photoreceptors. However, the mechanism of photosensitization is not completely understood, although the authors found that it binds to a wide range of ion channels, and was not selective to neurons.[3]

Voltage-gated sodium channels (VGSCs or Na_v) are a family of polytopic transmembrane proteins that are activated by depolarization of the cell membrane. In excitable cells, opening of these channels initiates an action potential, making them crucial for electrical signaling between cells.[4–6] VGSCs are part of the larger protein class of ion channels called voltage-gated ion channels (VGICs) that, among others, includes voltage-gated potassium

channels (VGKCs). The voltage-gated sodium channel family consists of several isoforms that are associated with various diseases such as epilepsy, cardiac arrhythmia, chronic pain, and insensitivity to pain.[7,8] In 1952, Hodgkin and Huxley recorded the first currents attributed to Na_V activity.[9] Since then, various biophysical studies have been performed using a number of animal toxins that target this specific class of VGIC. However, much remains unknown about the mechanistic basis of channel function, and in particular voltage gating. New ways to probe and control channel function will be valuable to gain more insight into and develop treatments for dysfunction of this complex system.

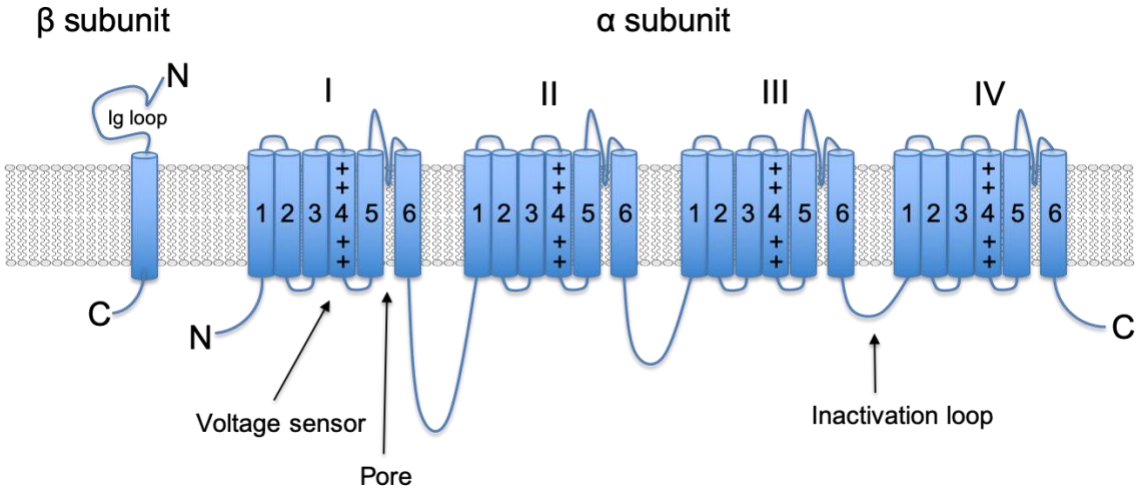

Figure 4.1 | Schematic representation of a VGSC. Structural topology of the eukaryotic Na_v channel α- and β subunits. The center peptide chain is a generalized depiction of an α subunit containing four homologous domains, each comprising six helical segments referred to as S1-S6. The β subunits all contain a characteristic V-shaped Ig loop and one transmembrane helix (except for β1B). β1 and β3 are structurally similar and contain an intracellular phosphorylation site, whereas β2 and β4 do not.

A eukaryotic VGSC is a large complex consisting of one single α-subunit (260 kDa) and one or more smaller, auxiliary β-subunits (33-36 kDa).[11] Nine α-subunits (Na_v 1.1-1.9) and three β-subunits (β1-3) have been characterized so far.[11] Although the α-subunit alone contains the sodium-conducting pore and the gating domain, it requires heterodimerization

with one or more β subunits to reconstitute the channel's full native properties. The β-subunits modulate the kinetics and voltage-dependence of channel gating, including inactivation.[8] The α-subunit contains four homologous domains (D) that assemble in a pseudotetrameric structure (**Figure 4.1**).[12] Each domain consists of six helical segments (S): S1-S4 constitute the voltage sensor domain (VSD, total of four), and the four S5-S6 make up one sodium-conducting pore (**Figure 4.1**). The pore and four VSDs are physically separated by phospholipids of the cell membrane and have been shown to be able to function independently in other studies.[13,14] Both N- and C-termini are located on the intracellular side of the membrane. Furthermore, the connecting loop between DIII and DIV, containing a hydrophobic IFM motif, has been shown to play a crucial part in the inactivation of the channel.[4,15]

Based on several crystallographic and mutagenesis studies, four arginines in S4 (the voltage sensor) interact with negatively charged residues within the VSD.[16–20] This led to the hypothesis that negative charges on the outer membrane leaflet could stabilize S4 in the upward position, and thus the activated conformation of the VSD. Several studies have investigated the effects of different membrane lipid compositions on potassium channel function and found that for channels reconstituted in neutral lipid membranes the voltage sensor became nonfunctional.[21–24] Additionally, polyunsaturated fatty acids (PUFAs) have been found to interact with a variety of membrane proteins, including VGICs, either through direct allosteric modulation or by alteration of the physical properties of the surrounding membrane.[23,25–30] Docosahexaenoic acid (DHA), an ω-3 PUFA, has been shown to shift the half-activation potential of VGKCs to the left, and upon substitution of the negatively charged carboxylate group for positively charged amino group, to the right.[31,32] The effects were even more dramatic at higher pH, suggesting modulation of these channels could be biased by the

overall charge of the molecule. A similar study was performed by Dr. Kristina Daeffler in our group using linoleic acid (LOA), an ω-6 PUFA, who observed a similar leftward shift for Shaker IR potassium channels expressed in *Xenopus laevis* oocytes.[33]

Expanding on these previous studies, we hypothesized that a light-absorbing ruthenium bipyridine complex linked to a fatty acid could have similar effects upon irradiation. The molecule tris(bipyridine)ruthenium(II) $[Ru(bpy)_3]^{2+}$ has been extensively studied and is, by adjusting the bipyridine (bpy) ligands, greatly tunable for various biological purposes.[34] Remarkably, our collaborators showed that upon irradiation with 488-nm light and in the presence of a reductant or oxidant, a ruthenium bipyridine complex containing one C_{17}-saturated chain (RubpyC17) can alter the cell membrane potential in both excitable cells (mouse chromaffin cells) and non-excitable cells (INS, HEK293).[35] For clarity, the authors did not express specific VGICs and solely focused on membrane depolarization. The ruthenium metal center of $[Ru(bpy)_3]^{2+}$ can be excited with visible light (488 nm) (**Figure 4.2**) and the excited state can either be reduced or oxidized, resulting in a Ru(I) or Ru(III) species, respectively. Modification of the bipyridine ligands determines the reactivity of the photoexcited complex and thus enables us to tune the overall charge and reduction potential of the complex. Thus, the RubpyC17 is an excellent candidate for consideration as a photoswitch to light-control VGSCs.

In this chapter, the ultimate goal was to photochemically control the activation of the VGSCs and thus make progress towards developing a RubpyC17-based photoswitch that could be used in an artificial retina. To this end, we determined the functional effects of RubpyC17 on VGSCs and VGKCs. To evaluate changes in ion channel function we expressed these proteins in *Xenopus laevis* oocytes and performed two-electrode voltage clamp (TEVC)

electrophysiology. Additionally, we used multiple RubpyC17 derivatives to establish whether we could bias any modulatory effects.

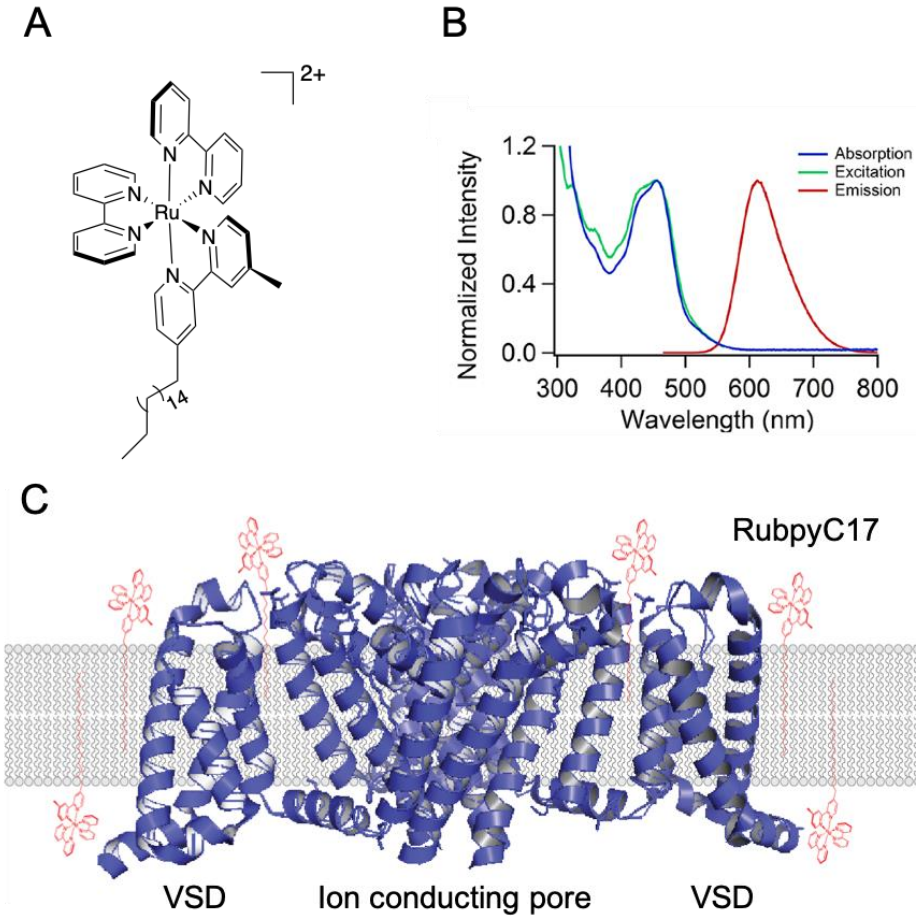

Figure 4.2 | RubpyC17. (A) The chemical structure of RubpyC17 and (B) its absorbance/emission spectrum. Adapted from Rohan *et al.*[35] (C) Depiction of experimental design. Structure of a VGSC is located in the membrane, RubpyC17 is thought to embed in the membrane through its C17 tail and create a local depolarization near the VSD of the channel or even directly modulate the VSD (PDB: 3RVY).

4.3 Results and discussion

4.3.1 Optimization of TEVC protocol for Na_v channels using the OpusXpress

The OpusXpress is a medium-throughput instrument that allows for two-electrode voltage clamp experiments on eight cells at a time. This experimental set up is therefore often used for measuring the function of ligand-gated ion channels at a fast pace.[36] Generally, such

channels reach a steady state and currents can be averaged over about 20-50-ms, which allows for accurate current recordings ranging from 0.2 μA up to 10 μA. In contrast, Na_v channels demonstrate remarkably fast activation and inactivation, all within about a 10-ms timescale.[37] This poses challenges for our group's conventional, experimental setup. Therefore, some degree of experimental optimization was first necessary.

To accurately record Na_v currents, an exceptionally fast clamp is necessary. To achieve this, several aspects of the model system had to be adjusted. 1) To minimize the capacitive transient and consequently allow a fast clamp, few channels on the membrane are desired that generate minimal amounts of current (max. ~5 μA). **Figure 4.3A** is an example of an unsuccessful voltage clamp due to high ionic currents (-38 μA). 2) The access resistance comprises the resistance of the cell membrane and the electrodes used. To minimize the access resistance, low-resistance electrodes are used (0-0.3 mΩ compared to 1-4 mΩ for ligand-gated ion channels). **Figure 4.3B** and **C** show wave forms obtained using either 1.5 mΩ or 0.1 mΩ electrodes, respectively. **Figure 4.3B** shows ringing in the wave form, which impairs accurate reading of the signal. 3) After several recordings the voltage wave forms obtained from the eight different head stages were compared and significant variability in voltage-clamp accuracy was observed. Some head stages consistently differed by 3 to 5 mV from the command voltage. For future experiments, it was then decided to use only one head stage to enhance reproducibility (1-2 mV error).

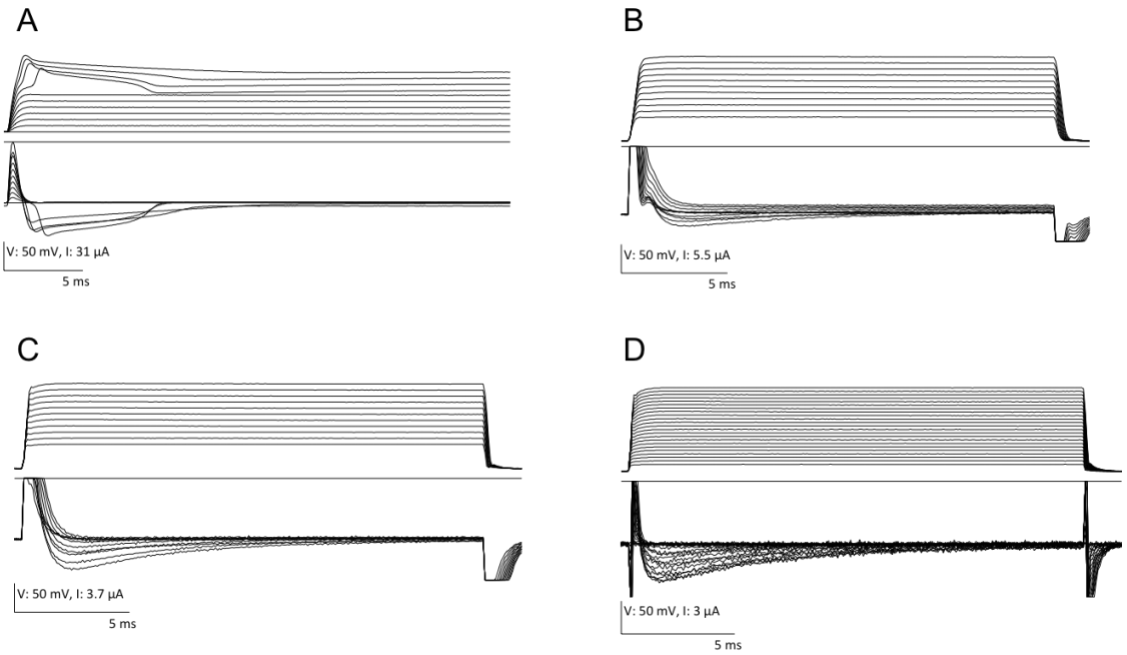

Figure 4.3 | Optimization of voltage clamping. Upper figure depicts the voltage wave form, lower figure depicts the corresponding wave form. Ionic sodium current is an inward current and therefore by convention a negative current. (A) Voltage clamp of cells showing ~33 μA. (B) Voltage clamp of cells showing ~3 μA, using 1.5-mΩ glass electrodes are used. (C) Voltage clamp of cells expressing ~3.7 μA, using 0.1-mΩ glass electrodes are used. (D) Similar expressing oocytes as in C, using 0.1 mΩ glass electrodes and P/4 method subtraction.

A commonly used method to eliminate or at least minimize the capacitive transient from the wave form is to apply a P/4 subtraction. This P/4 method involves an additional voltage jump event preceding the experiment's protocol that is identical to that of the protocol, except that the holding potential is more negative and the voltage jumps are only one quarter of the amplitude of the command voltage steps.[38,39] A schematic representation is shown in **Figure 4.4**. For example, in a desireable protocol the holding potential is -100 mV, and the membrane is depolarized with 10-mV increments up to 20 mV. The P/4 method would start at -170 mV with increments of 2.5-mV ending at -140 mV. Presumably, the channels will not open at these hyperpolarized potentials and the only current observed will be the capacitive current. The recorded capacitive currents during the P/4 procedure are then multiplied by four and subtracted from the actual wave forms, in order to correct for the

expected capacitive transients during the command voltage application. Unfortunately, when this method was applied to our experiments, the capacitive current was never completely eliminated, and in some cases disturbed the signal even more (**Figure 4.3D**). Several different settings for the P/N subtractions were applied, but none gave desirable results. We therefore decided not to employ the P/N method for future recordings on the OpusXpress.

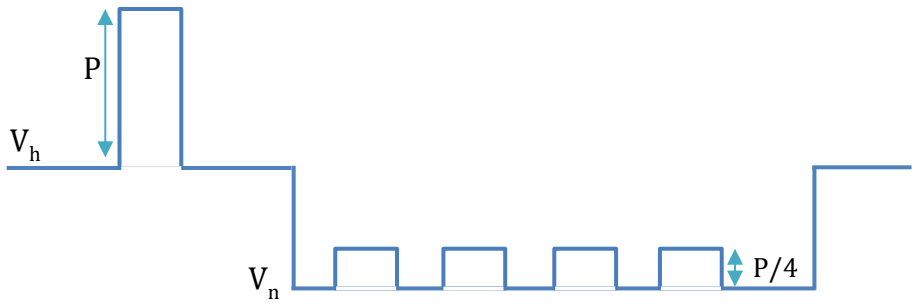

Figure 4.4 | Schematic representation of the P/4 method. V_h is the holding potential, V_n is the holding potential during P/4 procedure and P is the voltage jump/step.

4.3.2 Expression of rat Na_v1.4 α subunits and heteromers with β1

As described earlier, no previous study has applied the *OpusXpress* to record VGSC currents. To confirm that our data represent wild type currents and kinetics, the next step was to express the wild type α-subunit and the wild type α-β-heteromer and compare our findings with previous studies. Although we are most interested in modulating Na_v 1.6 channels, we decided to start by optimizing our experimental setup using Na_v 1.4 channels, as previous studies have shown that Na_v 1.4 is more readily expressed in *Xenopus leavis* oocytes. **Figure 4.5** shows typical wave forms of the Na_v1.4 α subunit alone (A) and responses from cells injected with mRNA for the α and β subunits in a 5:1 ratio (B). As we expected from previous studies, we observe a significant change in inactivation kinetics (τ = 15 ms compared to 4 ms) when the β subunit is co-expressed.

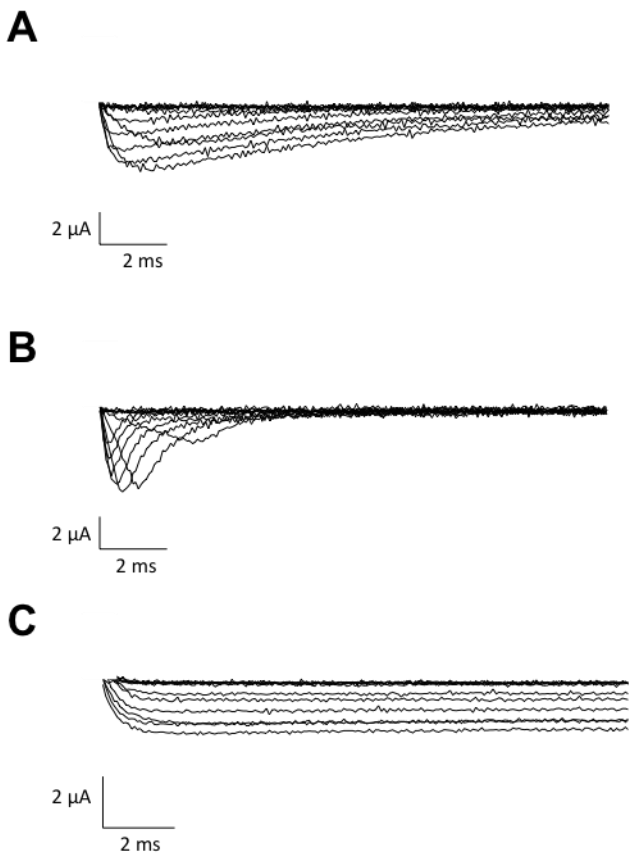

Figure 4.5 | Representative wave forms of sodium channel currents. (A) $Na_v1.4$ α subunit only, (B) $Na_v1.4$ αβ-heteromer (injected mRNA in 5:1 ratio) and (C) $Na_v1.4$IR, slow-inactivating mutant α(F1304Q).

Our goal is to photochemically control activation of the VGSCs. Therefore, we are most interested in parameters that determine activation kinetics and in particular creating a left-shift in the half-activation potential ($V_{0.5}$). A left shift indicates that the channels are activated at a lower potential than the wild type response (channels will open earlier upon depolarization). The half-activation potential ($V_{0.5}$) and the corresponding slope (*k*-factor) can be determined from a conductance versus membrane potential (G-V) plot. A typical experiment comprises depolarizing the membrane potential from -100 mV up to 20 mV and recording the resulting ionic current that is generated upon opening of the channels in response to the depolarization. Another diagnostic tool is the steady-state inactivation (SSI)

curve. This plot presents the current amplitude resulting from a test pulse at -20 mV (at which conductance should be maximal), as a function of a variable conditioning pulse given immediately before the test pulse. Effectively, this plot is a representation of what proportion of the channel population is inactivated by the prepulse. For example, if the test pulse only reveals a conductance that is 20% of the maximum conductance after a conditioning pulse at -50 mV, this means that 80% of the ion channels transitioned into the inactive state during the conditioning pulse. Changes in SSI parameters are thus a good indicator of stabilization of the activate state. A more stabilized open state will result into a right shift of the SSI. The protocols used to obtain the G-V and SSI plots are depicted in **Figure 4.6A** and **B**. For the G-V plot, the cells were subjected to step polarizations of 5-mV increments from -100 mV to 0 mV (**Figure 4.6A**). Sodium conductances were determined from peak currents and plotted against the corresponding membrane potentials (**Figure 4.6C**: α: black, α-β: blue). For the SSI plot, the cells were subjected to a test pulse at -20 mV after a conditioning pulse at varying depolarizations ranging from -100 mV to 20 mV. The normalized peak currents are plotted against the potentials of the conditioning pulses (**Figure 4.6D**; α: black, αβ: blue).

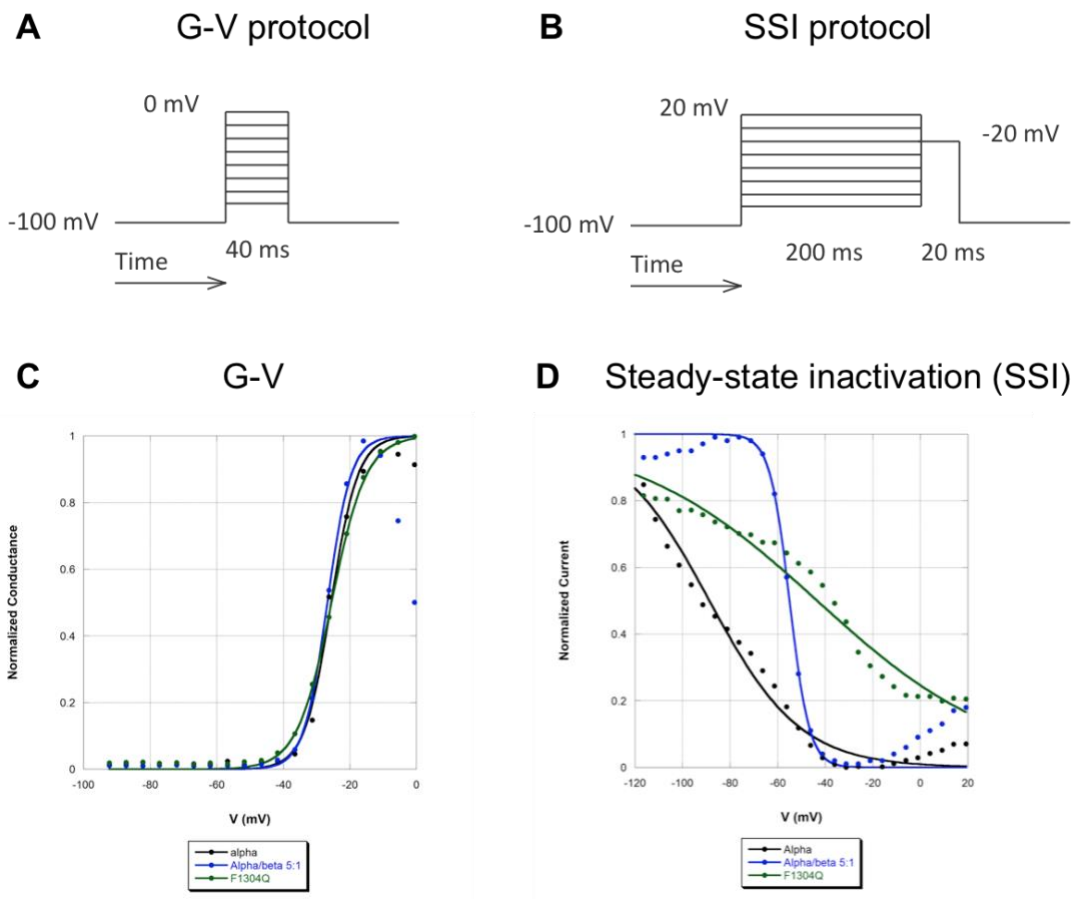

Figure 4.6 | Voltage jump protocols for G-V and SSI plots. Voltage-jump protocols for the G-V (A) and SSI plots (B). G-V (C) and steady state inactivation (D) $Na_v1.4$ α (black), $Na_v1.4$ αβ heteromer (blue) and $Na_v1.4$ IR (green). Every fit represents one cell.

The calculated parameters for both activation and inactivation of the αβ-heteromer closely resemble those described previously by Pless *et al.*[40] and Islas *et al.*[41] (**Table 1**). The α-subunit alone rendered a similar $V_{0.5}$ of activation as for αβ, but a distinct *k*-factor and severely deviating values for the inactivation kinetics. This is also clear from **Figure 4.6D**, where only the αβ-heteromer forms a good fit to the Boltzmann equation. Perhaps for the α only, the test pulse at -20 mV does not generate the maximum conductance (see G-V **Figure 4.6C**). A test pulse of -10 mV might yield better results.

Table 4.1 | Voltage dependence parameters of α and αβ channels. Values are shown as mean ± SEM. WT: wild type.

rNa$_v$1.4	**G-V**				**SSI**				
Construct	**$V_{0.5}$ (mV)**	***k*-factor**	***N***	**$\|I_{max}\|$ (μA)**	**$V_{0.5}$ (mV)**	***k*-factor**	***N***	**Ca^{2+}**
α	-28 ± 2.0	5.3 ± 0.9	14	1.0-6.0	-98 ± 3.0	14 ± 1.6	9	-
α	-23 ± 3.7	3.4 ± 1.1	4	1.0-4.0	-89 ± 5.7	19 ± 0.6	3	+
αβ1, 5:1	-32 ± 2.6	3.8 ± 0.9	3	4.0-5.0	-66 ± 2.0	4.0 ± 0.2	2	-
αβ1, 5:1	-27 ± 1.9	3.5 ± 0.3	11	0.8-5.0	-56 ± 1.3	4.5 ± 0.5	11	+
α(F1304Q)	-27 ± 3.3	6.4 ± 1.1	9	1.5-5.5	-38 ± 16.8	18 ± 9.2	5	-
α(F1304Q)	-21 ± 0.19	5.0 ± 0.2	23	0.5-7.0	-40 ± 0.9	17 ± 3.9	2	+
α(F1304Q) β1 5:1	-25 ± 3.2	4.0 ± 0.3	9	1.4-4.0	-31 ± 0.9	6.5 ± 1.4	9	+
αβ1, 5:1[40]	-26 ± 0.5	3.0 ± 0.1	-	-	-53 ± 0.5	5.7 ± 0.1	-	+
αβ1, 5:1[39]	-33 ± 0.2	3.1 ± 0.1	-	-	-62 ± 0.3	4.7 ± 0.1	-	-
α[39]	-26 ± 0.5	1.8 ± 0.3	-	-	-55 ± 0.4	5 ± 0.3	-	-

At this point the most relevant information is observed in the first part of the wave form that exhibits the activation of the channels. To achieve better reproducibility, we made one point-mutation in the IFM motif in the intracellular loop connecting D3 and D4 at position F1304 that previously has been reported in rat Na_v 1.2 (equivalent residue: F1203) to prolong inactivation significantly, but not affect voltage dependence of activation.[42] Comparison of inactivation of the mutant compared to wild type α subunit shows substantially slower inactivation (**Figure 4.5C**), but no significant change in activation dependence parameters ($V_{0.5}$ = -28.3 mV ± 2.0 for α and -27.3 mV ± 3.3 for α F1304Q in ND96$^+$ without Ca^{2+}) (**Table 4.1**). Cell health and favorably small leak currents are better maintained in Ca^{2+} supplemented buffer, leading to improvements in data reproducibility. Therefore, subsequent experiments were performed using Ca^{2+}-supplemented ND96.

4.3.3 Functional effects of RubpyC17 on Nav1.4 channels

To determine if RupbyC17 affects channel function in the absence of a sacrificial electron donor or acceptor, conductance curves were obtained from cells expressing Na_v1.4

IR in the presence of RubpyC17. The voltage clamp protocol that was used for this experiment (**Figure 4.7A**) comprises four separate voltage 'jump' events. Each event consists of membrane potential changes starting at -100 mV up to +20 mV in increments of 5 mV.

Briefly, the first event was performed in buffer without RubpyC17 and therefore serves as a reference. The second event occurred directly after application of RupbyC17 to the bath ("No light"). After 30-s of incubation, the oocyte was illuminated with a 470 nm LED for 30 s, directly followed by the third voltage-jump event while continuously illuminated for a total of 60 s ("470 nm light" in **Figure 4.7, Table 4.2**). The oocyte bath was then perfused for 1 min with- ND96 (no RubpyC17 present), followed by voltage jump event four. After an additional 4 min perfusion the fifth and last voltage jump occurred ("Post 5 min wash").

To gain insight into the concentration dependence of the effects of RubpyC17 application, this procedure was performed in the presence of a range of concentrations. Application of increasing concentrations of RubpyC17 (10 μM, 50 μM, 100 μM) resulted in a right-shifted G-V curve of 4 mV, 8 mV, and 9 mV respectively. This suggests that the channels required a greater degree of depolarization to open. Additional irradiation for 52 s with 470 nm light increased that right shift to 5 mV, 11 mV, and 14 mV for 10 μM, 50 μM, and 100 μM respectively (**Figure 4.7C**). Perfusion with buffer for 5 min resulted in a slight recovery for 50 μM, and complete recovery for 10 μM. The *k*-factors did not substantially change under these conditions. From this experiment we concluded that at concentrations upwards of 10 μM, RubpyC17 either directly or indirectly interacts with the $Na_v1.4$ IR, resulting in an increased $V_{0.5}$. Thus, the presence of RubpyC17 at concentrations over 10 μM appears to affect the channel in such a way that it favors the closed state. This effect appears to be irreversible at 100 μM on this time scale. To minimize this effect, we decided to use 5 μM of RubpyC17 for future experiments.

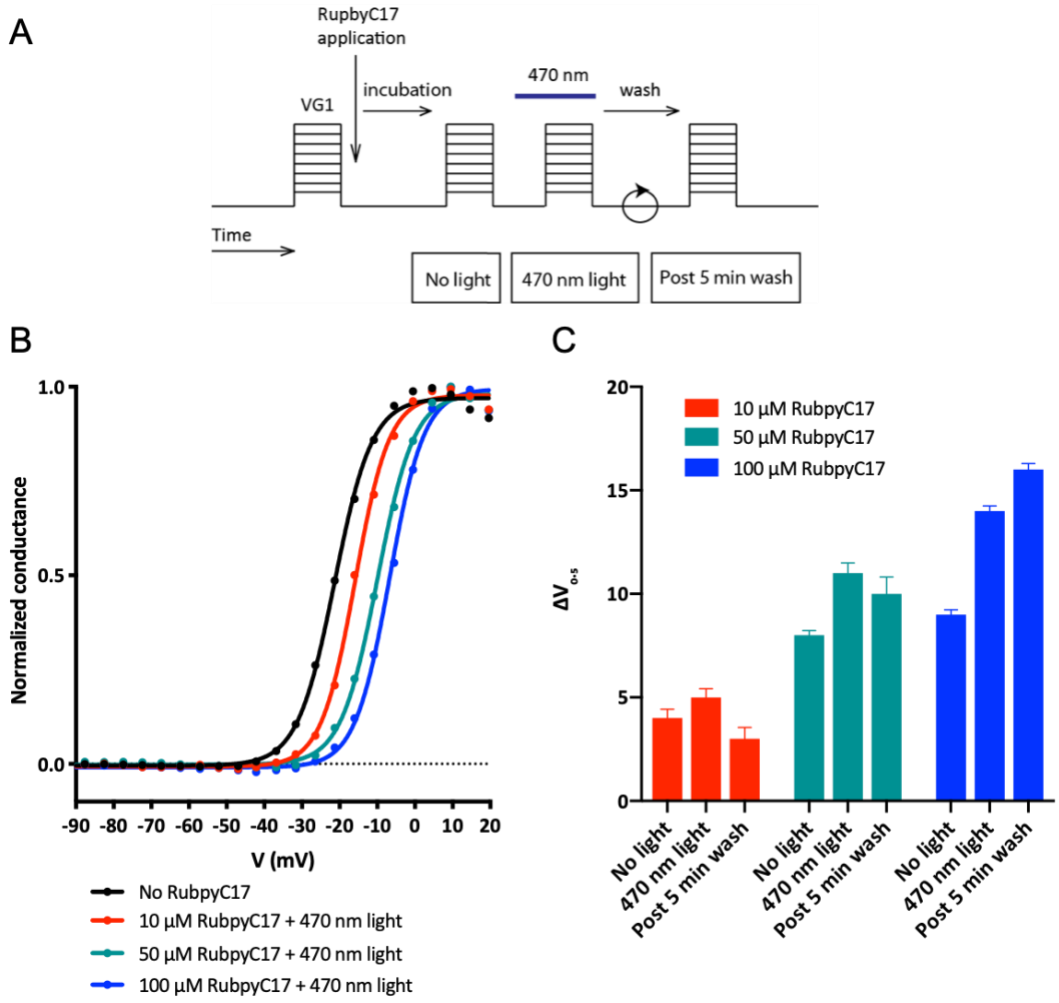

Figure 4.7 | Functional effects of RubpyC17 at various concentrations at $Na_v1.4$ IR. (A) Typical voltage-jump protocol. Rectangles with lines are symbols for voltage-jump events, VG1: voltage-jump event 1, blue bar indicates irradiation with 470 nm light, circles: perfusion of recording chamber with ND96. Boxed texted underneath voltage jump events refer to labels used in B and C for the corresponding recordings. (B) G-V plot presenting the averaged, normalized conductance of oocytes upon irradiation with 470 nm light at indicated concentrations of RubpyC17 fitted to a Boltzmann equation. (C) Shift in $V_{0.5}$ observed during different voltage jumps. A positive shift is an increase in $V_{0.5}$ that corresponds to a right shift in the G-V plot. Labels correspond to events depicted in A.

Table 4.2 | $V_{0.5}$ and slope values for Nav1.4 IR in presence of different concentrations of RubpyC17.

[RubpyC17] (µM)	Time point	$V_{0.5}$ (mV)	Slope	$\Delta V_{0.5}$	$\lvert I_{max} \rvert$ (µA)	N
0	-	-21 ± 0.19	5.0 ± 0.2	0	0.5-7.0	23
10	No light	-17 ± 0.43	4.6 ± 0.4	4	1.0-4.0	4
10	470 nm light	-16 ± 0.42	4.5 ± 0.4	5	1.0-4.0	4
10	Post 5 min wash	-18 ± 0.55	5.1 ± 0.5	3	1.0-4.0	4

50	No light	-13	±	0.23	4.9	±	0.2	8	0.6-2.5	3
50	470 nm light	-10	±	0.49	4.9	±	0.4	11	0.6-2.5	3
50	Post 5 min wash	-11	±	0.81	5.1	±	0.7	10	0.6-2.5	3
100	No light	-12	±	0.23	4.8	±	0.2	9	2.2-2.5	2
100	470 nm light	-6.7	±	0.25	4.6	±	0.2	14	2.2-2.5	2
100	Post 5 min wash	-4.6	±	0.29	4.6	±	0.2	16	2.2-2.5	2

Next, we aimed to determine if we could influence the RubpyC17-induced $V_{0.5}$ shift by adding a reductant or an oxidant. For this experiment, 2 mM ascorbic acid (AA), a reductant, was supplemented to the ND96 perfusion buffer throughout all voltage jumps. AA would serve as an electron donor to favor reduction of the Ru^{2+} complex upon light absorption to Ru^{1+} over oxidation to Ru^{3+}. This change in charge of the complex upon irradiation with light might be expected to render a leftward shift in $V_{0.5}$ resembling the effects seen previously for PUFAs.

However, upon application of 5 μM RubpyC17 and 2 mM ascorbic acid to the oocyte, a slight increase of 4 mV in $V_{0.5}$ was observed (**Figure 4.8, Table 4.3**). Upon irradiation with 470 nm light, the $V_{0.5}$ shift increased to 9 mV and a substantial increase in the slope was observed. Although changes in the slope can sometimes indicate unstable clamping, these cells were properly clamped. The right shift in $V_{0.5}$ persisted even 5 min after irradiation, which suggests an irreversible effect. It is unclear whether this effect is due to irradiation. Future experiments without irradiation could provide more insight. The presence of 2 mM AA alone resulted in a minor left shift in $V_{0.5}$ (**Table 4.3**).

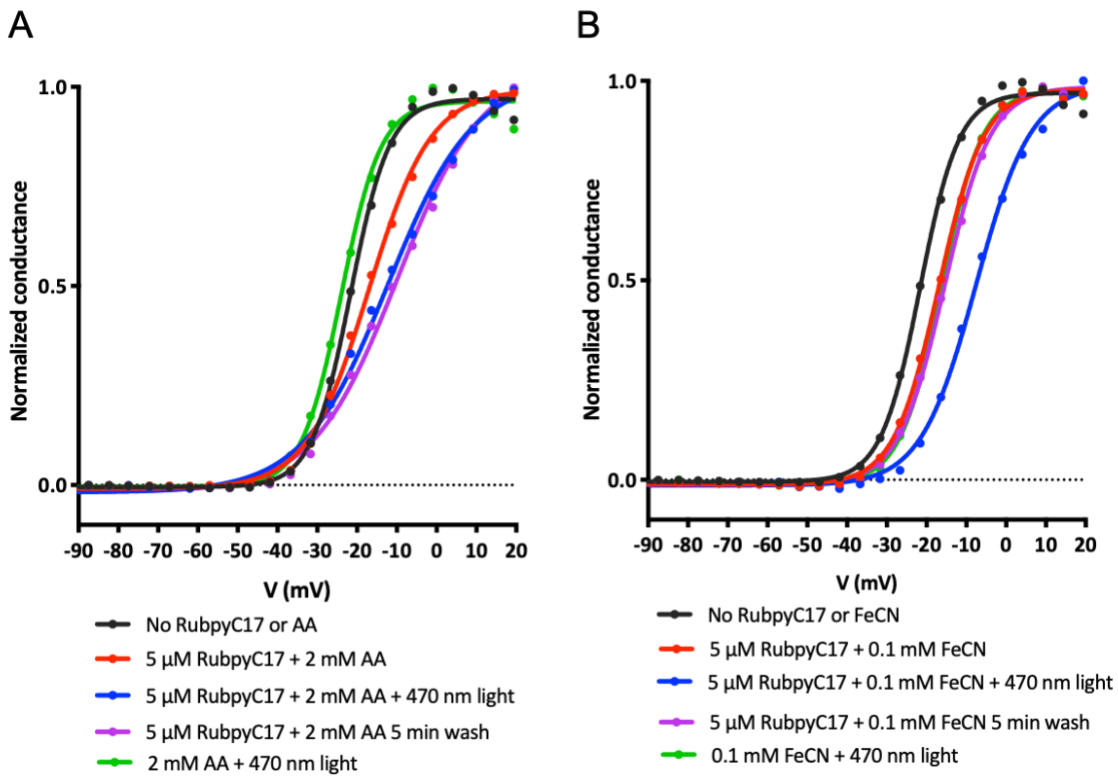

Figure 4.8 | Functional effects of RubpyC17 in presence of AA or FeCN at $Na_v1.4$ IR (A) G-V plot of $Na_v1.4$ IR channels with RubpyC17 and reductant (AA) (B) G-V plot of $Na_v1.4$ IR channels with RubpyC17 and an oxidant (ferricyanide). Duration of irradiation with 470 nm light was ~60s.

Table 4.3 | $V_{0.5}$ and slope values for Nav1.4 IR in presence of RubpyC17 and AA or FeCN.

Compound	Time point	$V_{0.5}$ (mV)	Slope	$\Delta V_{0.5}$	$\lvert I_{max} \rvert$ (µA)	N
-		-21 ± 0.19	5.0 ± 0.2	0	0.5-7.0	23
AA		-23 ± 0.32	5.1 ± 0.3	-2	1.5-5.0	3
AA	Irradiated	-24 ± 0.41	5.0 ± 0.4	-3	1.5-5.0	3
AA	Post 5 min washout	-23 ± 0.34	5.1 ± 0.3	-2	1.5-5.0	3
RubpyC17 + AA		-17 ± 0.99	7.8 ± 0.9	4	0.9-2.2	6
RubpyC17 + AA	Irradiated	-12 ± 2.1	11 ± 1.6	9	0.9-2.2	6
RubpyC17 + AA	Post 5 min washout	-9.9 ± 2.2	11 ± 1.6	11	0.9-2.2	6
FeCN		-20 ± 0.22	4.6 ± 0.19	1	0.5-3.0	5
FeCN	Irradiated	-16 ± 0.20	5.2 ± 0.2	5	0.5-3.0	5

FeCN	Post 5 min washout	-22	±	0.21	4.6	±	0.2	-1	0.5-3.0	5
RubpyC17 + FeCN		-17	±	0.24	5.7	±	0.2	4	0.5-1.5	6
RubpyC17 + FeCN	Irradiated	-7.6	±	0.34	7.0	±	0.3	13	0.5-1.5	6
RubpyC17 + FeCN	Post 5 min washout	-15	±	0.24	5.9	±	0.2	6	0.5-1.5	6

In contrast, we expected that adding ferricyanide (FeCN) would serve as an electron acceptor to favor the oxidation of the Ru^{2+} complex upon light absorption to Ru^{3+} over reduction to Ru^{1+}. We might expect the change from Ru^{2+} to Ru^{3+} to produce a right shift of $V_{0.5.}$ Indeed, the presence of ferricyanide and RubpyC17 upon irradiation rendered a 4-mV right shift in $V_{0.5}$. Upon irradiation, $V_{0.5}$ increased to 13 mV (**Figure 4.8, Table 4.3)**. Unlike the sustained right shift observed with AA, the $V_{0.5}$ shift decreased during washout to 6 mV. Thus, these observations indicate a reversible, light-induced right shift in $V_{0.5}$ in the presence of ferricyanide. We conclude that on the timescale studied here, RubpyC17 remains associated with the membrane, as a small right shift persists even after 5 min of perfusion. Only in the presence of both RubpyC17 and ferricyanide have we observed a reversible, light-induced shift in $V_{0.5}$. As a control, we followed the same protocol with ferricyanide alone (no RubpyC17) and a minor right shift was observed only upon irradiation (**Table 4.3**). Note that for convenience the pre-irradiation and 5 min washout values for AA and FeCN only in **Table 4.3** are not shown in **Figure 4.8**.

4.3.4 Functional effects of a series of Rubpy derivatives on VGSCs and VGKCs

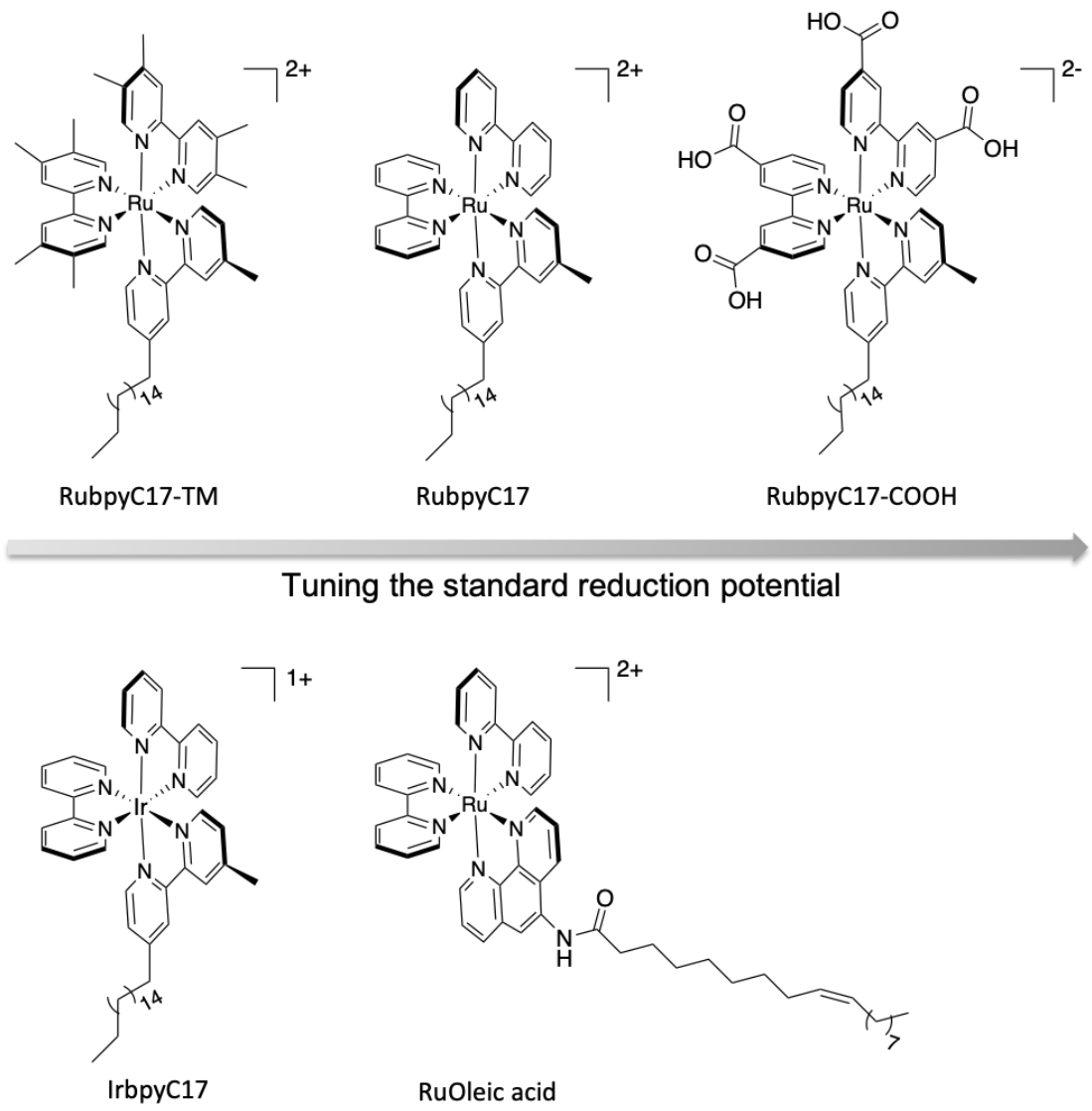

Figure 4.9 | Series of RubpyC17 derivatives. The standard reduction potential of the RubpyC17 is adjusted by substituting the bipyridine ligands with either electron-donating groups (top left) or electron-withdrawing groups (top right). Additionally, Ru was substituted for Ir (below left) and the C17 tail was substituted for oleic acid (below right).

In a different approach to gain more insight into the RubpyC17 effect on $V_{0.5}$, four derivatives of RubpyC17, differing in substitutions and overall charge, were designed and synthesized. The synthesis of these compounds was performed by Melanie Pribisko-Yen in the Grubbs group at Caltech. The derivatives are shown in **Figure 4.9**. Incorporation of

electron-donating groups at the 4- and 4'-positions and the 5- and 5'-positions on the 2,2'-bipyridine ligands will decrease the reduction potential of $Ru^{3+/2+}$ up to about 100 mV. Electron-withdrawing groups at those positions would yield an increase to a similar extent (**Figure 4.9**).[41–43] Also, alkyl groups will increase the driving force of electron transfer, favoring oxidation of the excited state of RubpyC17 (Ru^{2+} to Ru^{3+}). The electron-withdrawing carboxylic acid groups might serve another purpose besides providing a higher reduction potential. As previously discussed, negatively charged head groups of phospholipids in the lipid membrane are necessary for proper channel function.[21,23] Since RubpyC17 is overall positively charged, this might negatively interfere with the necessary movements of the voltage-sensing domain for channel activation. RubpyC17 containing carboxylic acids on the bipyridine ligands could alleviate this issue by interacting favorably with the positively charged arginine residues in the voltage sensor. Furthermore, in one of the compounds the Ruthenium is replaced by Iridium, which results in a net charge of 1+, instead of 2+. The fourth compound contains the same Ruthenium complex as RubpyC17 with the substitution of the C17 tail with oleic acid. We hypothesized that a PUFA might yield improved membrane incorporation and potentially better localization around the ion channels.

Two compounds were tested for membrane incorporation into oocytes using microcsopy. Oocytes were injected with either $Na_v1.4$ IR or Shaker IR mRNA and incubated in $ND96^+$ for 24 hours. Next, cells were incubated for 15-20 min with either 5 μM RubpyC17 or 10 μM RuOleic acid in $ND96^+$ and rinsed three times with fresh $ND96^+$ prior to imaging. Oocytes were not fixed, but imaged while in low level of buffer to prevent movement. Oocytes were imaged at 488 nm (RubpyC17) or 455 nm (RuOleic acid). Both RubpyC17 and RuOleic acid showed luminescence at the cell membrane upon irradiation (**Figure 4.10 center and right column**) in cells overexpressing either $Na_v1.4$ channels or Shaker potassium channels.

Oocytes incubated with $ND96^+$ only did not show luminescence (**Figure 4.10** left column). Despite the lack of additional co-localization experiments with plasma membrane markers, this obsveration suggests both compounds incorporate into the plasma membrane. The lack of additional puncta inside the cell could suggest that RubpyC17 does not accumulate in the cell and form aggregates, although further microscopy would be necessary to verify this.

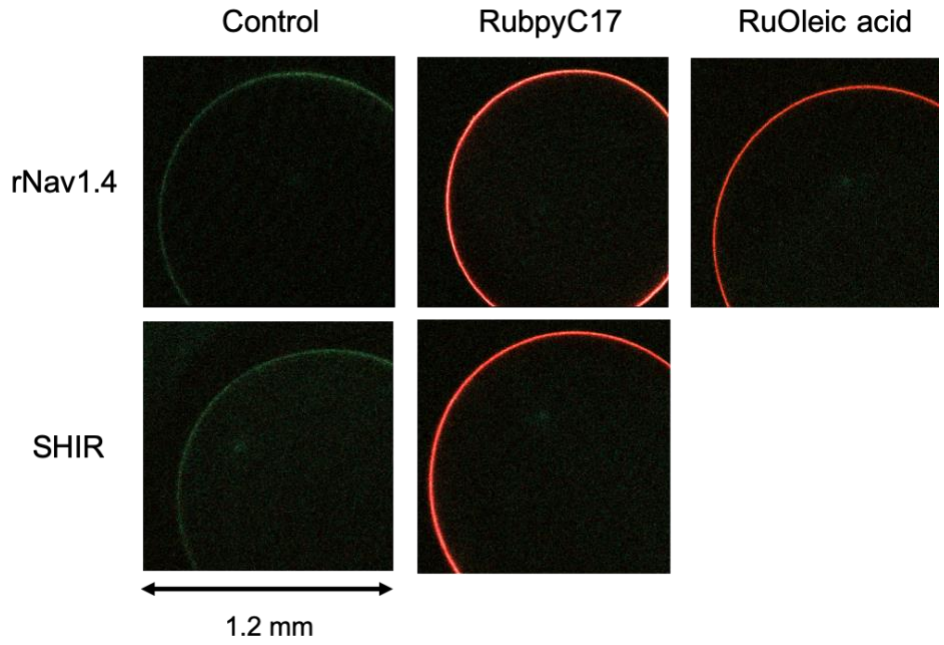

Figure 4.10 | Microscopy images of *Xenopus laevis* oocytes labeled with RubpyC17 and RuOleic acid. Oocytes were incubated in ND96 supplemented with 5 μM RubpyC17 or 10 μM RuOleic acid for 15-20 min prior to imaging.

Next, we performed voltage clamp experiments described in **Figure 4.7A** to evaluate changes in activation potential of $Na_v1.4$ IR channels by the new Rubpy derivatives. For this analysis we focused only on the voltage jump events upon irradiation, as other voltage jumps did not render large deviations from the reference. As shown in **Figure 4.11A** and **Table 4.4**, RubpyC17-TM and RubpyC17-COOH combined with 470 nm light have no effect on the $V_{0.5}$ of $Na_v1.4$ IR channels. This results suggest that neither the standard reduction potential nor the overall charge of the complexes plays a large role in the effects seen for RubpyC17.

IrbpyC17 also did not show any shift. However, RuOleic acid resulted in a rightshifted $V_{0.5}$ ($\Delta V_{0.5}$ 8 mV) upon irradiation with 470 nm light, resembling the response of RubpyC17, see **Figure 4.11A and Table 4.4**. We expected to see better membrane incorporation for RuOleic acid as the C17 tail now contains one unsaturated bond, however the $V_{0.5}$ shift did not equal or exceed that of RubpyC17, which suggests less membrane incorporation.

RubpyC17-COOH, IrbpyC17, and RuOleic acid were also tested in the presence of AA. The $V_{0.5}$ values for RubpyC17-COOH and RuOleic acid increased marginally relative to the $V_{0.5}$ without AA. The combination of IrbpyC17 and AA, however, resulted in a slight leftward shift ($\Delta V_{0.5}$ -4 mV). We decided not to pursue any experiments with concentrations larger than 50 µM, since we find those to have a detrimental effect on cell health.

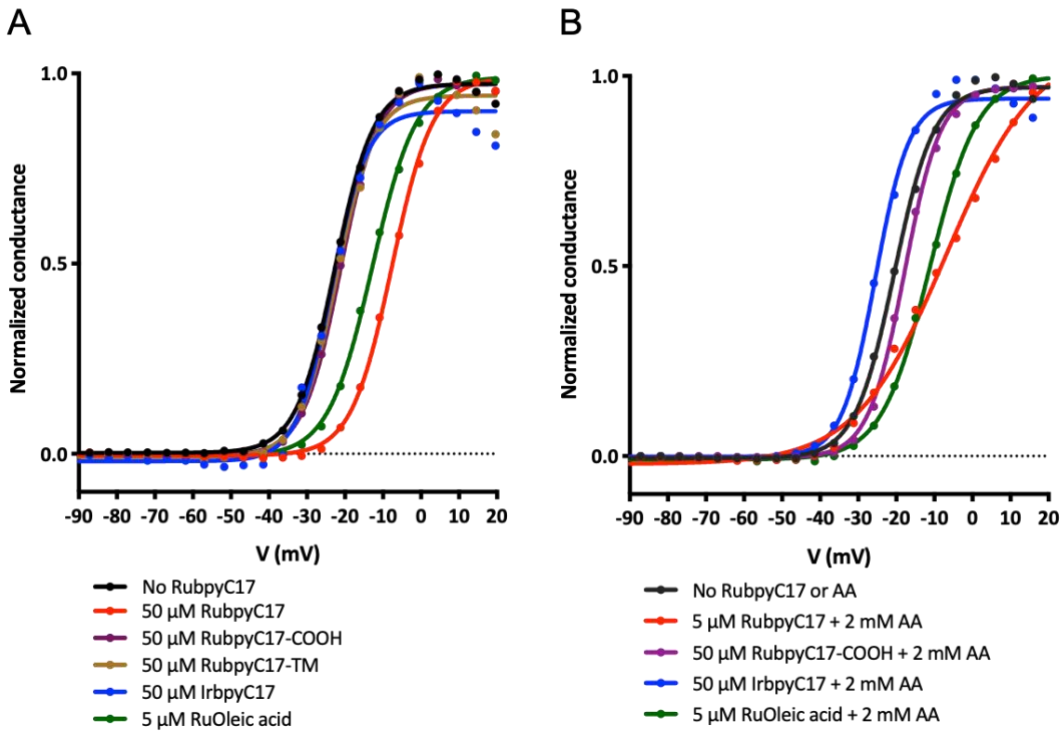

Figure 4.11 | Functional effects of RubpyC17 derivatives on $Na_v1.4$ IR channels. (A) G-V plot of RubpyC17 and derivatives. (B) G-V plot of RubpyC17-COOH, IrbpyC17, and RuOleic acid in combination with 2 mM AA. RubpyC17, -COOH, and –TM were irradiated with 470 nm light for ~60s. IrbpyC17 and RuOleic acid were irradiated with 455 nm light for ~60s. All compounds were applied at a 50 µM concentration, except for RuOleic acid at 5 µM.

Table 4.4 | $V_{0.5}$ and slope values for Nav1.4 IR in response to RubpyC17 derivatives. All compounds were applied at a 50 μM concentration, except for RuOleic acid at 5 μM. AA was applied at 2 mM.

Compound	$V_{0.5}$			Slope			$\Delta V_{0.5}$	$\lvert I_{max} \rvert$ (μA)	N
-	-21	±	0.19	5.0	±	0.2	0	0.5-7.0	23
RubpyC17	-7.7	±	0.72	5.4	±	0.6	13	0.6-2.5	4
RubpyC17-COOH	-21	±	0.30	5.0	±	0.3	0	0.9-2.5	6
RubpyC17-TM	-22	±	0.51	4.9	±	0.4	-1	2.0-6.0	3
IrbpyC17	-23	±	1.02	4.6	±	0.9	-2	0.6-1.3	5
RuOleic acid	-13	±	0.41	5.8	±	0.4	8	1.5-7.0	5
RubpyC17-COOH + AA	-18	±	0.30	4.8	±	0.3	3	2-3.5	4
RubpyC17-TM + AA	NR	±		NR	±				
IrbpyC17 + AA	-25	±	0.43	4.4	±	0.4	-4	1.5-8	5
RuOleic acid + AA	-11	±	0.55	6.4	±	0.5	10	2.0-3.0	3

Next, we set out to determine if these compounds affect VGKCs in a similar fashion. Therefore, we repeated the voltage jump experiments (**Figure 4.7A**) with Shaker IR potassium channels (SHIR) to determine changes in activation potential. The results are shown in **Figure 4.12** and **Table 4.5**. Similar to what was observed for Nav1.4, neither RubpyC17-COOH or IrbpyC17 caused a meaningful shift in $V_{0.5}$. RubpyC17, at a 5 μM concentration, resulted in a 28 mV $\Delta V_{0.5}$. This shift is much larger than what we previously observed for $Na_v1.4$, which was 13 mV at 50 μM RubpyC17. We also tested these compounds and RuOleic acid in combination with AA. RubpyC17-COOH and IrbpyC17 demonstrated small $V_{0.5}$ shifts, resembling those of $Na_v1.4$ channels, while RubpyC17 and RuOleic acid in combination with AA show the biggests shifts, but not exceeding those seen without AA (**Table 4.5**).

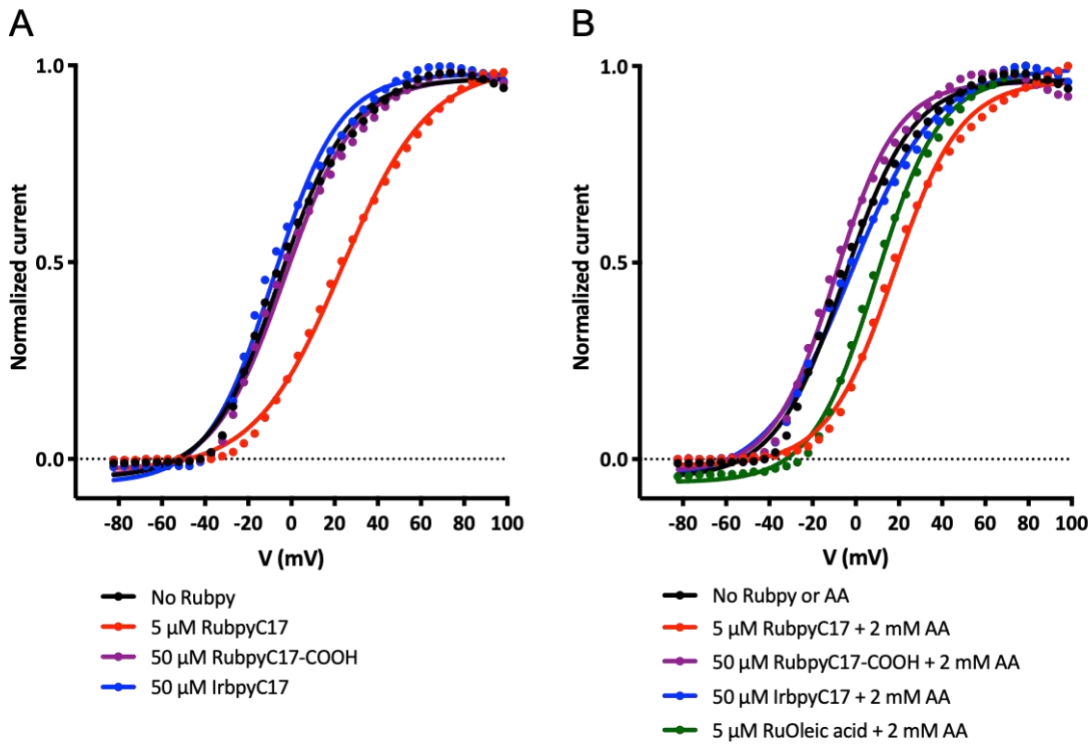

Figure 4.12 | Functional effects of Rubpy derivatives on Shaker IR channels. (A) I-V plot of RubpyC17, RubpyC17-COOH, and IrbpyC17. (B) I-V plot of RubpyC17, RubpyC17-COOH, IrbpyC17, and RuOleic acid in combination with 2 mM AA. RubpyC17, -COOH, and –TM were irradiated with 470 nm light for ~60s. IrbpyC17 and RuOleic acid were irradiated with 455 nm light for ~60s. RubpyC17-COOH and IrbpyC17 were applied at a 50 µM concentration, and RubpyC17 and RuOleic acid at 5 µM.

Table 4.5 | $V_{0.5}$ and slope values for Shaker IR in response to RubpyC17 derivatives. RubpyC17-COOH and IrbpyC17 were applied at a 50 µM concentration, and RubpyC17 and RuOleic acid at 5 µM. AA was applied at 2 mM.

Compound	$V_{0.5}$			Slope			$\Delta V_{0.5}$	$\lvert I_{max} \rvert$ (µA)	N
-	-5.4	±	0.34	16	±	0.3	0	1.0-18	32
RubpyC17	23	±	2.0	20	±	1.9	28	9.0-18	4
RubpyC17-COOH	-3.1	±	1.0	16	±	0.9	2.3	2.5-15	4
IrbpyC17	-8.4	±	0.59	15	±	0.5	-3	4.0-16	4
RubpyC17 + AA	18	±	1.1	16	±	1.0	23	3.5-12	4
RubpyC17-COOH + AA	-9.5	±	0.77	14	±	0.7	-4.1	3.0-12	4
IrbpyC17 + AA	-2.4	±	0.63	20	±	0.6	3	8.0-12	4
RuOleic acid and AA	9.4	±	0.72	15	±	0.7	17	1.0-4.0	5

As previously seen in **Figure 4.7C** and **Figure 4.8A**, the RubpyC17-induced rightward $\Delta V_{0.5}$ persists even after 5 min perfusion with buffer only. This was also the case for the RuOleic acid-induced shift. IrbpyC17, however, barely caused a shift upon irradiation after 60 s incubation as seen in **Figure 4.11** and **4.12**, but a rightward shift did arise after the 5 min washout. These observations raised two questions: 1) is a longer incubation time needed to reach the maximum $\Delta V_{0.5}$ at the used concentration? and 2) does the Rubpy (or Irbpy) washout of the membrane eventually or is the consequent right shifted $V_{0.5}$ irreversible? In order to answer these questions we performed the same voltage jump experiments with longer incubation times (5, 10, 15 min), and longer washout times (10, 15, 25 min) (**Figure 4.13A**). In previous experiments oocytes were incubated with in the Rubpy solution for about 1 min total, and the washout time was 5 min. Although we were able to record currents from oocytes at all these conditions, oocytes typically started dying during longer incubation (>10 min), and washout (>15 min) times. For these experiments we focused on RubpyC17 and IrbpyC17 only, because both demonstrated persisting or increasing right shifts in $V_{0.5}$ after 5 min washout.

Figure 4.13B shows the $V_{0.5}$ shifts recorded after various incubation durations, and **Figure 4.13C** shows those after increasing wash durations. For RubpyC17 recordings from Nav1.4 IR channels $V_{0.5}$ shifts increased with longer incubation times (up to 35 mV), while those from SHIR channels were the same for 1 and 5 min (19 and 20 mV). IrbpyC17 demonstrated a very small left shift after 1 min incubation, but a slight right shift after 5 min in both channel types. However, these shifts are too small to be meaningfully different (2.0 and 3.7 mV).

Regarding the extended washout times, no recovery in $V_{0.5}$ appears to occur for $Na_v1.4$ channels as all three 10, 15 and 25 min durations provide a comparable shift of 30, 29, 33 mV

respectively. In contrast, IrbpyC17 does show a substantially lower shift after 15 min washout relative to a 5 min washout, suggesting reversible incorporation into the plasma membrane for IrbpyC17.

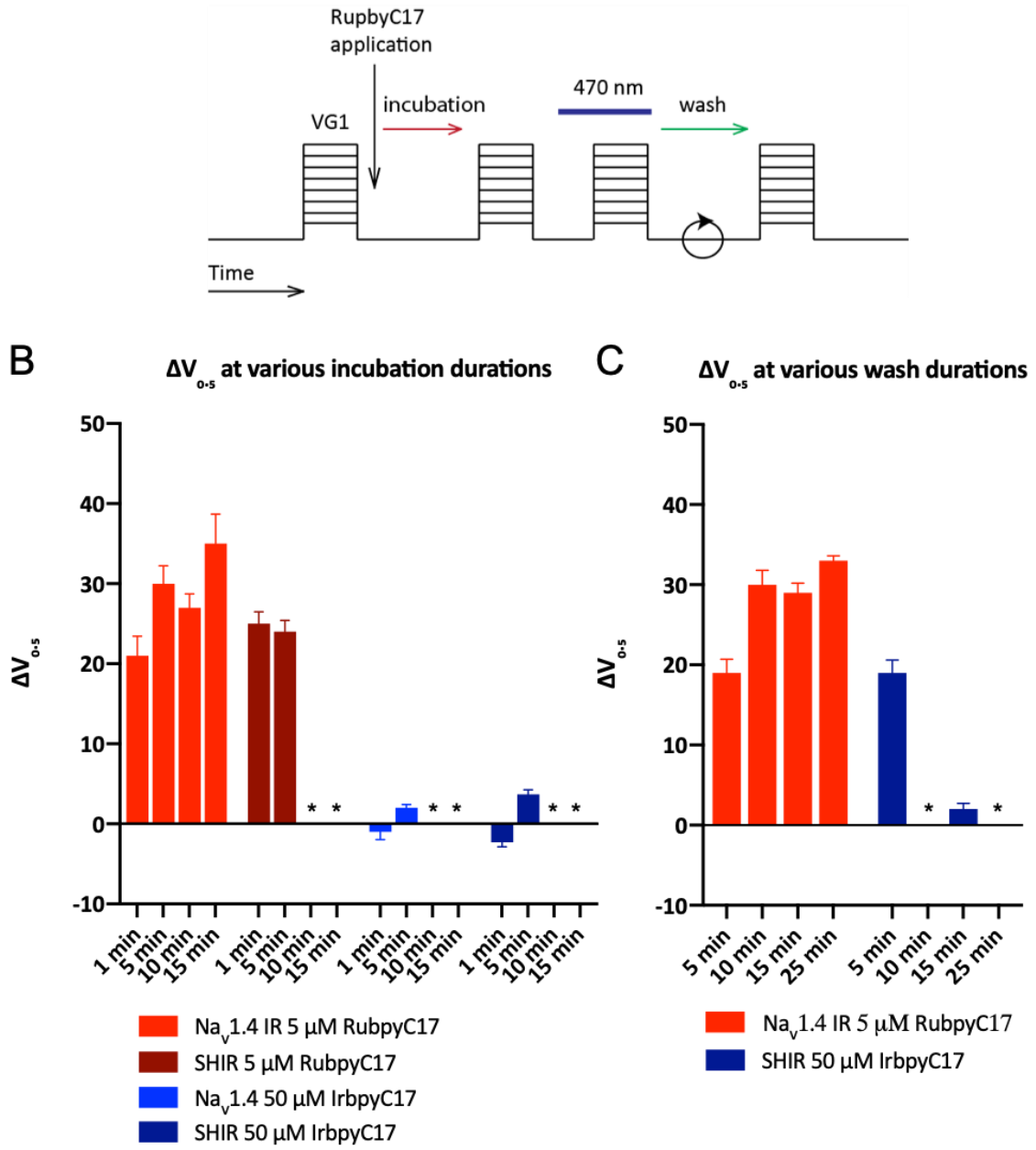

Figure 4.13 | RubpyC17 and IrbpyC17 effects at various incubation and washout durations. (A) Experimental protocol from Figure 4.7A with incubation and washout moments highlighted. (B) Bar graph of measured $\Delta V_{0.5}$ values after irradiation with 470 nm light at various incubation durations. (C) Bar graph of measured $\Delta V_{0.5}$ values after various wash durations. During the wash step oocyte chambers are perfused with fresh ND96. A positive shift is an increase in $V_{0.5}$ that corresponds to a

right shift in the G-V plot. All other aspects of the experiment protocol remain the same as previously described. RubpyC17 and IrbpyC17 were applied at a 5 μM and 50 μM concentration respectively. * indicates values not recorded.

Table 4.6 | $\Delta V_{0.5}$ and slope values for Nav1.4 and Shaker IR in response to RubpyC17 and IrbpyC17 at various incubation and washout durations. RubpyC17 and IrbpyC17 were applied at a 5 μM and 50 μM concentration respectively.

VGIC	Compound	Duration	$V_{0.5}$			Slope			$\Delta V_{0.5}$	$\lvert I_{max} \rvert$ (μA)	N
$Na_v1.4$IR	-		-21	±	0.19	5.0	±	0.2	0	0.5-7.0	23
SHIR	-		-5.4	±	0.34	16	±	0.3	0	1.0-18	32
		Incubation									
$Na_v1.4$IR	RubpyC17	1 min	0.26	±	2.5	11	±	1.4	21	1.0-4.0	6
$Na_v1.4$IR	RubpyC17	5 min	8.5	±	2.2	8.8	±	1.0	30	2.5-5.0	4
$Na_v1.4$IR	RubpyC17	10 min	6.1	±	1.7	8.3	±	0.9	27	1.2-4.0	2
$Na_v1.4$IR	RubpyC17	15 min	14	±	3.7	8.1	±	1.3	35	2.5-6.0	2
$Na_v1.4$IR	IrbpyC17	1 min	-22	±	0.96	5.3	±	0.8	-1.0	0.6-1.3	5
$Na_v1.4$IR	IrbpyC17	5 min	-19	±	0.43	5.4	±	0.4	2.0	1.4-3.0	4
		Wash									
$Na_v1.4$IR	RubpyC17	5 min	-2.2	±	1.7	10	±	1.1	19	1.0-4.0	6
$Na_v1.4$IR	RubpyC17	10 min	8.8	±	1.8	9.1	±	0.8	30	4.0-5.0	4
$Na_v1.4$IR	RubpyC17	15 min	8.0	±	1.2	7.5	±	0.6	29	2.5-5.0	3
$Na_v1.4$IR	RubpyC17	25 min	12	±	0.59	7.8	±	0.2	33	3.5	1
		Incubation									
SHIR	RubpyC17	1 min	20	±	1.5	19	±	1.4	25	1.2-4.0	6
SHIR	RubpyC17	5 min	19	±	1.4	15	±	1.2	24	3.0-7.0	3
SHIR	IrbpyC17	1 min	-7.7	±	0.55	16	±	0.5	-2.3	4.0-16	5
SHIR	IrbpyC17	5 min	-1.7	±	0.55	17	±	0.5	3.7	3.0-5.0	5
		Wash									
SHIR	IrbpyC17	5 min	14	±	1.6	23	±	1.6	19	1.2-4.0	5
SHIR	IrbpyC17	15 min	-3.4	±	0.73	17	±	0.7	2	3.0-8.0	5

From the Rubpy derivatives studied here, the largest effects on $V_{0.5}$ has still been observed for RubpyC17. To further investigate this, we performed voltage jump experiments, similar to those described earlier, after directly injecting RubpyC17 into the oocyte. We speculated that if RubpyC17 only incorporates into the outer leaflet of the plasma membrane, direct injection might give the opposite or no $\Delta V_{0.5}$ at all. If RubpyC17 does fully penetrate the membrane, it could interact with both the extracellular and intracellular faces of the ion

channels (**Figure 4.14A**). Direct injection would then likely result in a similar $\Delta V_{0.5}$ as observed earlier from incubating the oocyte in a RubpyC17 solution.

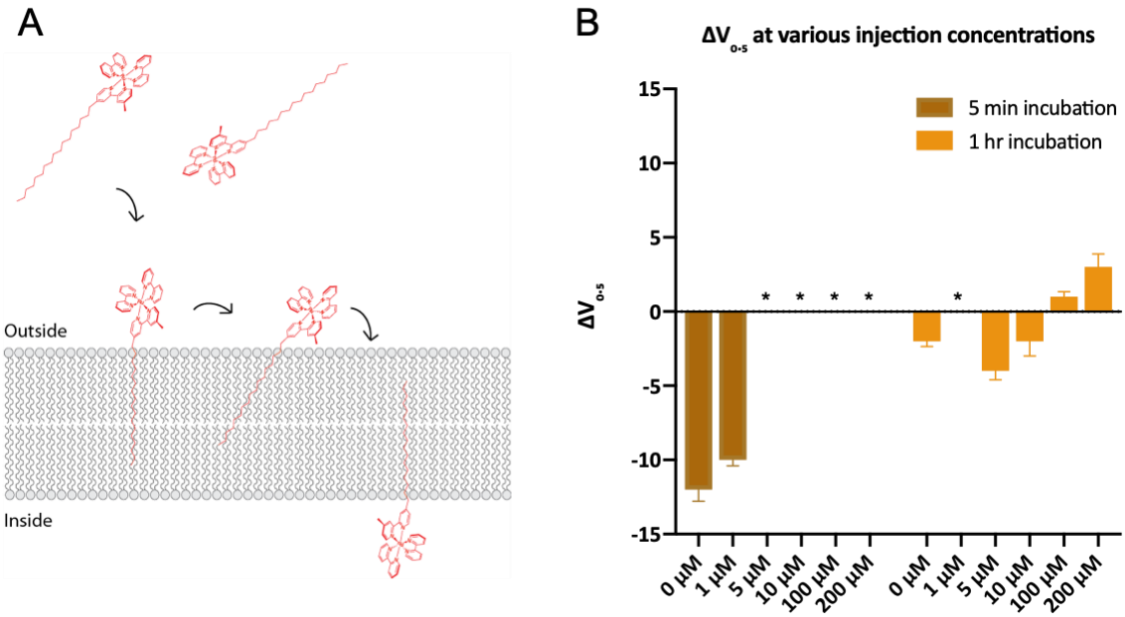

Figure 4.14 | Functional effects after injection of RubpyC17 directly into oocytes expressing $Na_v1.4$ IR. (A) Schematic view of RubpyC17 membrane flipping. (B) Bar graph of measured $\Delta V_{0.5}$ values after irradiation with 470 nm light at various injection concentrations of RubpyC17. * indicates values not recorded.

Oocytes were injected with 50 nL of a RubpyC17 solution in ND96 at various concentrations, 1, 5, 10, 100, and 200 µM. The negative control solution was supplemented with 0.08% DMSO, to control for trace amounts of DMSO in which the RubpyC17 stock solution was prepared. After 5 min or 1 hr incubation oocytes were subjected to the previously described voltage jump experiments (Figure 4.7A). The 5 min incubation at 1 µM resulted in a $\Delta V_{0.5}$ of -10 mV, but the control rendered a comparable shift. We reasoned that the oocytes need more time to recover post-injection, to adjust for the added volume and provide time to reseal the membrane from the puncture. Therefore, we extended the incubation time to 1 hr. Additionally, we continued the injections with higher concentrations of RubpyC17 to mimick the outside contreation used in previous experiments. A 50 nL injection of 100 µM and 200

μM should result in a intracellular concentration of 5 and 10 μM respectively. However, small shifts in $V_{0.5}$ were observed as shown in **Figure 4.14B and Table 4.7**. The injection with the highest concentration (200 μM) only rendered a 3 mV right shift, which resembles the earlier observation of 5 mV in **Figure 4.7**. From these observations we conclude that RubpyC17 fully incorporates into the membrane and is likely to interact with the channel from both the intracellular and extracellular side.

Table 4.7 | $\Delta V_{0.5}$ and slope values for Nav1.4 in response to injected RubpyC17.

[RubpyC17]	Incubation time	$V_{0.5}$			Slope			$\Delta V_{0.5}$	$\lvert I_{max} \rvert$ (μA)	N
		-21	±	0.19	5.0	±	0.2	0	0.5-7.0	23
0	5 min	-33	±	0.78	4.9	±	0.7	-12	10-12	5
1 μM	5 min	-31	±	0.39	4.0	±	0.3	-10	5.0-7.0	3
0	1 hr	-23	±	0.36	4.8	±	0.3	-2	1.5-5.0	4
5 μM	1 hr	-25	±	0.6	5.1	±	0.5	-4	3.0-11	4
10 μM	1 hr	-23	±	1.0	5.0	±	0.9	-2	1.0-6.0	2
100 μM	1 hr	-20	±	0.34	4.6	±	0.29	1	1.4-5.0	4
200 μM	1 hr	-18	±	0.88	3.7	±	0.76	3	0.8-6.0	6

Next, we decided to further explore the effects of RuOleic acid. Recall that the application of 5 μM RuOleic acid to both $Na_v1.4$ channels and SHIR resulted in an irreversible right shift in $V_{0.5}$ (**Figure 4.11, 4.12, 4.13**). After reanalyzing the current responses, we found that RuOleic acid also affects the maximum peak current for SHIR channels. This effect has not been observed for $Na_v1.4$ channels. As shown in **Figure 4.15A** in the top waveform, application of RuOleic acid and AA cause a decrease in peak current (red) relative to the peak current recorded prior, and irradiation with 455 nm light increases the peak current. To test if this is due to the Rubpy-complex, we performed the voltage jump experiment with Oleic acid and AA as well. Oleic acid in combination with AA does yield a mild shift in $V_{0.5}$ (2.4 mV) and

no change in peak current, as shown in **Figure 4.15A** bottom waveform and **Table 4.8**. This suggests that the peak current-effect is caused by the Ruthenium complex.

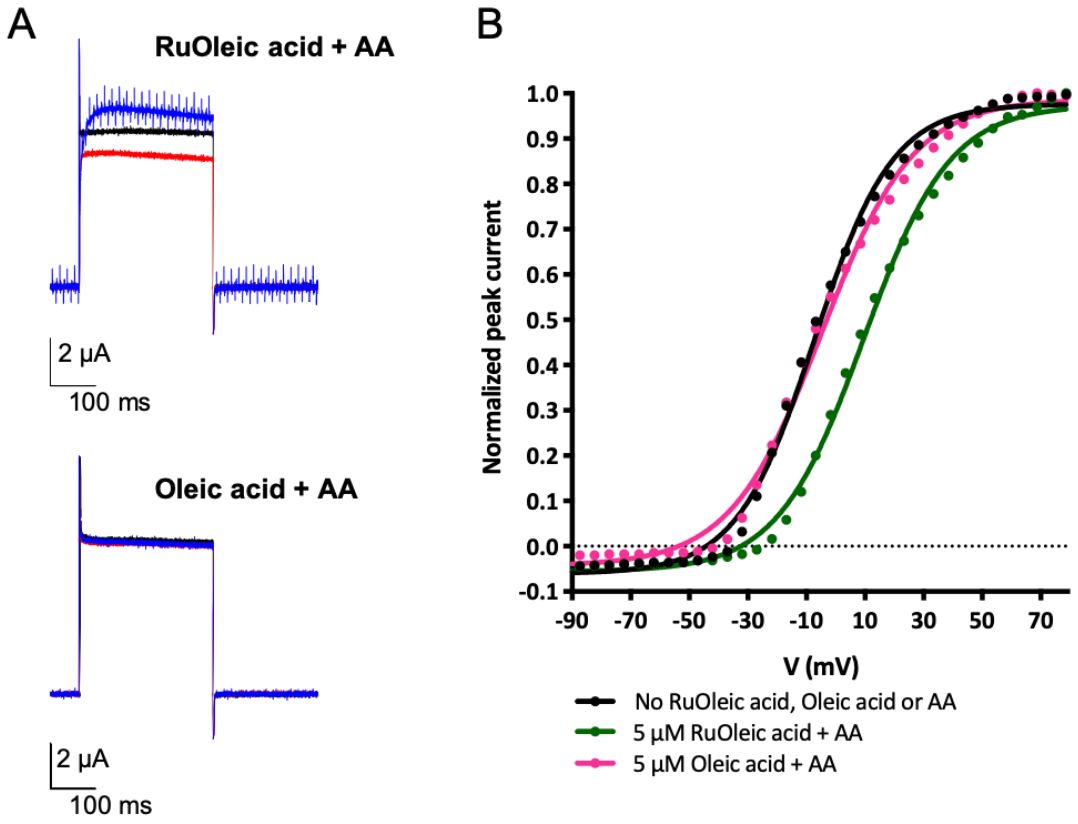

Figure 4.15 | Functional effects of RuOleic acid and Oleic acid on SHIR channels. (A) Current waveforms of SHIR channels at +100 mV in presence of RuOleic acid and AA (top), and Oleic acid and AA (bottom). Recorded current prior to Rubpy application (black), recorded current after Rubpy application prior to irradiation (red), and recorded current after irradiation with 455 nm light (blue). (B) I-V plot of SHIR channels after prior to Rubpy application (black), after RuOleic + AA application and 455 nm light (green), Oleic acid + AA and 455 nm light (pink). All samples were irradiated with 455 nm light for ~60s.

Table 4.8 | $V_{0.5}$ and slope values for Shaker IR in response to RuOleic acid with AA. RuOleic acid and Oleic acid at 5 µM, AA at 2 mM

Compound	$V_{0.5}$			Slope			$\Delta V_{0.5}$	$\lvert I_{max} \rvert$ (µA)	N
-	-7.1	±	0.43	13.3	±	0.40		1.0-4.0	5
RuOleic acid and AA	9.6	±	0.67	14.7	±	0.60	17	1.0-4.0	5
Oleic acid and AA	-4.7	±	0.61	15.6	±	0.56	2.4	3.0-6.7	4

To determine if the light-dependent increase in peak current is reversible, we conducted a dark/light cycle experiment. This protocol resembles the one discussed in **Figure 4.7A**, but includes an extended washout phase with four more voltage jump events and additional irradiation steps. First, we performed a control voltage jump (black) to create a baseline peak current per oocyte, which we followed by applying 5 μM RuOleic acid. After 5 min incubation a voltage jump was performed (red), followed by 40s irradiation with 455 nm light and a third voltage jump (blue). From this point fresh buffer was perfused into the oocyte chamber (no RuOleic acid) and every 400s the cell was briefly irradiated with 455 nm light up to three times. In between irradiations a voltage jump was performed every 100s, while fresh buffer was perfused.

We observed a gradual decrease (~17%) in peak current in the dark, but an increase (~5%) in current upon irradiation and any subsequent irradiation, as shown in **Figure 4.16A and Table 4.9**. As a control experiment we performed the same sequence of voltage jumps, without irradiation (Figure 4.16B). We observed a comparable decrease in peak current (13%) as shown in **Figure 4.16A**. The 'irradiation step' does not yield an increase, as expected, but we did observe a gradual increase in peak current (15%) upon perfusion with buffer. A small, but gradual current increase is often seen when recording currents on ion channels for extended periods of time. In the second control experiment no RuOleic acid was applied. Indeed, no decrease in peak current was observed after application of buffer, neither did the peak current increase upon irradiation with 455 nm light. Here also, a gradual increase in peak current (19%) was observed over the course of the experiment.

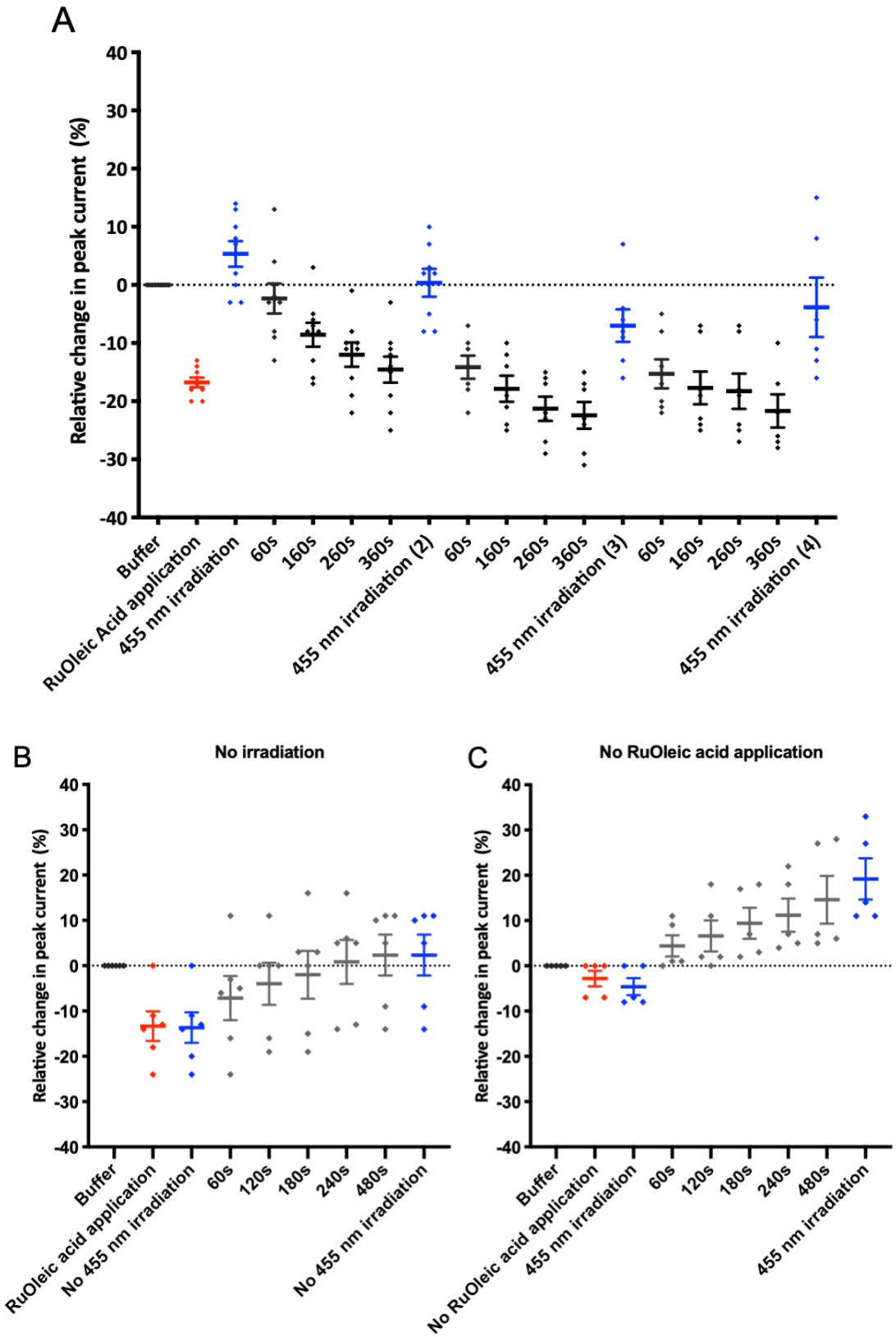
A
Relative change in peak current (%)
40
30
20
10
0
-10
-20
-30
-40
Buffer
RuOleic Acid application
455 nm irradiation
60s
160s
260s
360s
455 nm irradiation (2)
60s
160s
260s
360s
455 nm irradiation (3)
60s
160s
260s
360s
455 nm irradiation (4)
B
No irradiation
Relative change in peak current (%)
Buffer
RuOleic acid application
No 455 nm irradiation
60s
120s
180s
240s
480s
No 455 nm irradiation
C
No RuOleic acid application
Relative change in peak current (%)
Buffer
No RuOleic acid application
455 nm irradiation
60s
120s
180s
240s
480s
455 nm irradiation

Figure 4.16 | RuOleic acid dark/light cycle experiment showing differential effects on peak currents of SHIR. (A) Relative change in peak current as a function of time. Reference voltage jump ("buffer", black), application of 5 μM RuOleic acid (red), irradiation with 455 nm light (blue), voltage jump after oocyte chamber perfusion with ND96 (no RuOleic acid) (grey). (B) Control experiment 1, similar to the first 'cycle' in A except without 455 nm light irradiation. (C) Control experiment 2, similar to the first 'cycle' of the experiment in A, except without RuOleic acid application.

Based on these results, we conclude that the RuOleic acid persists in the membrane and, in addition to a rightward shift in $V_{0.5}$, causes a decrease in peak current. We can temporarily attenuate this decrease by irradiation with 455 nm light.

Table 4.9 | Relative changes in SHIR peak current during RuOleic acid dark/light cycle experiment. Values are reported as mean ± SEM.

Step	Relative change in peak current (%)			$\lvert I_{max} \rvert$ (μA)	N
Buffer	0	±	0	3.6-13	9
RuOleic acid application	-17	±	0.83	3.1-9.9	9
455 nm irradiation	5.3	±	2.2	3.9-12	9
60s wash	-2.3	±	2.6	3.5-11	9
160s wash	-8.6	±	2	3.3-10	9
260s wash	-12	±	2.1	3.2-9.7	9
360s wash	-15	±	2.2	3.2-9.4	9
455 nm irradiation (2)	0.38	±	2.4	3.7-11	8
60s wash	-14	±	2	3.2-9.9	7
160s wash	-18	±	2.2	3.1-9.1	7
260s wash	-21	±	2.1	3-8.8	7
360s wash	-22	±	2.3	3-8.5	7
455 nm irradiation (3)	-7.0	±	2.8	3.4-11	7
60s wash	-15	±	2.5	3-11	7
160s wash	-18	±	2.8	2.9-11	7
260s wash	-18	±	3	2.9-11	7
360s wash	-22	±	2.9	2.8-10	6
455 nm irradiation (4)	-3.8	±	5.1	3.2-13	6
Control 1 – No irradiation					
Buffer	0	±	0	5.5-31	6
RuOleic acid application	-13	±	3.3	4.5-27	6
No 455 nm irradiation	-14	±	3.4	4.4-27	6
60s wash	-7.2	±	4.9	4.6-29	6
120s wash	-4.0	±	4.6	4.6-31	6
180s wash	-2.0	±	5.3	4.7-32	6
240s wash	0.83	±	4.8	4.8-33	6

480s wash	2.3	±	4.5	5-34	6
No 455 nm irradiation (2)	2.3	±	4.5	5-34	6
Control 2 – No RuOleic acid application					
Buffer	0	±	0	8.3-18	5
No RuOleic acid application	-2.8	±	1.7	7.7-18	5
455 nm irradiation	-4.6	±	1.9	7.6-18	5
60s wash	4.4	±	2.3	8.4-20	5
120s wash	6.6	±	3.4	8.5-20	5
180s wash	9.4	±	3.4	8.5-21	5
240s wash	11	±	3.7	8.6-22	5
480s wash	15	±	5.3	8.7-23	5
455 nm irradiation (2)	19	±	4.5	9.2-24	5

4.4 Conclusions and future directions

The ultimate goal of this study was to photochemically control the activation of the VGSCs and thus make progress towards developing a RubpyC17-based photoswitch that could be used in an artificial retina. To evaluate Rubpy-induced changes in ion channel function we expressed both $Na_v1.4$ and SHIR channels in *Xenopus laevis* oocytes and performed two-electrode voltage clamp (TEVC). After optimization of TEVC protocols we were able to record currents from Nav1.4 channels with the *OpusXpress*, however not in the medium-throughput fashion as one can with ligand-gated ion channels. We found that RubpyC17 causes an increasing, irreversible rightward shift in $V_{0.5}$ with increasing concentrations. Application of RubpyC17 in combination with either a reductant or oxidant also yields a right shift in $V_{0.5}$ in $Na_v1.4$ channels. Confocal imaging confirmed cell membrane incorporation of both RuOleic acid and RubpyC17. From the derivatives tested, only RuOleic acid demonstrated a meaningful function effect: a right shift in $V_{0.5}$ in both $Na_v1.4$ and SHIR channels as well as a decrease in peak current for SHIR channels. This decrease in peak current can be temporarily attenuated by irradiation of 455 nm light. Light alone does not alter the

peak current. Oleic acid alone does not yield a right shift in $V_{0.5}$, nor a difference in maximum current response.

Future studies could include subjecting α-β1-heteromers to RubpyC17. In **Table 1** we have shown different inactivation kinetics for the heteromer and α-subunit alone. Dependent upon the sites of specific interaction of RubpyC17 with the α-subunit, modulation by the β subunit could be altered by the ruthenium complex. Additionally, looking at the effects of RubpyC17 on other VGSC subtypes could provide more useful information, since any direct modulation could be subtype dependent.

4.5 Experimental procedures

Chemicals

The compounds: RupbyC17, RubpyC17-TM, RubpyC17-COOH, IrbpyC17, and RuOleic acid were synthesized by Melanie Pribisko-Yen in the Grubbs Lab at Caltech. Ascorbic acid and potassium ferricyanide were commercially obtained (Sigma).

Molecular biology

The rat $Na_v1.4$ gene was in a pBSTA plasmid. To obtain the inactivation resistant mutant, position F1304 was mutated by conventional site-directed mutagenesis to code for Glutamine (Gln). The Shaker IR gene, which contains a T449V mutation to limit C-type inactivation, was also in the pBSTA plasmid. Both constructs were a generous gift of the Ahern Lab at the University of Iowa. After DNA linearization with NotI, mRNA was transcribed using an mMessage mMachine T7 kit (Ambion) and purified using a RNeasy kit (Qiagen).

Oocyte preparation and RNA injection

Stage V-VI Xenopus laevis oocytes were harvested and injected with RNA as previously described. [32,34] Oocytes were stored in filtered ND96 solution supplemented with 0.5% gentamicin: 96 mM NaCl, 2 mM KCl, 1 mM $MgCl_2*6H_2O$, 5 mM HEPES, pH 7.5. For

a typical experiment, oocytes were injected with 0.5 ng mRNA in a total volume of 50 μL, followed by incubation at 18˚C for 24 hours to allow expression of the protein and transport to the membrane.

Electrophysiology and light-stimulation

Two-electrode voltage clamp experiments were performed using an *OpusXpress* 6000A (Axon Instruments). Voltage-clamped sodium currents were recorded using two glass microelectrodes with resistances between 0.1 and 0.3 MΩ (backfilled with 3 M KCl). Recordings were performed at 18-20˚C in ND96 solution (see above). The recording chamber was automatically perfused with ND96 at a flow rate of 3 mL/min and the RupbyC17 solutions were applied separately at a flow rate of 2 mL/min (chamber volume = 500 μL). Sodium currents were generated by step depolarizations from a holding potential of -100 mV to +20 mV, unless otherwise indicated. Only cells with minimal leak currents (≤ 0.1 μA) were used. Data were digitized at 125 Hz and filtered at 5000 Hz. Light stimulation was performed using a 470 nm (M470L1, 625 mW, Thor Labs) or 455 nm (M455L3, 900 mW, ThorLabs) mounted LED at full intensity.

Data analysis

Current signals were analyzed using pClamp software version 10.2 (Axon Instruments) and data were further processed using Microsoft Excel v14.4.7, KaleidaGraph v4.5, and Graphpad Prism 8. Sodium conductances (G_{Na}) were determined from peak tail currents generated by step depolarizations starting at -90 mV to +20 mV with 5 mV increments using the equation:

$$G_{Na} = \frac{I_{Na}}{(E_m - E_{rev})}$$

Where G_{Na} is the sodium conductance, I_{Na} is current amplitude, E_m is the membrane potential and E_{rev} is the reversal potential calculated for each individual cell. The reversal potential was calculated by extrapolating a linear regression of the I-V trace starting from the maximal current amplitude upwards to higher depolarizations. Individual activation curves (G-V) were normalized to the maximum current amplitude per cell and then fitted using the Boltzmann distribution equation:

$$G_{norm} = \frac{1}{1 + e^{\frac{V - V_{0.5}}{k}}}$$

where G_{norm} is the normalized sodium conductance, V_m the membrane potential of that depolarization step, $V_{0.5}$ is the membrane potential at which half of the channel population is activated (in the open conformation), k is the slope. Calculated parameters $V_{0.5}$ and k from individual cells were averaged and are shown as mean ± SEM. Current responses from Potassium channels were determined from step depolarizations from -80 mV to +100 mV. Current responses were then normalized to the maximum current amplitude per cell and fitted using the Boltzmann distribution equation.

Steady-state inactivation data were obtained using two pulses. First, a variable conditioning pulse was given (-120 mV to +20 mV, 500 ms duration), followed by a second 'test' pulse to -20 mV of 15 ms duration. The current amplitude resulting from the second pulse was plotted as a function of the variable potential of the first conditioning pulse. These I-V curves were also fitted against the previously described Boltzmann distribution equation.

Microscopy

Live oocytes were imaged at room temperature on a Nikon Eclipse TE2000-U inverted microscope.

4.6 References

(1) Tochitsky, I.; Kramer, R. H. Optopharmacological Tools for Restoring Visual Function in Degenerative Retinal Diseases. *Curr Opin Neurobiol* **2015**, *34C*, 74–78. https://doi.org/10.1016/j.conb.2015.01.018.

(2) Boiko, T.; Van Wart, A.; Caldwell, J. H.; Levinson, S.; Trimmer, J. S.; Matthews, G. Functional Specialization of the Axon Initial Segment by Isoform-Specific Sodium Channel Targeting. *J Neurosci* **2003**, *23* (6), 2306–2313.

(3) Tochitsky, I.; Polosukhina, A.; Degtyar, V. E.; Gallerani, N.; Smith, C. M.; Friedman, A.; Van Gelder, R. N.; Trauner, D.; Kaufer, D.; Kramer, R. H. Restoring Visual Function to Blind Mice with a Photoswitch That Exploits Electrophysiological Remodeling of Retinal Ganglion Cells. *Neuron* **2014**, *81* (4), 800–813. https://doi.org/10.1016/j.neuron.2014.01.003.

(4) Yu, F. H.; Catterall, W. A. Overview of the Voltage-Gated Sodium Channel Family. *Genome Biol* **2003**, *4* (3), 207. https://doi.org/10.1186/gb-2003-4-3-207.

(5) Armstrong, C. M.; Hille, B. Voltage-Gated Ion Channels and Electrical Excitability. *Neuron* **1998**, *20* (3), 371–380.

(6) Catterall, W. A. Voltage-Gated Sodium Channels at 60: Structure, Function and Pathophysiology. *J. Physiol.* **2012**, *590* (11), 2577–2589. https://doi.org/10.1113/jphysiol.2011.224204.

(7) Payandeh, J.; M, G. E.-D., Tamer; Scheuer, T.; Zheng, N.; Catterall, W. A. Crystal Structure of a Voltage-Gated Sodium Channel in Two Potentially Inactivated States. *Nature* **2012**, *486* (7401), 135–139. https://doi.org/10.1038/nature11077.

(8) A, O., Heather; Isom, L. L. Sodium Channel β Subunits: Emerging Targets in Channelopathies. *Annu Rev Physiol* **2015**, *77*, 481–504. https://doi.org/10.1146/annurev-physiol-021014-071846.

(9) Hodgkin, A.; Huxley, A. A Quantitative Description of Membrane Current and Its Application to Conduction and Excitation in Nerve. *J Physiol Lond* **1952**, *117* (4), 500–544.

(10) Brackenbury, W. J.; Isom, L. L. Na+ Channel β Subunits: Overachievers of the Ion Channel Family. *Front Pharmacol* **2011**, *2*. https://doi.org/10.3389/fphar.2011.00053.

(11) Catterall, W. A.; Goldin, A. L.; Waxman, S. G. International Union of Pharmacology. XLVII. Nomenclature and Structure-Function Relationships of Voltage-Gated Sodium Channels. *Pharmacol Rev* **2005**, *57* (4), 397–409. https://doi.org/10.1124/pr.57.4.4.

(12) Catterall, W. A 3D View of Sodium Channels. *Nature* **2001**, *409* (6823), 988–989, 991. https://doi.org/10.1038/35059188.

(13) Swartz, K. J. Sensing Voltage across Lipid Membranes. *Nature* **2008**, *456* (7224), 891–897. https://doi.org/10.1038/nature07620.

(14) Li, Q.; Wanderling, S.; Paduch, M.; Medovoy, D.; Singharoy, A.; Ryan, M.; A, V.-G., Carlos; Hulse, R. E.; Roux, B.; Schulten, K.; et al. Structural Mechanism of Voltage-Dependent Gating in an Isolated Voltage-Sensing Domain. *Nat Struct Mol Biol* **2014**, *21* (3), 244–252. https://doi.org/10.1038/nsmb.2768.

(15) West, J.; Patton, D.; Scheuer, T.; Wang, Y.; Goldin, A.; Catterall, W. A Cluster of Hydrophobic Amino Acid Residues Required for Fast Na(+)-Channel Inactivation. *Proc Natl Acad Sci USA* **1992**, *89* (22), 10910–10914. https://doi.org/10.1073/pnas.89.22.10910.

(16) Stühmer, W.; Conti, F.; Suzuki, H.; Wang, X. D.; Noda, M.; Yahagi, N.; Kubo, H.; Numa, S. Structural Parts Involved in Activation and Inactivation of the Sodium Channel. *Nature* **1989**, *339* (6226), 597–603. https://doi.org/10.1038/339597a0.

(17) Chen, L.; Santarelli, V.; Horn, R.; Kallen, R. A Unique Role for the S4 Segment of Domain 4 in the Inactivation of Sodium Channels. *J Gen Physiol* **1996**, *108* (6), 549–556.

(18) Kontis, K. J.; Goldin, A. L. Sodium Channel Inactivation Is Altered by Substitution of Voltage Sensor Positive Charges. *J. Gen. Physiol.* **1997**, *110* (4), 403–413. https://doi.org/10.1085/jgp.110.4.403.

(19) Groome, J. R.; Fujimoto, E.; George, A. L.; Ruben, P. C. Differential Effects of Homologous S4 Mutations in Human Skeletal Muscle Sodium Channels on Deactivation Gating from Open and Inactivated States. *J. Physiol.* **1999**, *516 (Pt 3)*, 687–698.

(20) Groome, J. R. The Voltage Sensor Module in Sodium Channels. *Handb Exp Pharmacol* **2014**, *221*, 7–31. https://doi.org/10.1007/978-3-642-41588-3_2.

(21) Schmidt, D.; Jiang, Q.-X. X.; Roderick, M. Phospholipids and the Origin of Cationic Gating Charges in Voltage Sensors. *Nature* **2006**, *444* (7120), 775–779. https://doi.org/10.1038/nature05416.

(22) Long, S. B.; Campbell, E. B.; Mackinnon, R. Voltage Sensor of Kv1.2: Structural Basis of Electromechanical Coupling. *Science* **2005**, *309* (5736), 903–908. https://doi.org/10.1126/science.1116270.

(23) Xu, Y.; Ramu, Y.; Lu, Z. Removal of Phospho-Head Groups of Membrane Lipids Immobilizes Voltage Sensors of K+ Channels. *Nature* **2008**, *451* (7180), 826–829. https://doi.org/10.1038/nature06618.

(24) Ramu, Y.; Xu, Y.; Lu, Z. Enzymatic Activation of Voltage-Gated Potassium Channels. *Nature* **2006**, *442* (7103), 696–699. https://doi.org/10.1038/nature04880.

(25) Feller, S. E.; Gawrisch, K. Properties of Docosahexaenoic-Acid-Containing Lipids and Their Influence on the Function of Rhodopsin. *Curr. Opin. Struct. Biol.* **2005**, *15* (4), 416–422. https://doi.org/10.1016/j.sbi.2005.07.002.

(26) Feller, S. E.; Gawrisch, K.; MacKerell, A. D. Polyunsaturated Fatty Acids in Lipid Bilayers: Intrinsic and Environmental Contributions to Their Unique Physical Properties. *J. Am. Chem. Soc.* **2002**, *124* (2), 318–326.

(27) Grossfield, A.; Feller, S. E.; Pitman, M. C. Contribution of Omega-3 Fatty Acids to the Thermodynamics of Membrane Protein Solvation. *J. Phys. Chem. B* **2006**, *110* (18), 8907–8909. https://doi.org/10.1021/jp060405r.

(28) Bendahhou, S.; Cummins, T. R.; Agnew, W. S. Mechanism of Modulation of the Voltage-Gated Skeletal and Cardiac Muscle Sodium Channels by Fatty Acids. *Am. J. Physiol.* **1997**, *272* (2 Pt 1), C592-600. https://doi.org/10.1152/ajpcell.1997.272.2.C592.

(29) Kang, J.; Leaf, A. Evidence That Free Polyunsaturated Fatty Acids Modify Na+ Channels by Directly Binding to the Channel Proteins. *Proc Natl Acad Sci USA* **1996**, *93* (8), 3542–3546.

(30) Xiao, Y.-F.; Sigg, D. C.; Leaf, A. The Antiarrhythmic Effect of N-3 Polyunsaturated Fatty Acids: Modulation of Cardiac Ion Channels as a Potential Mechanism. *J. Membr. Biol.* **2005**, *206* (2), 141–154. https://doi.org/10.1007/s00232-005-0786-z.

(31) Börjesson, S. I.; Hammarström, S.; Elinder, F. Lipoelectric Modification of Ion Channel Voltage Gating by Polyunsaturated Fatty Acids. *Biophys. J.* **2008**, *95* (5), 2242–2253. https://doi.org/10.1529/biophysj.108.130757.

(32) Börjesson, S. I.; Parkkari, T.; Hammarström, S.; Elinder, F. Electrostatic Tuning of Cellular Excitability. *Biophys. J.* **2010**, *98* (3), 396–403. https://doi.org/10.1016/j.bpj.2009.10.026.

(33) Daeffler, K. N.-M. Functional Evaluation of Noncovalent Interactions in Neuroreceptors and Progress Toward the Expansion of Unnatural Amino Acid Methodology. phd, California Institute of Technology, 2014. https://doi.org/Daeffler, Kristina Nicole-McCleary (2014) Functional Evaluation of Noncovalent Interactions in Neuroreceptors and Progress Toward the Expansion of Unnatural Amino Acid Methodology. Dissertation (Ph.D.), California Institute of Technology. doi:10.7907/ST7S-DB65. http://resolver.caltech.edu/CaltechTHESIS:05042014-135648744 <http://resolver.caltech.edu/CaltechTHESIS:05042014-135648744>.

(34) Zhang, W.; Zhang, R.; Zhang, J.; Ye, Z.; Jin, D.; Yuan, J. Photoluminescent and Electrochemiluminescent Dual-Signaling Probe for Bio-Thiols Based on a Ruthenium(II) Complex. **2012**, *740*, 8087. https://doi.org/10.1016/j.aca.2012.06.028.

(35) Rohan, J. G.; Citron, Y.; Durrell, A. C.; Cheruzel, L. E.; Gray, H. B.; Grubbs, R. H.; Humayun, M.; Engisch, K. L.; Pikov, V.; Chow, R. H. Light-Triggered Modulation of Cellular

Electrical Activity by Ruthenium Diimine Nanoswitches. *ACS Chem Neurosci* **2013**, *4* (4), 585–593. https://doi.org/10.1021/cn300213f.

(36) Papke, R. L.; Stokes, C. Working with OpusXpress: Methods for High Volume Oocyte Experiments. *Methods* **2010**, *51* (1), 121–133. https://doi.org/10.1016/j.ymeth.2010.01.012.

(37) Catterall, W. A. Structure and Function of Voltage-Gated Sodium Channels at Atomic Resolution. *Exp. Physiol.* **2014**, *99* (1). https://doi.org/10.1113/expphysiol.2013.071969.

(38) Bezanilla, F.; Armstrong, C. Inactivation of the Sodium Channel. I. Sodium Current Experiments. *J Gen Physiol* **1977**, *70* (5), 549–566.

(39) Armstrong, C.; Bezanilla, F. Inactivation of the Sodium Channel. II. Gating Current Experiments. *J Gen Physiol* **1977**, *70* (5), 567–590.

(40) Pless, S. A.; Elstone, F. D.; Niciforovic, A. P.; Galpin, J. D.; Yang, R.; Kurata, H. T.; Ahern, C. A. Asymmetric Functional Contributions of Acidic and Aromatic Side Chains in Sodium Channel Voltage-Sensor Domains. *J Gen Physiol* **2014**, *143* (5), 645–656. https://doi.org/10.1085/jgp.201311036.

(41) Islas, A. A.; Alfredo, S.-S.; Scior, T.; Lourdes, M.-P.; M, S.-S., Eduardo. Identification of Navβ1 Residues Involved in the Modulation of the Sodium Channel Nav1.4. *PLoS ONE* **2013**, *8* (12), e81995. https://doi.org/10.1371/journal.pone.0081995.

(42) Wang, S.-Y. Y.; Bonner, K.; Russell, C.; Wang, G. K. Tryptophan Scanning of D1S6 and D4S6 C-Termini in Voltage-Gated Sodium Channels. *Biophys J* **2003**, *85* (2), 911–920. https://doi.org/10.1016/S0006-3495(03)74530-5.

Appendix 1

Heterologous Expression of Mouse and Human α3β4 Nicotinic Acetylcholine Receptors in *Xenopus laevis* Oocytes

A1.1 Abstract

The α3β4 nicotinic acetylcholine receptor (nAChR) subtype is the predominant subtype in the autonomic ganglion, but is also the highest expressed subtype in the brain after α4β2 and α7. Nicotine decreases appetite,[1] an event that has been strongly correlated with the activity of β4, and particularly α3β4 stimulation.[2] In addition, α3β4 depolarizes brown adipose tissue (BAT) and increases lipolysis.[3–5] Taken together, these results have made α3β4 a therapeutic target for obesity and type 2 diabetes.[6] Additionally, most agonists developed for the α4β2 receptor also activate the α3β4 to some extent.[7] For these reasons, it is crucial to determine the binding behaviors of agonists, such as cytisine and varenicline, at the α3β4 binding site relative to other subtypes. In order to elucidate functionally-relevant interactions in this binding site, we need to first be able to robustly express this subtype in a heterologous system, such as *Xenopus laevis* oocytes. The α3β4 subtype has been found to assemble in two stoichiometries similar to the α4β2 receptor, giving rise to a potential binding site at the α3/α3-interface. Thus, it is necessary to establish a way to readily verify receptor stoichiometry prior to further elucidation of binding site interactions.

In this study, we set out to optimize expression of α3β4 nAChRs in *Xenopus laevis* oocytes to enable future binding site studies using noncanonical amino acid mutagenesis. We were able to record currents from both mouse and human α3β4 receptors. By varying mRNA injection ratios, we identified two populations likely corresponding to two stoichiometries. Besides distinctive acetylcholine (ACh) and cytisine EC_{50} values, we observed a difference in Zn^{2+} sensitivity between the two receptor populations.

A1.2 Results and discussion

First, we started with the expression of mouse α3β4 receptors. It is known from previous studies that receptor stoichiometry can be biased by altering the mRNA injection ratio.[8] So, we injected *Xenopus laevis* oocytes with α3β4 mRNA ratios ranging from 100:1 to 1:30. Examples of current waveforms (α3β4 1:5) are shown in **Figure A1.1A** and resemble waveforms of α4β2 receptors. The resulting dose-response relationships and EC_{50} values are shown in **Figure A1.1B and Table A1.1** respectively. Injection of the α3 or β4 subunits alone did not result in functional receptors. A previous study by Papke *et al.* reported a 79 μM acetylcholine EC_{50} for mouse α3β4 receptors injected in a 1:1 ratio.[9] We found acetylcholine EC_{50} values ranging from 63.6 μM (1:5 injection ratio) to 243 μM (30:1 injection ratio), which are likely to correspond to the $(\alpha3)_2(\beta4)_3$ and $(\alpha3)_3(\beta4)_2$ stoichiometries. Biasing the injection ratios further in either direction resulted in lower expression. The previously reported value of 79 μM falls in between the values we observed and is likely the result of two mixed receptor populations.

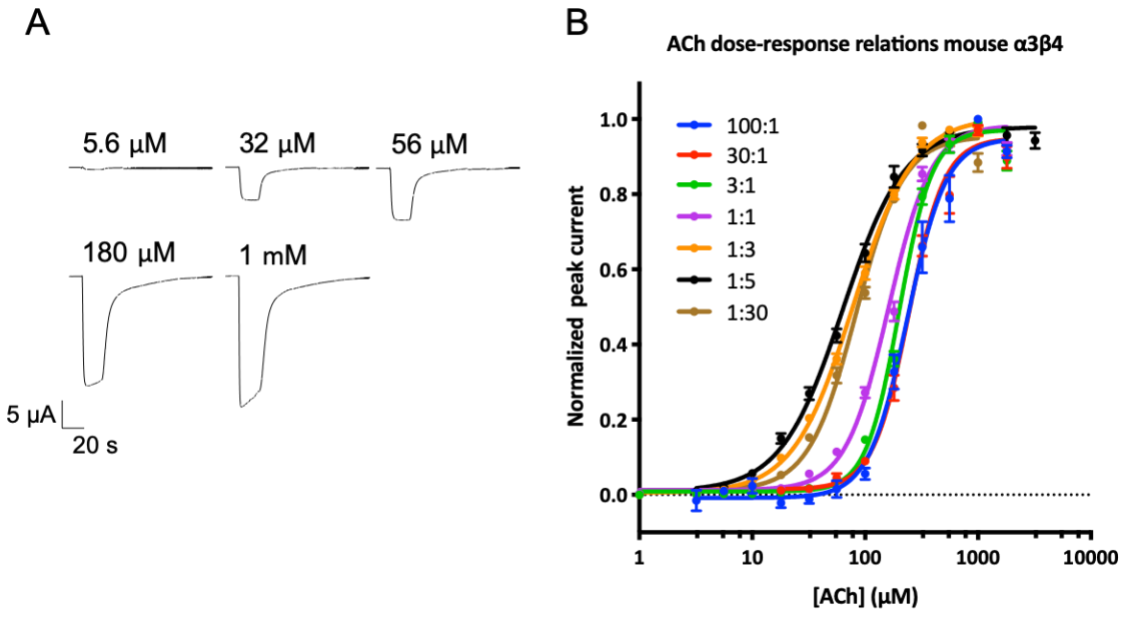

Figure A1.1 | Acetylcholine dose-response relationships of mouse α3β4 at different α3:β4 mRNA injection ratios. (A) Current waveforms of increasing doses of acetylcholine recorded from oocytes injected with a 1:5 α3β4 mRNA ratio. (B) Acetylcholine dose-response relationships of mouse α3β4 nAChRs at different α3β4 mRNA injection ratios.

Table A1.1 | EC_{50} and n_H values for mouse α3β4 receptors at different α3:β4 mRNA injection ratios. Values are reported as mean ± SEM.

Injection ratio	EC_{50} (μM)	n_H	N	$\lvert I_{max} \rvert$ (μA)
α3β4 1:30	83.2 ± 2.6	2.0 ± 0.12	16	2.6-9.6
α3β4 1:5	63.6 ± 2.3	1.6 ± 0.09	8	9.6-22
α3β4 1:3	78.6 ± 1.9	1.6 ± 0.06	12	12-30
α3β4 1:1	161 ± 4.1	2.3 ± 0.11	12	3.4-14
α3β4 3:1	201 ± 4.1	3.0 ± 0.13	13	2.1-7.1
α3β4 30:1	243 ± 8.7	2.7 ± 0.24	11	0.13-0.32
α3β4 100:1	237 ± 14	2.5 ± 0.32	3	0.10-0.13

Being able to robustly express the mouse α3β4 receptor in oocytes provides confidence that the human subtype should express well also. We are most interested in receptor responses from human receptors, so we obtained the genes for the human α3β4 subtype and repeated the same experiment as described above. We injected *Xenopus laevis* oocytes with α3β4 mRNA ratios ranging from 100:1 to 1:30. The resulting dose-response relationships and EC_{50} values are shown in **Figure A1.2 and Table A1.2** respectively. In a different study, Stokes *et al.* have reported acetylcholine EC_{50} values for the human α3β4 subtype either obtained through injection of monomeric mRNA (131 μM) and concatemeric mRNA (154 μM and 349 μM).[7] We observed acetylcholine EC_{50} values ranging from 32.3 μM (1:3 injection ratio) to 326 μM (30:1 injection ratio), which are likely to correspond to the $(\alpha3)_2(\beta4)_3$ and $(\alpha3)_3(\beta4)_2$ stoichiometries. We measured a dramatic decrease in expression level for the 30:1 injection ratio. The 326 μM value for $(\alpha3)_3(\beta4)_2$ is very close to the value reported by Stokes *et al.* from a α3β4 concatemer supplemented with α3 monomer mRNA. The EC_{50} value for the $(\alpha3)_2(\beta4)_3$ stoichiometry is almost 5-fold lower than Stokes *et al.* reported based on concatenated

subunits. This finding suggests that the Stokes-EC_{50} for $(\alpha3)_2(\beta4)_3$ probably resulted from a mixed population of receptor stoichiometries. Recent studies on concatenated $GABA_A$ subunits emphasize that concatenated subunits are often flexible in their orientation and may therefore assemble with themselves or monomeric subunits in unexpected ways.[10] Our results appear to support this claim.

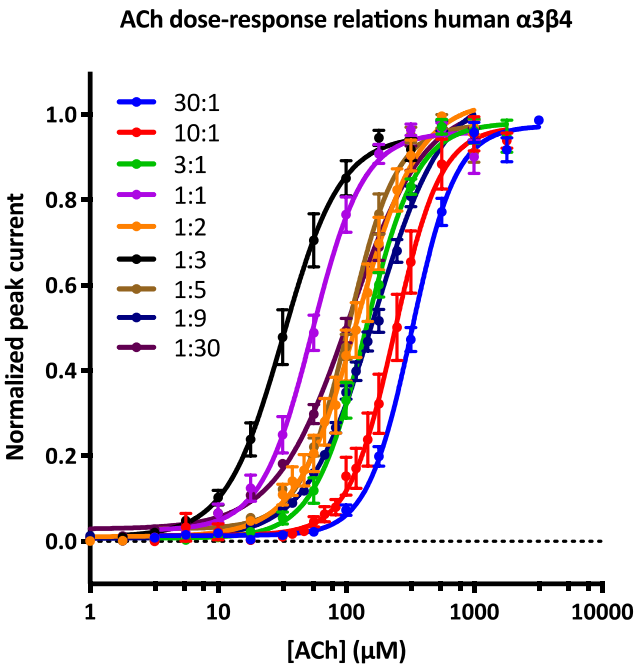

Figure A1.2 | Acetylcholine dose-response relationships of human α3β4 at different α3:β4 mRNA injection ratios.

Table A1.2 | EC_{50} and n_H values for human α3β4 receptors at different α3:β4 mRNA injection ratios.

Injection ratio	EC_{50} (µM)	n_H	N	$\lvert I_{max} \rvert$ (µA)
α3β4 1:30	107 ± 5.1	1.5 ± 0.10	12	0.10-14
α3β4 1:9	168 ± 5.8	1.6 ± 0.07	7	2.8-18
α3β4 1:5	104 ± 4.1	2.3 ± 0.18	8	5.2-36
α3β4 1:3	32.3 ± 2.4	1.9 ± 0.26	14	4.9-76
α3β4 1:2	123 ± 7.3	1.8 ± 0.16	4	7.1-24
α3β4 1:1	54.6 ± 2.8	2.2 ± 0.22	12	12-51
α3β4 3:1	142 ± 5.6	2.1 ± 0.16	6	4.0-35
α3β4 10:1	240 ± 12.7	2.4 ± 0.26	6	5.4-43
α3β4 30:1	326 ± 9.4	2.5 ± 0.16	7	0.13-0.32

Next, we determined the cytisine dose-response relationships for the mouse and human α3β4 receptors at both stoichiometries as shown in **Figure A1.3 and Table A1.3.** Previously reported values for mouse α3β4 were 20 μM[9] and 890 μM for human α3β4.[7] Concatenated subunits resulted in EC_{50}s of 214 μM and 1750 μM for the $(\alpha3)_2(\beta4)_3$ and $(\alpha3)_3(\beta4)_2$ stoichiometries respectively. We observed a cytisine EC_{50} value for mouse $(\alpha3)_2(\beta4)_3$ of 20 μM, which corresponds to the previously reported value. For mouse $(\alpha3)_3(\beta4)_2$ we measured an EC_{50} of 120 μM. For the human subtype we measured similar sensitivities for cytisine, 30.8 μM for $(\alpha3)_2(\beta4)_3$ and 172 μM for $(\alpha3)_3(\beta4)_2$. As discussed earlier for acetylcholine, the human subtype cytisine EC_{50}s are distinct from those in earlier reports also. We should note that the dose-response curve for human α3β4 at 30:1 ratio did not completely turn over and recordings at higher concentrations are necessary for conclusive results.

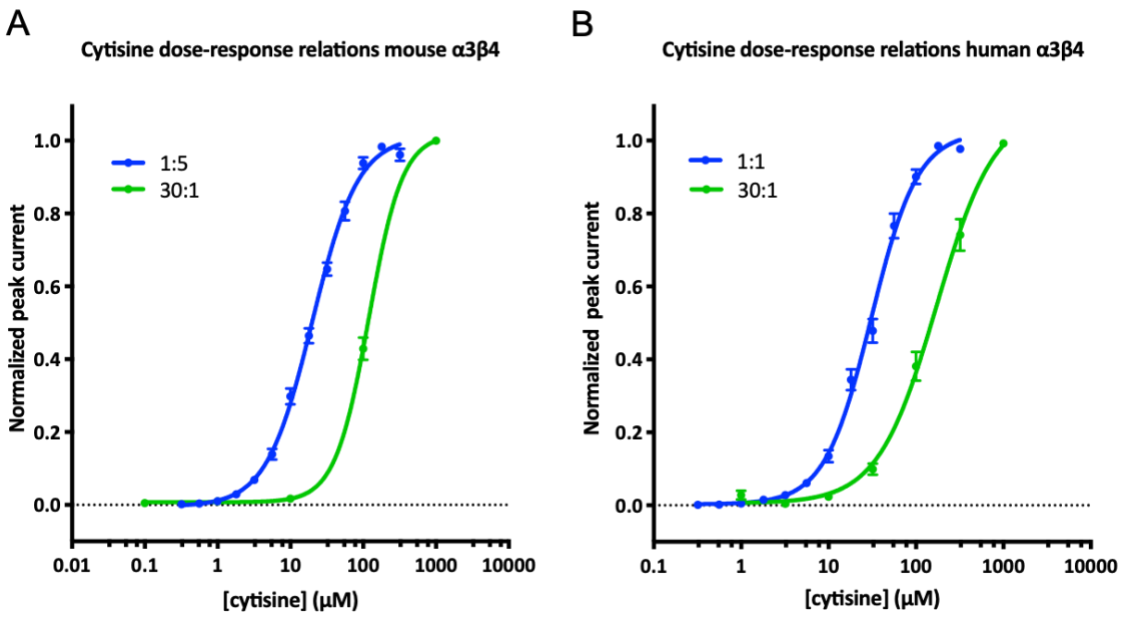

Figure A1.3 | Cytisine dose-response relationships of two stoichiometries of α3β4 from mouse and human.

Table A1.3 | EC_{50} and n_H values for mouse α3β4 receptors at different α3:β4 mRNA injection ratios.

Subtype	Compound	EC_{50} (μM)			n_H			N	$\lvert I_{max} \rvert$ (μA)
mα3β4 1:5	Cytisine	20.0	±	0.76	1.4	±	0.07	8	17 – 57
mα3β4 30:1	Cytisine	120	±	12	1.9	±	0.76	4	0.24 – 0.49
hα3β4 1:1	Cytisine	30.8	±	1.3	1.6	±	0.10	7	22-63
hα3β4 30:1	Cytisine	172	±	20	1.3	±	0.15	8	0.60-5.8

Lastly, we set out to establish an assay to readily verify receptor stoichiometry. Earlier work from Hsiao et al. has suggested differential zinc sensitivity among the two α3β4 receptor stoichiometries.[11] We determined zinc dose-response relations for both human α3β4 stoichiometries using increasing concentrations of $ZnCl_2$ supplemented with an EC_{20} dose of acetylcholine. The results are shown **in Figure A1.4** and the corresponding half-maximal potentiation and inhibition values are reported in **Table A1.4**. We observed a distinct response from the two stoichiometries of α3β4. The acetylcholine-induced current response of the $(\alpha3)_3(\beta4)_2$ stoichiometry is inhibited by zinc with an IC_{50} of 436 μM. In contrast, current response of the $(\alpha3)_2(\beta4)_3$ stoichiometry is potentiated at lower doses of zinc with an EC_{50} of 316 μM, but inhibited at higher doses with an IC_{50} of 1000 μM.

These results allow for a relatively straightforward way of verifying receptor stoichiometry. One can envision including two test doses to any experiment recording the response of acetylcholine EC_{20} and subsequently the response of a co-application of acetylcholine EC_{20} and 320 μM $ZnCl_2$. An increased response from the second dose suggests the $(\alpha3)_2(\beta4)_3$ stoichiometry and a decreased response suggests the $(\alpha3)_3(\beta4)_2$ stoichiometry.

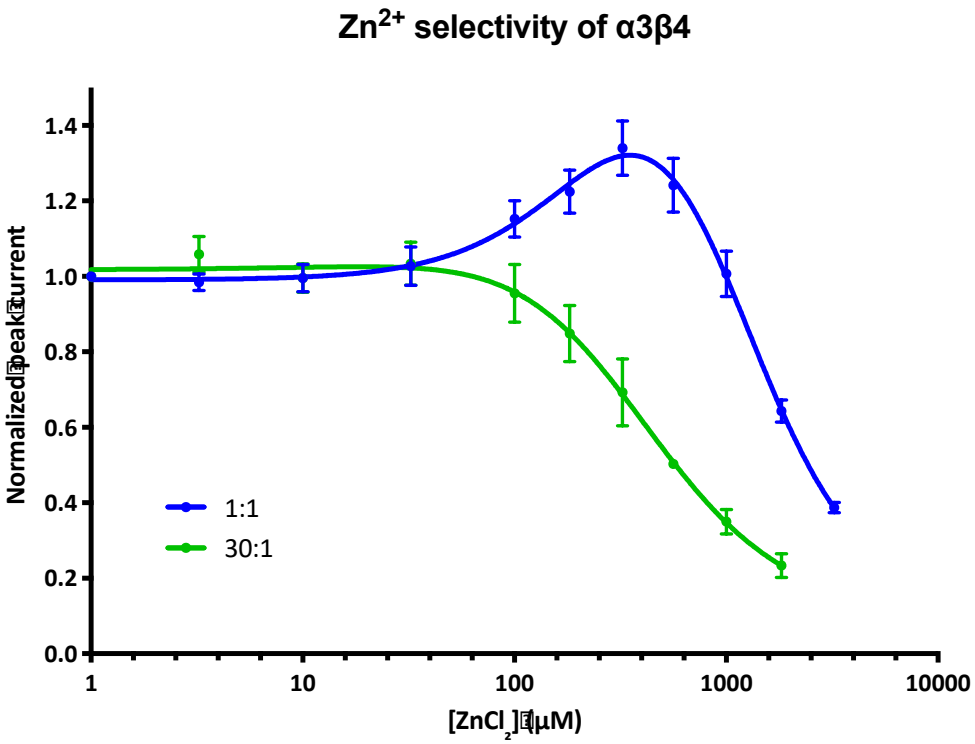

Figure A1.4 | Two stoichiometries of human α3β4 receptors demonstrate differential Zn^{2+} sensitivity. Zinc dose-response relations were determined for both α3β4 stoichiometries using increasing concentrations of $ZnCl_2$ supplemented with an EC_{20} dose of acetylcholine.

Table A1.4 | EC_{50}, IC_{50} and corresponding n_H values for human α3β4 receptors at two different α3:β4 mRNA injection ratios.

Subtype	EC_{50} (μM)	n_H	IC_{50} (μM)	n_H	N	$\lvert I_{max} \rvert$ (μA)
α3β4 1:1	316 ± 2.0	1.4 ± 1.0	1000 ± 1.1	-1.5 ± 2.3	6	0.69–5.4
α3β4 30:1			436 ± 0.09	-1.6 ± 0.4	6	0.080-0.19

A1.3 Experimental procedures

Circular DNA of mouse nAChR α3 and β4 subunits were in a pcDNA vector provided by the Lester lab. The gene of the human nAChR α3 subunit variant 1 was ordered from IDT. The mouse and human genes of both the α3 and β4 subunits were subcloned in a pGEMhe plasmid for expression in *Xenopus laevis*. cDNA in pGEMhe was linearized with restriction enzyme SbfI (New England Biolabs). Purified linear DNA (Qiaquick PCR Purification kit, Qiagen) was then transcribed *in vitro* using the T7 mMessage Machine kit (Ambion). The

resulting mRNA was isolated using the RNeasy RNA purification kit (Qiagen) and quantified by UV-vis spectroscopy (NanoDrop 2000, ThermoFisher Scientific). cDNA and mRNA were stored at -20˚C and -80˚C respectively.

Xenopus laevis oocytes (stage V-VI) were harvested and injected with RNAs according to previously described protocols.[12] Oocytes were injected with 50 nl mRNA in nuclease-free water. Post injection, oocytes were incubated at 18˚C in ND96 solution (96 mM NaCl, 2mM KCl, 1mM $MgCl_2$, 1.8 mM $CaCl_2$, 5 mM HEPES, pH 7.5) supplemented with 0.05 mg/ml gentamycin (Sigma), 2.5 mM sodium pyruvate (Acros Organics), and 0.67 mM theophylline (Sigma). Each cell was injected with 20 ng mRNA in a single injection and incubated for 24 h before recording.

All electrophysiological recordings were performed using the OpusXpress 6000A (Axon Instruments) in two-electrode voltage clamp mode at ambient temperature (20-25˚C). Oocytes were impaled with borosilicate glass pipettes filled with 3 M KCl (R = 0.3-3.0 MΩ) and clamped at a holding potential of -60 mV. Ca^{2+} free ND96 solution was used as running buffer for the first ACh dose-response experiment of mouse α3β4 receptors. All subsequent experiments have been performed in ND96 supplemented with Ca^{2+}. Agonists were prepared in ND96 with Ca^{2+} and 1 mL was applied over 15 s followed by a 2 min washout with buffer at a rate of 3 mL min^{-1} (chamber volume, 500 μL). Dose-response measurements were performed using a series of ~2-fold concentration steps, spanning multiple orders of magnitude, for a total of 8-24 doses. Data were sampled at 50 Hz.

Two-electrode voltage-clamp traces were processed in Clampfit 10.3 (Axon Instruments). Raw traces were filtered using a low pass Gaussian filter at 5 Hz, followed by a subtraction of the average baseline current preceding agonist application. Peak currents were normalized to the maximum current observed for that cell. Normalized peak currents were

averaged and fit to the Hill equation, $I = 1/(1 + (EC_{50}/[agonist])^{nH}$ in Prism 8 (GraphPad Software, Inc.), where I is the normalized peak current at a given agonist concentration, EC_{50} is the agonist concentration that elicits a half-maximum response, and n_H is the Hill coefficient. The zinc sensitivity experiment showed some zinc concentrations may be exerting both potentiating and inhibiting effects. For these data we fitted the normalized peak currents to a more complex equation that combines stimulation and inhibition components, $I = I_{min} + (I_{max}-I_{min})\{[1/(1 + (EC_{50}/X)^n] - [1/(1 + (IC_{50}/X)^m]\}$, where I is the normalized peak current at a given zinc concentration X; I_{min} is the minimal current, I_{max} is the maximal current; EC_{50} and IC_{50} are the zinc concentrations yielding half-maximal potentiation and inhibition, respectively; n and m are the Hill coefficients for potentiation and inhibition respectively. Unless otherwise stated, EC_{50}, IC_{50} and n_H data are shown as mean ± standard error of the mean (SEM).

A1.4 References

(1) Grunberg, N.; Winders, S.; Popp, K. Sex Differences in Nicotine's Effects on Consummatory Behavior and Body Weight in Rats. *Psychopharmacol. Berl* **1987**, *91* (2), 221–225.

(2) Mineur, Y. S.; Abizaid, A.; Rao, Y.; Salas, R.; J, D., Ralph; Gündisch, D.; Diano, S.; Biasi, M.; Horvath, T. L.; Gao, X.-B.; et al. Nicotine Decreases Food Intake Through Activation of POMC Neurons. *Science* **2011**, *332* (6035), 1330–1332. https://doi.org/10.1126/science.1201889.

(3) Fink, S.; Williams, J. Adrenergic Receptors Mediating Depolarization in Brown Adipose Tissue. *Am J Physiol* **1976**, *231* (3), 700–706. https://doi.org/10.1152/ajplegacy.1976.231.3.700.

(4) Batt, R.; Topping, D. Acute Effects of Nicotine on Plasma Free Fatty Acid Concentrations and on the Response to Cold Stress, in Lean and Obese (Genotype Ob/Ob) Mice. *Int J Obes* **1979**, *3* (1), 7–13.

(5) Steiner, G.; Evans, S. Sympathetic Ganglia in Brown Adipose Tissue: A New Tool to Study Ganglionic Stimulants. *Am J Physiol* **1972**, *222* (1), 111–113. https://doi.org/10.1152/ajplegacy.1972.222.1.111.

(6) Clemmensen, C.; Jall, S.; Kleinert, M.; Quarta, C.; Gruber, T.; Reber, J.; Sachs, S.; Fischer, K.; Feuchtinger, A.; Karlas, A.; et al. Coordinated Targeting of Cold and Nicotinic Receptors Synergistically Improves Obesity and Type 2 Diabetes. *Nat Commun* **2018**, *9* (1), 4304. https://doi.org/10.1038/s41467-018-06769-y.

(7) Stokes, C.; Papke, R. L. Use of an A3β4 Nicotinic Acetylcholine Receptor Subunit Concatamer to Characterize Ganglionic Receptor Subtypes with Specific Subunit Composition Reveals Species-Specific Pharmacologic Properties. *Neuropharmacology* **2012**, *63* (4), 538–546. https://doi.org/10.1016/j.neuropharm.2012.04.035.

(8) Post, M. R.; Limapichat, W.; Lester, H. A.; Dougherty, D. A. Heterologous Expression and Nonsense Suppression Provide Insights into Agonist Behavior at A6β2 Nicotinic

Acetylcholine Receptors. *Neuropharmacology* **2015**, *97*, 376–382. https://doi.org/10.1016/j.neuropharm.2015.04.009.

(9) Papke, R. L.; Wecker, L.; Stitzel, J. A. Activation and Inhibition of Mouse Muscle and Neuronal Nicotinic Acetylcholine Receptors Expressed in Xenopus Oocytes. *J Pharmacol Exp Ther* **2010**, *333* (2), 501–518. https://doi.org/10.1124/jpet.109.164566.

(10) Liao, V. W. Y.; Chua, H. C.; Kowal, N. M.; Chebib, M.; Balle, T.; Ahring, P. K. Concatenated γ-Aminobutyric Acid Type A Receptors Revisited: Finding Order in Chaos. *J. Gen. Physiol.* **2019**, jgp.201812133. https://doi.org/10.1085/jgp.201812133.

(11) Hsiao, B.; Dweck, D.; Luetje, C. Subunit-Dependent Modulation of Neuronal Nicotinic Receptors by Zinc. *J Neurosci* **2001**, *21* (6), 1848–1856.

(12) Nowak, M.; Gallivan, J.; Silverman, S.; Labarca, C.; Dougherty, D.; Lester, H. In Vivo Incorporation of Unnatural Amino Acids into Ion Channels in Xenopus Oocyte Expression System. *Methods Enzymol.* **1998**, *293*, 529.

Appendix 2

Screening of Phenolic Compounds for Allosteric Modulation of the $GABA_A$ Receptor*

A2.1 Abstract

Autism Spectrum Disorders (ASDs) are neurodevelopmental conditions characterized by social and behavioral impairments.[1] They are also associated with gut impairment and changes in intestinal microbiota.[1–4] Researchers in the Mazmanian group at Caltech have found that the serum of ASD mice contained 46 times the normal amount of the molecule 4-ethylphenyl sulfate (4-EPS, shown in **Figure A2.1**), which is a gut microbial metabolite.[5] This molecule is chemically similar to 4-methylphenol (4-MP), also known as *p*-cresol (**Figure A2.1**), of which elevated levels have been observed in the urine of children diagnosed with Autism Spectrum Disorder (ASD).[6,7] Direct injection of 4-EPS into mice results in anxiety, which further supports the idea that this metabolite directly affects behavior. When ASD mice are treated with the bacterial strain *B. fragilis*, the blood levels of 4-EPS decrease, the assortment of bacterial species in the gut starts to resemble that of the control group, and mice appear to be less anxious.

Accumulating data suggest that gut microbiota communicate with the central nervous system influencing brain function and behavior (microbiota-gut-brain axis), potentially through neural, endocrine and immune pathways.[8] As discussed in earlier chapters, positive allosteric modulators for the $GABA_A$ receptor, such as benzodiazepines, have been used as anxiolytic drugs for years. Therefore, we hypothesized that 4-EPS exerts its anxiogenic effects via direct interaction with $GABA_A$ receptors. To test for agonism and modulation of $GABA_A$

* This work has been performed in collaboration with Dr. Brittany Needham, Prof. Sarkis Mazmanian, Prof. Henry A. Lester, and Prof. Sarah Reisman.

receptors, we expressed both α1β2γ2 and α1β2 $GABA_A$ receptors in *Xenopous laevis* oocytes and measured ion channel function using two-electrode voltage clamp electrophysiology. Since 4-EPS is structurally similar to *p*-cresol, we included this molecule as well as the other closely related microbial metabolites 4-EP and 4-MPS. Chemical structures are shown in **Figure A2.1**.

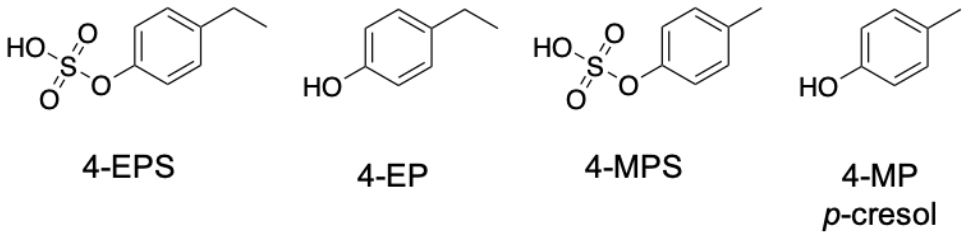

Figure A2.1 | Structures of small molecules screened in this study. 4-etylphenyl sulfate (4-EPS), 4-ethylphenol (4-EP), 4-methylphenyl sulfate (4-MPS), and 4-methylphenol (4-MP/p-cresol).

A2.2 Results and discussion

To assess functional effects of 4-EPS and related metabolites, a similar protocol was used as previously described in Chapter 3. Briefly, the current responses of three identical GABA concentration were recorded, followed by a dose of the test-compound at 40 μM. After a 30 s incubation period, a test dose was applied containing both GABA and the test-ligand. Finally, two doses of GABA were applied. The first test dose evaluates agonism properties, the second dose tests for modulation of the GABA response, which can be potentiating or inhibiting. The first three GABA doses aim to establish a baseline of the GABA response at that concentration, and the purpose of the last two GABA doses is to verify proper functioning of the receptor post modulation and control for independent rise in current amplitude.

None of the four compounds tested here demonstrated activation of either the α1β2γ2 or α1β2 receptor by its own (data not shown). When co-applied with a GABA EC_{50} we observe

different effects for the four compounds, as shown in **Figure A2.2** and **Table A2.1**. Only 4-EP shows a slight positive modulation of both $GABA_A$ subtypes of 16% and 26% respectively. In the α1β2 receptor, *p*-cresol shows a minor positive modulation of 9.7%. In contrast, 4-EPS demonstrates a slight inhibition of the GABA EC_{50} response in the α1β2 receptor of -6.7%. These effects are small, so we decided to repeat this experiment at a lower GABA concentration.

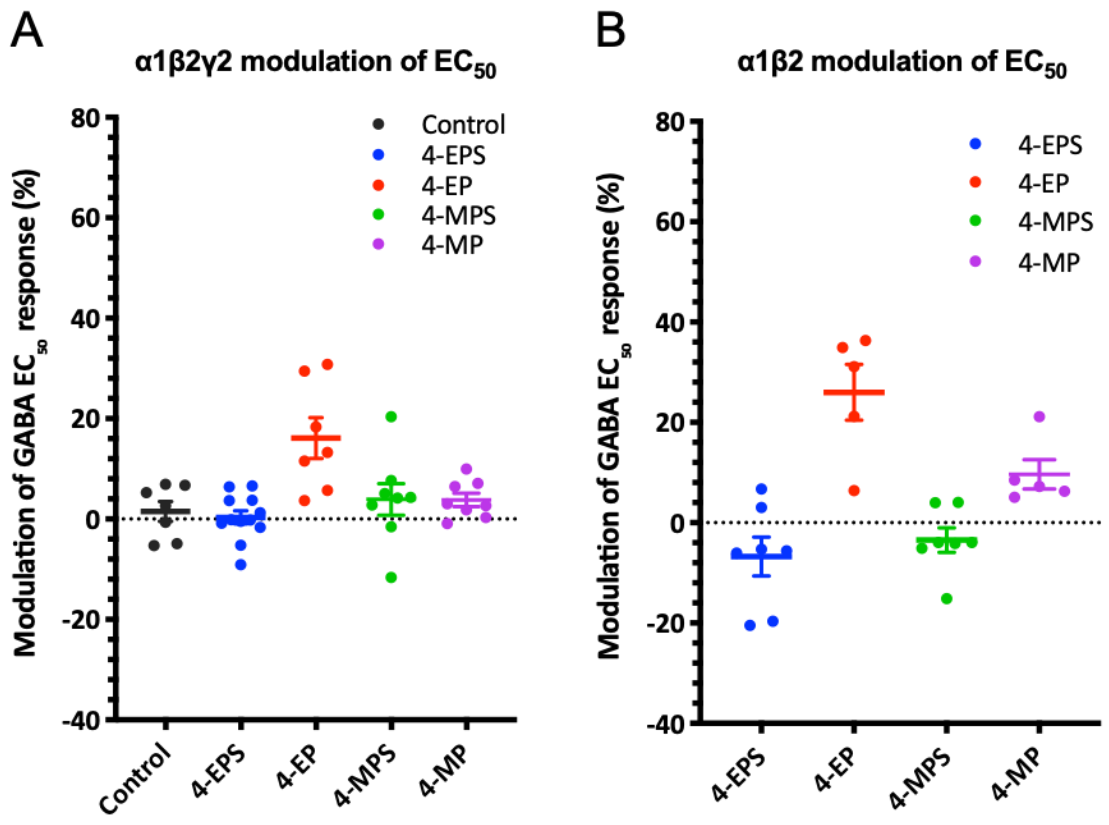

Figure A2.2 | Modulation of GABA EC_{50} response of α1β2γ2 $GABA_A$ receptors by phenolic compounds. All compounds were applied at 40 μM concentration.

Table A2.1 | Relative modulation of GABA EC_{50} α1β2γ2 $GABA_A$ receptors by phenolic compounds. All compounds were applied at 40 μM concentration.

Subtype	Ligand	Relative modulation of GABA EC_{50} (%)	N	$\lvert I_{max} \rvert$ (μA)
α1β2γ2	GABA only	1.5 ± 2.0	7	4.4-10.
α1β2γ2	4-EPS	0.33 ± 1.3	12	1.9-13

α1β2γ2	4-EP	16	±	4.1	7	3.1-10
α1β2γ2	4-MPS	3.9	±	3.2	8	3.4-13
α1β2γ2	4-MP	3.8	±	1.3	8	3.6-18
α1β2	4-EPS	-6.7	±	3.9	7	0.66-2.8
α1β2	4-EP	26	±	5.6	5	0.60-2.4
α1β2	4-MPS	-3.5	±	2.4	7	0.81-3.3
α1β2	4-MP	9.7	±	2.9	5	2.2-3.4

The modulation effects of these compounds at 40 μM co-applied with GABA EC_5, are shown in **Figure A2.3** and **Table A2.2**. As expected, 4-EP shows a positive modulation in both subtypes, but with greater amplitudes (28% and 38%) than was observed at GABA EC_{50}. In contrast to the results in **Figure A2.2**, 4-EPS also demonstrates positive modulation at both α1β2γ2 and α1β2 at 20% and 14% respectively. The two 4-methyl compounds do not show any functional effects.

Overall, the functional effects we observed here are fairly small, but modulation of 38% by 4-EP is still considerable. However, the concentration used here, 40 μM, is a factor 10 higher than the concentration measured in ASD mice serum of (3 μM). Taken together, these results do not strongly suggest that the behavioral effects observed by Hsiao *et al.* are a result of direct modulation of $GABA_A$ receptors. Future studies could involve screening other $GABA_A$ subtypes or even other Cys-loop receptors such as the $5HT_3$-receptor, which also could play a role in the development of anxiety-like behavioral effects.

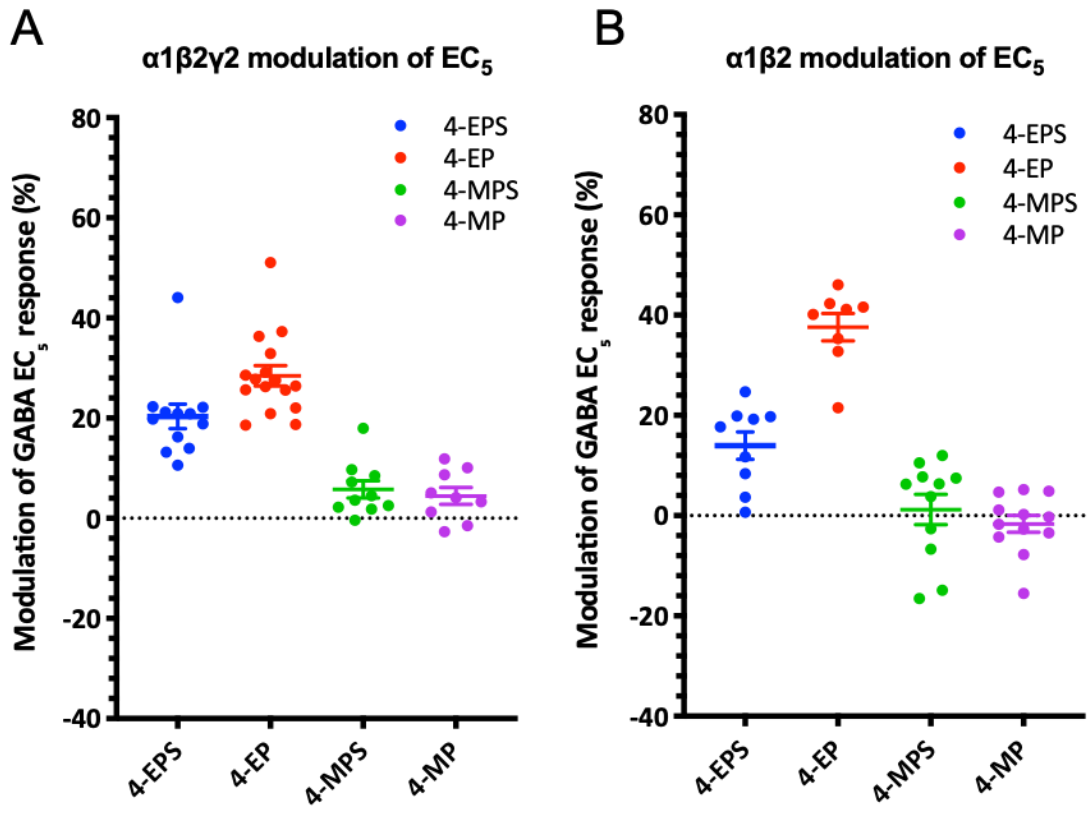

Figure A2.3 | Modulation of of GABA EC_5 response of α1β2γ2 $GABA_A$ receptors by phenolic compounds. All compounds were applied at 40 μM concentration.

Table A2.2 | Relative modulation of GABA EC_5 α1β2γ2 $GABA_A$ receptors by phenolic compounds. All compounds were applied at 40 μM concentration.

Subtype	Ligand	Relative modulation of GABA EC_5 (%)			N	$\lvert I_{max} \rvert$ (μA)
α1β2γ2	4-EPS	20	±	2.4	12	0.050-0.89
α1β2γ2	4-EP	28	±	2	16	0.050-1.0
α1β2γ2	4-MPS	5.8	±	1.7	10	0.080-0.72
α1β2γ2	4-MP	4.5	±	1.7	9	0.040-0.65
α1β2	4-EPS	14	±	2.7	9	0.060-0.83
α1β2	4-EP	38	±	2.7	9	0.060-0.88
α1β2	4-MPS	1.2	±	3	11	0.10-0.91
α1β2	4-MP	-1.6	±	1.7	12	0.070-0.62

A2.3 Experimental procedures

Circular DNA of human $GABA_A$ receptor α1, β2s and γ2s subunits were in a pGEMhe plasmid. For both β2s and γ2s only the short isoforms were used, however for convenience we refer to the subunits as β2 and γ2. cDNA in pGEMhe was linearized with restriction enzyme NheI (for α1 and γ2 subunits), and Sph1 (for the β2 subunit) (New England Biolabs). Purified linear DNA (Qiaquick PCR Purification kit, Qiagen) was then transcribed *in vitro* using the T7 mMessage Machine kit (Ambion). The resulting mRNA was isolated using the RNeasy RNA purification kit (Qiagen) and quantified by UV-vis spectroscopy (NanoDrop 2000, ThermoFisher Scientific). cDNA and mRNA were stored at -20˚C and -80˚C respectively.

Xenopus laevis oocytes (stage V-VI) were harvested and injected with mRNA according to previously described protocols.[9] Oocytes were injected with 50-75 nl mRNA in nuclease-free water. Post injection, oocytes were incubated at 18˚C in ND96 solution (96 mM NaCl, 2mM KCl, 1mM $MgCl_2$, 1.8 mM $CaCl_2$, 5 mM HEPES, pH 7.5) supplemented with 0.05 mg/ml gentamycin (Sigma), 2.5 mM sodium pyruvate (Acros Organics), and 0.67 mM theophylline (Sigma).

For expression of α1β2γ2 receptors, α1, β2, and γ2 mRNA were mixed in 2:2:1 ratio by mass. For expression of α1β2 receptors, α1 and β2 mRNA were mixed in 1:1 ratio by mass. Each cell was injected with 5 ng or 15 ng mRNA in a single injection for the α1β2γ2 and α1β2 respectively. Oocytes were then incubated for 24 h before recording.

All electrophysiological recordings were performed using the OpusXpress 6000A (Axon Instruments) in two-electrode voltage clamp mode at ambient temperature (20-25˚C). Oocytes were impaled with borosilicate glass pipettes filled with 3 M KCl (R = 0.3-3.0 MΩ) and clamped at a holding potential of -60 mV. ND96 solution with Ca^{2+} was used as running

buffer. GABA and test-ligand solutions were prepared in ND96 with Ca^{2+} and 1 mL was applied over 15 s followed by a 5 min washout with buffer at a rate of 3 mL min^{-1} (chamber volume, 500 μL). Data for each condition were obtained from at least two different batches of oocytes. Data were sampled at 50 Hz.

For potentiation experiments the potentiation protocol previously described in Chapter 3 was used. The protocol is as follows: three identical GABA doses were applied, followed by a dose of the test-ligand at 40 μM. After a 30 s incubation period, a test dose was applied containing both GABA and the test-ligand. Finally, two doses of GABA were applied. The first test dose evaluates agonism properties, the second dose tests for modulation of the GABA response, which can be potentiating or inhibiting. The first three GABA doses aim to establish a baseline of the GABA response at that concentration, while the purpose of the last two GABA doses is to verify proper functioning of the receptor post modulation and control for independent rise in current amplitude.

Two-electrode voltage-clamp traces were processed in Clampfit 10.3 (Axon Instruments). Raw traces were filtered using a low pass Gaussian filter at 5 Hz, followed by a subtraction of the average baseline current preceding ligand application. The current responses from the five GABA doses were averaged (GABA only) and subtracting this from the response of the co-application dose (GABA + test-ligand) gave the calculated change in response. Multiplying this value by 100% rendered the relative modulation (inhibition/potentiation) of the GABA response by the test-ligand. Relative modulation is reported as the mean ± standard error of the mean (SEM). For the GABA concentrations either the EC_{50} or EC_5 were used as specified in the results section.

Syntheses of the four compounds were performed by members of the Reisman group at Caltech.

A2.4 References

(1) Strati, F.; Cavalieri, D.; Albanese, D.; De Felice, C.; Donati, C.; Hayek, J.; Jousson, O.; Leoncini, S.; Renzi, D.; Calabrò, A.; et al. New Evidences on the Altered Gut Microbiota in Autism Spectrum Disorders. *Microbiome* **2017**, *5*. https://doi.org/10.1186/s40168-017-0242-1.

(2) Kang, D.-W. W.; Ilhan, Z. E.; Isern, N. G.; Hoyt, D. W.; Howsmon, D. P.; Shaffer, M.; Lozupone, C. A.; Hahn, J.; Adams, J. B.; Rosa, K.-B. Differences in Fecal Microbial Metabolites and Microbiota of Children with Autism Spectrum Disorders. *Anaerobe* **2018**, *49*, 121–131. https://doi.org/10.1016/j.anaerobe.2017.12.007.

(3) Needham, B. D.; Tang, W.; Wu, W.-L. Searching for the Gut Microbial Contributing Factors to Social Behavior in Rodent Models of Autism Spectrum Disorder: Gut Microbiota and Social Behavior. *Dev. Neurobiol.* **2018**, *78* (5), 474–499. https://doi.org/10.1002/dneu.22581.

(4) Li, Q.; Han, Y.; Dy, A. B. C.; Hagerman, R. J. The Gut Microbiota and Autism Spectrum Disorders. *Front. Cell. Neurosci.* **2017**, *11*. https://doi.org/10.3389/fncel.2017.00120.

(5) Hsiao, E. Y.; W, M., Sara; Hsien, S.; Sharon, G.; Hyde, E. R.; Tyler, M.; Codelli, J. A.; Chow, J.; Reisman, S. E.; Petrosino, J. F.; et al. Microbiota Modulate Behavioral and Physiological Abnormalities Associated with Neurodevelopmental Disorders. *Cell* **2013**, *155* (7), 1451–1463. https://doi.org/10.1016/j.cell.2013.11.024.

(6) Persico, A. M.; Napolioni, V. Urinary P-Cresol in Autism Spectrum Disorder. *Neurotoxicol Teratol* **2013**, *36*, 82–90. https://doi.org/10.1016/j.ntt.2012.09.002.

(7) Altieri, L.; Neri, C.; Sacco, R.; Curatolo, P.; Benvenuto, A.; Muratori, F.; Santocchi, E.; Bravaccio, C.; Lenti, C.; Saccani, M.; et al. Urinary P-Cresol Is Elevated in Small Children with Severe Autism Spectrum Disorder. *Biomarkers* **2011**, *16* (3), 252–260. https://doi.org/10.3109/1354750X.2010.548010.

(8) Cryan, J. F.; Dinan, T. G. Mind-Altering Microorganisms: The Impact of the Gut Microbiota on Brain and Behaviour. *Nat Rev Neurosci* **2012**, *13* (10), 701–712. https://doi.org/10.1038/nrn3346.

(9) Nowak, M.; Gallivan, J.; Silverman, S.; Labarca, C.; Dougherty, D.; Lester, H. In Vivo Incorporation of Unnatural Amino Acids into Ion Channels in Xenopus Oocyte Expression System. *Methods Enzymol.* **1998**, *293*, 529.

Appendix 3

Revised Synthetic Route for the Preparation of the Non-Canonical Amino Acid 4,5,6,7-F_4-Trp

A3.1 Abstract

In chapter two, the use of non-canonical acids has been described to probe functional interactions in the α4β2 nAChR. To probe for a cation-π interaction with residue W154, 4,5,6,7-tetrafluoro-tryptophan (4,5,6,7-F_4-Trp) was used. This appendix describes a revised synthetic route to obtain the non-canonical amino acid 4,5,6,7-tetrafluoro-tryptophan starting from the 4,5,6,7-tetrafluoro-indole.

A3.2 Results and discussion

Scheme A3.2.1 | Preparation of NVOC-protected 4,5,6,7-tetrafluoro-tryptophan.

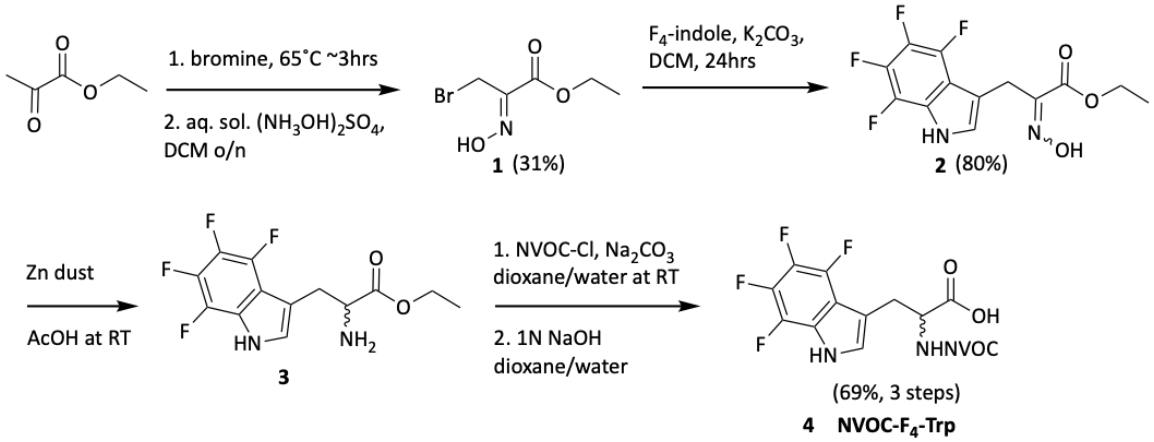

We performed all steps following the thesis of Wenge Zhong, including the synthesis of 4,5,6,7-tetrafluoro-indole (3 steps), except for the reduction of oxime **2** to obtain the amine **3** (**Scheme A3.2.1**).[1] The reduction of **2** was first attempted using zinc dust and ammonium formate while refluxing in methanol overnight as described by Abiraj *et al.,*[2] but no product formation was observed. Replacing ammonium formate with ammonium chloride did not yield the desired product **3** either. Performing the reduction of the oxime with zinc and acetic

acid[3] was successful and produced amine **3.** Nitroveratryloxycarbonyl (NVOC) protection, followed by ester hydrolysis yielded 4,5,6,7-tetrafluorotryptophan in 69% over three steps.

A3.3 Experimental procedures

Unless otherwise stated, reactions were carried out under ambient conditions in air. Commercially available reagents were obtained from Sigma Aldrich and used without further purification. Thin-layer chromatography with Sigma Aldrich silica gel coated plates with fluorescent indicator (0.25 mm) was used to monitor reactions. Silica gel chromatography was conducted as described by Still *et al.,*[4] with silica gel purchased from Alfa Aesar (60 Å, 230-400 mesh). NMR spectra were recorded on a Varian 500 MHz spectrometer. Resonances for NMR spectra are reported relative to Me_4Si (δ 0.0). Syntheses are described below.

Ethyl-3-bromo-2-(hydroxyimino)-propanoate (1)

To a three-necked 250 mL flask was added 10 g (9.6 mL, 0.086 mol) of ethyl pyruvate. At 65°C and under a constant flow of nitrogen, was added dropwise 5.3 mL (1.2 eq.) of bromine over 1 hour. (By-product HBr was taken away by nitrogen, which was passed through a 3N NaOH solution.) Two hours later, a golden liquid resulted and was dissolved in 65 mL dichloromethane (DCM). An 80 mL aqueous solution containing 14.1 g of hydroxylamine sulfate was added. The reaction was kept stirring vigorously overnight. The two layers were separated, and the aqueous layer was extracted with 30 mL of DCM twice. The organic layers were combined and dried over sodium sulfate. DCM was rotoevaporated off and the resulting oil was redissolved in a minimal amount of ethyl acetate. Hexane was added until the solution turned cloudy. Crystallization overnight yielded 5.5 g (31%) of pure product. ^{1}H NMR ($CDCl_3$) δ 9.92 (s, 1H), 4.38 (q, 2H), 4.26 (s, 2H), 1.39 (t, 3H).

4,5,6,7-tetrafluoro-tryptophan precursor (2)

In a 100 mL flask, 0.42 g (2 mmol) of **1** and 0.95 g (5 mmol, 2.5 eq.) of 4,5,6,7-tetrafluoro-indole were dissolved in 20 mL of dry DCM. To the solution, 0.34 g (3.2 mmol, 1.6 eq.) of sodium carbonate was added. The reaction was kept stirring vigorously for 24 hours. DCM was rotoevaporated off. Residue was dissolved in ethyl acetate and washed with water twice. The aqueous layer was extracted with ethyl acetate twice. Combined organic layers were dried over magnesium sulfate. After flash chromatography using methanol/DCM, 500 mg of product was isolated (1.6 mmol, 80%). ^{1}H NMR (CD_3CN) δ 9.93 (b, 1H), 9.76 (b, 1H), 7.04 (s, 1H), 4.19 (q, 2H), 4.05 (s, 2H), 1.22 (t, 3H).

4,5,6,7-tetrafluoro-tryptophan ethyl ester (3)

In a 25 mL flask, 20 mg (0.06 mmol) of **2** was dissolved in 1 mL acetic acid. 16 mg (0.24 mmol, 4 eq.) of zinc dust was added and the reaction was stirred overnight at room temperature. After 24 hours, the reaction was filtered over celite and concentrated. Product was used in next step without purification.

NVOC-4,5,6,7-tetrafluoro-tryptophan (4)

In a 50 mL flask, 156 mg (0.51 mmol) of **3** was dissolved in 14 mL dioxane and 6 mL water. 57 mg (1.05 eq.) of sodium carbonate was added, as well as a solution of 149 mg (1.05 eq.) NVOC-Cl dissolved in 10 mL dioxane. The reaction was stirred for 2 hours at room temperature and monitored with LCMS. The reaction was diluted with water and ethyl acetate and the mixture was extracted with ethyl acetate three times. The combined organic layers were dried over magnesium sulfate and ethyl acetate was rotoevaporated off. The resulting oil was dissolved in 15 mL dioxane and 4 mL water. 1.43 mL (1.53 mmol, 3 eq.) of sodium hydroxide solution (1N) was added. The reaction was stirred overnight at room temperature. The reaction mixture was heated and 0.5 mL of sodium hydroxide solution was added. After

3 hours, 1 M HCl was added and the mixture was diluted with ethyl acetate. After extractions with ethyl acetate, the solvent was rotoevaporated off. Flash chromatography using hexanes/ethyl acetate resulted in 182 mg (0.35 mmol, 69% over 3 steps) of product.

^{1}H NMR (DMSO-d6) δ 12.00 (s, 1H), 7.87 (dd, 1H), 7.69 (s, 1H), 7.32 (s, 1H), 7.11 (s, 1H), 5.3 (q, 2H), 4.24 (m, 1H), 3.85 (s, 6H), 3.27 (m, 2H).

A3.4 References

(1) Zhong, W. Physical Organic Chemistry on the Nicotinic Acetylcholine Receptor. Ph.D., California Institute of Technology: Pasadena, CA, 1998.

(2) Abiraj, K.; Gowda, D. C. Zinc/Ammonium Formate: A New Facile System for the Rapid and Selective Reduction of Oximes to Amines. *J. Chem. Res.* **2003**, *2003* (6), 332–334. https://doi.org/10.3184/030823403103174281.

(3) Park, K.; Gopalsamy, A.; Aplasca, A.; Ellingboe, J. W.; Xu, W.; Zhang, Y.; Levin, J. I. Synthesis and Activity of Tryptophan Sulfonamide Derivatives as Novel Non-Hydroxamate TNF-Alpha Converting Enzyme (TACE) Inhibitors. *Bioorg. Med. Chem.* **2009**, *17* (11), 3857–3865. https://doi.org/10.1016/j.bmc.2009.04.033.

(4) Still, W. C.; Kahn, M.; Mitra, A. Rapid Chromatographic Technique for Preparative Separations with Moderate Resolution. *J. Org. Chem.* **1978**, *43* (14), 2923–2925. https://doi.org/10.1021/jo00408a041.